NASA/TP—2005-212505

Lifetime Reliability Prediction of Ceramic Structures Under Transient Thermomechanical Loads

Noel N. Nemeth
Glenn Research Center, Cleveland, Ohio

Osama M. Jadaan
University of Wisconsin, Platteville, Platteville, Wisconsin

John P. Gyekenyesi
Glenn Research Center, Cleveland, Ohio

Errata

An errata was added to this document, August 2011.

September 2005

NASA STI Program . . . in Profile

Since its founding, NASA has been dedicated to the advancement of aeronautics and space science. The NASA Scientific and Technical Information (STI) program plays a key part in helping NASA maintain this important role.

The NASA STI Program operates under the auspices of the Agency Chief Information Officer. It collects, organizes, provides for archiving, and disseminates NASA's STI. The NASA STI program provides access to the NASA Aeronautics and Space Database and its public interface, the NASA Technical Reports Server, thus providing one of the largest collections of aeronautical and space science STI in the world. Results are published in both non-NASA channels and by NASA in the NASA STI Report Series, which includes the following report types:

- TECHNICAL PUBLICATION. Reports of completed research or a major significant phase of research that present the results of NASA programs and include extensive data or theoretical analysis. Includes compilations of significant scientific and technical data and information deemed to be of continuing reference value. NASA counterpart of peer-reviewed formal professional papers but has less stringent limitations on manuscript length and extent of graphic presentations.

- TECHNICAL MEMORANDUM. Scientific and technical findings that are preliminary or of specialized interest, e.g., quick release reports, working papers, and bibliographies that contain minimal annotation. Does not contain extensive analysis.

- CONTRACTOR REPORT. Scientific and technical findings by NASA-sponsored contractors and grantees.

- CONFERENCE PUBLICATION. Collected papers from scientific and technical conferences, symposia, seminars, or other meetings sponsored or cosponsored by NASA.

- SPECIAL PUBLICATION. Scientific, technical, or historical information from NASA programs, projects, and missions, often concerned with subjects having substantial public interest.

- TECHNICAL TRANSLATION. English-language translations of foreign scientific and technical material pertinent to NASA's mission.

Specialized services also include creating custom thesauri, building customized databases, organizing and publishing research results.

For more information about the NASA STI program, see the following:

- Access the NASA STI program home page at *http://www.sti.nasa.gov*

- E-mail your question via the Internet to *help@sti.nasa.gov*

- Fax your question to the NASA STI Help Desk at 443–757–5803

- Telephone the NASA STI Help Desk at 443–757–5802

- Write to:
  NASA Center for AeroSpace Information (CASI)
  7115 Standard Drive
  Hanover, MD 21076–1320

NASA/TP—2005-212505

Lifetime Reliability Prediction of Ceramic Structures Under Transient Thermomechanical Loads

Noel N. Nemeth
Glenn Research Center, Cleveland, Ohio

Osama M. Jadaan
University of Wisconsin, Platteville, Platteville, Wisconsin

John P. Gyekenyesi
Glenn Research Center, Cleveland, Ohio

National Aeronautics and
Space Administration

Glenn Research Center
Cleveland, Ohio 44135

September 2005

Acknowledgments

This work was jointly performed under Department of Energy (DOE) contract no. DE–A101–97EE50464, the NASA Higher Operating Temperature Propulsion Components (HOTPC) program, and the NASA Ultra-Efficient Engine Technology (UEET) Program. The authors wish to acknowledge the contributions of Eric Baker of Connecticut Reserve Technologies, Lynn Powers of Case Western Reserve University, Tamas Palfi of Budapest University of Technology and Economics, Albert Segall of Pennsylvania State University, Matt Ferber of Oak Ridge National Laboratory, Mark Andrews of Caterpillar, Inc., and Uwe Rettig of Siemens AG.

Errata

Issued August 2011 for

NASA/TP—2005-212505
Lifetime Reliability Prediction of Ceramic Structures Under Transient Thermomechanical Loads
Noel N. Nemeth, Osama M. Jadaan, and John P. Gyekenyesi

September 2005

See page iii for changes.

Level of Review: This material has been technically reviewed by a committee of peers.

Available from

NASA Center for Aerospace Information
7115 Standard Drive
Hanover, MD 21076–1320

National Technical Information Service
5301 Shawnee Road
Alexandria, VA 22312

Available electronically at http://www.sti.nasa.gov

Errata

Page 122, figure D.6. has been changed to read as follows:

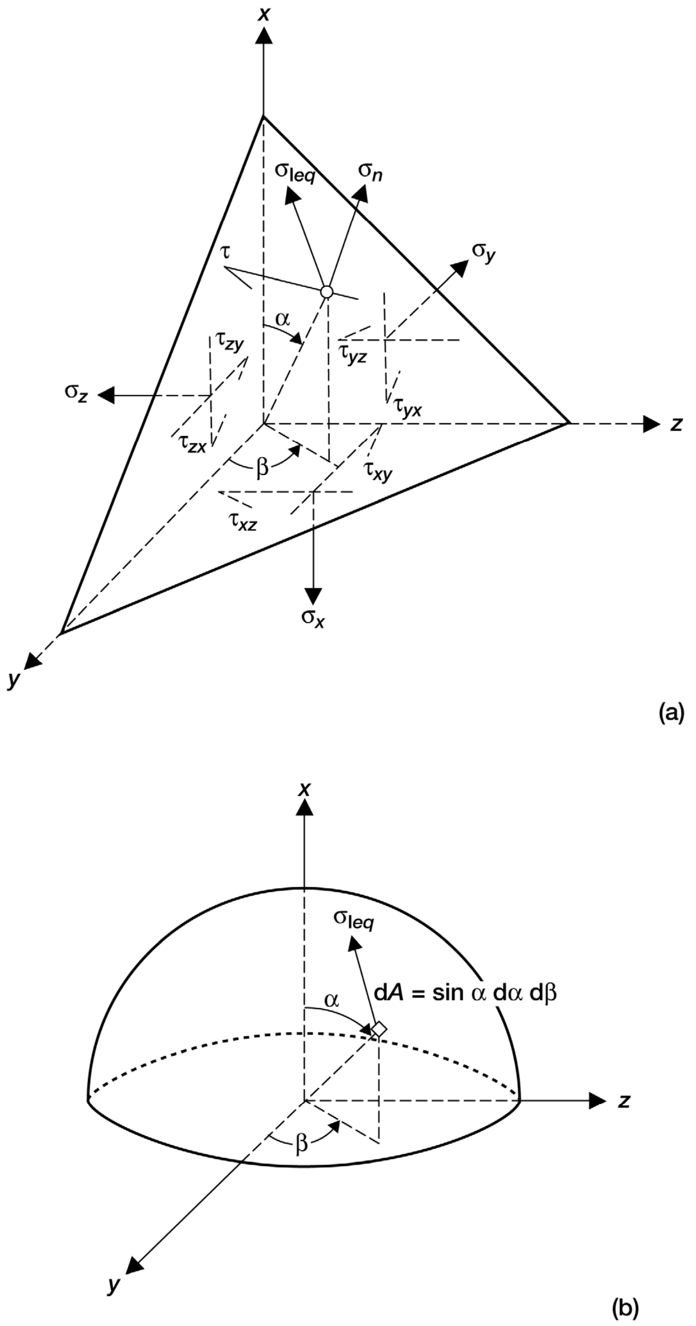

Figure D.6.—Projection of equivalent stress onto the upper half of a unit radius sphere in the global coordinate system. (a) Cauchy stress components on an infinitesimal tetrahedron. Direction cosines: $\ell = \cos\alpha$, $m = \sin\alpha\cos\beta$, $n = \sin\alpha\sin\beta$; $\sigma_n = \ell^2\sigma_x + m^2\sigma_y + n^2\sigma_z + 2(\ell m\tau_{xy} + mn\tau_{yz} + n\ell\tau_{zx})$; $\tau = \sqrt{(\ell\sigma_x + m\tau_{yx} + n\tau_{zx})^2 + (\ell\tau_{xy} + m\sigma_y + n\tau_{zy})^2 + (\ell\tau_{xz} + m\tau_{yz} + n\sigma_z)^2 - \sigma_n^2}$. (b) Global coordinate system.

Contents

Lifetime Reliability Prediction of Ceramic Structures Under Transient Thermomechanical Loads

Noel N. Nemeth
National Aeronautics and Space Administration
Glenn Research Center
Cleveland, Ohio 44135

Osama M. Jadaan
University of Wisconsin, Platteville
Platteville, Wisconsin 53818

John P. Gyekenyesi
National Aeronautics and Space Administration
Glenn Research Center
Cleveland, Ohio 44135

Summary

An analytical methodology is developed to predict the probability of survival (reliability) of ceramic components subjected to harsh thermomechanical loads that can vary with time (transient reliability analysis). This capability enables more accurate prediction of ceramic component integrity against fracture in situations such as turbine startup and shutdown, operational vibrations, atmospheric reentry, or other rapid heating or cooling situations (thermal shock). The transient reliability analysis methodology developed herein incorporates the following features:

- Fast-fracture transient analysis (reliability analysis without slow crack growth, SCG)
- Transient analysis with SCG (reliability analysis with time-dependent damage due to SCG)
- A computationally efficient algorithm to compute the reliability for components subjected to repeated transient loading (cyclic or block loading)
- Cyclic fatigue modeling using a combined SCG and Walker fatigue law
- Proof testing for transient loads
- Weibull and fatigue parameters that are allowed to vary with temperature or time

Component-to-component variation in strength (stochastic strength response) is accounted for with the Weibull distribution, and either the principle of independent action or the Batdorf theory is used to predict the effect of multiaxial stresses on reliability. The reliability analysis can be performed either as a function of the component surface (for surface-distributed flaws) or the component volume (for volume-distributed flaws). The transient reliability analysis capability has been added to the NASA CARES/*Life* (Ceramics Analysis and Reliability Evaluation of Structures/*Life*) code. CARES/*Life* was modified to interface with commercially available finite element analysis software, such as ANSYS,[1] when used to model the effects of transient load histories. Examples are provided to demonstrate the features of the methodology as implemented in the CARES/*Life* program.

1.0 Introduction

1.1 General Overview

Ceramics are being used, or being considered for use, for a wide variety of high-performance applications that operate in harsh environments, including static and rotating turbine parts, thermal protection systems, dental prosthetics, fuel cells, oxygen transport membranes, radomes, and microelectromechanical systems (MEMS). To use these high-technology ceramics successfully in structural applications that push the envelope of materials

---

[1] Swanson Analysis Systems, Inc., Houston, PA.

capability, design engineers must consider that brittle materials are designed and analyzed differently than metallic materials.

Brittle materials tend to abruptly shatter or fail catastrophically when under load. There is little or no warning of impending failure because large cracks or damaged areas do not appear prior to rupture (except under certain circumstances such as excessive compressive loadings). They are also susceptible to damage from impact. Consequently, ceramic components must be handled carefully to avoid scratching or damaging their surfaces, and they must be designed to resist damage from the impact of foreign objects as much as possible without severely compromising performance. The strength from one ceramic component to the next tends to vary considerably, or even greatly, because of the variability in severity and random distribution of difficult-to-control microscopic flaws that arise from processing. In addition, the strength degrades over time because of a variety of effects, such as slow crack growth (SCG), creep, and oxidation.

In ceramics, SCG initiates at preexisting flaws and continues until a flaw reaches a critical crack length, whereupon unstable crack growth ensues, resulting in catastrophic component failure (Wiederhorn, 1974a). SCG occurs because of the interaction between the environment and the high-stress fields near the crack tip. This can be from a chemical reaction between the environment and the material constituents, from temperature affecting the material constituents themselves, or some combination thereof. For some ceramics, SCG can be exacerbated by cyclic loading. In this case, repetitive loading and unloading causes irreversible degradation at or near the crack tip, thereby worsening SCG. In ceramics, SCG or fatigue-assisted SCG proceeds from inherent (existing) flaws. Conversely, creep rupture occurs because of bulk damage in the material in the form of void nucleation (new flaw creation) and coalescence that eventually leads to macrocracks, which can then propagate to failure (Grathwohl, 1984). Hence, for ceramics to be successfully introduced in structural applications, life prediction and design methodologies that account for the various brittle material failure modes and that can calculate the tradeoffs between service life, performance, and optimized material usage are required.

Because of the brittleness of ceramics and the random nature of their inherent flaws, the lifetime of ceramic structures is predicted using probabilistic analysis and design methodologies. Several design codes such as CARES/*Life* (Ceramics Analysis and Reliability Evaluation of Structures/*Life*, Nemeth et al., 2003), CERAMIC/ERICA (Peralta et al., 1996), and STAU (Heger, 1991) have been created. These codes predict the failure probability of ceramic components subjected to fast fracture and SCG, where fast fracture refers to component rupture in the absence of SCG and where component strength is strictly controlled by the size, distribution, and orientation of inherent flaws relative to the imposed loading.

The purpose of this report is to describe a methodology to perform reliability analysis for generalized transient loading (loads that vary over time—including temperature loading) for fast-fracture and SCG failure modes. This capability, which is known as transient reliability analysis, has been added to the CARES/*Life* program. Prior to this development, the SCG and cyclic fatigue theories in CARES/*Life* were limited to static loading and simple constant-amplitude cyclic loading for specific waveforms, such as sawtooth or sinusoidal (Nemeth et al., 2003). Also, the fatigue and fracture response (i.e., the parameters that describe SCG and the Weibull parameters that describe the probabilistic distribution of strength) were not allowed to vary over time, so situations involving fluxuating temperatures could not be properly analyzed.

A number of researchers have contributed to the development of transient reliability analysis methodology (Paluszny and Nicholls, 1978; Barnett et al., 1967; Jakus and Ritter, 1981; Stanley and Chau, 1983; Mencik, 1984; Brückner-Foit and Ziegler, 1999a and 1999b; and Ziegler, 1998). Paluszny and Nicholls (1978) described a generalized algorithm for SCG where they used Wiederhorn's power law formulation (Wiederhorn, 1974a) to model SCG and the principle of independent action (PIA) model (Barnett et al., 1967; and Freudenthal, 1968), which is based on the Weibull distribution (Weibull, 1939a), to predict the effect of multiaxial stress states. Transient loads were broken into discrete time steps where the load was assumed to be constant over the duration of the time step. However, Weibull and fatigue (power law) parameters were assumed to remain constant. Therefore, the effects of fluctuating temperature—where Weibull and fatigue parameters varied over the temperature range—could not be accounted for. Jakus and Ritter (1981) developed a life-prediction methodology in terms of probabilistic parameters for both applied stress and component strength. They assumed that the applied stress varies according to a truncated Gaussian distribution, and they used the Weibull distribution to model strength. They also assumed that the Weibull and SCG parameters remained constant with time. Stanley and Chau (1983) described a fast-fracture transient reliability prediction for non-monotonically increasing loads. They considered the previous load history in their procedure such that failure probability never decreased when loads decreased. Mencik (1984) developed closed-form expressions for reliability with SCG for cyclic loading waveforms such as sawtooth and sinusoidal. Brückner-Foit and Ziegler (1999a and 1999b) and Ziegler (1998) developed a time-dependent reliability formulation for three cases: fast fracture, SCG governed by a power law, and SCG governed by a power law with a threshold. Brückner-Foit and Ziegler accounted for multiaxial stress states by using a methodology similar to Batdorf's theory (Batdorf and Crose, 1974; and Batdorf and Heinisch, 1978a). Batdorf's theory uses principles of fracture mechanics and assumes that strength-controlling flaws are randomly distributed and randomly oriented microcracks. In Ziegler's thesis (Ziegler, 1998) transient reliability was solved such that SCG parameters could vary with time and temperature. However, the Weibull modulus (a parameter used to describe the degree of scatter in strength) was assumed to remain constant. This algorithm was similar to that of Paluszny and Nicholls (1978) in that the power law and Weibull distribution were used and that transient loads were broken into discrete time steps where the load and material response (Weibull and fatigue parameters) were assumed to be constant over the duration of the time step. Ziegler included methodology similar to that of Stanley and Chau (1983) to account for non-monotonically increasing loads.

In this report, transient reliability analysis methodology is developed with the following capabilities:

- Fast-fracture transient analysis (reliability analysis without SCG)
- Transient analysis with SCG (reliability analysis with time-dependent damage due to SCG)
- Computationally efficient algorithm to compute the reliability for components subjected to repeated transient loading (cyclic or block loading)
- Cyclic fatigue modeling using a combined SCG and Walker fatigue law (Walker, 1970; and Rahman et al., 1998)
- Proof testing for transient loads
- Weibull parameters and fatigue parameters that are allowed to vary with temperature or time

The effect of multiaxial stresses can be predicted with either the PIA or Batdorf theories. This report only shows the development for using the Batdorf theory. Transient reliability analysis can be performed over the component surface (for surface-residing flaw populations) or volume (for volume-residing flaw populations). As previous authors have (Paluszny and Nicholls, 1978; Stanley and Chau, 1983; Brückner-Foit and Ziegler, 1999a and 1999b; and Ziegler, 1998), we break down transient loads into discrete time steps where the loads and material response are held constant over the time step. The technique developed herein is based on using flaw strength (as opposed to crack length) and on maintaining the compatibility of failure probability between discrete time steps. This allows for the introduction of Weibull parameters that can vary with time and temperature. Allowing for a variable Weibull modulus (the parameter describing variation in component strength) is useful for materials that show *R*-curve behavior (materials where fracture toughness $K_{\mathrm{I}c}$ varies with crack size—typically increasing with crack size) as a function of temperature. The methods were refined to maintain compatibility with the uniaxial stress state for fast-fracture (inert strength) failure probability for the Batdorf method. These methodologies have been added to the CARES/*Life* code and have been made to interoperate with commercial finite element analysis (FEA) programs such as ANSYS[1] (ANSYS, 2004) when transient FEA is performed.

This report describes the detailed development of a generalized transient reliability analysis methodology for the capabilities mentioned above. This includes appendixes A to E. Appendix A contains the nomenclature for this report. Appendix B is the numerical algorithm for transient reliability analysis. Appendix C shows an inductive line of reasoning by which cyclic (repeated) loading is incorporated into the transient reliability formulation in a computationally efficient manner. Appendixes D and E contain helpful background information for the readers' convenience. Appendix D is the reproduced theory section of Nemeth et al. (2003). It explains the Batdorf and PIA multiaxial theories for fast-fracture and time-dependent reliability analysis, as well as the Weibull and fatigue parameter estimation methodologies. Appendix E reproduces Rahman et al. (1998), showing the combined law formulation and parameter estimation methodology. This report also includes four example problems (section 3.0):

---

[1] Swanson Analysis Systems, Inc., Houston, PA.

(1) a disk in thermal shock to illustrate fast-fracture transient analysis, (2) a diesel engine exhaust valve simulation to contrast predictions for cyclic loading and proof testing, (3) the hypothetical effect of changing Weibull and fatigue parameters over time on the reliability of alumina flexure bars in static fatigue, and (4) transient thermal shock reliability analysis of Hexoloy SiC tubes.

1.2 Weibull Modulus Variability

The transient reliability methodology described in this report was developed to include SCG and Weibull parameters that can vary over time and temperature. It is well known that SCG parameters can vary with temperature. There is also evidence in the literature that the Weibull parameters, including the Weibull modulus (scatter parameter), can vary as well. For example, some ceramic materials—such as silicon nitride (Wereszczak et al., 1998; and Salem et al., 1992), alumina (Ritter and Humenik, 1979), and zirconia (Munz and Fett, 1999)—have been reported to exhibit temperature and stress-rate dependence. The CARES/*Life* program (Nemeth et al., 2003) operates under the assumption that the Weibull modulus can vary with temperature. A potential mechanism behind this behavior was described by Kendall et al. (1986) and by Cook and Clarke (1988). They experimentally demonstrated and theoretically showed (see fig. 1) that the Weibull modulus is influenced by *R*-curve behavior. Shetty and Wang (1989), and Munz and Fett (1999) pointed out that, for *R*-curve behavior modeled with a power law, the Weibull distribution for measured strengths is different from the hypothetical strength distribution based on the fracture toughness K_{Ic} treated as a constant with crack size (a flat *R*-curve). Therefore, the Weibull modulus is not only controlled by the statistical distribution of the sizes of flaws, but is also influenced by the physics of crack growth (fracture toughness K_{Ic} changing with crack size).

Various mechanisms may be responsible for the change of Weibull modulus with temperature. Salem et al. (1992) concluded, “At 1371 °C the failure origins were frequently within the volume, and the Weibull modulus decreased to approximately 11 from a room temperature value of 19. The increased incidence of volume failure and lower Weibull modulus were probably due to softening of the glassy secondary phases surrounding large grains, the healing of surface flaws, and a possible loss of crack-growth resistance.” *R*-curve behavior can be strongly temperature dependent, and just as importantly, we believe, it can be a reversible phenomena. For example, for materials

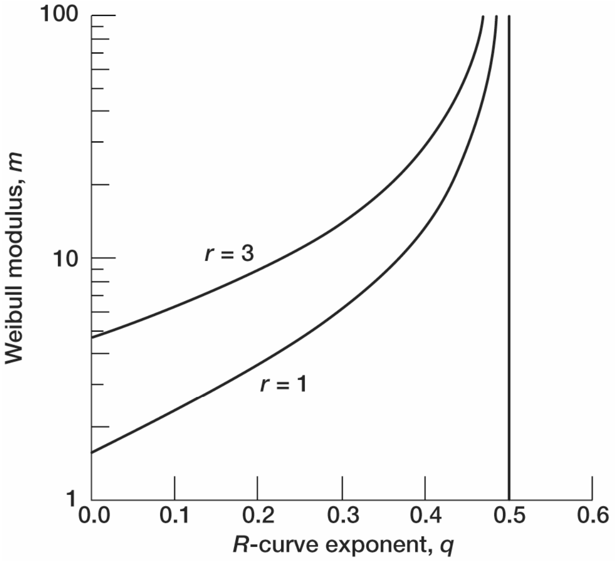

Figure 1.—Relationship between the *R*-curve and the Weibull modulus (Cook and Clarke, 1988), where *r* is a numerical constant characterizing the geometry of localized loading, *r* = 1 for line-force center loading of a linear crack, and *r* = 3 for the point-force center loading of a circular crack. The exponent *q* characterizes the rate at which toughness increases. (Copyright Acta Metall.; used with permission.)

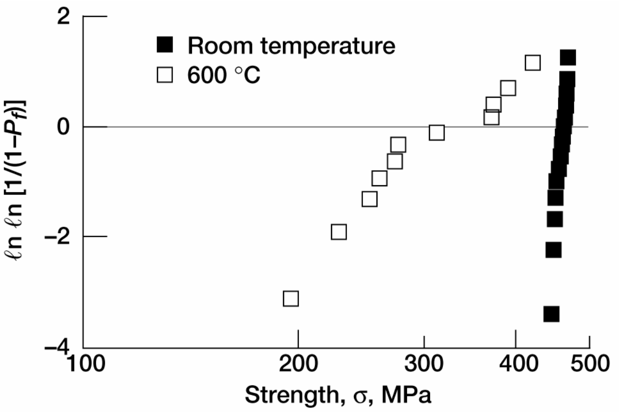

Figure 2.—Weibull plot of failure probability P_f versus strength σ for bending strength of 12Ce-TZP at room temperature and 600 °C (Munz and Fett, 1999). Copyright Springer-Verlag; used with permission.

toughened with an elongated (in situ reinforced) grain structure, grain bridging near the crack tip at room temperature causes *R*-curve behavior and, hence, the Weibull strength modulus appears to be large (reduced scatter in strength). At elevated temperatures, softening of the viscous phases between the grain boundaries can mute the toughening effect and, consequently, lower the Weibull modulus. Lowering from an elevated temperature back to room temperature resolidifies glassy-phase boundaries, and *R*-curve behavior reappears—without imparting additional damage to the material. Transformation toughening also affects the observed Weibull modulus and is temperature dependent, as shown in figure 2 (Munz and Fett, 1999).

In summary, developing a transient reliability analysis methodology that can include a variable Weibull modulus is useful for materials that show *R*-curve behavior as a function of temperature. *R*-curve behavior may or may not be a reversible phenomenon as a function of temperature. Transformation-toughened materials show temperature-dependent (and probably reversible) *R*-curve behavior through changes in the materials' crystalline structure with temperature. Mechanically toughened materials show *R*-curve behavior through grain bridging near crack tips. This may or may not be reversible depending on the conditions. For example, crack blunting or flaw healing could irreversibly alter the response. Repeated cyclic loading could also degrade bridging ligaments in an irreversible manner. Other examples include high-temperature corrosion (where pits may be generated on the material surface), oxidation, erosion, creep, and impact damage. It is important to ascertain if the changing Weibull modulus is due to reversible or irreversible changes in the material because the changing Weibull parameters become either a function of temperature or time, respectively. The third example in this report (section 3.3) shows the hypothetical (irreversible) effect of changing Weibull and fatigue parameters over time on the reliability of alumina flexure bars in static fatigue. This effect is likely due to the crystallization of glassy phases between the grains.

A limitation of the modeling in this report is that the effect of *R*-curve behavior on ceramic component reliability is not explicitly considered. Instead, Weibull modulus variability is treated in a phenomenological manner. However, this still is an improvement over the previous capability and represents a significant step toward having *R*-curve modeling explicitly incorporated into transient reliability analysis.

A varying Weibull modulus is directly applicable under conditions where monotonic thermal or environmental loading take place (where the temperature or environment does not change cyclically). Under such conditions, as the temperature or environment changes, new flaws could be generated which, in turn, would cause the Weibull parameters to vary accordingly.

2.0 Theoretical Development

The purpose of this report is to describe a generalized transient reliability analysis methodology for brittle material components. The authors have tried to make this document as self-contained as possible. This report builds upon Nemeth et al. (2003), and for the readers' convenience, the theory section of Nemeth et al. is reproduced in appendix D. It is recommended that readers first become familiar with the nomenclature and concepts described in this appendix. This will make the task of understanding this report substantially easier. In particular, appendix D should be consulted when readers are trying to understand the Weibull distribution and how it relates to the Batdorf and PIA multiaxial theories.

The transient reliability formulation depends on finding the amount of strength degradation that occurs to a flaw from an applied loading over a specified time. The material failure probability over an elapsed amount of time for an arbitrarily small volume of material (but larger than any embedded flaw) under stress represents the percentage of the flaw population that has a degraded strength equal to or less than the applied far-field stress at the end of a specified time interval (at time $t = t_f$). We define "flaw population" as a randomly distributed collection of a specified type of flaw where the size of the flaws, and hence the strength, varies. Since the strength of the strongest flaw that will (just) fail is known (because its degraded strength at $t = t_f$ is equal to the applied far-field stress at $t = t_f$), calculations are performed to find the strength of that flaw at the initiation of loading (at $t = t_i = 0$). This inert, or intrinsic, strength of the flaw is plugged into a mathematical description of the (inert) distribution of flaw strengths in the material element (in this case, the mathematical description is the Weibull distribution). This last calculation yields the failure probability of the material element from the applied transient loads. The solution process essentially involves calculations that go backward in time to solve for an initial condition.

In this methodology, the probabilistic entity is the distribution of inert flaw strengths (strength prior to SCG at $t = 0$). Crack growth is not treated as a stochastic process. Fracture toughness K_{Ic} also is not assumed to be a probabilistic quantity. A justification for this is that since strength (on which this methodology is based) is a function of both crack size and fracture toughness, then variability in measured strength actually represents the combined effect of variability in crack size and fracture toughness. So even though stochastic K_{Ic} is not explicitly modeled, its behavior is captured phenomenologically in practice.

2.1 Strength Degradation Due to Slow Crack Growth

In this section, an equation is developed to describe how the strength of a flaw degrades over time due to SCG. This equation requires that SCG parameters are constant over the elapsed time. This establishes the equation of strength degradation over a discrete time interval and is subsequently used in the generalized methodology for transient reliability analysis (section 2.3).

The methodology in this report depends on well-known and fundamental relations developed to describe the conditions necessary to initiate crack growth—a field of study that is known as linear elastic fracture mechanics (LEFM). Investigations in the area of mode-I crack extension (where the crack surfaces displace perpendicular, or normal, to the plane of the crack from a far-field stress applied normal to the crack plane) have resulted in the following relationship (Paris and Sih, 1965):

$$K_I(t) = \sigma(t)\, Y \sqrt{a(t)} \tag{1}$$

where, in the nomenclature of this report, the parentheses with enclosed arguments indicate that the variable is a function of the enclosed arguments, which in this case means that the variable is a function of time. The term K_I is known as the stress intensity factor (at the crack tip), Y is a nondimensional constant that is a function of the crack geometry (the shape and relative size of the crack), $\sigma(t)$ is the far-field uniaxial stress applied normal to a crack at time t, and $a(t)$ is the crack length at time t. The geometry factor Y is assumed herein to be independent of crack size and time (the crack shape is assumed not to change over time, although its size may change over time). Equation (1) is for pure mode I (the opening mode). Similar relationships exist and are discussed, for example, in Broek (1982) for mode-II stress intensity factors (the sliding mode—displacement of the crack surfaces in the plane of the crack and perpendicular to the leading edge of the crack from an in-plane far-field shear stress) and mode-III stress intensity factors (the tearing mode—where the crack surfaces displace in the plane of the crack and are parallel to the leading edge of the crack from an out-of-plane far-field shear stress) stress intensity factors. These factors are denoted by K_{II} and K_{III}, respectively, for modes II and III.

For a crack arbitrarily located within a solid body experiencing a far-field multiaxial stress state, the equivalent (or effective) mode-I stress intensity factor is functionally defined as

$$K_{\mathrm{I}eq}(\Psi,t)=\sigma_{\mathrm{I}eq}(\Psi,t)\,Y\sqrt{a(\Psi,t)} \tag{2}$$

where $K_{\mathrm{I}eq}$ is the equivalent mode-I stress intensity factor, $\sigma_{\mathrm{I}eq}(\Psi, t)$ is the equivalent mode-I far-field uniaxial stress normal to a crack located at Ψ at time t, $a(\Psi, t)$ is the crack length located at Ψ at time t, and Ψ represents the location (x, y, z) and the orientation (α, β) of the crack within the body. In some reliability models, such as PIA, Ψ represents a location only, whereas for others, such as the Batdorf theory, $\Psi = (x, y, z, \alpha, \beta)$ for volume-residing flaws and $\Psi = (x, y, \alpha)$ for surface-residing flaws. The subscript eq represents an equivalent quantity. For $\sigma_{\mathrm{I}eq}$ it represents the effect of a multiaxial stress state that has the same, or equivalent, effect as a uniaxial stress of magnitude σ applied normal to the crack face.

The critical mode-I (effective) stress intensity factor $K_{\mathrm{I}eqc}$ is defined as the value of $K_{\mathrm{I}eq}$ where unstable crack extension is initiated from an applied far-field (equivalent) stress of magnitude $\sigma_{\mathrm{I}eqc}$ applied normal to the crack face. Thus,

$$K_{\mathrm{I}eqc}(\Psi,t)=\sigma_{\mathrm{I}eqc}(\Psi,t)Y\sqrt{a(\Psi,t)} \tag{3}$$

where $\sigma_{\mathrm{I}eqc}$ is defined as the (equivalent) mode-I strength of a crack of size a. For pure modes I, II, and III loading, the critical stress intensity factors are denoted by $K_{\mathrm{I}c}$, $K_{\mathrm{II}c}$, and $K_{\mathrm{III}c}$, respectively. The term $K_{\mathrm{I}c}$ is known as the fracture toughness of the material in mode I and is considered to be a material property. The term $K_{\mathrm{I}eqc}(\Psi, t)$ is expressed as a function of Ψ because $K_{\mathrm{I}eqc}$ is dependent on location and time (that is, it can depend on temperature, which can be a function of time and location). For an isotropic material, it does not depend on the orientation of the crack.

The effective stress $\sigma_{\mathrm{I}eq}$ represents an equivalent normal stress on the crack face from the combined action of the normal stress σ_n and the shear stress τ on the crack face, oriented normal to α and β (see app. D). Shetty (1987) performed experiments on polycrystalline ceramics and glass where he investigated crack propagation as a function of an applied far-field multiaxial stress state. He proposed a multimodal interaction fracture criterion to empirically fit the data, which takes the form

$$\frac{K_{\mathrm{I}}}{K_{\mathrm{I}c}}+\left(\frac{K_{\delta}}{\overline{C}\,K_{\mathrm{I}c}}\right)^2=1 \tag{4}$$

where K denotes the stress intensity factor; K_δ is either K_{II} or K_{III}, whichever is dominant; and $\overline{C}$ is the Shetty shear-sensitivity coefficient, with values typically in the range $0.80 \le \overline{C} \le 2.0$. As $\overline{C}$ increases, the response becomes progressively more shear insensitive. For a Griffith crack with the Shetty mixed-mode fracture criterion, the effective stress becomes

$$\sigma_{\mathrm{I}eq}(\Psi,t)=\frac{1}{2}\left[\sigma_n(\Psi,t)+\sqrt{\sigma_n^2(\Psi,t)+4\left[\frac{\tau(\Psi,t)}{\overline{C}}\right]^2}\,\right] \tag{5}$$

Equations (4) and (5) are provided to help illustrate the methodology. Appendix D from Nemeth et al. (2003) gives effective stress relations for other crack geometries and mixed-mode fracture criteria. Equation (5) does not consider changes of crack trajectory over time. Although this is a simplifying assumption, rigorously accounting for this effect is computationally complex and intensive. The authors assume that this assumption is adequate for most cases of transient loading in ceramic materials where critical-sized flaws tend to be small and SCG crack velocity is low until a crack becomes nearly critical. Two mixed-mode studies using angled grinding damaged specimens (Salem et al., 1996; and Holland et al., 1999) tended to support the adequacy of this methodology, although more work in this area is needed using naturally flawed specimens (versus specimens with introduced cracks).

The time-dependent formulation of crack growth depends on modeling the crack velocity. Expressing equation (3) in terms of crack length yields

$$a(\Psi,t)=\frac{K_{\mathrm{I}eqc}^{2}(\Psi,t)}{\sigma^{2}{}_{\mathrm{I}eqc}(\Psi,t)Y^{2}} \tag{6}$$

Taking the derivative of equation (6) with respect to time yields

$$\frac{\mathrm{d}a(\Psi,t)}{\mathrm{d}t}=\frac{-2K_{\mathrm{I}eqc}^{2}(\Psi,t)}{Y^{2}\sigma_{\mathrm{I}eqc}^{3}(\Psi,t)}\left[\frac{\mathrm{d}\sigma_{\mathrm{I}eqc}(\Psi,t)}{\mathrm{d}t}\right] \tag{7}$$

SCG refers to the stable extension of a crack over time. Similar to stress corrosion in metals, SCG is a result of the combination of stress at the crack tip and chemical attack or loosening of viscous phases (at high temperature) such that chemical bonds at the crack tip break or that material displaces and the crack tip extends. The crack length as a function of time can be expressed as a power law (Wiederhorn, 1974a) with the following form

$$\frac{\mathrm{d}a(\Psi,t)}{\mathrm{d}t}=A_{1}(\Psi,t)\,K_{\mathrm{I}eq}^{N(\Psi,t)}(\Psi,t) \tag{8}$$

where $A_1(\Psi, t)$ and $N(\Psi, t)$ are time-dependent material parameters that also depend on the temperature and environment. These parameters are described as a function of time and location in equation (8) because in a transient loading analysis the temperature and/or environment can vary with time and location, thus causing them to change accordingly. For an isotropic material, $A_1(\Psi, t)$ and $N(\Psi, t)$ are not a function of orientation. Equating equations (7) and (8) gives

$$A_{1}(\Psi,t)\,K_{\mathrm{I}eq}^{N(\Psi,t)}(\Psi,t)=\frac{-2K_{\mathrm{I}eqc}^{2}(\Psi,t)}{Y^{2}\sigma_{\mathrm{I}eqc}^{3}(\Psi,t)}\frac{\mathrm{d}\sigma_{\mathrm{I}eqc}(\Psi,t)}{\mathrm{d}t} \tag{9}$$

which, upon rearranging, yields

$$\frac{\mathrm{d}\sigma_{\mathrm{I}eqc}(\Psi,t)}{\mathrm{d}t}=A_{1}(\Psi,t)\,K_{\mathrm{I}eq}^{N(\Psi,t)}(\Psi,t)\frac{Y^{2}\sigma_{\mathrm{I}eqc}^{3}(\Psi,t)}{-2K_{\mathrm{I}eqc}^{2}(\Psi,t)} \tag{10}$$

Substituting the crack length given in equation (6) into equation (2) and then substituting that result into equation (10) for $K_{\mathrm{I}eq}$ gives

$$\frac{\mathrm{d}\sigma_{\mathrm{I}eqc}(\Psi,t)}{\mathrm{d}t} = \frac{A_1(\Psi,t)\,\sigma_{\mathrm{I}eq}^{N(\Psi,t)}(\Psi,t)\,K_{\mathrm{I}eqc}^{N(\Psi,t)-2}(\Psi,t)\,Y^2}{-2\sigma_{\mathrm{I}eqc}^{N(\Psi,t)-3}(\Psi,t)} \tag{11}$$

then

$$\sigma_{\mathrm{I}eqc}^{N(\Psi,t)-3}(\Psi,t)\,\mathrm{d}\sigma_{\mathrm{I}eqc}(\Psi,t) = \frac{A_1(\Psi,t)\,Y^2\;K_{\mathrm{I}eqc}^{N(\Psi,t)-2}(\Psi,t)}{-2}\;\sigma_{\mathrm{I}eq}^{N(\Psi,t)}(\Psi,t)\,\mathrm{d}t \tag{12}$$

So that equation (12) can be integrated with respect to strength and time, the material parameters N, A_1, and $K_{\mathrm{I}eqc}$ are assumed to be constant with respect to time (within the interval of integration). Therefore, the integration over the time interval between the initial time t_{int} and the final time t_{fin}, where $t_{\mathrm{int}} < t_{\mathrm{fin}}$, is

$$\int_{\sigma_{\mathrm{I}eqc}(\Psi,t_{\mathrm{int}})}^{\sigma_{\mathrm{I}eqc}(\Psi,t_{\mathrm{fin}})} \sigma_{\mathrm{I}eqc}^{N(\Psi)-3}(\Psi,t)\,\mathrm{d}\sigma_{\mathrm{I}eqc}(\Psi,t) = \frac{A_1(\Psi)\,Y^2\;K_{\mathrm{I}eqc}^{N(\Psi)-2}(\Psi)}{-2}\;\int_{t_{\mathrm{int}}}^{t_{\mathrm{fin}}} \sigma_{\mathrm{I}eq}^{N(\Psi)}(\Psi,t)\,\mathrm{d}t \tag{13}$$

where $N(\Psi)$, $A(\Psi)$, and $K_{\mathrm{I}eqc}(\Psi)$, are no longer shown as functions of time, and the limits of integration are the initial strength, $\sigma_{\mathrm{I}eqc}(\Psi,\, t_{\mathrm{int}})$ and the final strength $\sigma_{\mathrm{I}eqc}(\Psi,\, t_{\mathrm{fin}})$. This integral evaluates to

$$\sigma_{\mathrm{I}eqc}(\Psi,t_{\mathrm{int}}) = \left[\frac{\int_{t_{\mathrm{int}}}^{t_{\mathrm{fin}}} \sigma_{\mathrm{I}eq}^{N(\Psi)}(\Psi,t)\,\mathrm{d}t}{B(\Psi)} + \sigma_{\mathrm{I}eqc}^{N(\Psi)-2}(\Psi,t_{\mathrm{fin}})\right]^{\frac{1}{N(\Psi)-2}} \tag{14}$$

where the fatigue parameter B is defined as

$$B(\Psi) = \frac{2}{A_1(\Psi)\,Y^2\;K_{\mathrm{I}eqc}^{N(\Psi)-2}(\Psi)\,[N(\Psi)-2]} \tag{15}$$

The fatigue exponent N is dimensionless, and the fatigue parameter B has units of stress^2 × time.

Equation (14) describes how the strength of an initial crack, $\sigma_{\mathrm{I}eqc}(\Psi,\, t_{\mathrm{int}})$, at $t = t_{\mathrm{int}}$ degrades to strength $\sigma_{\mathrm{I}eqc}(\Psi,\, t_{\mathrm{fin}})$ at $t = t_{\mathrm{fin}}$ because of the applied loading. The equation does not imply material rupture through unstable crack growth.

2.2 Stochastic Strength Response

In this section, a relationship is established between the stochastic strength response and SCG. Modeling is shown for predicting the failure probability of a component under transient loading when the Weibull and SCG parameters are assumed to be held constant. The Batdorf model for predicting the failure probability response due to multiaxial loading is also introduced. The Batdorf theory is developed in detail in appendix D reproduced from Nemeth et al. (2003).

The Weibull distribution (Weibull, 1939a) is typically used to describe the stochastic strength response of a brittle material. For an incremental volume of material ΔV under a uniform uniaxial stress of magnitude σ, such that there is no SCG (i.e., an instantaneous applied load over an infinitesimally small time interval, or a material that does not react with its environment), the failure probability P_{fV} for the two-parameter Weibull distribution (Weibull, 1939a) is expressed as

$$P_{fV} = 1 - P_{sV} = 1 - \exp\left[-\Delta V \left(\frac{\sigma}{\sigma_{oV}} \right)^{m_V} \right] \tag{16}$$

where the strength-controlling flaws are assumed to be randomly distributed in the material volume (volume flaw distributed), P_{sV} is the probability of survival, σ_{oV} is the Weibull scale parameter, and m_V is the Weibull modulus (or the scatter, or shape, parameter). The subscript V denotes a property associated with the material volume. The shape parameter m_V is a unitless measure of the dispersion of strength, whereas the scale parameter σ_{oV} is the strength, at a level of 0.6321 probability of failure, of a unit volume of material in uniform uniaxial tension. The scale parameter has units of stress·volume$^{1/m}$. This can be understood by considering that, when $\sigma = \sigma_{oV}$ and $\Delta V = 1.0$, then $P_{fV} = 0.6321$ in equation (16). The term σ in equation (16) actually represents the strength value of a flaw, and the equation is a statement that the probability of a flaw being present in ΔV with a strength equal to or less than σ is P_{fV}. For a brittle material, if a flaw is present in ΔV with a strength equal to or less than σ, then catastrophic crack propagation ensues and the material element (and hence the body) has failed. Equation (16) describes the fast-fracture probability of failure of the material element ΔV.

For a uniaxially stressed component where the magnitude of the stress changes depending on the location within the component, the fast-fracture failure probability of the entire component is

$$P_{fV} = 1 - \exp\left[-\frac{1}{\sigma_{oV}{}^{m_V}} \int_V \sigma^{m_V}(\Psi)\,\mathrm{d}V \right] \tag{17}$$

where $\sigma(\Psi)$ is a function of the location (x, y, z), and not the orientation (α, β), of a flaw within the body of the component. Equations (16) and (17) represent the failure response at $t = t_{\text{int}} = 0$ (the undegraded, or pristine, strength distribution of the flaw population).

The effect of SCG on the failure probability of the component can be found by specifying appropriate boundary conditions for equation (14) and combining that equation with equation (17). In equation (14), the initial strength of the flaw needs to be found for $t = t_{\text{int}} = 0$, and it is assumed that the strength of the flaw at $t = t_{\text{fin}}$, equals the applied equivalent stress at that moment. Therefore, any flaw that exists in the incremental volume ΔV located at Ψ and at $t = t_f = t_{\text{fin}}$, with strength equal to or less than $\sigma_{\text{I}eqc}(\Psi, t_{\text{fin}})$, will be unstable and will catastrophically propagate. Here we use the time t_f to indicate the time to failure. Equivalently, any of these same flaws that cause failure at $t = t_f$ will have a strength less than or equal to $\sigma_{\text{I}eqc}(\Psi, t_{\text{int}})$ at $t = t_{\text{int}} = 0$. This last statement means that $\sigma_{\text{I}eqc}(\Psi, t_{\text{int}})$ in equation (14), solved for $t_{\text{int}} = 0$, can be directly substituted for σ in equation (17). Performing this substitution results in

$$P_{fV}(t_f) = 1 - P_{sV}(t_f) = 1 - \exp\left[-\frac{1}{\sigma_{oV}{}^{m_V}} \int_V \sigma_{\text{I}eq,0}^{m_V}(\Psi)\,\mathrm{d}V \right] \tag{18}$$

where

$$\sigma_{\text{I}eq,0}(\Psi) = \left[\frac{\int_0^{t_f} \sigma_{\text{I}eq}^{N(\Psi)}(\Psi, t)\,\mathrm{d}t}{B(\Psi)} + \sigma_{\text{I}eq}^{N(\Psi)-2}(\Psi, t_f) \right]^{\frac{1}{N(\Psi)-2}} \tag{19}$$

Here, the convention of $\sigma_{\mathrm{I}eq,0}(\Psi) = \sigma_{\mathrm{I}eqc}(\Psi, t_{\mathrm{int}})$ is used when $t_{\mathrm{int}} = 0$ and $P_{fV}(t_f)$ is the failure probability at $t = t_f$. This is consistent with the convention of appendix D from Nemeth et al. (2003). Also the equivalent stress $\sigma_{\mathrm{I}eq}(\Psi, t_f)$ at $t = t_f$ is used instead of the strength $\sigma_{\mathrm{I}eqc}(\Psi, t_f)$. This can be done because $\sigma_{\mathrm{I}eq}(\Psi, t_f) = \sigma_{\mathrm{I}eqc}(\Psi, t_f)$ by definition of the condition that failure occurs at $t = t_f$. Equations (18) and (19) are shown with equivalent stress expressions; however, only uniaxial stresses can be used there. These two equations show the effect of SCG and transient loading on failure probability and require that Weibull and fatigue (SCG) parameters remain constant over time. When the material parameters N and B vary over the load history, equation (19) must be solved by breaking the time to failure t_f into discrete time intervals, where N and B are held constant over a time interval but are allowed to vary between each interval. Section 2.3 shows how this is done.

The following is a brief description of the Batdorf methodology. Appendix D from Nemeth et al. (2003) describes this development in more detail. The following description should be sufficient for the reader to understand how SCG is incorporated into the Batdorf multiaxial theory. The Batdorf formulation is shown henceforth throughout this report, with the exception of appendixes B and C.

The Batdorf theory was developed to predict the effect of multiaxial stress states on component reliability (Batdorf and Crose, 1974; and Batdorf and Heinisch, 1978a). It combines the weakest link mechanism (where the material is analogous to links in a chain such that the weakest link in the chain causes the chain to fail) and linear elastic fracture mechanics. It is based on the calculation of the combined probability of a (critical) flaw existing in the material with a strength equal to or less than the effective stress (determined from the applied multiaxial stress) and having this critical flaw being located and oriented so that it can cause the component to rupture. When this methodology is used, the fast-fracture and time-dependent reliability of a ceramic component is expressed as

$$P_{sV}\left(t_f\right) = \exp\left\{-\frac{\bar{k}_{BV}(\Psi)}{4\pi}\int_V\int_\Omega\left[\frac{\sigma_{\mathrm{I}eq,0}(\Psi)}{\sigma_{oV}(\Psi)}\right]^{m_V(\Psi)}\mathrm{d}\Omega\;\mathrm{d}V\right\} \tag{20}$$

where $\bar{k}_{BV}$ is the normalized Batdorf crack-density coefficient for volume flaws, $\sigma_{\mathrm{I}eq,0}(\Psi)$ is from equation (19) and is the transformed critical strength at $t = 0$ from the applied effective stress, Ψ represents a term that depends on the location (x, y, z) and crack orientation (α, β), and $\mathrm{d}\Omega = \sin\alpha\ \mathrm{d}\alpha\ \mathrm{d}\beta$. The terms $\bar{k}_{BV}$, m_V, and σ_{oV} depend on the location (x, y, z) and are independent of the orientation (α, β) for an isotropic material. The term $\sigma_{\mathrm{I}eq,0}(\Psi)$ depends on the appropriate fracture criterion, crack shape, and t_f. The term $\bar{k}_{BV}$ is used in the reliability equation for compatibility purposes. It ensures that the multiaxial Batdorf theory collapses to the basic uniaxial Weibull equation (17) in fast fracture when a uniaxial stress state is applied. The constant term 4π represents the surface area of a sphere of unit radius. Equation (20) is a form of the Weibull distribution.

To calculate a component's probability of survival, we use results from FEA in conjunction with equation (20). FEA enables the discretization of the component into incremental volume elements. For enhanced numerical accuracy, the stress state and volume associated with an element's gaussian integration points are used. Using the information associated with the element integration points subdivides the element into subelements, where V_{isub} corresponds to the volume of an individual subelement. The stress state, temperature, and environment for each subelement are assumed to be uniform throughout its volume. In this case, the volume integral is replaced with a volume summation, and equation (20) takes the following form:

$$P_{sV}\left(t_f\right) = \exp\left(-\sum_{isub=1}^{n_{\mathrm{sub}}}\frac{V_{isub}}{4\pi}\left\{\bar{k}_{BV}(\Psi)\int_\Omega\left[\frac{\sigma_{\mathrm{I}eq,0}(\Psi)}{\sigma_{oV}(\Psi)}\right]^{\mathrm{m}_V(\Psi)}\mathrm{d}\Omega\right\}_{isub}\right) \tag{21}$$

where n_{sub} is the total number of subelements.

2.3 Generalized Transient Reliability Formulation

In this section the generalized transient reliability formulation is derived. The methodology accounts for changing Weibull and SCG parameters over time or temperature. The solution approach shows how the reliability formulation develops for each new time step, beginning with the first time step. In this case, only three time steps are required before a pattern emerges such that a generalized equation can be written. The methodology shown subsequently is also applicable to fast-fracture transient analysis.

In the following sections, not all the equations have variables expressed as functions of time t and location Ψ because some expressions would have become too long and repetitive. By now, the reader should be aware of what parameters are functions of time and/or location and orientation.

So that the time dependence of the loading and material response can be taken into account, the stress history for each subelement *isub* is discretized into short time steps Δt_j. The applied stress and material parameters (Weibull and SCG parameters) are assumed to remain constant over each time step, but they are allowed to vary between time steps. For a given time step j, the applied equivalent stress of a flaw oriented at (α, β) in a given subelement *isub* is denoted by $\sigma_{\mathrm{I}eq,j}$, the temperature is T_j, the scale parameter is $\sigma_{oV,j}$, the Weibull modulus is $m_{V,j}$, the fatigue constant is $B_{V,j}$, and the fatigue exponent is $N_{V,j}$.

The expression for the inert equivalent strength $\sigma_{\mathrm{I}eq,0}$ from the applied equivalent stress distribution is derived for the first three time steps of a general fluctuating stress history that a given subelement *isub* experiences. From this, a pattern for the inert strength expression emerges that can then be generalized and coded for any arbitrary number of time steps.

2.3.1 Time step 1.—Time step 1 spans the time interval between $t = t_0 = 0$ and $t = t_1$, and the time step interval is $\Delta t_1 = t_1 - t_0$. During this time step, henceforth denoted by Δt_1, and for a given subelement *isub*, the applied equivalent stress is $\sigma_{\mathrm{I}eq,1}$, the temperature is T_1, the scale parameter is $\sigma_{oV,1}$, the Weibull modulus is $m_{V,1}$, the fatigue constant is $B_{BV,1}$, and the fatigue exponent is $N_{V,1}$. The inert strength expression $(\sigma_{\mathrm{I}eq,0})_{isub}$ for the *isub*th subelement corresponding to the first time step is obtained directly from equation (14). In that equation, the stress history integral existing in the first term within the brackets is evaluated by setting the stress history $\sigma_{\mathrm{I}eq}(\Psi, t)$ equal to a constant applied equivalent stress $\sigma_{\mathrm{I}eq,1}$, the initial time $t_{\mathrm{int}} = t_0$, and the final time $t_f = t_1$. This means that the integral term in equation (14) becomes equal to $\sigma_{\mathrm{I}eq,1}^{N_{V,1}} \Delta t_1$. The inert strength at $t = t_{\mathrm{int}} = 0$, denoted by $\sigma_{\mathrm{I}eq,0}$, is then given by

$$\sigma_{\mathrm{I}eq,0} = \left[\frac{\sigma_{\mathrm{I}eq,1}^{N_{V,1}} \Delta t_1}{B_{BV,1}} + \sigma_{\mathrm{I}eqc,1}^{N_{V,1}-2}(t_1) \right]^{\frac{1}{(N_{V,1}-2)}} \tag{22}$$

Denoting parameters as a function of location and orientation Ψ is not shown here, but it is implied. The fatigue constant for the Batdorf criterion is denoted by B_B. This is the value of B that normalizes the Batdorf criterion to the uniaxial Weibull criterion shown in equations (18) and (19). See appendix D, section D.2.2.4, reproduced from Nemeth (2003), for further details. Equation (22) shows the remaining (degraded) strength at the end of time step 1, denoted by $\sigma_{\mathrm{I}eqc,1}(t_1)$. The failure probability at the end of time step 1 is found by assuming that the critical strength of the flaw is reached at the end of the time step. Hence, as discussed in the previous section for equation (19), by setting the degraded strength term $\sigma_{\mathrm{I}eqc,1}(t_1)$ equal to the applied stress $\sigma_{\mathrm{I}eq,1}$(at $t = t_1$) during this time step, the probability of survival expression for the Batdorf methodology is given by

$$P_{sV}(t_1) = \exp\left\{ -\sum_{isub=1}^{n_{\mathrm{sub}}} \frac{V_{isub}}{4\pi} \left[\bar{k}_{BV,1} \int_{\Omega} \left(\frac{\sigma_{\mathrm{I}eq,0}}{\sigma_{oV,1}} \right)^{m_{V,1}} \mathrm{d}\Omega \right]_{isub} \right\} \tag{23}$$

$$\sigma_{\mathrm{I}eq,0} = \left(\frac{\sigma_{\mathrm{I}eq,1}^{N_{V,1}} \Delta t_1}{B_{BV,1}} + \sigma_{\mathrm{I}eq,1}^{N_{V,1}-2} \right)^{\frac{1}{(N_{V,1}-2)}} \tag{24}$$

2.3.2 Time step 2.—Time step 2 spans the time interval between $t = t_1$ and $t = t_2$, and the time step interval is $\Delta t_2 = t_2 - t_1$. During this time step, denoted by Δt_2, and for a given subelement *isub*, the applied equivalent stress is $\sigma_{\mathrm{I}eq,2}$, the temperature is T_2, the scale parameter is $\sigma_{oV,2}$, the Weibull modulus is $m_{V,2}$, the fatigue constant is $B_{BV,2}$, and the fatigue exponent is $N_{V,2}$. The task is to compute $\sigma_{\mathrm{I}eq,0}$, but to now include the contributions of both time steps where $t_2 = t_f$.

Using equation (14) and assuming that $\sigma_{\mathrm{I}eq,2}$ is constant over the interval Δt_2, yields an initial strength $\sigma_{\mathrm{I}eqc,2}(t_1)$ at the beginning of time step 2 of

$$\sigma_{\mathrm{I}eqc,2}(t_1) = \left[\frac{\sigma_{\mathrm{I}eq,2}^{N_{V,2}} \Delta t_2}{B_{BV,2}} + \sigma_{\mathrm{I}eqc,2}^{N_{V,2}-2}(t_2) \right]^{\frac{1}{N_{V,2}-2}} \tag{25}$$

To perform the reliability analysis for the two time steps, we assume that the strength of the strongest flaw that will just initiate failure in the material is equal to the applied stress $\sigma_{\mathrm{I}eq,2}$ at $t_2 = t_f$. In other words, $\sigma_{\mathrm{I}eqc,2}(t_2) = \sigma_{\mathrm{I}eq,2}$, and equation (25) becomes

$$\sigma_{\mathrm{I}eqc,2}(t_1) = \left(\frac{\sigma_{\mathrm{I}eq,2}^{N_{V,2}} \Delta t_2}{B_{BV,2}} + \sigma_{\mathrm{I}eq,2}^{N_{V,2}-2} \right)^{\frac{1}{N_{V,2}-2}} \tag{26}$$

If the material response does not vary significantly from one step to the next, the initial strength at the beginning of time step 2, $\sigma_{\mathrm{I}eqc,2}(t_1)$, will be equal to the remaining strength at the end of time step 1, $\sigma_{\mathrm{I}eqc,1}(t_1)$. However, in real applications, changes in temperature and environment are the norm. For such cases, the remaining strength at the end of one time step does not (necessarily) equal the initial strength of the subsequent time step even though the crack size does not change from the end of one time step and the beginning of the next. An example of this would be when $K_{\mathrm{I}c}$ changes with temperature. One can account for this situation by specifying that the percenttage of the flaw population (located and oriented at Ψ in a discrete volume of material) that survives at the end of one time step will be the exact same percentage that survives at the beginning of the next time step. Notice that this statement says nothing about strength, loading, or crack size. Rather, it is a statement saying that the survival probability (or equivalently the failure probability) of a discrete element at Ψ at the end of a time step and the beginning of the next step are equal. In other words, compatibility of survival probability is maintained between the time steps. This can be done by equating the survival probabilities associated with these two strengths and their corresponding Weibull parameters. Equating the survival probabilities at the end of time step 1 to that at the beginning of time step 2 yields

$$\exp\left(-\sum_{isub=1}^{n_{\text{sub}}}\frac{V_{isub}}{4\pi}\left\{\bar{k}_{BV,1}\int_{\Omega}\left[\frac{\sigma_{\mathrm{I}eqc,1}(t_1)}{\sigma_{oV,1}}\right]^{m_{V,1}}\mathrm{d}\Omega\right\}_{isub}\right)$$
$$=\exp\left(-\sum_{isub=1}^{n_{\text{sub}}}\frac{V_{isub}}{4\pi}\left\{\bar{k}_{BV,2}\int_{\Omega}\left[\frac{\sigma_{\mathrm{I}eqc,2}(t_1)}{\sigma_{oV,2}}\right]^{m_{V,2}}\mathrm{d}\Omega\right\}_{isub}\right) \tag{27}$$

which reduces to an expression that can be solved for $\sigma_{\mathrm{I}eqc,1}(\Psi, t_1)$, which is local to Ψ, and for subelement *isub*

$$\sigma_{\mathrm{I}eqc,1}(t_1)=\left[\frac{\sigma_{oV,1}}{\left(\bar{k}_{BV,1}\right)^{\frac{1}{m_{V,1}}}}\right]\left\{\frac{\sigma_{\mathrm{I}eqc,2}(t_1)}{\left[\dfrac{\sigma_{oV,2}}{\left(\bar{k}_{BV,2}\right)^{\frac{1}{m_{V,2}}}}\right]}\right\}^{\frac{m_{V,2}}{m_{V,1}}}=\sigma_{oBV,1}\left[\frac{\sigma_{\mathrm{I}eqc,2}(t_1)}{\sigma_{oBV,2}}\right]^{\frac{m_{V,2}}{m_{V,1}}} \tag{28}$$

Equation (28) provides an expression for the degraded strength at the end of time step 1, $\sigma_{\mathrm{I}eqc,1}(\Psi, t_1)$, as a function of the initial strength at the beginning of time step 2, $\sigma_{\mathrm{I}eqc,2}(\Psi, t_1)$. Note that, when the Weibull parameters remain constant, equation (28) collapses to the basic case where the remaining strength at the end of a given time step is equal to the initial strength of the subsequent step. Also in equation (28), use of the normalized Batdorf crack-density coefficient $\bar{k}_{BV}$ is essential to normalize the relationship to the uniaxial stress state. The term σ_{oBV} includes the effect of $\bar{k}_{BV}$ and is used henceforth. This is how the methodology described in this report takes into account the transience in the Weibull parameters throughout the load history.

To obtain the expression for the inert strength at $t = 0$, we substitute equation (26) for $\sigma_{\mathrm{I}eqc,2}(\Psi, t_1)$ in equation (28) and then substitute $\sigma_{\mathrm{I}eqc,1}(\Psi, t_1)$ in equation (28) into equation (22), with the resulting expression

$$\sigma_{\mathrm{I}eq,0}=\left[\frac{\sigma_{oBV,1}^{N_{V,1}-2}}{\sigma_{oBV,2}^{m_{V,2}/m_{V,1}\left(N_{V,1}-2\right)}}\left(\sigma_{\mathrm{I}eq,2}^{N_{V,2}-2}+\frac{\sigma_{\mathrm{I}eq,2}^{N_{V,2}}\,\Delta t_2}{B_{BV,2}}\right)^{\frac{m_{V,2}\left[N_{V,1}-2\right]}{m_{V,1}\left[N_{V,2}-2\right]}}+\frac{\sigma_{\mathrm{I}eq,1}^{N_{V,1}}\,\Delta t_1}{B_{BV,1}}\right]^{\frac{1}{N_{V,1}-2}} \tag{29}$$

Equation (29), as expressed, can lead to decreasing inert strength as time elapses. For example, if the applied stress decreases monotonically with time while the material gets stronger, then equation (29) can result in decreasing inert strength as time elapses. This means that when this time-dependent inert strength is substituted in equation (23), we could predict that reliability would improve as time elapsed. This is obviously incorrect since a structure's reliability cannot increase with time. Hence, adjustments to the methodology are necessary to ensure that the reliability never increases with time.

The procedure proposed here to ensure that the reliability does not improve with time is based on maximizing the fast-fracture potential of the applied stresses $\sigma_{\mathrm{I}eq,j}$ of all time steps—that is, finding the applied stress with the highest potential fast-fracture probability of failure and using a transformed value of that stress as the final strength of the last time step. In other words, the stress history (all time steps) is transformed in such a way that the material properties for the entire history remain constant. The material properties during the last time step (step 2) are used to normalize (transform) the load history. In this procedure, the stress history (all time steps) is transformed using equation (28) and the Weibull parameters of the last time step (which in this case is step 2). The largest value of these transformed stresses is also the one with the highest fast-fracture failure probability. This value is then used as the final strength term of the last time step. In this case for the two-time-step loading history, the applied stress during time step 1, $\sigma_{\mathrm{I}eq,1}$, is transformed to an equivalent value, $\sigma_{\mathrm{I}eq,1,2}$, that is based on the Weibull parameters of time step 2 (with the transformed value having the same probability of failure as the untransformed value). Obviously, the stress during time step 2 remains the same since the material properties of step 2 are used to transform the stresses. According to equation (28), the transformed applied stress of time step 1 on the basis of the properties of time step 2 is

$$\sigma_{\mathrm{I}eq,1,2} = \sigma_{oBV,2}\left(\frac{\sigma_{\mathrm{I}eq,1}}{\sigma_{oBV,1}}\right)^{\frac{m_{V,1}}{m_{V,2}}} \tag{30}$$

and this maximization for two time steps is described as

$$\sigma_{\mathrm{I}eq,2,T\max} = \max\left(\sigma_{\mathrm{I}eq,1,2}, \sigma_{\mathrm{I}eq,2,2}\right) \tag{31}$$

The final strength term in equation (29) is set equal to the maximum transformed stress, $\sigma_{\mathrm{I}eq,2,T\mathrm{max}}$, which is equal to the maximum of either $\sigma_{\mathrm{I}eq,1,2}$ or $\sigma_{\mathrm{I}eq,2,2}$. The second subscript in $\sigma_{\mathrm{I}eq,2,T\mathrm{max}}$ indicates that the stresses during all time steps have been transformed using the Weibull parameters of the last time step (step 2), whereas the third subscript, *T*max, indicates that the maximum transformed stress during all time steps was selected. This maximization procedure ensures that both stress magnitudes and material properties are taken into account when maximizing the final strength term in the $\sigma_{\mathrm{I}eq,0}$ inert strength formulation.

Substituting the maximum transformed stress into equation (29) and subsequently equation (29) into equation (23), yields the following reliability formula for the entire component at the end of time step 2:

$$P_{sV}(t_2) = \exp\left(-\sum_{isub=1}^{n_{\mathrm{sub}}} \frac{V_{isub}}{4\pi}\left\{\int_{\Omega}\left[X_1(\Psi)\right]^{\frac{m_{V,1}}{N_{V,1}-2}}\,\mathrm{d}\Omega\right\}_{isub}\right) \tag{32}$$

$$X_1(\Psi) = \left\{\left[\left(\frac{\sigma_{\mathrm{I}eq,2,T\max}}{\sigma_{oBV,2}}\right)^{N_{V,2}-2} + \frac{\sigma_{\mathrm{I}eq,2}^{N_{V,2}}\,\Delta t_2}{\sigma_{oBV,2}^{N_{V,2}-2}\,B_{BV,2}}\right]^{\frac{m_{V,2}\left[N_{V,1}-2\right]}{m_{V,1}\left[N_{V,2}-2\right]}} + \frac{\sigma_{\mathrm{I}eq,1}^{N_{V,1}}\,\Delta t_1}{\sigma_{oBV,1}^{N_{V,1}-2}\,B_{BV,1}}\right\} \tag{33}$$

2.3.3 Time step 3.—Time step 3 spans the time interval between $t = t_2$ and $t = t_3$, and the time step interval is $\Delta t_3 = t_3 - t_2$. During this time step (Δt_3) and for a given element *isub*, the applied stress is $\sigma_{\mathrm{I}eq,3}$, the temperature is T_3, the scale parameter is $\sigma_{oV,3}$, the Weibull modulus is $m_{V,3}$, the fatigue constant is $B_{BV,3}$, and the fatigue exponent is $N_{V,3}$.

For time step 3, a similar procedure to that performed for time step 2 yields the expression for the inert strength at $t = 0$. It is assumed that the strength of the strongest flaw that will just initiate failure in the material is equal to the maximum transformed applied stress $\sigma_{\mathrm{I}eq,3,T\max}$ at $t_3 = t_f$. The initial strength at the beginning of time step 3 is

$$\sigma_{\mathrm{I}eqc,3}(t_2) = \left(\frac{\sigma_{\mathrm{I}eq,3}^{N_{V,3}} \Delta t_3}{B_{BV,3}} + \sigma_{\mathrm{I}eq,3,T\max}^{N_{V,3}-2} \right)^{\frac{1}{N_{V,3}-2}} \tag{34}$$

where the maximum transformed stress is

$$\sigma_{\mathrm{I}eq,3,T\max} = \max\left(\sigma_{\mathrm{I}eq,1,3}, \sigma_{\mathrm{I}eq,2,3}, \sigma_{\mathrm{I}eq,3,3}\right) \tag{35}$$

and

$$\sigma_{\mathrm{I}eq,j,3} = \sigma_{oBV,3} \left(\frac{\sigma_{\mathrm{I}eq,j}}{\sigma_{oBV,j}} \right)^{\frac{m_{V,j}}{m_{V,3}}} \tag{36}$$

The stresses for all the time steps are transformed using the Weibull parameters of the last time step—in this case time step 3—to obtain $\sigma_{\mathrm{I}eq,3,T\max}$, which has the highest fast-fracture probability of failure of all the time steps. The initial strength at the beginning of time step 3 is related to the final strength of time step 2 by

$$\sigma_{\mathrm{I}eqc,2}(t_2) = \sigma_{oBV,2} \left[\frac{\sigma_{\mathrm{I}eqc,3}(t_2)}{\sigma_{oBV,3}} \right]^{\frac{m_{V,3}}{m_{V,2}}} \tag{37}$$

The inert strength, $\sigma_{\mathrm{I}eq,0}$, is found by (first) substituting equation (34) for the initial strength, $\sigma_{\mathrm{I}eqc,3}(t_2)$, at the beginning of time step 3 into equation (37) for the final strength, $\sigma_{\mathrm{I}eqc,2}(t_2)$, at the end of time step 2; then (second) substituting the final strength, $\sigma_{\mathrm{I}eqc,2}(t_2)$, from equation (37) into equation (25) to find the initial strength, $\sigma_{\mathrm{I}eqc,2}(t_1)$, of time step 2; then (third) substituting equation (25) for $\sigma_{\mathrm{I}eqc,2}(t_1)$ into equation (28) to find the final strength, $\sigma_{\mathrm{I}eqc,1}(t_1)$, at the end of time step 1; and (fourth) substituting $\sigma_{\mathrm{I}eqc,1}(t_1)$ in equation (28) into equation (22) to obtain the inert strength, $\sigma_{\mathrm{I}eq,0}$. Performing these operations and rearranging gives

$$\sigma_{\mathrm{I}eq,0} = \left\{ \frac{\sigma_{oBV,1}^{N_{V,1}-2}}{\sigma_{oBV,2}^{(m_{V,2}/m_{V,1})(N_{V,1}-2)}} \left[\frac{\sigma_{oBV,2}^{N_{V,2}-2}}{\sigma_{oBV,3}^{(m_{V,3}/m_{V,2})(N_{V,2}-2)}} \left(\sigma_{\mathrm{I}eq,3,T\max}^{N_{V,3}-2} + \frac{\sigma_{\mathrm{I}eq,3}^{N_{V,3}} \Delta t_3}{B_{BV,3}} \right)^{\frac{m_{V,3}[N_{V,2}-2]}{m_{V,2}[N_{V,3}-2]}} + \frac{\sigma_{\mathrm{I}eq,2}^{N_{V,2}} \Delta t_2}{B_{BV,2}} \right]^{\frac{m_{V,2}[N_{V,1}-2]}{m_{V,1}[N_{V,2}-2]}} + \frac{\sigma_{\mathrm{I}eq,1}^{N_{V,1}} \Delta t_1}{B_{BV,1}} \right\}^{\frac{1}{N_{V,1}-2}} \tag{38}$$

The reliability for the entire component at the end of time step 3 is

$$P_{sV}\left(t_3\right) = \exp\left(- \sum_{isub=1}^{n_{\text{sub}}} \frac{V_{isub}}{4\pi} \left\{ \int_{\Omega} \left[X_1(\Psi)\right]^{\frac{m_{V,1}}{N_{V,1}-2}} \, \mathrm{d}\Omega \right\}_{isub} \right) \tag{39}$$

$$X_1(\Psi) = \left(\left\{ \left[\left(\frac{\sigma_{\mathrm{I}eq,3,T\max}}{\sigma_{oBV,3}} \right)^{N_{V,3}-2} + \frac{\sigma_{\mathrm{I}eq,3}^{N_{V,3}}\, \Delta t_3}{\sigma_{oBV,3}^{N_{V,3}-2}\, B_{BV,3}} \right]^{\frac{m_{V,3}\left[N_{V,2}-2\right]}{m_{V,2}\left[N_{V,3}-2\right]}} + \frac{\sigma_{\mathrm{I}eq,2}^{N_{V,2}}\, \Delta t_2}{\sigma_{oBV,2}^{N_{V,2}-2}\, B_{BV,2}} \right\}^{\frac{m_{V,2}\left[N_{V,1}-2\right]}{m_{V,1}\left[N_{V,2}-2\right]}} + \frac{\sigma_{\mathrm{I}eq,1}^{N_{V,1}}\, \Delta t_1}{\sigma_{oBV,1}^{N_{V,1}-2}\, B_{BV,1}} \right) \tag{40}$$

2.3.4 General transient reliability formulation for k number of time steps.—When a comparison is made of the reliability formulations of equations (23) and (24) for one time step, equations (32) and (33) for two time steps, and equations (39) and (40) for three time steps, a clear pattern emerges. It can be seen from these functions that the transient reliability equation (when the change in material response is taken into account) is an ever-expanding function, which adds nested terms as more time steps are considered. Hence, for *k* time steps

$$P_{sV}\left(t_k\right) = \exp\left(- \sum_{isub=1}^{n_{\text{sub}}} \frac{V_{isub}}{4\pi} \left\{ \int_{\Omega} \left[X_1(\Psi)\right]^{\frac{m_{V,1}}{N_{V,1}-2}} \mathrm{d}\Omega \right\}_{isub} \right) \tag{41}$$

$$X_1(\Psi) = \left(\left[\cdots \left\{ \left[\left(\frac{\sigma_{\mathrm{I}eq,k,T\max}}{\sigma_{oBV,k}} \right)^{N_{V,k}-2} + \frac{\sigma_{\mathrm{I}eq,k}^{N_{V,k}}\, \Delta t_k}{\sigma_{oBV,k}^{N_{V,k}-2}\, B_{BV,k}} \right]^{\frac{m_{V,k}\left[N_{V,(k-1)}-2\right]}{m_{V,(k-1)}\left[N_{V,k}-2\right]}} + \frac{\sigma_{\mathrm{I}eq,(k-1)}^{N_{V,(k-1)}}\, \Delta t_{(k-1)}}{\sigma_{oBV,(k-1)}^{N_{V,(k-1)}-2}\, B_{BV,(k-1)}} \right\}^{\frac{m_{V,(k-1)}\left[N_{V,(k-2)}-2\right]}{m_{V,(k-2)}\left[N_{V,(k-1)}-2\right]}} + \cdots + \frac{\sigma_{\mathrm{I}eq,2}^{N_{V,2}} \Delta t_2}{\sigma_{oBV,2}^{N_{V,2}-2}\, B_{V,2}} \right]^{\frac{m_{V,2}\left[N_{V,1}-2\right]}{m_{V,1}\left[N_{V,2}-2\right]}} + \frac{\sigma_{\mathrm{I}eq,1}^{N_{V,1}}\, \Delta t_1}{\sigma_{oBV,1}^{N_{V,1}-2}\, B_{BV,1}} \right) \tag{42}$$

where the maximum transformed stress is

$$\sigma_{\mathrm{I}eq,k,T\max} = \max\left(\sigma_{\mathrm{I}eq,1,k}, \sigma_{\mathrm{I}eq,2,k}, \sigma_{\mathrm{I}eq,3,k}, \ldots, \sigma_{\mathrm{I}eq,k,k}\right) \tag{43}$$

and

$$\sigma_{\mathrm{I}eq,j,k} = \sigma_{oBV,k}\left(\frac{\sigma_{\mathrm{I}eq,j}}{\sigma_{oBV,j}}\right)^{\frac{m_{V,j}}{m_{V,k}}} \tag{44}$$

where $1 \le j \le k$. Appendix B shows the numerical algorithm of equation (42).

2.3.5 Transient reliability without SCG.—In the case where a component is manufactured using a material resistant to SCG and thus does not degrade with time, the transient reliability formulation becomes much simpler. Since the inherent flaws do not grow with time, one simply needs to track the applied stress history and compute the corresponding failure probability as a function of time.

This analysis is identical to the fast-fracture analysis with the exception that it has to be done as many times as there are time steps. Hence, a given stress history is broken into short time steps during which the stress, temperature, and environment are assumed to be constant. Then, the following equation is used to calculate the reliability $P_{sV}(t_j)$ at the end of each time step j:

$$P_{sV}\left(t_j\right) = \exp\left\{-\sum_{isub=1}^{n_{\mathrm{sub}}} \frac{V_{isub}}{4\pi}\left[\bar{k}_{BV,j}\int_{\Omega}\left(\frac{\sigma_{\mathrm{I}eq,j}}{\sigma_{oV,j}}\right)^{m_{V,j}} \mathrm{d}\Omega\right]_{isub}\right\} \tag{45}$$

It is apparent from equation (45) that the reliability increases as the applied stress decreases. Although this is true for instantaneous fast-fracture loading, prudence should be exercised when applying that equation to time-dependent loading when no damage occurs. For example, if a given component is subjected to decreased loading, then equation (45) will numerically predict increased reliability for that component as time elapses. However, a component's reliability cannot improve with time. Hence, for cases where the loading eases at a given time step, $j + 1$ (the computed reliability increases), the reliability is set equal to that at the previous time step. In other words, decreased loading does not result in increased reliability but keeps it constant. In the case of repeated block loading when the material does not degrade with time, the transient reliability analysis needs to be conducted for only one load block. This is because the reliability versus time curves are identical for all load blocks since no damage takes place.

The authors of this report developed the general transient reliability formulation initially for one, then two, then three, and finally k number of time steps. By showing the development of this methodology in a slow, gradual manner, the authors hope that they have made the task of understanding this work easier for readers.

It is apparent from equations (41) to (44) that the transient reliability formulation depends on the load and thermal/environmental history. The dependence on the thermal/environmental load history comes from the sequential order of the exponential term $m_{V,k}[N_{V,(k-1)} - 2]/m_{V,(k-1)}[N_{V,k} - 2]$ and the rigid ordering of the nested terms. When the material parameters, m and N, remain constant with time (temperature and environment do not vary with time), the exponential terms cancel out. Under such circumstances, the transient reliability becomes independent of both the load and the thermal/environmental history sequence, and simplification, such as Mencik's g-factor approach (Mencik, 1984), becomes possible. It is worth mentioning that the general transient reliability formulation shows that the g-factor approach is only applicable under the special circumstances of constant Weibull and fatigue parameters versus time.

All the derivations shown earlier were based on the assumption that volume flaws control failure. When surface flaws dominate the failure process, similar equations integrated over the surface area of the component are used to compute the transient reliability.

2.4 Computationally Efficient Algorithm for Cyclic Loading

In many engineering applications, structural components are subjected to repeated block loading. This section shows a computationally efficient algorithm to perform transient reliability analysis for repeated cyclic loading. The algorithm is derived in appendix C. This methodology is shown for power law SCG, as developed in previous sections of this report.

Before proceeding, the terminology used must be explained. In the analysis in this section and in the proof-testing sections, a load cycle refers to a segment of the transient load history. Figure 3 shows a schematic diagram of such a loading history where a component is subjected to Z_1 number of repeated load cycles. Such repeated cyclic loading and its damage to the ceramic structural component can be incorporated into the transient reliability analysis. An example of such a load cycle is the load history acting on a component of an aircraft from takeoff, through cruising, to landing. This report uses a load block to indicate a collection of several load cycles. Thus, for the aircraft example, a load block of 10 cycles represents a load history of 10 takeoffs, cruises, and landings.

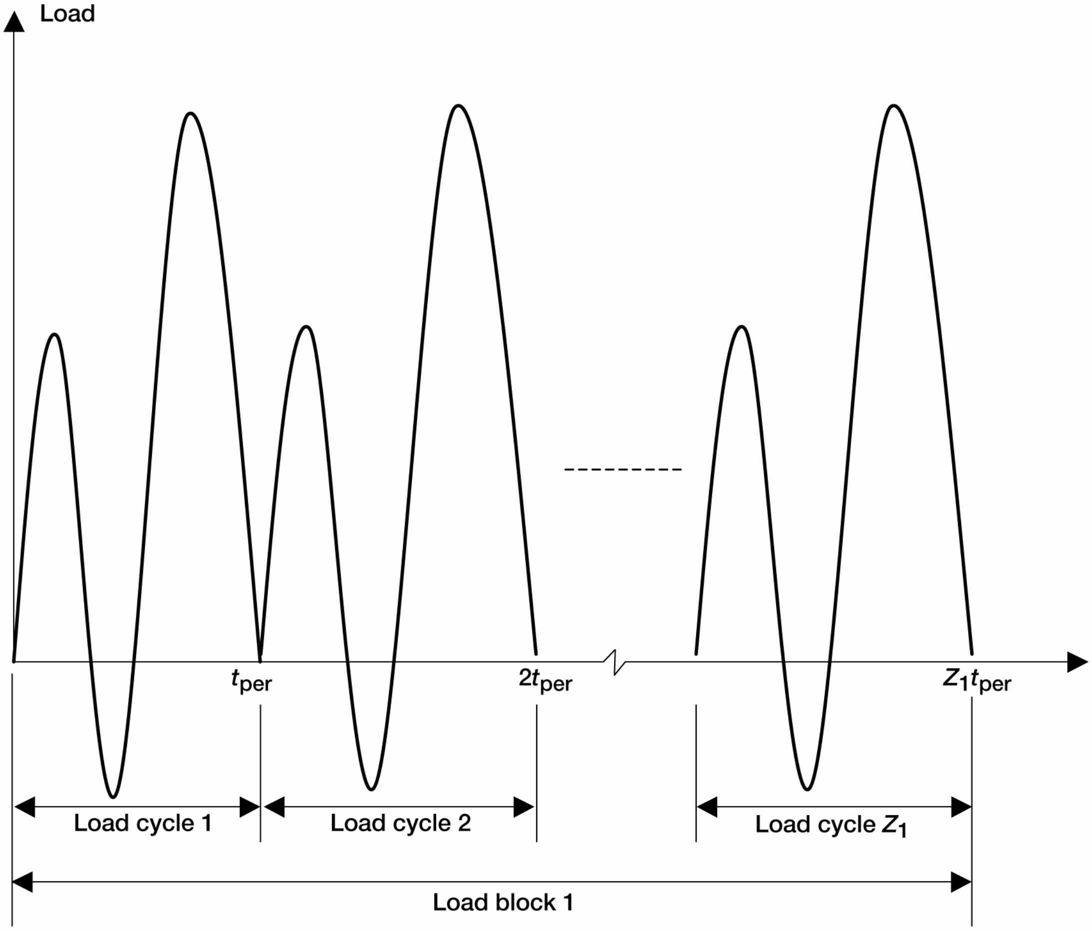

Figure 3.—Repeated cyclic loading. Number of repeated cycles, Z_1.

Equations (41) to (44) are computationally inefficient when used to compute reliability for cyclic loading. For example, if k is the number of time steps in the first load cycle (load cycle 1 in fig. 3), then equation (42) requires kZ_1 time steps to calculate a reliability solution for Z_1 cycles. Obviously, this quickly becomes computationally intensive when reliability solutions for large cycle counts are desired. As an alternative, the authors developed a more computationally efficient means to perform this task—which is described in detail in appendixes B and C. This approximation method allows for a tradeoff between solution accuracy and numerical efficiency. The method is developed by approximating equation (42) with a truncated binomial series expansion of the form

$$(x+y)^{\mu} = x^{\mu} + \mu x^{\mu-1} y + \frac{\mu(\mu-1)}{2!} x^{\mu-2} y^2 + \frac{\mu(\mu-1)(\mu-2)}{3!} x^{\mu-3} y^3 + \dots \tag{46}$$

where $x^2 > y^2$. When $x >> y$, the higher order terms in the series become negligible and the series can be approximated as a two-term expression:

$$(x+y)^{\mu} \approx x^{\mu} + \mu x^{\mu-1} y \qquad \text{when } x >> y \tag{47}$$

This approximation of equation (42) is generally valid after a sufficient number of time steps have been accounted for in the calculation. What that sufficient number is depends on the level of loading, the load history, and the number of time steps in a block. For example, $(1 + 0.01)^{10} = 1.1046$, instead of 1.1000 with equation (47), and $(1 + 0.01)^{0.1} = 1.0009955$, instead of 1.001000 with equation (47). The level of error is on the order of 5 percent with the two-term approximation. Certainly by 100 cycles, the two-term binomial approximation of equation (42) would have the y term at most 0.01 the size of the x term. Also, since the exponent is likely to be between the bounds of 0.1 and 10, the associated error is not likely to be serious beyond 100 or so cycles.

Whereas the previous solution (eqs. (41) to (44)) requires kZ_1 calculation steps per load block with k time steps per load cycle, the cyclic approximation method of appendix C requires $k\lambda$ calculation steps where λ is the number of load blocks making up the entire load history. The λ solution increments are constructed such that

$$Z_{\text{total}} = \sum_{\iota=1}^{\lambda} Z_{\iota} \tag{48}$$

where Z_{ι} represents the number of load cycles within load block ι. Component survival probability is expressed as

$$P_{sV}\left(Z_{\text{total}} t_k\right) = \exp\left\{ - \sum_{isub=1}^{n_{\text{sub}}} \frac{V_{isub}}{4\pi} \left[\int_{\Omega} \left(X_1\right)^{\frac{m_{V,1}}{N_{V,1}-2}} \mathrm{d}\Omega \right]_{isub} \right\} \tag{49}$$

where

$$
\begin{aligned}
X_1 = \Bigg\{ [[\ldots [[\ldots \Bigg\{ [\ldots [[\Bigg\{ [\ldots [[\left(\frac{\sigma_{\mathrm{I}eq,k,T\max}}{\sigma_{oBV,k}} \right)^{N_{V,k}-2} \\
& + \left. \frac{\sigma_{\mathrm{I}eq,k}^{N_{V,k}} Z_{\lambda} \Delta t_k}{\sigma_{oBV,k}^{N_{V,k}-2} B_{BV,k}} \right]_k^{\frac{m_{V,k}\left[N_{V,(k-1)}-2\right]}{m_{V,(k-1)}\left[N_{V,k}-2\right]}} + \left. \frac{\sigma_{\mathrm{I}eq,(k-1)}^{N_{V,(k-1)}} Z_{\lambda} \Delta t_{(k-1)}}{\sigma_{oBV,(k-1)}^{N_{V,(k-1)}-2} B_{BV,(k-1)}} \right]_{k-1}^{\frac{m_{V,(k-1)}\left[N_{V,(k-2)}-2\right]}{m_{V,(k-2)}\left[N_{V,(k-1)}-2\right]}} + \ldots + \left. \frac{\sigma_{\mathrm{I}eq,1}^{N_{V,1}} Z_{\lambda} \Delta t_1}{\sigma_{oBV,1}^{N_{V,1}-2} B_{BV,1}} \right]_1^{\frac{m_{V,1}\left[N_{V,k}-2\right]}{m_{V,k}\left[N_{V,1}-2\right]}} \Bigg\}_{\lambda} \\
& + \left. \frac{\sigma_{\mathrm{I}eq,k}^{N_{V,k}} Z_{(\lambda-1)} \Delta t_k}{\sigma_{oBV,k}^{N_{V,k}-2} B_{BV,k}} \right]_k^{\frac{m_{V,k}\left[N_{V,(k-1)}-2\right]}{m_{V,(k-1)}\left[N_{V,k}-2\right]}} + \left. \frac{\sigma_{\mathrm{I}eq,(k-1)}^{N_{V,(k-1)}} Z_{(\lambda-1)} \Delta t_{(k-1)}}{\sigma_{oBV,(k-1)}^{N_{V,(k-1)}-2} B_{BV,(k-1)}} \right]_{k-1}^{\frac{m_{V,(k-1)}\left[N_{V,(k-2)}-2\right]}{m_{V,(k-2)}\left[N_{V,(k-1)}-2\right]}} + \ldots + \left. \frac{\sigma_{\mathrm{I}eq,1}^{N_{V,1}} Z_{(\lambda-1)} \Delta t_1}{\sigma_{oBV,1}^{N_{V,1}-2} B_{BV,1}} \right]_1^{\frac{m_{V,1}\left[N_{V,k}-2\right]}{m_{V,k}\left[N_{V,1}-2\right]}} \Bigg\}_{\lambda-1} \\
& + \ldots + \left. \frac{\sigma_{\mathrm{I}eq,k}^{N_{V,k}} Z_1 \Delta t_k}{\sigma_{oBV,k}^{N_{V,k}-2} B_{BV,k}} \right]_k^{\frac{m_{V,k}\left[N_{V,(k-1)}-2\right]}{m_{V,(k-1)}\left[N_{V,k}-2\right]}} + \left. \frac{\sigma_{\mathrm{I}eq,(k-1)}^{N_{V,(k-1)}} Z_1 \Delta t_{(k-1)}}{\sigma_{oBV,(k-1)}^{N_{V,(k-1)}-2} B_{BV,(k-1)}} \right]_{k-1}^{\frac{m_{V,(k-1)}\left[N_{V,(k-2)}-2\right]}{m_{V,(k-2)}\left[N_{V,(k-1)}-2\right]}} + \ldots + \left. \frac{\sigma_{\mathrm{I}eq,2}^{N_{V,2}} Z_1 \Delta t_2}{\sigma_{oBV,2}^{N_{V,2}-2} B_{V,2}} \right]_2^{\frac{m_{V,2}\left[N_{V,1}-2\right]}{m_{V,1}\left[N_{V,2}-2\right]}} + \left. \frac{\sigma_{\mathrm{I}eq,1}^{N_{V,1}} Z_1 \Delta t_1}{\sigma_{oBV,1}^{N_{V,1}-2} B_{BV,1}} \right]_1 \Bigg\}_1
\end{aligned}
\tag{50}
$$

As the number of load blocks λ gets smaller (for a fixed number of total cycles Z_{total}), the computational efficiency increases, but with some loss of accuracy. A numerical example at the end of appendix C illustrates this tradeoff. For $\lambda = 1$, equation (50) simplifies to

$$\begin{aligned} X_1 = \Bigg\{ [\ldots \Bigg[\Bigg[& \left(\frac{\sigma_{\mathrm{I}eq,k,T\max}}{\sigma_{oBV,k}} \right)^{N_{V,k}-2} + \frac{\sigma_{\mathrm{I}eq,k}^{N_{V,k}} Z_{\mathrm{total}} \Delta t_k}{\sigma_{oBV,k}^{N_{V,k}-2} B_{BV,k}} \Bigg]_k^{\frac{m_{V,k}\left[N_{V,(k-1)}-2\right]}{m_{V,(k-1)}\left[N_{V,k}-2\right]}} \\ & + \frac{\sigma_{\mathrm{I}eq,(k-1)}^{N_{V,(k-1)}} Z_{\mathrm{total}} \Delta t_{(k-1)}}{\sigma_{oBV,(k-1)}^{N_{V,(k-1)}-2} B_{BV,(k-1)}} \Bigg]_{(k-1)}^{\frac{m_{V,(k-1)}\left[N_{V,(k-2)}-2\right]}{m_{V,(k-2)}\left[N_{V,(k-1)}-2\right]}} + \ldots + \frac{\sigma_{\mathrm{I}eq,2}^{N_{V,2}} Z_{\mathrm{total}} \Delta t_2}{\sigma_{oBV,2}^{N_{V,2}-2} B_{V,2}} \Bigg]_2^{\frac{m_{V,2}\left[N_{V,1}-2\right]}{m_{V,1}\left[N_{V,2}-2\right]}} + \frac{\sigma_{\mathrm{I}eq,1}^{N_{V,1}} Z_{\mathrm{total}} \Delta t_1}{\sigma_{oBV,1}^{N_{V,1}-2} B_{BV,1}} \Bigg\}_1 \end{aligned} \tag{51}$$

This equation represents the most computationally efficient solution for repeated block loading. Unfortunately, there does not appear to be an easy way to make any general statements regarding error. The amount of error appears to depend on the problem. It is, therefore, up to users to determine if the error associated with equation (51) is acceptable (see the numerical example at the end of appendix C).

It is important to point out that in equations (50) and (51) the block loading component *Z* appears within the individual time steps. Mencik (1984) conversely indicates *Z* as a multiplier of all the time steps—which is true only when material properties are constant over the time steps. Therefore, *g*-factors, as introduced by Mencik, cannot be used except under constant Weibull and SCG parameters.

2.5 Transient Reliability and Cyclic Fatigue

In this section, the effect of cyclic fatigue (i.e., increased damage due to cyclic loading) is added to the transient reliability analysis methodology. This new equation assumes that loading amplitude and frequency are constant, and there is no provision for the effect of temperature history on the load cycle. Thus, this methodology does not model thermomechanical fatigue phenomena or the effect of a fluctuating (spectrum or random) load history. The Walker law (Walker, 1970) is used here to model the effect of cyclic fatigue; in particular, it accounts for the effect of *R*-ratio (ratio of minimum stress to maximum stress) on crack growth. Overall crack growth is modeled with a superposed SCG power law and fatigue Walker law. This work is an extension of Rahman et al. (1998) and requires that the SCG power law fatigue exponent and the Walker law fatigue exponent be equal. Rahman et al. is reproduced in appendix E for the reader's convenience and includes a procedure for parameter estimation of specimen rupture data.

Subcritical crack growth is a complex phenomenon involving a combination of simultaneous and synergistic failure mechanisms. These can be grouped into two classes: static effects and cyclic effects. "Static effects" refers to the slow propagation of cracks under cyclic stresses and can be explained by the same environmental and corrosive processes responsible for subcritical crack growth under static loads. Previous sections of this report deal entirely with modeling associated with static effects (e.g., the power law model of SCG shown in equation (8)). Cyclic effects are functionally dependent on the number of cycles, the peak cyclic load, the range of the stress intensity factor, and possibly on the frequency of the loading. The subcritical crack growth phenomenon can be caused by a variety of effects, such as debris wedging or the degradation of bridging ligaments near the crack tip, but essentially it is based on the accumulation of some type of irreversible damage that enhances the crack growth. Not all materials display cyclic effects. Glasses seem to show only static effects, whereas polycrystalline materials are more susceptible to cyclic effects—particularly if crack growth is intergranular (around the grains) rather than transgranular (through the grains). Modeling SCG using the power law is well accepted, whereas a standard procedure for modeling cyclic effects has not been established.

To empirically account for cyclic effects, the CARES/*Life* program (see app. D from Nemeth et al., 2003) implemented the Paris law (Paris and Erdogan, 1963) and Walker law (Walker, 1970), which traditionally have been used for metal fatigue. The Walker Law is an extension of the Paris law to account for the effect of the stress ratio (R-ratio) on fatigue lifetime. The Walker law is expressed as

$$\frac{\mathrm{d}a(\Psi,n)}{\mathrm{d}n} = A_2 K_{\mathrm{I}eq,\max}^{N_2-Q}(\Psi,n)\ \Delta K_{\mathrm{I}eq}^{Q}(\Psi,n) \tag{52}$$

and from equation (2), for the definition of the stress intensity factor,

$$K_{\mathrm{I}eq,\max}(\Psi,n) = \sigma_{\mathrm{I}eq,\max}(\Psi,n) Y \sqrt{a(\Psi,n)} \tag{53}$$

$$\Delta K_{\mathrm{I}eq}(\Psi,n) = \left[\sigma_{\mathrm{I}eq,\max}(\Psi,n) - \sigma_{\mathrm{I}eq,\min}(\Psi,n)\right] Y \sqrt{a(\Psi,n)} \tag{54}$$

where n is the number of cycles; A_2, N_2, and Q are material parameters that depend on temperature; $\Delta K_{\mathrm{I}eq}(\Psi, n)$ is the mode-I equivalent stress-intensity factor range at cycle count n and location/orientation Ψ; $K_{\mathrm{I}eq,\max}(\Psi, n)$ is the maximum mode-I equivalent stress-intensity factor (i.e., the maximum value of $K_{\mathrm{I}eq}$ over cycle n at location/orientation Ψ); $\Delta K_{\mathrm{I}eq}(\Psi, n)$ is the range of the mode-I equivalent stress-intensity factor at n and Ψ; $\sigma_{\mathrm{I}eq,\max}$ is the peak applied far-field equivalent stress over the cycle; and $\sigma_{\mathrm{I}eq,\min}$ is the minimum applied far-field equivalent stress over the cycle. Equation (52) is easily expressed as a function of time by multiplying it by the cyclic frequency f_c:

$$\frac{\mathrm{d}a(\Psi,t)}{\mathrm{d}t} = f_c \frac{\mathrm{d}a(\Psi,n)}{\mathrm{d}n} = f_c A_2 K_{\mathrm{I}eq,\max}^{N_2-Q}(\Psi,t)\ \Delta K_{\mathrm{I}eq}^{Q}(\Psi,t) \tag{55}$$

where, for example, $\Delta K_{\mathrm{I}eq,\max}(\Psi, t)$ is the maximum value of $K_{\mathrm{I}eq}$ over the cycle n (that is associated with the particular value of t) at location/orientation Ψ. It is assumed that $[\mathrm{d}a(\Psi, t)]/\mathrm{d}t$ in equation (55) is continuous at fractions of a cycle: that is, it is assumed that $[\mathrm{d}a(\Psi, t)]/\mathrm{d}t$ could be computed for noninteger (real number) cycle counts.

Rahman et al. (1998), reproduced in appendix E, describes a crack growth law that is a superposition of the Walker law and the power law (eq. (8)). This equation has the desirable feature for ceramics that, when the loading is static (not varying with time), the crack growth is not zero. The philosophy behind this approach is that, for ceramics (unlike metals), cyclic loading enhances environmentally assisted SCG through the processes described at the beginning of this section. Adding equations (8) and (55) yields the equivalent mode-I crack extension for a superimposed power law and Walker law:

$$\frac{\mathrm{d}a(\Psi,t)}{\mathrm{d}t} = A_1 K_{\mathrm{I}eq}^{N_1}(\Psi,t) + f_c A_2 K_{\mathrm{I}eq,\max}^{N_2-Q}(\Psi,t)\ \Delta K_{\mathrm{I}eq}^{Q}(\Psi,t) \tag{56}$$

where A_1, A_2, N_1, N_2, and Q are material constants that depend on the temperature and environment.

The g-factor (Mencik, 1984) (defined for constant material parameters versus time) is

$$g(\Psi) = \frac{1}{t_{\mathrm{per}}} \int_0^{t_{\mathrm{per}}} \left[\frac{\sigma_{\mathrm{I}eq}(\Psi,t)}{\sigma_{\mathrm{I}eq,\max}(\Psi)}\right]^{N_1} \mathrm{d}t \tag{57}$$

where t_{per} is the period of the cycle. The crack-growth rate in equation (56) can be reexpressed with the *g*-factor as

$$\frac{\mathrm{d}a(\Psi,t)}{\mathrm{d}t} = A_1 g(\Psi,t) K_{\mathrm{I}eq,\max}^{N_1}(\Psi,t) + f_c(\Psi,t) A_2 [1 - R(\Psi,t)]^Q K_{\mathrm{I}eq,\max}^{N_2}(\Psi,t) \tag{58}$$

where the *R*-ratio is defined as

$$R(\Psi,t) = \frac{\sigma_{\mathrm{I}eq,\min}(\Psi,t)}{\sigma_{\mathrm{I}eq,\max}(\Psi,t)} \tag{59}$$

The terms $g(\Psi, t)$; $\Delta K_{\mathrm{I}eq,\max}(\Psi, t)$; $f_c(\Psi, t)$; $R(\Psi, t)$; $\sigma_{\mathrm{I}eq,\max}(\Psi, t)$; and $\sigma_{\mathrm{I}eq,\min}(\Psi, t)$ are indicated as a function of time, although they are assumed to be constant values over the period of any given cycle *n*. Examining equation (58) shows that $A_1 g(\Psi,t) K_{\mathrm{I}eq,\max}^{N_1}(\Psi,t)$ is an equivalent static (non-time-varying) term that produces the same amount of crack growth as the periodic cyclic stress distribution over the period of the cycle.

A strength degradation equation analogous to equation (14) can be obtained from equation (58). By comparing equations (58) and (7) and noting that

$$\frac{K_{\mathrm{I}eq,\max}(\Psi,t)}{K_{\mathrm{I}eqc}(t)} = \frac{\sigma_{\mathrm{I}eq,\max}(\Psi,t)}{\sigma_{\mathrm{I}eqc}(\Psi,t)} \tag{60}$$

we can show that, analogous to equation (11),

$$\begin{aligned}\frac{\mathrm{d}\sigma_{\mathrm{I}eqc}(\Psi,t)}{\mathrm{d}t} = \sigma_{\mathrm{I}eqc}^{3}(\Psi,t)\left[\frac{Y}{-2K_{\mathrm{I}eqc}(t)}\right]^2 &\left\{A_1 g(\Psi,t) K_{\mathrm{I}eqc}^{N_1}(t)\left[\frac{\sigma_{\mathrm{I}eq,\max}(\Psi,t)}{\sigma_{\mathrm{I}eqc}(\Psi,t)}\right]^{N_1}\right.\\ &\left.+ f_c(\Psi,t) A_2 [1 - R(\Psi,t)]^Q K_{\mathrm{I}eqc}^{N_2}(t)\left[\frac{\sigma_{\mathrm{I}eq,\max}(\Psi,t)}{\sigma_{\mathrm{I}eqc}(\Psi,t)}\right]^{N_2}\right\}\end{aligned} \tag{61}$$

Following the separation of variables $\sigma_{\mathrm{I}eq}$ and *t* in equation (61), it is theoretically possible to calculate the initial and final strength over a given time interval. However, no closed-form explicit solution exists using equation (61) directly. A closed-form solution is desired to minimize the amount of computation involved with the reliability analysis that is coupled with results from finite element models. A closed-form solution can be obtained if it is assumed that the fatigue exponents for static and cyclic fatigue are identical. If $N_1 = N_2 = N$, equation (61) can be solved analogous to equation (13) over the time interval t_{int} to t_{fin}:

$$\begin{aligned}&\int_{\sigma_{\mathrm{I}eqc}(\Psi,t_{\mathrm{int}})}^{\sigma_{\mathrm{I}eqc}(\Psi,t_{\mathrm{fin}})} \sigma_{\mathrm{I}eqc}^{N-3}(\Psi,t)\,\mathrm{d}\sigma_{\mathrm{I}eqc}(\Psi,t) = \\ &\qquad -\frac{1}{2}\left\{A_1(\Psi) g(\Psi) + f_c(\Psi) A_2(\Psi)[1 - R(\Psi)]^{Q(\Psi)}\right\} Y^2 K_{\mathrm{I}eqc}^{N(\Psi)-2}(\Psi)\,\sigma_{\mathrm{I}eq,\max}^{N(\Psi)}(\Psi)\int_{t_{\mathrm{int}}}^{t_{\mathrm{fin}}} \mathrm{d}t\end{aligned} \tag{62}$$

In arriving at equation (62), we assume that the material parameters A_1, A_2, *N*, and $K_{\mathrm{I}eqc}$ are constant over the time interval. The integral, similar to equation (14), evaluates to

$$\sigma_{\mathrm{I}eqc}\left(\Psi,t_{\mathrm{int}}\right)=\left(\frac{\sigma_{\mathrm{I}eq,\max}^{N(\Psi)}\left(\Psi\right)\left\{g\left(\Psi\right)+f_c\left(\Psi\right)\left[\frac{A_2\left(\Psi\right)}{A_1\left(\Psi\right)}\right]\left[1-R\left(\Psi\right)\right]^{Q(\Psi)}\right\}\left(t_{\mathrm{fin}}-t_{\mathrm{int}}\right)}{B\left(\Psi\right)}+\sigma_{\mathrm{I}eqc}^{N(\Psi)-2}\left(\Psi,t_{\mathrm{fin}}\right)\right)^{\frac{1}{N(\Psi)-2}} \tag{63}$$

where

$$B\left(\Psi\right)=\frac{2}{A_1\left(\Psi\right)Y^2K_{\mathrm{I}eqc}^{N(\Psi)-2}\left[N\left(\Psi\right)-2\right]} \tag{64}$$

Equation (64) is actually identical to equation (15), the value of $B(\Psi)$ for the power law. The convenient form of equation (63) considerably simplifies the task of estimating the model parameters from cyclic fatigue specimen rupture data (see app. E from Rahman et al., 1998). Because equation (63) uses a single fatigue exponent N, the equation's form makes cyclic loading appear to assist power-law crack growth. In other words, the equation appears to model the underlying mechanism of crack growth as a time-dependent (not cycle-dependent) process, and the effect of cyclic loading is only to enhance time-dependent crack growth. Also, note that there is nothing in equation (63) that prevents making the parameters A_1, A_2, N, B, and Q functionally dependent on the frequency.

For the Walker law by itself (independent of the power law), equations (63) and (64) become

$$\sigma_{\mathrm{I}eqc}\left(\Psi,n_{\mathrm{int}}\right)=\left[\frac{\sigma_{\mathrm{I}eq,\max}^{N(\Psi)}\left(\Psi\right)\left[1-R\left(\Psi\right)\right]^{Q(\Psi)}\left(n_{\mathrm{fin}}-n_{\mathrm{int}}\right)}{B\left(\Psi\right)}+\sigma_{\mathrm{I}eqc}^{N(\Psi)-2}\left(\Psi,n_{\mathrm{fin}}\right)\right]^{\frac{1}{N(\Psi)-2}} \tag{65}$$

where

$$B\left(\Psi\right)=\frac{2}{A_2\left(\Psi\right)Y^2K_{\mathrm{I}eqc}^{N(\Psi)-2}\left[N\left(\Psi\right)-2\right]} \tag{66}$$

and where n_{int} is the initial number of cycles and n_{fin} is the final number of cycles. The terms $N(\Psi)$, $B(\Psi)$, and $Q(\Psi)$ are determined from cyclic fatigue experiments. (See app. E from Rahman et al. (1998) for an example.)

Equations (63) and (65) assume that material properties are constant over the time interval between t_{int} and t_{fin}. The process of extending these equations to account for changing material parameters over time and temperature is identical to that of equations (22) to (51) and, hence, is not repeated here. Instead, it is shown that equation (63) can be presented in the same general form as equations (22), (25), and (34). Therefore, since equation (63) has the same form as equations (22), (25), and (34), the procedure to generalize equation (63) for discrete time steps and changing material parameters must be the same as that previously described in sections 2.3 and 2.4.

Assume that the loading cycle is broken into k discrete time steps where the material parameters and loading are assumed to be constant over the duration of each time increment. For the j^{th} time step,

$$\sigma_{\mathrm{I}eqc}\left(t_{(j-1)}\right)=\left\{\frac{\sigma_{\mathrm{I}eq,j}^{N_{V,j}}\left[1+f_c\left(\frac{\sigma_{\mathrm{I}eq,\max}}{\sigma_{\mathrm{I}eq,j}}\right)^{N_{V,j}}\left(\frac{A_2}{A_1}\right)_{V,j}\left(1-R\right)^{Q_{V,j}}\right]\Delta t_j}{B_{V,j}}+\sigma_{\mathrm{I}eqc}^{N_{V,j}-2}\left(t_j\right)\right\}^{\frac{1}{N_{V,j}-2}} \tag{67}$$

where $1 \leq j \leq k$ and use of the location and orientation parameter Ψ is dropped. Notice in equation (67) that the bracketed term involving the R-ratio is not history dependent. That is, regardless of the value of $\sigma_{\mathrm{I}eq,\max}/\sigma_{\mathrm{I}eq,j}$, the contribution of the term in square brackets containing the R-ratio will be the same. Therefore, equation (67) is not a true thermomechanical fatigue criterion for ceramics.

Equation (67) can be generalized as

$$\sigma_{\mathrm{I}eqc}\left(t_{(j-1)}\right)=\left[\frac{\sigma_{\mathrm{I}eq,j}^{N_{V,j}}\left\{U_j\right\}\Delta t_j}{B_{V,j}}+\sigma_{\mathrm{I}eqc}^{N_{V,j}-2}\left(t_j\right)\right]^{\frac{1}{N_{V,j}-2}}=\left[\frac{\sigma_{\mathrm{I}eq,j}^{N_{V,j}}\,\Delta t_{eq,j}}{B_{V,j}}+\sigma_{\mathrm{I}eqc}^{N_{V,j}-2}\left(t_j\right)\right]^{\frac{1}{N_{V,j}-2}} \tag{68}$$

where

$$\Delta t_{eq,j}=U_j\Delta t_j=\left[1+f_c\left(\frac{\sigma_{\mathrm{I}eq,\max}}{\sigma_{\mathrm{I}eq,j}}\right)^{N_{V,j}}\left(\frac{A_2}{A_1}\right)_{V,j}\left(1-R\right)^{Q_{V,j}}\right]\Delta t_j \tag{69}$$

The term $\Delta t_{eq,j}$ is an equivalent time increment for time step j. Equation (68) is in a form that is identical to that of equation (14)—for a constant applied load—and to that of equations (22), (25) and (34). Because equation (63) can be generalized as a power law expression for SCG, the methodology developed for the power law in sections 2.3 and 2.4 also applies here. Consequently, showing the generalized transient reliability formulation development for equation (63) would be redundant. Instead, only the final formulation is shown; that formulation is analogous to equation (51) for k time steps that define a single cycle and for n total cycles (so that $n\,t_k = n\,t_{\mathrm{per}}$ is the total time).

$$
\begin{aligned}
X_1(\Psi) = \Bigg\{ \Bigg[\cdots \Bigg[\Bigg[& \left(\frac{\sigma_{\mathrm{I}eq,k,T\max}}{\sigma_{\mathrm{o}BV,k}} \right)^{N_{V,k}-2} + \frac{\sigma_{\mathrm{I}eq,k}^{N_{V,k}} \left[1 + \left(\frac{\sigma_{\mathrm{I}eq,\max}}{\sigma_{\mathrm{I}eq,k}} \right)^{N_{V,k}} f_c \left(\frac{A_2}{A_1} \right)_{V,k} (1-R)^{Q_{V,k}} \right] n\Delta t_k}{\sigma_{oBV,k}^{N_{V,k}-2} B_{BV,k}} \Bigg]_k^{\frac{m_{V,k}\left[N_{V,(k-1)}-2\right]}{m_{V,(k-1)}\left[N_{V,k}-2\right]}} \\
& + \frac{\sigma_{\mathrm{I}eq,(k-1)}^{N_{V,(k-1)}} \left[1 + \left(\frac{\sigma_{\mathrm{I}eq,\max}}{\sigma_{\mathrm{I}eq,(k-1)}} \right)^{N_{V,(k-1)}} f_c \left(\frac{A_2}{A_1} \right)_{V,(k-1)} (1-R)^{Q_{V,(k-1)}} \right] n\Delta t_{(k-1)}}{\sigma_{oBV,(k-1)}^{N_{V,(k-1)}-2} B_{BV,(k-1)}} \Bigg]_{(k-1)}^{\frac{m_{V,(k-1)}\left[N_{V,(k-2)}-2\right]}{m_{V,(k-2)}\left[N_{V,(k-1)}-2\right]}} \\
& + \cdots + \frac{\sigma_{\mathrm{I}eq,2}^{N_{V,2}} \left[1 + \left(\frac{\sigma_{\mathrm{I}eq,\max}}{\sigma_{\mathrm{I}eq,2}} \right)^{N_{V,2}} f_c \left(\frac{A_2}{A_1} \right)_{V,2} (1-R)^{Q_{V,2}} \right] n\Delta t_2}{\sigma_{oBV,2}^{N_{V,2}-2} B_{BV,2}} \Bigg]_2^{\frac{m_{V,2}\left[N_{V,1}-2\right]}{m_{V,1}\left[N_{V,2}-2\right]}} \\
& + \frac{\sigma_{\mathrm{I}eq,1}^{N_{V,1}} \left[1 + \left(\frac{\sigma_{\mathrm{I}eq,\max}}{\sigma_{\mathrm{I}eq,1}} \right)^{N_{V,1}} f_c \left(\frac{A_2}{A_1} \right)_{V,1} (1-R)^{Q_{V,1}} \right] n\Delta t_1}{\sigma_{oBV,1}^{N_{V,1}-2} B_{BV,1}} \Bigg\}_1
\end{aligned}
\tag{70}
$$

where the R-ratio is determined as

$$R = \frac{\min\left(\sigma_{\mathrm{I}eq,\,1}, \sigma_{\mathrm{I}eq,\,2}, \ldots, \sigma_{\mathrm{I}eq,\,k}\right)}{\max\left(\sigma_{\mathrm{I}eq,\,1}, \sigma_{\mathrm{I}eq,\,2}, \ldots, \sigma_{\mathrm{I}eq,\,k}\right)} \tag{71}$$

R-ratio is related to $\Delta K_{\mathrm{I}eq}$, shown in equation (54), which depends only on the applied stress, the crack size a, and the geometry factor Y. It does not depend on any material property such as $K_{\mathrm{I}c}$. Hence the R-ratio is only related to the applied stress and is independent of any other temperature- or environment-dependent parameter.

Equation (70) represents the most computationally efficient form for solving the reliability equation (49) for cyclic loading. The analogous formulation, similar to equations (48) to (50) for λ load blocks, is not shown because of the large size of the resultant equation; equation (70) should be sufficient to illustrate the methodology.

2.6 Generalized Transient Reliability Formulation for Proof Testing

In this section, the effect of proof testing is incorporated into the generalized transient reliability formulation for power law SCG. For the sake of brevity, the analogous formulation for the combined Walker-power law is not shown. We recommend that readers first review the proof-test methodology for static loading that is described in appendix D reproduced from Nemeth et al. (2003). This will help readers to understand how this methodology is applied to transient loading, where fluctuating temperatures may affect the material response (i.e., changing SCG and Weibull parameters) over time.

A proof test assesses whether or not a given ceramic component can survive in conditions similar to or worse than what would be expected in service. The proof test is performed prior to placing the part in service, and it increases the likelihood that the part will survive over its intended service life. Proof testing is performed on all parts, and those parts that survive the test without apparent damage are placed in service. In other words, the weakest components should fail in the proof test, leaving the stronger components to be used in the service application. The proof test should closely simulate the worst expected service loads, where the proof loads are designed to be appropriately greater in magnitude and applied in the same direction or directions as the service loads. In addition, the proof test should be of short duration to avoid or reduce damage to the part from SCG and handling. Components that survive proof testing should have a higher inservice reliability than components that are not proof tested. The components that survive the proof test should display a predictable minimum service life t_{min} where no failure should theoretically occur.

The "attenuated" probability of failure P_{faV}, assuming a volume-flaw failure mode, of a component surviving proof testing over time t_p and subjected to operational (service) loading over a time interval t_ε is

$$P_{faV}\left(t_q\right) = 1 - P_{saV}\left(t_q\right) = 1 - \frac{P_{sV}\left(t_q\right)}{P_{sV}\left(t_p\right)} = \frac{P_{sV}\left(t_p\right) - P_{sV}\left(t_q\right)}{P_{sV}\left(t_p\right)} \tag{72}$$

where $t_q = t_p + t_\varepsilon$. The term $P_{sV}(t_p)$ is the probability of survival of a component subjected to a proof test over a time interval denoted by t_p. The term $P_{sV}(t_q)$ is the probability of survival of a component subjected to a proof test over time interval t_p and service loading over the time interval t_ε. From equation (72), the inservice reliability of the survived components $P_{saV}(t_q)$ increases as the ratio of the proof-test stress to the service stress increases. This is because the proof-test reliability $P_{sV}(t_p)$ decreases as the proof-test load increases.

Because the Batdorf multiaxial methodology is used, the computation associated with equation (72) is not performed at the component level, but rather is performed at Ψ—a given location (x, y, z) and flaw orientation (α, β). This enables computing the reliability for the situation when the proof-test loading does not mimic the service loading. For example, the attenuated reliability can be computed for the case when the proof-test load and service load are misaligned or applied in different directions. Appendix D reproduced from Nemeth et al. (2003) gives further details of using the Batdorf theory with proof testing.

The transient proof-test methodology developed herein is based on taking the applied transient stresses and describing them as an equivalent static stress applied over an equivalent time. The magnitude of the equivalent static stress is set equal to the peak stress found over the history of the proof-test and service life. The weakest (lowest strength) flaw that could survive the proof test (at Ψ) is assumed to be of a strength just greater than the peak applied proof-test stress at $t = t_p$. As a result, this methodology does not consider the circumstance where the weakest flaw that could survive the proof test is lower in strength than the peak proof-test load at the end of the proof test (at $t = t_p$). This circumstance is considered herein as an unusual (and poorly designed) situation that can occur only if significant SCG occurs during the proof test and if the magnitude of the proof-test load systematically (and slowly) decays toward the end of the proof test. A well-designed proof test is of short duration, and unloading is performed quickly so that SCG and, thus, damage to the component are minimized. In that (typical) scenario, a component does not survive the proof test if its weakest flaw (at Ψ) has a strength (significantly) less than the peak applied stress. It is subsequently up to users to determine which of these situations best describes their proof test and if the methodology described herein is appropriate for their situations. Figure 4 is a schematic of the proof-test and service loading scenario that this methodology attempts to account for.

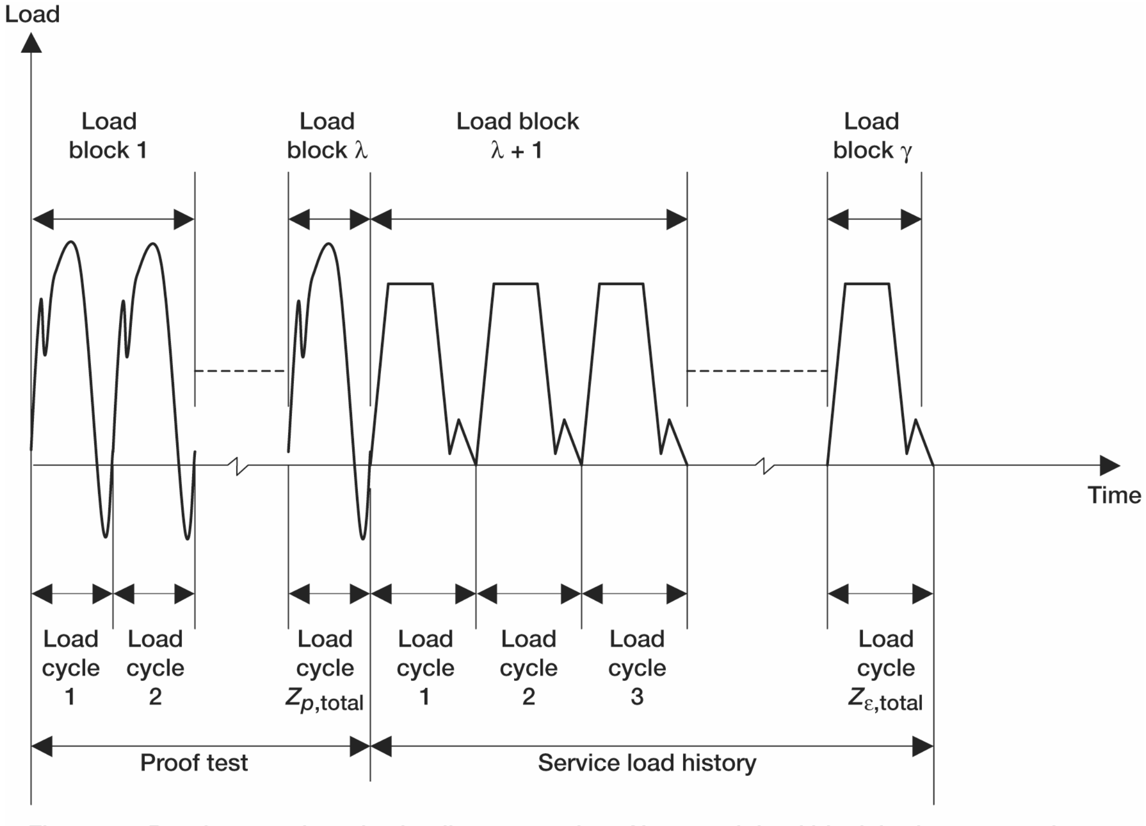

Figure 4.—Proof-test and service loading versus time. Note, each load block is shown spanning an arbitrary number of load cycles.

In this solution methodology, the proof-test and the service loading are described with a total of γ load blocks. Of this total, λ load blocks are for the proof test and $\gamma - (\lambda + 1)$ load blocks are for the service load. The term $Z_{p,\text{total}}$ represents the total number of proof-test load cycles, and $Z_{\varepsilon,\text{total}}$ represents the total number of service load cycles.

$$Z_{p,\text{total}} = \sum_{\iota=1}^{\lambda} Z_{p,\iota} \tag{73}$$

$$Z_{\varepsilon,\text{total}} = \sum_{\delta=\lambda+1}^{\gamma} Z_{\varepsilon,\delta} \tag{74}$$

The term $Z_{p,\iota}$ represents the number of cycles within proof-test load block ι, and $Z_{\varepsilon,\delta}$ represents the number of cycles within service load block δ. The equation for the survival probability for the proof test $P_{sV}(t_p)$ is straightforward and is identical to equations (48) to (50), except that it is shown here with different subscripts representing the proof-test conditions. The component survival probability $P_{sV}(t_p)$ at the end of proof testing is

$$P_{sV}\left(t_p\right) = \exp\left(- \sum_{isub=1}^{n_{\text{sub}}} \frac{V_{isub}}{4\pi} \left\{ \int_{\Omega} \left[X_{1p}\left(\Psi\right)\right]_1^{\frac{m_{V,1}}{N_{V,1}-2}} \, \mathrm{d}\Omega \right\}_{isub} \right) \tag{75}$$

where

$$
\begin{aligned}
X_{1p}(\Psi) = \Bigg\{ [[\ldots [[\ldots \Bigg\{ [\ldots [[\Bigg\{ \ldots \Bigg[\Bigg[\left(\frac{\sigma_{\mathrm{I}eq,\kappa,T\max}}{\sigma_{oBV,\kappa}} \right)^{N_{V,\kappa}-2} \\
+ \frac{\sigma_{\mathrm{I}eq,\kappa}^{N_{V,\kappa}} Z_{p,\lambda} \Delta t_{\kappa}}{\sigma_{oBV,\kappa}^{N_{V,\kappa}-2} B_{BV,\kappa}} \Bigg]_{\kappa}^{\frac{m_{V,\kappa}[N_{V,(\kappa-1)}-2]}{m_{V,(\kappa-1)}[N_{V,\kappa}-2]}}
+ \frac{\sigma_{\mathrm{I}eq,(\kappa-1)}^{N_{V,(\kappa-1)}} Z_{p,\lambda} \Delta t_{(\kappa-1)}}{\sigma_{oBV,(\kappa-1)}^{N_{V,(\kappa-1)}-2} B_{BV,(\kappa-1)}} \Bigg]_{\kappa-1}^{\frac{m_{V,(\kappa-1)}[N_{V,(\kappa-2)}-2]}{m_{V,(\kappa-2)}[N_{V,(\kappa-1)}-2]}}
+ \ldots + \frac{\sigma_{\mathrm{I}eq,1}^{N_{V,1}} Z_{p,\lambda} \Delta t_{1}}{\sigma_{oBV,1}^{N_{V,1}-2} B_{BV,1}} \Bigg]_{1}^{\frac{m_{V,1}[N_{V,\kappa}-2]}{m_{V,\kappa}[N_{V,1}-2]}} \Bigg\}_{\lambda} \\
+ \frac{\sigma_{\mathrm{I}eq,\kappa}^{N_{V,\kappa}} Z_{p,(\lambda-1)} \Delta t_{\kappa}}{\sigma_{oBV,\kappa}^{N_{V,\kappa}-2} B_{BV,\kappa}} \Bigg]_{\kappa}^{\frac{m_{V,\kappa}[N_{V,(\kappa-1)}-2]}{m_{V,(\kappa-1)}[N_{V,\kappa}-2]}}
+ \frac{\sigma_{\mathrm{I}eq,(\kappa-1)}^{N_{V,(\kappa-1)}} Z_{p,(\lambda-1)} \Delta t_{(\kappa-1)}}{\sigma_{oBV,(\kappa-1)}^{N_{V,(\kappa-1)}-2} B_{BV,(\kappa-1)}} \Bigg]_{\kappa-1}^{\frac{m_{V,(\kappa-1)}[N_{V,(\kappa-2)}-2]}{m_{V,(\kappa-2)}[N_{V,(\kappa-1)}-2]}}
+ \ldots + \frac{\sigma_{\mathrm{I}eq,1}^{N_{V,1}} Z_{p,(\lambda-1)} \Delta t_{1}}{\sigma_{oBV1}^{N_{V,1}-2} B_{BV1}} \Bigg]_{1}^{\frac{m_{V,1}[N_{V,\kappa}-2]}{m_{V,\kappa}[N_{V,1}-2]}} \Bigg\}_{\lambda-1} \\
+ \ldots + \frac{\sigma_{\mathrm{I}eq,\kappa}^{N_{V,\kappa}} Z_{p,1} \Delta t_{\kappa}}{\sigma_{oBV,\kappa}^{N_{V,\kappa}-2} B_{BV,\kappa}} \Bigg]_{\kappa}^{\frac{m_{V,1}[N_{V,\kappa}-2]}{m_{V,\kappa}[N_{V,1}-2]}}
+ \frac{\sigma_{\mathrm{I}eq,(\kappa-1)}^{N_{V,(\kappa-1)}} Z_{p,1} \Delta t_{(\kappa-1)}}{\sigma_{oBV,(\kappa-1)}^{N_{V,(\kappa-1)}-2} B_{BV,(\kappa-1)}} \Bigg]_{\kappa-1}^{\frac{m_{V,(\kappa-1)}[N_{V,(\kappa-2)}-2]}{m_{V,(\kappa-2)}[N_{V,(\kappa-1)}-2]}}
+ \ldots + \frac{\sigma_{\mathrm{I}eq,2}^{N_{V,2}} Z_{p,1} \Delta t_{2}}{\sigma_{oBV,2}^{N_{V,2}-2} B_{BV,2}} \Bigg]_{2}^{\frac{m_{V,2}[N_{V,1}-2]}{m_{V,1}[N_{V,2}-2]}}
+ \frac{\sigma_{\mathrm{I}eq,1}^{N_{V,1}} Z_{p,1} \Delta t_{1}}{\sigma_{oBV,1}^{N_{V,1}-2} B_{BV,1}} \Bigg]_{1} \Bigg\}_{1}
\end{aligned}
\qquad (76)
$$

or in its most computationally efficient form (analogous to eq. (51)),

$$
\begin{aligned}
X_{1p}(\Psi) = \Bigg\{ \Bigg[\Bigg[\cdots \Bigg[\Bigg[\left(\frac{\sigma_{\mathrm{I}eq,\kappa,T\max}}{\sigma_{oBV,\kappa}} \right)^{N_{V,\kappa}-2} \\
+ \frac{\sigma_{\mathrm{I}eq,\kappa}^{N_{V,\kappa}} Z_{p,\mathrm{total}} \Delta t_{\kappa}}{\sigma_{oBV,\kappa}^{N_{V,\kappa}-2} B_{BV,\kappa}} \Bigg]_{\kappa}^{\frac{m_{V,\kappa}\left[N_{V,(\kappa-1)}-2\right]}{m_{V,(\kappa-1)}\left[N_{V,\kappa}-2\right]}}
+ \frac{\sigma_{\mathrm{I}eq,(\kappa-1)}^{N_{V,(\kappa-1)}} Z_{p,\mathrm{total}} \Delta t_{(\kappa-1)}}{\sigma_{oBV,(\kappa-1)}^{N_{V,(\kappa-1)}-2} B_{BV,(\kappa-1)}} \Bigg]_{\kappa-1}^{\frac{m_{V,(\kappa-1)}\left[N_{V,(\kappa-2)}-2\right]}{m_{V,(\kappa-2)}\left[N_{V,(\kappa-1)}-2\right]}}
+ \ldots + \frac{\sigma_{\mathrm{I}eq,2}^{N_{V,2}} Z_{p,\mathrm{total}} \Delta t_{2}}{\sigma_{oBV,2}^{N_{V,2}-2} B_{BV,2}} \Bigg]_{2}^{\frac{m_{V,2}\left[N_{V,1}-2\right]}{m_{V,1}\left[N_{V,2}-2\right]}}
+ \frac{\sigma_{\mathrm{I}eq,1}^{N_{V,1}} Z_{p,\mathrm{total}} \Delta t_{1}}{\sigma_{oBV,1}^{N_{V,1}-2} B_{BV,1}} \Bigg]_{1} \Bigg\}_{1}
\end{aligned}
\tag{77}
$$

The proof-test time steps are from 1 to κ for the first cycle of loading and a total of $\kappa Z_{p,\mathrm{total}}$ time steps for the entire proof-test duration. The service loading time steps for the first cycle of service loading are counted from κ + 1 to ζ. Therefore, a total of $(\zeta - \kappa) Z_{\varepsilon,\,\mathrm{total}}$ time steps are involved with the service loading. The overall component survival probability $P_{sV}(t_q)$ for the combination of the proof-test and the service loading is

$$
P_{sV}\left(t_q\right) = \exp\left(- \sum_{isub=1}^{n_{\mathrm{sub}}} \frac{V_{isub}}{4\pi} \left\{ \int_{\Omega} \left[X_{1q}(\Psi) \right]_{1}^{\frac{m_{V,1}}{N_{V,1}-2}} \mathrm{d}\Omega \right\}_{isub} \right)
\tag{78}
$$

where

$$
\begin{aligned}
X_{1q}(\Psi) = \Bigg\{ \Bigg[\Bigg[\ldots \Bigg[\Bigg[\ldots \Bigg\{ \Bigg[\ldots \Bigg[\Bigg[\Bigg\{ \Bigg[\ldots \Bigg[\Bigg[\Bigg\{ \Bigg[\ldots \Bigg[\Bigg[\ldots \Bigg\{ \Bigg[\ldots \Bigg[\Bigg[\Bigg\{ \Bigg[\ldots \Bigg[\Bigg[\left(\frac{\sigma_{\mathrm{I}eq,\zeta,T\max}}{\sigma_{oBV,\zeta}} \right)^{N_{V,\zeta}-2} \\
+ \frac{\sigma_{\mathrm{I}eq,\zeta}^{N_{V,\zeta}} Z_{\varepsilon,\gamma} \Delta t_{\zeta}}{\sigma_{oBV,\zeta}^{N_{V,\zeta}-2} B_{BV,\zeta}} \Bigg]_{\zeta}^{\frac{m_{V,\zeta}\left[N_{V,(\zeta-1)}-2\right]}{m_{V,(\zeta-1)}\left[N_{V,\zeta}-2\right]}}
+ \frac{\sigma_{\mathrm{I}eq,(\zeta-1)}^{N_{V,(\zeta-1)}} Z_{\varepsilon,\gamma} \Delta t_{(\zeta-1)}}{\sigma_{oBV,(\zeta-1)}^{N_{V,(\zeta-1)}-2} B_{BV,(\zeta-1)}} \Bigg]_{\zeta-1}^{\frac{m_{V,(\zeta-1)}\left[N_{V,(\zeta-2)}-2\right]}{m_{V,(\zeta-2)}\left[N_{V,(\zeta-1)}-2\right]}}
+ \ldots + \frac{\sigma_{\mathrm{I}eq,(\kappa+1)}^{N_{V,(\kappa+1)}} Z_{\varepsilon,\gamma} \Delta t_{(\kappa+1)}}{\sigma_{oBV,(\kappa+1)}^{N_{V,(\kappa+1)}-2} B_{BV,1}} \Bigg]_{\kappa+1}^{\frac{m_{V,(\kappa+1)}\left[N_{V,\zeta}-2\right]}{m_{V,\zeta}\left[N_{V,(\kappa+1)}-2\right]}} \Bigg\}_{\gamma}
\end{aligned}
$$

(continued on next page)

$$
\begin{aligned}
&+\left.\frac{\sigma_{Ieq,\zeta}^{N_{V,\zeta}}\,Z_{\varepsilon,(\gamma-1)}\Delta t_{\zeta}}{\sigma_{oBV,\zeta}^{N_{V,\zeta}-2}\,B_{BV,\zeta}}\right]_{\zeta}^{\frac{m_{V,\zeta}\left[N_{V,(\zeta-1)}-2\right]}{m_{V,(\zeta-1)}\left[N_{V,\zeta}-2\right]}}+\left.\frac{\sigma_{Ieq,(\zeta-1)}^{N_{V,(\zeta-1)}}\,Z_{\varepsilon,(\gamma-1)}\Delta t(\zeta-1)}{\sigma_{oBV,(\zeta-1)}^{N_{V,(\zeta-1)}-2}\,B_{BV,(\zeta-1)}}\right]_{\zeta-1}^{\frac{m_{V,(\zeta-1)}\left[N_{V,(\zeta-2)}-2\right]}{m_{V,(\zeta-2)}\left[N_{V,(\zeta-1)}-2\right]}}+\ldots+\left.\frac{\sigma_{Ieq,(\kappa+1)}^{N_{V,(\kappa+1)}}\,Z_{\varepsilon,(\gamma-1)}\Delta t(\kappa+1)}{\sigma_{oBV,(\kappa+1)}^{N_{V,(\kappa+1)}-2}\,B_{BV,(\kappa+1)}}\right]_{\kappa+1}^{\frac{m_{V,(\kappa+1)}\left[N_{V,\zeta}-2\right]}{m_{V,\zeta}\left[N_{V,(\kappa+1)}-2\right]}}\Bigg\}_{\gamma-1}\\
&+\ldots+\left.\frac{\sigma_{Ieq,\zeta}^{N_{V,\zeta}}\,Z_{\varepsilon,(\lambda+1)}\Delta t_{\zeta}}{\sigma_{oBV,\zeta}^{N_{V,\zeta}-2}\,B_{BV,\zeta}}\right]_{\zeta}^{\frac{m_{V,\zeta}\left[N_{V,(\zeta-1)}-2\right]}{m_{V,(\zeta-1)}\left[N_{V,\zeta}-2\right]}}+\left.\frac{\sigma_{Ieq,(\zeta-1)}^{N_{V,(\zeta-1)}}\,Z_{\varepsilon,(\lambda+1)}\Delta t(\zeta-1)}{\sigma_{oBV,(\zeta-1)}^{N_{V,(\zeta-1)}-2}\,B_{BV,(\zeta-1)}}\right]_{\zeta-1}^{\frac{m_{V,(\zeta-1)}\left[N_{V,(\zeta-2)}-2\right]}{m_{V,(\zeta-2)}\left[N_{V,(\zeta-1)}-2\right]}}+\ldots+\left.\frac{\sigma_{Ieq,(\kappa+1)}^{N_{V,(\kappa+1)}}\,Z_{\varepsilon,(\lambda+1)}\Delta t(\kappa+1)}{\sigma_{oBV,(\kappa+1)}^{N_{V,(\kappa+1)}-2}\,B_{BV,(\kappa+1)}}\right]_{\kappa+1}^{\frac{m_{V,(\kappa+1)}\left[N_{V,\kappa}-2\right]}{m_{V,\kappa}\left[N_{V,(\kappa+1)}-2\right]}}\Bigg\}_{\lambda+1} \qquad (79)\\
&+\left.\frac{\sigma_{Ieq,\kappa}^{N_{V,\kappa}}\,Z_{p,\lambda}\Delta t_{\kappa}}{\sigma_{oBV,\kappa}^{N_{V,\kappa}-2}\,B_{BV,\kappa}}\right]_{\kappa}^{\frac{m_{V,\kappa}\left[N_{V,(\kappa-1)}-2\right]}{m_{V,(\kappa-1)}\left[N_{V,\kappa}-2\right]}}+\left.\frac{\sigma_{Ieq,(\kappa-1)}^{N_{V,(\kappa-1)}}\,Z_{p,\lambda}\Delta t(\kappa-1)}{\sigma_{oBV,(\kappa-1)}^{N_{V,(\kappa-1)}-2}\,B_{BV,(\kappa-1)}}\right]_{\kappa-1}^{\frac{m_{V,(\kappa-1)}\left[N_{V,(\kappa-2)}-2\right]}{m_{V,(\kappa-2)}\left[N_{V,(\kappa-1)}-2\right]}}+\ldots+\left.\frac{\sigma_{Ieq,1}^{N_{V,1}}\,Z_{p,\lambda}\Delta t_{1}}{\sigma_{oBV,1}^{N_{V,1}-2}\,B_{BV,1}}\right]_{1}^{\frac{m_{V,1}\left[N_{V,\kappa}-2\right]}{m_{V,\kappa}\left[N_{V,1}-2\right]}}\Bigg\}_{\lambda}\\
&+\left.\frac{\sigma_{Ieq,\kappa}^{N_{V,\kappa}}\,Z_{p,(\lambda-1)}\Delta t_{\kappa}}{\sigma_{oBV,\kappa}^{N_{V,\kappa}-2}\,B_{BV,\kappa}}\right]_{\kappa}^{\frac{m_{V,\kappa}\left[N_{V,(\kappa-1)}-2\right]}{m_{V,(\kappa-1)}\left[N_{V,\kappa}-2\right]}}+\left.\frac{\sigma_{Ieq,(\kappa-1)}^{N_{V,(\kappa-1)}}\,Z_{p,(\lambda-1)}\Delta t(\kappa-1)}{\sigma_{oBV,(\kappa-1)}^{N_{V,(\kappa-1)}-2}\,B_{BV,(\kappa-1)}}\right]_{\kappa-1}^{\frac{m_{V,(\kappa-1)}\left[N_{V,(\kappa-2)}-2\right]}{m_{V,(\kappa-2)}\left[N_{V,(\kappa-1)}-2\right]}}+\ldots+\left.\frac{\sigma_{Ieq,1}^{N_{V,1}}\,Z_{p,(\lambda-1)}\Delta t_{1}}{\sigma_{oBV,1}^{N_{V,1}-2}\,B_{BV,1}}\right]_{1}^{\frac{m_{V,1}\left[N_{V,\kappa}-2\right]}{m_{V,\kappa}\left[N_{V,1}-2\right]}}\Bigg\}_{\lambda-1}\\
&+\ldots+\left.\frac{\sigma_{Ieq,\kappa}^{N_{V,\kappa}}\,Z_{p,1}\Delta t_{\kappa}}{\sigma_{oBV,\kappa}^{N_{V,\kappa}-2}\,B_{BV,\kappa}}\right]_{\kappa}^{\frac{m_{V,\kappa}\left[N_{V,(\kappa-1)}-2\right]}{m_{V,(\kappa-1)}\left[N_{V,\kappa}-2\right]}}+\left.\frac{\sigma_{Ieq,(\kappa-1)}^{N_{V,(\kappa-1)}}\,Z_{p,1}\Delta t(\kappa-1)}{\sigma_{oBV,(\kappa-1)}^{N_{V,(\kappa-1)}-2}\,B_{BV,(\kappa-1)}}\right]_{\kappa-1}^{\frac{m_{V,(\kappa-1)}\left[N_{V,(\kappa-2)}-2\right]}{m_{V,(\kappa-2)}\left[N_{V,(\kappa-1)}-2\right]}}+\ldots+\left.\frac{\sigma_{Ieq,2}^{N_{V,2}}\,Z_{p,1}\Delta t_{2}}{\sigma_{oBV,2}^{N_{V,2}-2}\,B_{BV,2}}\right]_{2}^{\frac{m_{V,2}\left[N_{V,1}-2\right]}{m_{V,1}\left[N_{V,2}-2\right]}}+\left.\frac{\sigma_{Ieq,1}^{N_{V,1}}\,Z_{p,1}\Delta t_{1}}{\sigma_{oBV,1}^{N_{V,1}-2}\,B_{BV,1}}\right]_{1}\Bigg\}_{1}
\end{aligned}
$$

or in its most computationally efficient form,

$$
\begin{aligned}
X_{1q}(\Psi) = \Bigg\{ \Bigg[[\ldots[[\Bigg[\ldots \Bigg[\Bigg[\left(\frac{\sigma_{\mathrm{I}eq,\zeta,T\,\max}}{\sigma_{oBV,\zeta}} \right)^{N_{V,\zeta}-2} & + \frac{\sigma_{\mathrm{I}eq,\zeta}^{N_{V,\zeta}} Z_{\varepsilon,\mathrm{total}} \Delta t_{\zeta}}{\sigma_{oBV,\zeta}^{N_{V,\zeta}-2} B_{BV,\zeta}} \Bigg]_{\zeta}^{\frac{m_{V,\zeta}\left[N_{V,(\zeta-1)}-2\right]}{m_{V,(\zeta-1)}\left[N_{V,\zeta}-2\right]}} + \frac{\sigma_{\mathrm{I}eq,(\zeta-1)}^{N_{V,(\zeta-1)}} Z_{\varepsilon,\mathrm{total}} \Delta t_{(\zeta-1)}}{\sigma_{oBV(\zeta-1)}^{N_{V(\zeta-1)}-2} B_{BV(\zeta-1)}} \Bigg]_{\zeta-1}^{\frac{m_{V,(\zeta-1)}\left[N_{V,(\zeta-2)}-2\right]}{m_{V,(\zeta-2)}\left[N_{V,(\zeta-1)}-2\right]}} \\
& + \ldots + \frac{\sigma_{\mathrm{I}eq,(\kappa+1)}^{N_{V,(\kappa+1)}} Z_{\varepsilon,\mathrm{total}} \Delta t_{(\kappa+1)}}{\sigma_{oBV,(\kappa+1)}^{N_{V,(\kappa+1)}-2} B_{BV,1}} \Bigg]_{\kappa+1}^{\frac{m_{V,(\kappa+1)}\left[N_{V,\kappa}-2\right]}{m_{V,\kappa}\left[N_{V,(\kappa+1)}-2\right]}} \Bigg]_{\kappa+1} + \frac{\sigma_{\mathrm{I}eq,\kappa}^{N_{V,\kappa}} Z_{p,\mathrm{total}} \Delta t_{\kappa}}{\sigma_{oBV,\kappa}^{N_{V,\kappa}-2} B_{BV,\kappa}} \Bigg]_{\kappa}^{\frac{m_{V,\kappa}\left[N_{V,(\kappa-1)}-2\right]}{m_{V,(\kappa-1)}\left[N_{V,\kappa}-2\right]}} \\
& + \frac{\sigma_{\mathrm{I}eq,(\kappa-1)}^{N_{V,(\kappa-1)}} Z_{p,\mathrm{total}} \Delta t_{(\kappa-1)}}{\sigma_{oBV,(\kappa-1)}^{N_{V,(\kappa-1)}-2} B_{BV,(\kappa-1)}} \Bigg]_{\kappa-1}^{\frac{m_{V,(\kappa-1)}\left[N_{V,(\kappa-2)}-2\right]}{m_{V,(\kappa-2)}\left[N_{V,(\kappa-1)}-2\right]}} + \ldots + \frac{\sigma_{\mathrm{I}eq,2}^{N_{V,2}} Z_{p,\mathrm{total}} \Delta t_{2}}{\sigma_{oBV,2}^{N_{V,2}-2} B_{BV,2}} \Bigg]_{2}^{\frac{m_{V,2}\left[N_{V,1}-2\right]}{m_{V,1}\left[N_{V,2}-2\right]}} + \frac{\sigma_{\mathrm{I}eq,1}^{N_{V,1}} Z_{p,\mathrm{total}} \Delta t_{1}}{\sigma_{oBV,1}^{N_{V,1}-2} B_{BV,1}} \Bigg]_{1} \Bigg\}_{1}
\end{aligned}
\tag{80}
$$

The proof-test time steps are from 1 to κ, and the service time steps are from κ + 1 to ζ. Substituting equations (75) and (78) into equation (72) yields the expression for the attenuated survival probability:

$$P_{saV}\left(t_q\right) = \exp\left[\sum_{isub=1}^{n_{\text{sub}}} \frac{V_{isub}}{4\pi}\left(\int_{\Omega}\left\{\left[X_{1q}(\Psi)\right]^{\frac{m_{V,1}}{N_{V,1}-2}} - \left[X_{1p}(\Psi)\right]^{\frac{m_{V,1}}{N_{V,1}-2}}\right\} H(\Psi)\,\mathrm{d}\Omega\right)_{isub}\right] \tag{81}$$

The Heaviside function $H(\Psi)$ in equation (81) was originally used in Nemeth et al. (2003) (see app. D) for static loads and constant Weibull and fatigue parameters. Its use here requires expressing variables in terms of equivalent peak static loads and equivalent times. Equivalent time is the comparable time interval for a static load situation that has the same amount of crack growth (or same reliability) as the actual transient load situation. The Heaviside function $H(\Psi)$ in equation (81) is used, where

$$H(\Psi) = 1 \quad \text{if} \quad \sigma_{\mathrm{I}eq,1,T\max,\varepsilon}(\Psi) \geq \sigma_{\mathrm{I}eq,1,T\max,p}(\Psi)$$

otherwise, if

$$\sigma_{\mathrm{I}eq,1,T\max,\varepsilon}(\Psi) < \sigma_{\mathrm{I}eq,1,T\max,p}(\Psi) \tag{82}$$

then

$$H(\Psi) = 1 \quad \text{if} \quad t_{\min,1,es}(\Psi) < t_{q,1,es}(\Psi) - t_{p,1,es}(\Psi)$$

and

$$H(\Psi) = 0 \quad \text{if} \quad t_{\min,1,es}(\Psi) \geq t_{q,1,es}(\Psi) - t_{p,1,es}(\Psi)$$

Figure 5 is a schematic diagram showing the relationship between the terms in equation (82). The Heaviside function accounts for $t_{\min,1,es}(\Psi)$, the minimum effective service time interval during which reliability cannot decrease on the basis of the properties of time step 1. It is obtained by satisfying the condition $P_{sV}(t_q) = P_{sV}(t_p)$ locally at Ψ (see eq. (72)). For the whole component, $t_{\min,1,es}$ denotes the minimum value of $t_{\min,1,es}(\Psi)$ when evaluated for all Ψ. If at any location the component proof-test stress level is less than the service stress level, then an assured minimum effective lifetime $t_{\min,1,es}$ does not exist and the component cannot be assured to survive for any given time during service loading. Note that $t_{\min}$ as used here would denote the real service time equivalent of $t_{\min,1,es}$ for the transient loading condition. The meaning of and the subscript notation for $t_{\min,1,es}$ are explained in the following paragraphs.

The subscript 1 in equation (82) indicates that values are transformed to equivalent values based on the properties of time step 1. Time step 1 is arbitrarily chosen; however, both equations (75) and (78) are expressed in terms of this property set. In equation (82), $\sigma_{\mathrm{I}eq,1,T\max,p}$ denotes the value of $\sigma_{\mathrm{I}eq,\kappa,T\max}$ converted to the properties of time step 1. The term $\sigma_{\mathrm{I}eq,1,T\max,p}$ can be computed from $\sigma_{\mathrm{I}eq,\kappa,T\max}$ by equating fast-fracture reliabilities for individual time steps (see eq. (28) and the described maximization procedure).

$$\left(\frac{\sigma_{\mathrm{I}eq,1,T\max,p}}{\sigma_{oBV,1}}\right)^{m_{V,1}} = \left(\frac{\sigma_{\mathrm{I}eq,\kappa,T\max}}{\sigma_{oBV,\kappa}}\right)^{m_{V,\kappa}} \tag{83}$$

Recall that $\sigma_{\mathrm{I}eq,\kappa,T\max}$ is the maximized fast-fracture stress for the first $\kappa Z_{p,\text{total}}$ time steps (the proof-test time steps) expressed in terms of the properties of time step κ. The maximization procedure is identical to that described

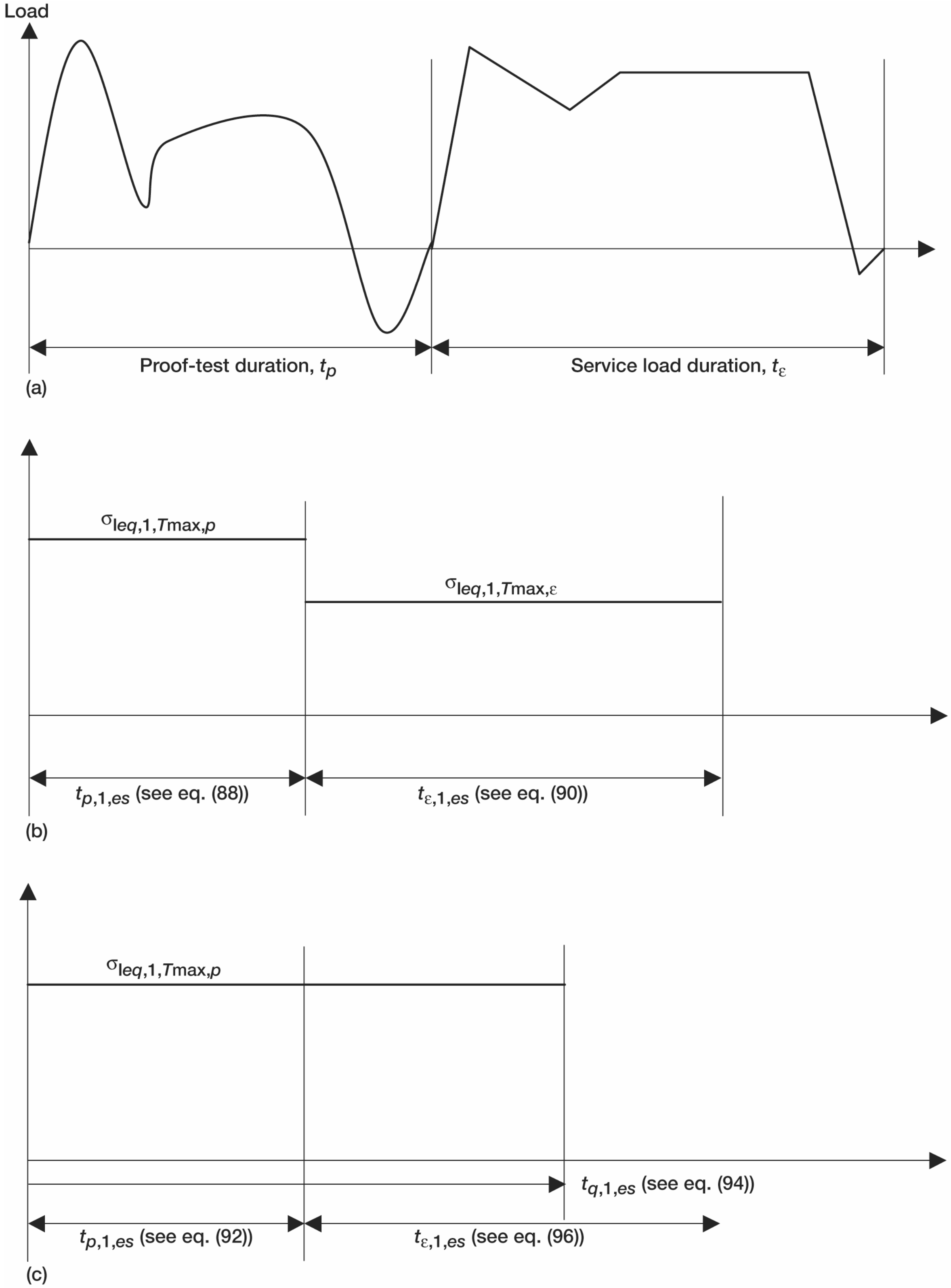

Figure 5.—Applied and transformed stress histories at a given location Ψ in the component. These stress histories are equivalent in the sense that they all yield the same reliability. (a) Applied load history. (b) Transformed load history associated with equation (91). (c) Transformed load history associated with equation (95).

previously (see eq. (43)) except that the maximization is performed only over the proof-test time steps 1 to κ. The term $\sigma_{\mathrm{I}eq,1,T\mathrm{max},p}$ can be computed by

$$\sigma_{\mathrm{I}eq,1,T\max,p} = \max\left(\sigma_{\mathrm{I}eq,1,1}, \sigma_{\mathrm{I}eq,2,1}, \ldots, \sigma_{\mathrm{I}eq,i,1}, \ldots, \sigma_{\mathrm{I}eq,\kappa,1}\right) \tag{84}$$

where

$$\sigma_{\mathrm{I}eq,i,1} = \sigma_{oBV,1}\left(\frac{\sigma_{\mathrm{I}eq,i}}{\sigma_{oBV,i}}\right)^{\frac{m_{V,i}}{m_{V,1}}} \tag{85}$$

and $\sigma_{\mathrm{I}eq,i,1}$ is the transformed stress during time step i, using the properties of time step 1. Similarly for the service loading time steps,

$$\sigma_{\mathrm{I}eq,1,T\max,\varepsilon} = \max\left[\sigma_{\mathrm{I}eq,(\kappa+1),1}, \sigma_{\mathrm{I}eq,(\kappa+2),1}, \ldots, \sigma_{\mathrm{I}eq,(\kappa+i),1}, \ldots, \sigma_{\mathrm{I}eq,\zeta,1}\right] \tag{86}$$

The methodology to solve for $t_{\mathrm{min},1,es}(\Psi)$ for the special case where Weibull and fatigue parameters do not vary over the time steps (but loading is allowed to vary) will be examined first. For this situation, a closed-form expression for $t_{\mathrm{min},1,es}(\Psi)$ can be obtained by using the concept of g-factors as explained in Mencik (1984). Basically, g-factors are terms with constant values that are used to express cyclic loading as an equivalent static load applied over an effective time (see eq. (57)). For proof-test reliability, this can be expressed as

$$P_{sV}(t_p) = \exp\left(-\sum_{isub=1}^{n_{\mathrm{sub}}} \frac{V_{isub}}{4\pi}\left\{\iint_{\Omega}\left[\left(\frac{\sigma_{\mathrm{I}eq,1,T_{\max},p}}{\sigma_{oBV,1}}\right)^{N_{V,1}-2} + \frac{\sigma_{\mathrm{I}eq,1,T_{\max},p}^{N_{V,1}}\, t_{p,1,es}}{\sigma_{oBV,1}^{N_{V,1}-2}\, B_{BV,1}}\right]^{\frac{m_{V,1}}{N_{V,1}-2}} \mathrm{d}\Omega\right\}_{isub}\right) \tag{87}$$

where (compare with eq. (57))

$$t_{p,1,es} = t_p g_{p,1} = \frac{t_p}{t_\kappa}\sum_{i=1}^{\kappa}\left(\frac{\sigma_{\mathrm{I}eq,i}}{\sigma_{\mathrm{I}eq,1,T\max,p}}\right)^{N_{V,1}} \Delta t_i \tag{88}$$

with $t_{p,1,es}(\Psi)$ as the effective time and $g_{p,1}$ as the g-factor for the proof test (both denoted in terms of property 1—which is the same over all the time steps). Similarly, for the combination of the proof-test and the service loading,

$$P_{sV}\left(t_q\right) = \exp\left(- \sum_{isub=1}^{n_{\text{sub}}} \frac{V_{isub}}{4\pi} \left\{ \iint_{\Omega} \left[\left(\frac{\sigma_{\mathrm{I}eq,1,T\max,\varepsilon}}{\sigma_{oBV,1}} \right)^{N_{V,1}-2} + \frac{\sigma_{\mathrm{I}eq,1,T\max,p}^{N_{V,1}}\; t_{p,1,es} + \sigma_{\mathrm{I}eq,1,T\max,\varepsilon}^{N_{V,1}}\; t_{e,1,es}}{\sigma_{oBV,1}^{N_{V,1}-2}\; B_{BV,1}} \right]^{\frac{m_{V,1}}{N_{V,1}-2}} \mathrm{d}\Omega \right\}_{isub} \right) \tag{89}$$

where

$$t_{\varepsilon,1,es} = t_\varepsilon g_{\varepsilon,1} = \frac{t_\varepsilon}{t_\zeta - t_\kappa} \sum_{i=\kappa+1}^{\zeta} \left(\frac{\sigma_{\mathrm{I}eq,i}}{\sigma_{\mathrm{I}eq,1,T\max,\varepsilon}} \right)^{N_{V,1}} \Delta t_i \tag{90}$$

It is important to point out that the term for final strength in equation (89) is $\sigma_{\mathrm{I}eq,1,T\max,\varepsilon}$, not $\sigma_{\mathrm{I}eq,1,T\max,q}$. This condition is necessary because the final strength takes place during service history, hence it must be set equal to $\sigma_{\mathrm{I}eq,1,T\max,\varepsilon}$ when $\sigma_{\mathrm{I}eq,1,T\max,p} > \sigma_{\mathrm{I}eq,1,T\max,\varepsilon}$. Recall that $\sigma_{\mathrm{I}eq,1,T\max,p} > \sigma_{\mathrm{I}eq,1,T\max,\varepsilon}$ is a stipulation of equation (82) in order for $t_{\min,1,es}(\Psi)$ to exist. Equating equations (87) and (89) and solving for $t_{\varepsilon,1,es}$ (which is now designated as $t_{\min,1,es}$) gives

$$t_{\min,1,es}\left(\Psi\right) = t_{\min} g_{\varepsilon,1} = \frac{B_{BV,1}}{\sigma_{\mathrm{I}eq,1,T\max,\varepsilon}^{2}\left(\Psi\right)} \left\{ \left[\frac{\sigma_{\mathrm{I}eq,1,T\max,p}\left(\Psi\right)}{\sigma_{\mathrm{I}eq,1,T\max,\varepsilon}\left(\Psi\right)} \right]^{N_{V,1}-2} - 1 \right\} \tag{91}$$

When Weibull and fatigue parameters do not vary over the time steps, then $g_{\varepsilon,1}$ and $g_{p,1}$ are constant values regardless of the values for t_ε and t_p. In that situation, equation (91) can be used irrespective of t_ε and t_p. In addition, rather than using equation (82) to evaluate the Heaviside function, only $t_{\min}$ from equation (91) needs to be compared with t_ε. If $t_\varepsilon \geq t_{\min}$, the Heaviside function has a value of 1, otherwise it is 0.

When the Weibull and fatigue parameters are not constant over the time steps, then $g_{p,1}$ and $g_{\varepsilon,1}$, as defined in equations (88) and (90), respectively, no longer apply. Their equivalent *g*-factor form is no longer constant with time, and an iterative procedure must be used to solve equation (91). For this more general case (where Weibull and fatigue parameters are not constant), the effective time for the proof test can be reexpressed by equating equations (75) and (87), resulting in

$$t_{p,1,es} = \frac{\sigma_{oBV1}^{N_{V,1}-2}\; B_{BV,1}}{\sigma_{\mathrm{I}eq,1,T\max,p}^{N_{V,1}}} \left[X_{1p}(\Psi) - \left(\frac{\sigma_{\mathrm{I}eq,1,T\max,p}}{\sigma_{oBV,1}} \right)^{N_{V,1}-2} \right] \tag{92}$$

and reexpressing equation (78) as

$$P_{sV}\left(t_q\right) = \exp\left(- \sum_{isub=1}^{n_{\mathrm{sub}}} \frac{V_{isub}}{4\pi} \left\{ \iint_{\Omega} \left[\left(\frac{\sigma_{\mathrm{I}eq,1,T\max,\varepsilon}}{\sigma_{oBV,1}} \right)^{N_{V,1}-2} + \frac{\sigma_{\mathrm{I}eq,1,T\max,p}^{N_{V,1}} \, t_{q,1,es}}{\sigma_{oBV,1}^{N_{V1}-2} \, B_{BV1}} \right]^{\frac{m_{V,1}}{N_{V,1}-2}} \mathrm{d}\Omega \right\}_{isub} \right) \tag{93}$$

so that

$$t_{q,1,es} = \frac{\sigma_{oBV,1}^{N_{V,1}-2} \, B_{BV,1}}{\sigma_{\mathrm{I}eq,1,T\max,p}^{N_{V,1}}} \left[X_{1q}\left(\Psi\right) - \left(\frac{\sigma_{\mathrm{I}eq,1,T\max,\varepsilon}}{\sigma_{oBV,1}} \right)^{N_{V,1}-2} \right] \tag{94}$$

Equating equations (87) and (93) then gives

$$t_{\min,1,es}\left(\Psi\right) = \frac{B_{V,1}}{\sigma_{\mathrm{I}eq,1,T\max,p}^{2}\left(\Psi\right)} \left\{ 1 - \left[\frac{\sigma_{\mathrm{I}eq,1,T\max,\varepsilon}\left(\Psi\right)}{\sigma_{\mathrm{I}eq,1,T\max,p}\left(\Psi\right)} \right]^{N_{V,1}-2} \right\} \tag{95}$$

where

$$t_{\min,1,es}\left(\Psi\right) = t_{q,1,es}\left(\Psi\right) - t_{p,1,es}\left(\Psi\right) \tag{96}$$

Although not obvious, equations (95) and (91) are actually identical when the Weibull and fatigue parameters do not vary between time steps. In this case, equation (95) is normalized by $\sigma_{\mathrm{I}eq,1,T\max,p}$, whereas equation (91) is normalized by $\sigma_{\mathrm{I}eq,1,T\max,\varepsilon}$. Making equations (95) and (96) both true requires iteratively finding the value of t_{ε} that satisfies the equality; however, this is computationally intensive. Fortunately, the attenuated failure probability evaluation can be performed for the component if the sign of the inequality in equation (82) is established locally at Ψ. This means that iteration is not necessary. Instead, equation (95) can be used to establish $t_{\min,1,es}(\Psi)$, which is used on the left side of the inequality in equation (82). The right side of the inequality in equation (82) is determined by computing $t_{q,1,es}(\Psi)$ from equation (94) and $t_{p,1,es}(\Psi)$ from equation (92).

For computational efficiency (and convenience) in the CARES/*Life* program, the term for X_{1q} in equation (94) is evaluated with $\sigma_{\mathrm{I}eq,1,T\max,p}$ instead of $\sigma_{\mathrm{I}eq,1,T\max,\varepsilon}$. This is conservative and avoids having to evaluate X_{1q} twice—once for equation (78) using $\sigma_{\mathrm{I}eq,1,T\max,p}$ and once for equation (94) using $\sigma_{\mathrm{I}eq,1,T\max,\varepsilon}$.

3.0 Examples

In this section, four example problems are provided to illustrate various aspects of the transient reliability methodology developed in this report:

(1) Silicon nitride disks undergoing thermal shock. This problem shows the fast-fracture transient analysis capability.

(2) Heavy-duty diesel engine exhaust valves tested in an experimental engine rig. This example is used to contrast predictions for cyclic loading over time using the power law, the combined Walker-power law, and proof testing.

(3) Failure response of alumina flexure bars in static fatigue at elevated temperature. This example looks at two possible modeling scenarios that can reproduce the failure response in an alumina material where the material properties and failure behavior are changing over time. The example problem examines the hypothetical effect of changing the Weibull and fatigue parameters over time on the failure probability of alumina four-point flexure bars in static fatigue.

(4) Hexoloy SiC tubes subjected to thermal shock. This example compares experimental to predicted failure probabilities. It also explores the effect of repeated thermal shock loading on the tube's reliability. Transient loading and material response were taken into account in this example.

3.1 Example 1: Thermal Shocked Disks Failing in Fast Fracture

In this example, the fast-fracture reliability response of laser-induced thermal shocked disks made of silicon nitride is examined. The purpose here is to see if the strength response of the thermally shocked disks can be predicted using the Weibull parameters obtained from rupture data of simple bend-bar beams. The transient fast-fracture reliability predictions of the disk versus the instantaneous fast-fracture reliability predictions are also compared. This example is derived from an international study (Ferber and Breder, 2001) involving laboratories from Germany, Japan, and the United States. Phase I of that study worked to develop and verify thermal upshock techniques in which disk specimens were centrally heated to fracture by an appropriate heating source, including a laser, a quartz lamp, a shaped heating element, and a gas torch. Phase II of the study was a round-robin activity that tested two silicon nitrides—AlliedSignal AS800 and Kyocera SN282—using the techniques developed in phase I. This example used disk results for the SN282 material from the Siemens AG organization, as provided by Rettig (Rettig, U.: Personal communication, Aug. 2002). These disks were tested using the laser irradiation technique described by Kirchhoff et al. (1994) and Rettig (1998). Three-point flexure bar data provided by Ferber (Ferber, M.: Personal communication, July 2002) were also used.

Thin disks 20 mm in diameter and 0.3 mm thick were centrally heated by an 800-W laser working in continuous-wave mode—the schematic of which is shown in figure 6. A large centrally heated area and a steep temperature gradient near the edge was created, which yielded high tensile stresses near the edge. The specimens were rapidly heated so that fracture would occur in less than a second. The temperature-versus-time response across the disk was measured with a fast scanning pyrometer. The heating time and the thinness of the disk were chosen such that through-the-thickness temperature gradients (and hence bending stresses) were negligible. Further details regarding the experimental setup are found in Ferber and Breder (2001), Kirchoff et al. (1994), and Rettig (1998).

A total of 15 disks were fractured. The time of rupture and the radius corresponding to the location of fracture were recorded for each specimen. Fracture stresses were computed by the study participants using the temperature profile at the instant of fracture, the temperature-dependent elastic modulus and thermal-expansion coefficient, and the integral equations from standard elasticity theory. Some of the disks were cut into three-point flexure specimens in order to independently quantify the strength characteristics. Fourteen of these flexure specimens were tested at room temperature. They had the following average dimensions: a thickness of 0.30 mm, a width of 3.25 mm, a length of 15.00 mm, and a support span of 9.44 mm. The specimen edges were not beveled.

An ANSYS finite element model of the disk was prepared as shown in figure 7 for the CARES/*Life* reliability analysis. The model comprised a 90° slice of the disk and spanned one-half the thickness (one-eighth of the disk was modeled). Solid elements were used in the model. The disk was not constrained (other than to prevent rigid-body motion), and thus was allowed to expand freely. Temperature-dependent thermal expansion and elastic modulus values from Ferber and Breder (2001) were used. The thermal loading profiles versus time for two specimens (specimens 3 and 9), as supplied by Rettig (Rettig, U.: Personal communication, Aug. 2002), were used for the thermal loading, and the temperatures were assumed to be constant through the thickness. Specimen 3 had the highest time to failure (0.65 s) and, hence, the highest reported fracture strength (430 MPa) from Ferber and Breder (2001). Specimen 9 had an intermediate fracture strength (340 MPa) from Ferber and Breder (2001). For specimen 3, figures 8 and 9 show the transient thermal profile and the transient stress analysis results from the FEA, respectively. Figure 9 shows the tangential (circumferential) stresses versus the distance from the disk center. The tangential stresses are compressive near the disk center and become tensile towards the disk edge. The radial

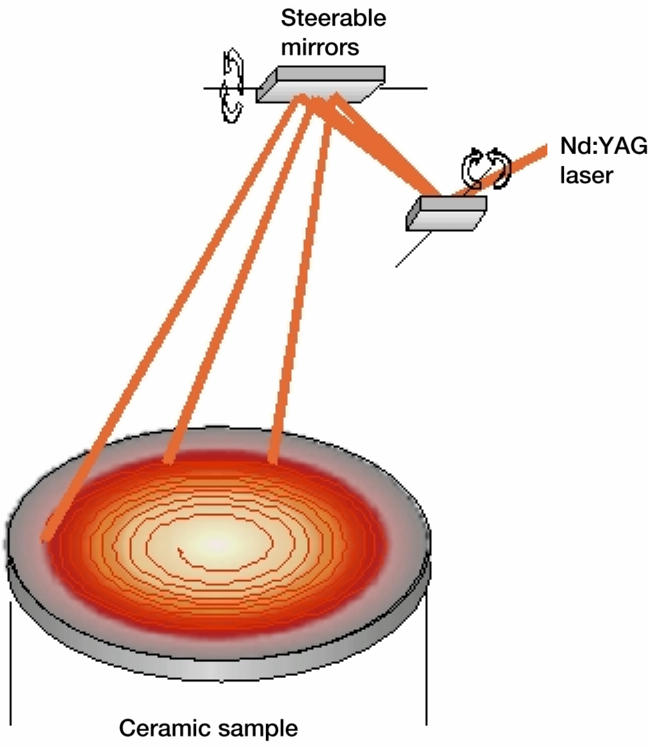

Figure 6.—Laser upshock technique of Kirchoff et al. (1994). (Copyright Uwe Rettig; used with permission.)

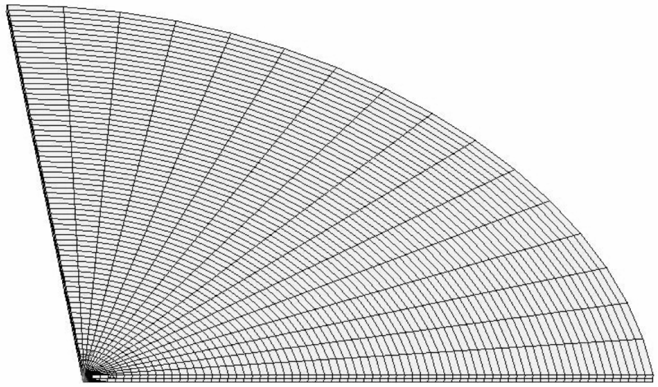

Figure 7.—Finite element mesh of the silicon nitride disk. Disk is freely supported and allowed to expand and contract without constraint.

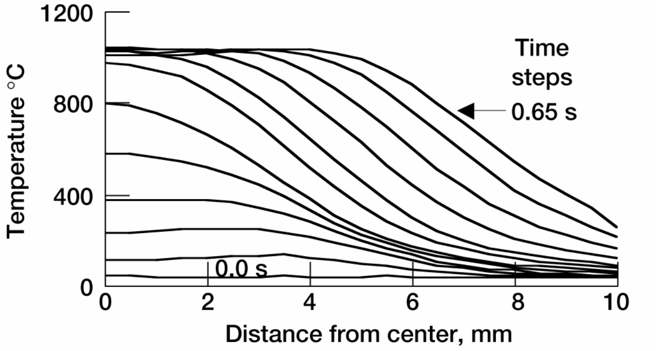

Figure 8.—Transient thermal profile for disk specimen 3. Time steps range from 0.0 to 0.65 s. Not all time steps are shown.

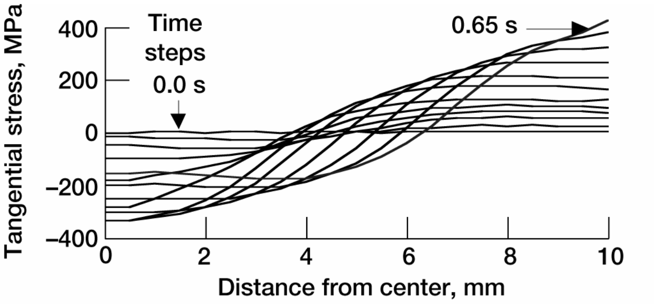

Figure 9.—Transient tangential stress profile for disk specimen 3. Time steps range from 0.0 to 0.65 s. Not all time steps are shown.

stresses are compressive over the entire disk and are not shown. The FEA analysis for specimen 3 consisted of 27 time steps ranging from 0.0 to 0.65 s, whereas the analysis for specimen 9 consisted of 15 time steps ranging from 0.0 to 0.35 s. The time steps corresponded to increments where experimental measurements were obtained. The FEA transient tangential stress results compared very well with the numerical calculations performed by the Siemens group.

For the CARES/*Life* reliability analysis, the Weibull parameters obtained from the three-point flexure bars were used to predict the strength response of the disks. The Weibull parameters are usually determined from rupture experiments of specimens in simple tension or flexure. Regression techniques, such as least squares and maximum likelihood (see app. D reproduced from Nemeth et al., 2003, for more details), have been developed that can determine these parameters from a simplified form of equation (17):

$$P_{fV} = 1 - \exp\left\{ -\int_V \left[\frac{\sigma(x,y,z)}{\sigma_f} \right]^{m_V} dV \left(\frac{\sigma_f}{\sigma_{oV}} \right)^{m_V} \right\} = 1 - \exp\left[-\left(\frac{\sigma_f}{\sigma_{\theta V}} \right)^{m_V} \right] = 1 - \exp\left[-V_e \left(\frac{\sigma_f}{\sigma_{oV}} \right)^{m_V} \right] \tag{97}$$

where σ_f is the peak stress in the specimen, $\sigma_{\theta V}$ is the specimen characteristic strength, and V_e is known as the effective volume. The strength $\sigma_{\theta V}$ is the value of σ_f where 63.21 percent of experimental rupture specimens fail. When the maximum likelihood parameter estimation method and the assumption of volume flaws were used, a Weibull modulus m_V of 11.96, a characteristic strength $\sigma_{\theta V}$ of 612.7 MPa, and a Weibull scale parameter σ_{oV} of 453.8 MPa-mm$^{3/m}$ were obtained for the flexure bars tested at room temperature. The material strength of ceramics (and hence the Weibull and fatigue parameters) are known to be temperature dependent. Ferber and Breder (2001) shows this relationship for SN282, where the average strength gradually decreases as temperature increases. However, this dependency was not considered in this analysis since only room temperature results were available for the bars cut from the disks. The authors believe this is still satisfactory since, from figure 8, the temperatures near the edge of the disk (where fracture is most likely to occur) are relatively low, so material properties should not deviate much from room temperature values.

The transient reliability response of the disk was calculated using the room temperature values of m_V and σ_{oV} and the results of the FEA with equation (45). Figure 10 shows the predicted failure probability versus time for specimens 3 and 9. These results were obtained using volume-based analysis with the Batdorf multiaxial methodology, a Griffith crack (eq. (5)), and $\overline{C} = 0.82$ (eq. (4)). The plot shows straight-line segments connecting the failure probability predictions for the various time steps. Each time step is based on analysis results from the experimentally measured temperature profile. The solid line shows the results of the transient analysis from equation (45), whereas the dotted line shows the results from the fast-fracture analysis of the individual time steps. Notice that the dotted line occasionally shows a lower failure probability than a previous time step, whereas the solid line for the transient analysis correctly does not show this trend. Also, there is a close correlation between the transient fast-fracture results (solid line) and the single-time-step fast-fracture results (dotted line), which increases confidence in the validity of the transient solution algorithm. The solid and dashed lines of disk 9 are virtually coincident. Disks 3 and 9 truncated at different failure probabilities because they failed at different maximum stresses σ_f. Another interesting observation is that disks 3 and 9 appear to have somewhat different failure probability responses versus time.

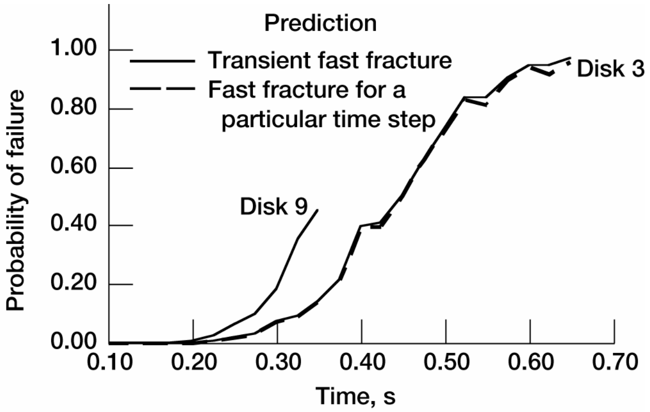

Figure 10.—Failure probability of disk specimens 3 and 9 as a function of time.

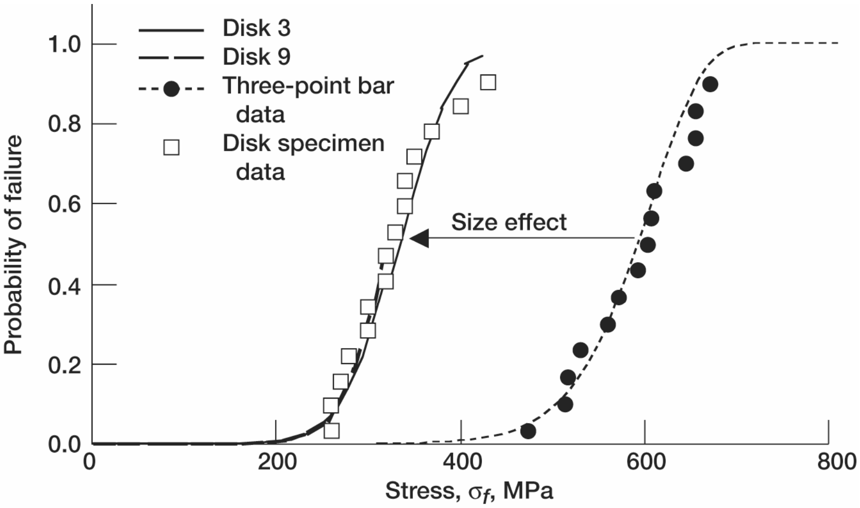

Figure 11.—Predicted failure probability of disk versus stress using the Weibull parameters estimated from the three-point flexure bar data. Experimental rupture data are also shown.

Figure 11 shows the predicted failure probability response of the disk versus the maximum stress σ_f in the disk. The experimentally obtained fracture stresses are overlaid for comparison. The curve for the three-point flexure bar results represents a line of best fit to the data, as previously described ($m_V = 11.96$ and $\sigma_{\theta V} = 612.7$ MPa), that was used to obtain the Weibull parameters used for the disk reliability analysis ($m_V = 11.96$ and $\sigma_{oV} = 453.8$ MPa-mm$^{3/m}$). The solid curve for the disk represents predictions based on the analysis of disk 3, whereas the more difficult to see dashed curve is the prediction from disk 9. Notice that the disk-9 results truncate around $P_f = 0.45$, consistent with figure 10. The curves for disks 3 and 9 follow nearly the same path in figure 11, unlike the results shown in figure 10. A striking observation about figure 11 is the difference in the median strength between the disk and the three-point flexure bar. This primarily represents the Weibull size effect: a component with a larger amount of volume under high stress will have a lower average strength than a component with a smaller amount of volume under high stress. This effect is a direct consequence of equation (17).

Another interesting item worth commenting on is the significant difference between the Weibull modulus m_V for the three-point flexure bar rupture data ($m_V = 11.96$ and $\sigma_{\theta V} = 612.7$ MPa) and for the thermal shocked disk experimental rupture data ($m_V = 6.91$ and $\sigma_{\theta V} = 345.9$ MPa) shown in figure 11, as determined by the CARES/*Life* maximum likelihood parameter estimation. A least-squares regression (using an Excel spreadsheet) on the CARES/*Life* disk prediction curves shown in figure 11 yields a Weibull modulus m_V of 8.72. This result is worthy of note because under usual circumstances the Weibull modulus for the test specimen and the designed component are presumed to be the same given that they are sampling similar flaw populations and that the effective volume V_e stays constant versus time. In other words, under usual circumstances, the Weibull modulus obtained from the regression of the predicted disk failure probability curve versus strength would be 11.96—the same value as for the three-point flexure specimen data. The fact that in this case the Weibull moduli between the predicted disk response curve and the flexure bar data are significantly different can be understood by examining figure 9.

Notice that as time increases the amount of volume under high tensile stress significantly decreases. This decreases the effective volume V_e with time, and through the size effect, increases the predicted failure stress σ_f. The overall effect of the effective volume changing with time is to decrease the observed (apparent) Weibull modulus for the thermally shocked disks according to σ_f. The fact that CARES/*Life* predicts that the Weibull modulus obtained from the failure-probability-versus-σ_f curve reduces to 8.7 in comparison to the flexure bar value of 12.0, compares favorably with the experimental disk result of 6.9. In other words, some of the discrepancy in the Weibull modulus values between the experimental disk and flexure bar results can be explained as a consequence of the transient thermal loads and how they influence the stress distribution in the disk as a function of time. The difference in values (12.0 versus 8.7), therefore does not necessarily indicate some error or inconsistency. The remainder of the difference (8.7 versus 6.9) can be explained as natural statistical variation (within 90-percent confidence bounds).

The excellent correlation in figure 11 to experimental results must be considered within the context of the underlying statistics, given that the effective volume V_e between the three-point bend bar and the disk is large and sensitive to the value chosen for the Weibull modulus m_V. Because of the relatively small number of samples tested (in this case, 14 flexure specimens) and the large size effect, using Weibull parameters based on 5- and 95-percent confidence bounds from the three-point flexure bar data could shift the disk predictions significantly to the left and right of the experimental data. In general, a good design practice would be to avoid large size-effect scalings between specimens and components unless experimental data exist for both the specimen and component such that data-pooling practices could be taken advantage of to obtain a set of best-fit Weibull parameters.

3.2 Example 2: Heavy-Duty Diesel Exhaust Valves Undergoing Cyclic Loading

This example, involving a heavy-duty diesel ceramic exhaust valve (Corum, et al., 1996), was selected to contrast failure probability predictions for the power law (eq. (8)), the combined Walker-power law (eq. (56)), and a proof-test condition. The valves were made of NT–551 silicon nitride material. Table I summarizes the Weibull and SCG parameters obtained from four-point flexure bars at three different temperatures (Andrews et al., 2000). CARES/*Life* and the raw data listed in Andrews et al. (2000) were used to obtain these parameters. Data to obtain values for the combined Walker-power law parameters did not exist, so assumed values for Q_V and A_2/A_1 were used (eq. (63)).

TABLE I.—NT–551 FAST-FRACTURE AND SCG MATERIAL PROPERTIES

Temperature, T, °C	Volume Weibull modulus, m_V	Volume Weibull scale parameter, σ_{oV}, MPa-mm$^{3/m}$	Weibull characteristic strength, σ_θ, MPa	Crack-velocity exponent, N_V	Volume SCG material parameter, B_{wV}, MPa^2-sec	Walker R-ratio exponent, Q_V	Crack-velocity ratio, A_2/A_1
20	9.4	1054	806	31.6	5.44×10^5	3.2	0.65
700	9.6	773	593	86.5	1.12×10^4	3.2	0.65
850	8.4	790	577	18.5	1.13×10^6	3.2	0.65

Fifteen valves were engine tested without failure. These valves consisted of seven longitudinally machined valves and eight transversely machined valves. The transversely machined valves had been engine tested for 1000 hr, whereas the longitudinally machined valves had been engine tested for 166 hr. These valves were subsequently tested in fast fracture to examine their retained strength. For both valve-machining orientations, failure was found to be volume induced.

Since all engine-tested valves failed because of volume flaws, the transient reliability of the valves was based on volume analysis. Figure 12 shows the pressure variation as a function of time during a typical combustion cycle of 0.0315 s. The pressure was applied to the valve face and other exposed surfaces within the cylinder. The maximum pressure attained during the combustion cycle was estimated to be 15.85 MPa (Corum, et al., 1996). A 445-N (100-lb) force due to spring preload was applied to the valve stem when it was in the open position. At the moment the valve closed, an impact force of 1335 N (300 lb) was applied to the valve stem. In addition, thermal stresses due to the temperature distribution in the valve were superposed to the mechanical stresses.

Figure 13 shows the approximate mean thermal profile in the valve. Steady-state thermal analysis using the ANSYS FEA code was conducted to compute these temperatures. This figure shows that the temperature is maximum near the valve face and decays towards the valve seat and stem.

Transient reliability analysis (using eqs. (49), (51), (70), (77), (80), (81), and (82)) for a PIA-style formulation (Barnett et al.,1967; and Freudenthal, 1968) was conducted by dividing the load history into 29 time steps. During each step, the load was assumed to be constant. The loads corresponding to these time steps were modeled within

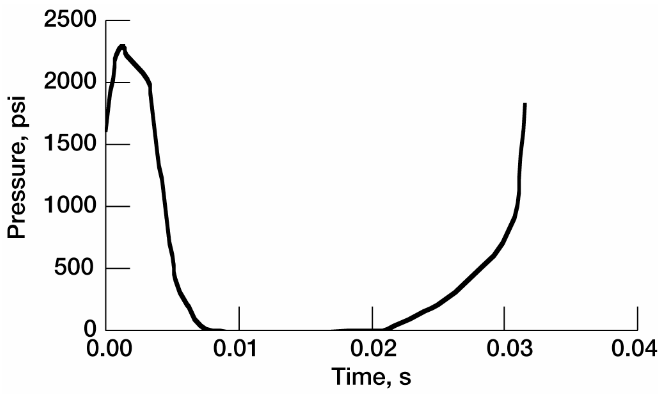

Figure 12.—Pressure variation applied to the face of a ceramic valve during a typical engine combustion cycle.

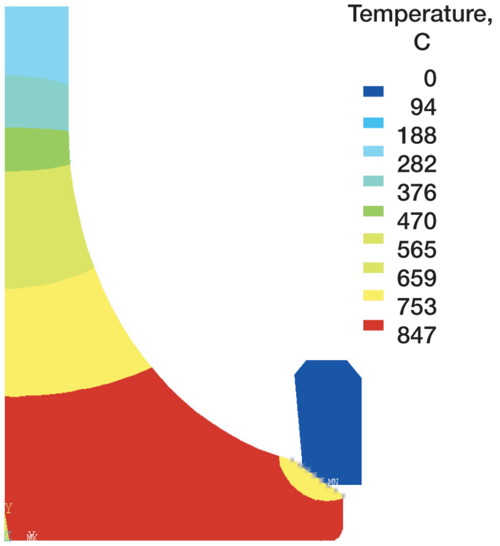

Figure 13.—Mean thermal profile of the valve. Maximum and minimum temperatures, 846 and 0 C. Time step, 0.01313 s.

the ANSYS FEA program, which yielded the stress results for these 29 time steps (stress history). Figure 14 highlights the first principal thermomechanical stress distribution in the valve at the moment of maximum applied pressure (at time step 6). From the figure, it is apparent that the maximum stress location is at the valve radius, which is in agreement with the FEA results of Corum et al. (1996).

The valve's stress history and other relevant terms (temperature, volume, material properties, etc.) were subsequently read into CARES/*Life*. Figure 15 shows the power-law transient reliability curve as a function of time (load cycles). As seen in the figure, the probability of failure increases with time, and it is apparent that the ceramic valve is very reliable. Figure 16 shows these same results on a log-log scale plot for the power law and time step 6 applied as a static load for low probabilities of failure. After 1 hr of operation, the failure probability P_f was predicted to be 6×10^{-5} (6 in 100 000 valves would have failed), whereas after 8.7 million hr of operation, the P_f was predicted to be 9.4×10^{-4} (94 in 100 000 valves would have failed).

A static reliability analysis using the maximum stress level during the load history (load step 6 in this analysis) was performed and compared with the transient reliability analysis. As seen in figure 16, the static loading at the maximum level yielded higher failure probabilities (more conservative) than for the transient loading case. Between 9 and 9×10^{15} hr of operation, the failure probability using static maximum stress analysis was predicted to be double the failure probability based on transient analysis. For example, transient reliability analysis predicted that approximately 20 in 100 000 valves would have failed after 1000 hr of operation, whereas maximum static stress reliability analysis predicted that approximately 40 in 100 000 valves would have failed. These results, showing higher failure probabilities for static maximum loading than for transient loading, make sense since the combustion load cycle contains a considerable duration of low to no loading for the valve.

Figure 16 also shows the predicted failure probability as a function of the number of cycles for various scenarios. None of the tested valves failed, even though 8 of the 15 valves were tested to 1000 hr (approximately 1.1×10^{8} cycles). Thus, the failure rate of the tested valves was less than 1 out of 8 at 1000 hr of operation. From figure 16 it can be seen that in fast fracture (at one cycle with no SCG) about 5 out of 100 000 valves are predicted to fail from the loading. With SCG and the power law, about 20 out of 100 000 valves are predicted to fail after 1000 hr of operation. If it is conservatively assumed that the worst-case load (time step 6) is applied over the whole engine cycle (static loading), then about 40 out of 100 000 valves would fail after 1000 hr. When the combined Walker-power law is used with the hypothetical parameters from table I, this rate increases to 70 out of 100 000 valves at 1000 hr. All of these rates were well below what was experimentally observed, but not enough valves were tested to make any firm conclusions. These three scenarios were presented to contrast the predictions. The

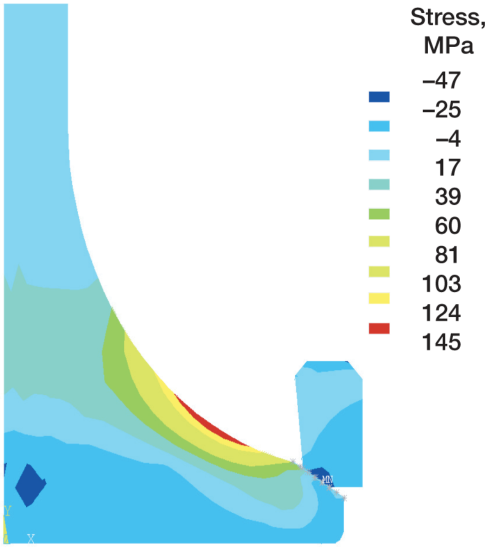

Figure 14.—First principal stress distribution in the valve at the moment of maximum applied pressure. Maximum and minimum stress, 145 and –46 MPa.

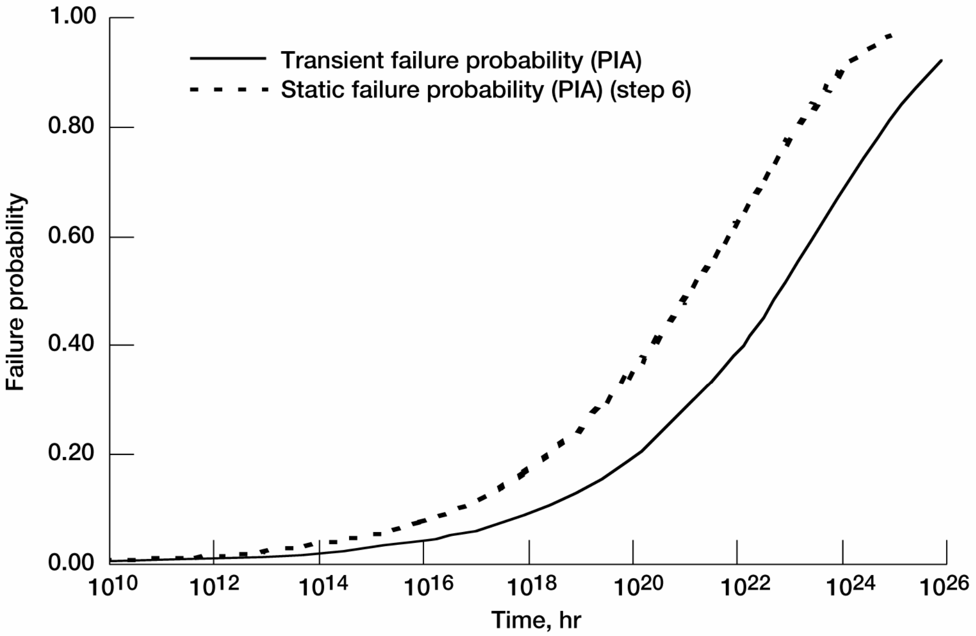

Figure 15.—Power-law transient and static probability of failure of the ceramic valve as a function of time. The static probability of failure is predicted for a worst-case constant applied load (time step 6).

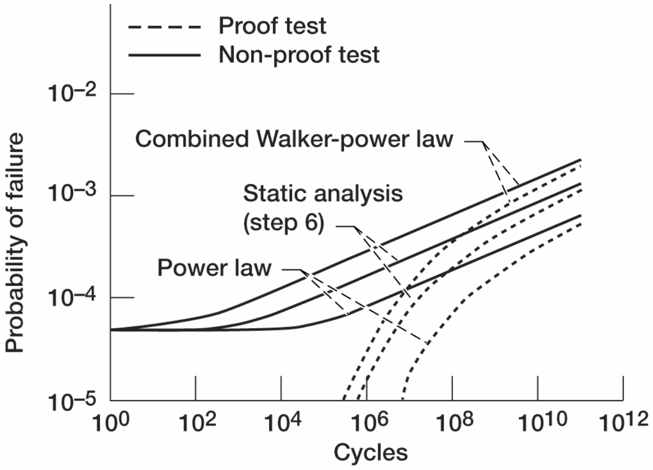

Figure 16.—Failure probability versus cycles for proof-test and non-proof-test conditions for a static load, the power law, and the combined Walker-power law.

power law with cyclic loading predicts the least damage. The static loading scenario is predicted to be more damaging at double the rate of the cyclic loading. The combined Walker-power law predicts the most damage because of the enhanced cyclic fatigue effect.

The predicted failure rate can be reduced even further if proof testing is applied to prevent the weakest components (those with the highest likelihood of failing) from being placed into service. Figure 16 also shows the predicted results for the three various scenarios for an applied proof test of 10 000 cycles at a loading factor of 1.1 of the service loading (dashed lines in the figure). Increasing the proof-test load would reduce the attenuated probability of failure even further.

The transient reliability methodology described in this report is based on discretizing the load history into short time steps during which everything is assumed to remain constant. Obviously as these time steps become shorter and shorter (the load history is divided into more and more time steps), the solution becomes more accurate. It is not possible to suggest how many time steps should be used, since the proper selection of time steps depends on the problem and load history at hand. Users are well advised to run a convergence analysis by running several transient reliability computations using different sets of time steps. There will be a tradeoff between computational efficiency and error.

3.3 Example 3: Alumina in Static Fatigue—Material Properties Changing With Time

This example examines how the reliability response of a vitreous bonded alumina is hypothetically affected by Weibull and fatigue parameters that change over time. The two scenarios that are presented are based strictly on curve fitting the data. The authors do not have sufficient information to physically specify which parameters are really responsible for the change in material response with time. However, the point of this analysis is to present an analytical model that might explain the nonlinear and changing rupture behavior of the material given that the physical parameters that are responsible for the changing material behavior are known. This capability could be useful in modeling materials with changing composition (or with changing physics of crack growth), including oxidation and crack blunting/healing phenomena.

The data for the example, which were obtained from Quinn (1987), consisted of the rupture lives of the alumina four-point flexure bars in static fatigue (loading at a constant stress level over time). The specimens had the following average dimensions: a height of 2.2 mm, a width of 2.8 mm, a load span of 19.0 mm, and a support span of 38.0 mm. This data set was chosen from the literature because of its nonideal behavior and because of the careful experimental technique reported by the author, which reduced the likelihood that equipment and measurement errors would significantly affect the results. The rupture data for the individual specimens are shown in figure 17. Testing was performed at 1000 °C. The report stated that very little creep deformation was detected, and although fractography was attempted, it did not reveal the source of the strength-limiting flaws.

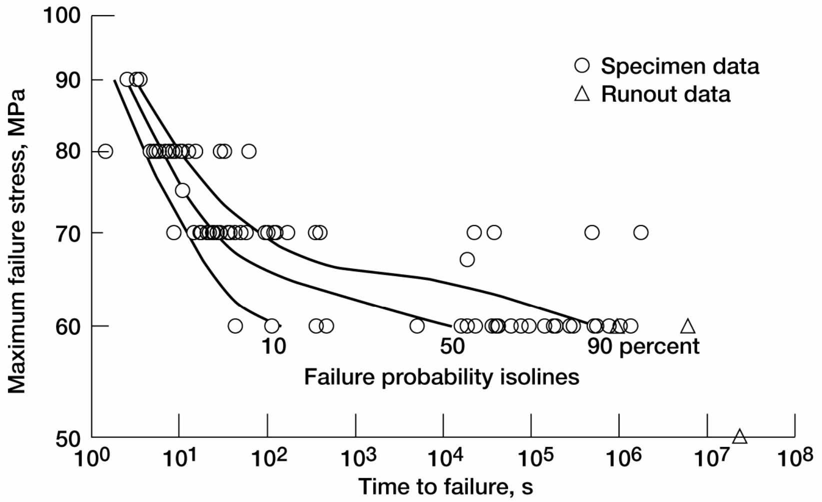

Figure 17.—Effect on failure probability of changing the fatigue exponent, *N*, with the log of time from table II on the static fatigue rupture data of alumina flexure bars at 1000 °C.

Two trends made these data nonideally behaved: (1) dramatically increased scatter at lower applied stresses and (2) pronounced nonlinear behavior in the stress rupture data as the applied stresses became lower (the strength data shifted to the right, which signified that the lives became longer than would have been predicted if the standard power law was applicable). An ideally behaved data set would show a straight line trend, indicating that the fatigue exponent was constant. In addition, the scatter band would appear with a constant width versus the applied stress, indicating that the Weibull modulus was constant.

A confirmatory piece of evidence that material properties were changing with time was obtained by performing static rupture experiments on specimens that were annealed (at no load) for either 1 or 24 hr at 1050 °C. The outcome of these treatments (not shown herein) was that life dramatically increased versus exposure time for an applied stress level (Quinn, 1987). Quinn indicated that the observed behavior is probably due to the partial devitrification of the material's glassy phase, resulting in an increased viscosity of the phase and a material with improved creep and stress rupture behavior. Quinn cites Wiederhorn et al. (1986) to support this, although he concedes that crack blunting, healing, or residual stress changes could also be operative.

Quinn's data defy the conventional modeling approach since the material properties could be changing over time. To account for this, the authors of the current report show what happens when Weibull and fatigue parameters change with time for two cases: (1) changing the fatigue exponent N and the Weibull modulus m over time and (2) changing the Weibull parameters (m and σ_0) over time. Tables II and III show the sets of parameters chosen to demonstrate these scenarios. Given the fact that no established parameter estimation techniques currently exist for this type of nonideally behaved data, these parameters were iteratively selected to fit the data. Table II contains a set of parameters versus time where N and m were varied to yield an improved fit to the data. Table III shows a set of parameters where m was varied while N was kept relatively constant. Note that in both cases the scale parameter σ_0 depends on the Weibull modulus and B depends on the fatigue exponent as well as the Weibull parameters. When these parameter sets are applied within a reliability analysis, the Weibull and fatigue parameters are linearly interpolated with the log of time within the time spans listed in the tables and are held constant outside of the time span.

TABLE II.—WEIBULL AND FATIGUE PARAMETERS ASSOCIATED WITH FIGURE 17

Time, t, s	Surface Weibull modulus, m_S	Surface Weibull scale parameter, σ_{oS}, MPa-mm$^{2/m}$	Surface crack-velocity exponent, N_S	Surface SCG material parameter, B_{wS}, MPa^2-s
1.6	29.4	156.8	6.7	2711.1
31.6	15.8	152.7	13.2	9707.7
1.0×10^5	13.1	127.3	36.4	2276.2

TABLE III.—WEIBULL AND FATIGUE PARAMETERS ASSOCIATED WITH FIGURE 18

Time, t, s	Surface Weibull modulus, m_S	Surface Weibull scale parameter, σ_{oS}, MPa-mm$^{2/m}$	Surface crack-velocity exponent, N_S	Surface SCG material parameter, B_{wS}, MPa^2-s
1.6	29.4	165.8	6.7	2 711.1
31.6	7.4	263.3	8.0	2 395.9
316.2	4.5	870.1	9.0	10 389.0

Because of the simplicity of the four-point specimen loading and geometry, results from the FEA were not needed for the reliability analysis. Instead, a closed-form expression for the effective area A_e was used to evaluate the integral of equation (17) for a surface flaw failure mode (see app. D reproduced from Nemeth et al., 2003). An effective area A_e (which is analogous to the effective volume in equation (97)) of 58.0 mm^2 was calculated on the basis of a Weibull modulus value of 7.7. This value was chosen because sensitivity analysis using equation (17) indicated that the maximum error in strength for a given failure probability would be 1 percent or less for Weibull modulus values ranging between 5.0 and 30.0. This level of error is negligible for the illustrative purposes of this example. In modeling the transient material response using equation (42), 10 time steps are used per decade of the log of the time. Hence, 10 time steps are used between 1 and 10 s, whereas 20 time steps are used between 1 and 100 s. The time steps are log increments of time; that is, they would appear as equally spaced increments in figure 17 with 10 steps per decade.

Figure 17 shows the predicted 10-, 50-, and 90-percent failure probability isolines for the parameters shown in table II, and figure 18 shows 1-, 10-, 30-, 50-, 70-, 90-, and 99-percent failure probability isolines for the parameters shown in table III. Neither plot represents an optimized set of fitted parameters. As previously stated, no established parameter estimation techniques currently exist for this type of nonideally behaved data. Parameters were obtained by segregating portions of the data and performing parameter estimation as described in appendix D from Nemeth et al. (2003) for the four-point bending bar specimen as well as by further refinements by trial and error. Figure 17 shows that the curvature in the data can be captured by changing the fatigue exponent N; however, accounting for the change in scatter still required modifying the Weibull modulus m. Figure 18 is interesting because a satisfactory fit to the data can be obtained by changing the Weibull modulus and scale parameter only (B changes mainly in response to these parameters). The kink shown in the failure probability isolines between 10 and 100 s is not purposely modeled: that is, parameter values were not specifically selected to obtain this response. The "outlier" rupture data (data that appear to be not part of, or not consistent with, the main body of data) at long times to failure at 70 MPa and the outlier data at short times to failure at 60 MPa are better accounted for in this model than they are in figure 17. That is, the data points that visually appear to be outliers are actually consistent with the flaw population failure probability response: they are predicted to be there.

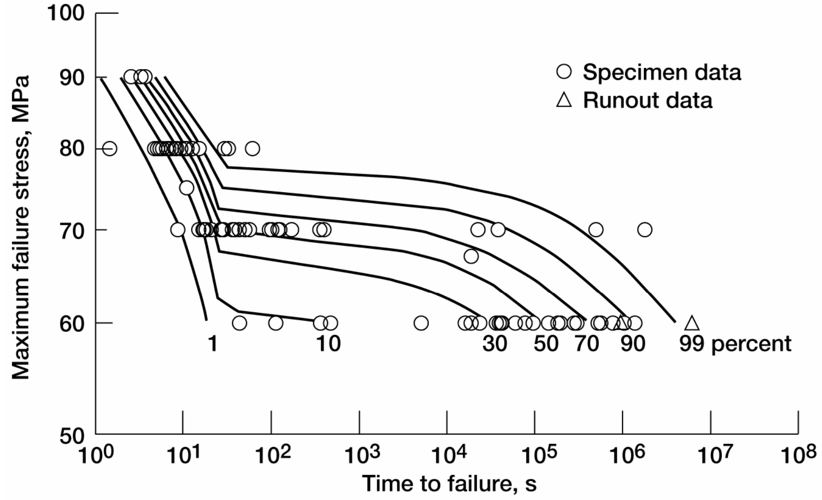

Figure 18.—Effect on failure probability of changing Weibull modulus, *m*, with the log of time from table III on static fatigue rupture data of alumina flexure bars at 1000 °C.

The modeling assumptions that produced the results in figure 18 reasonably capture all the trends in the data as well as or better than the approach used in figure 17. Also, both approaches required changing the Weibull modulus m to account for the range of scatter. A changing Weibull modulus could indicate new flaw generation or changes of the physics of crack growth associated with R-curve behavior. On the other hand, a changing fatigue exponent with time is consistent with crack blunting/healing phenomena, where the crack-velocity relationship in equation (8) is changing with time. In this case, further tests on the material would be needed to understand the underlying mechanism that was driving the SCG behavior.

3.4 Example 4: Thermally Shocked Hexoloy SiC Tubes

The thermal shock problem of Hexoloy (Saint-Gobain Ceramics, Niagara Falls, NY) sintered alpha silicon carbide (SASC) tubes was chosen in this study for four reasons:

(1) The thermal, elastic, Weibull, and SCG data for the SASC material (tables IV and V) are available.

(2) SASC SiC tubes were tested in fast fracture and thermal shock loading during earlier studies (Segall, 1992; Shelleman et al., 1991; Jadaan, 1990; Jadaan et al., 1991 and 1994; and Jadaan and Tressler, 1993), and hence, experimental data providing measured failure probability P_f for the shocked tubes are available. By using these data and the theory developed in this report, we can compare the measured P_f values with the predicted values and demonstrate the viability of the transient methodology.

(3) The SASC material was selected because of its use in industrial applications.

(4) Multiaxial thermoelastic stress states resulting from the localized quenching of the SASC tubes are very complex and highly transient. Such complex and transient thermal and stress states are desired in our example to demonstrate the full potential of the proposed theory.

TABLE IV.—WEIBULL AND SCG PARAMETERS OF HEXOLOY SiC

Specimen configuration	Temperature, °C	Average strength, MPa	Weibull modulus, m	Volume Weibull scale parameter, σ_{oV}, MPa-m$^{3/m}$	Area Weibull scale parameter, σ_{oS}, MPa-m$^{2/m}$	SCG exponent, N	Volume SCG coefficient, B_{WV}, MPa^2-s	Area SCG coefficient, B_{WA}, MPa^2-s
C-ring[a]	25	232	12.2	63.9	123.4	---	-----	-----
	1200	245	8.8	42.5	104.1	29.4	5826	6884
O-ring	25	---	---	----	114.7	----	-----	-----
	1200	287	9.9	----	115.4	27.2	-----	480.3

[a] C-ring tested in compression.

TABLE V.—THERMOELASTIC MATERIAL PROPERTIES FOR HEXOLOY SiC (Segall, 1992)
[Poisson's ratio, 0.14.]

Temperature, T, °C	25	200	500	700	800	900	1000	1100
Specific heat, C_p, J/kg-°C	485.3	682.2	790.8	857.6	898.2	945.3	999.8	1064
Thermal conductivity, κ, W/m-°C	133.5	99.9	57.8	45	41.1	37.1	36	35.4
Thermal diffusivity, D, cm^2/s	0.872	0.473	0.236	0.172	0.151	0.128	0.116	0.105
Elastic modulus, E, GPa	417.9	415.9	413.7	-----	407.1	-----	402.7	-----
Thermal expansion coefficient, α, 10^6/°C	3.30	4.20	4.90	-----	5.45	-----	5.75	-----

The experimental shock study was conducted by Segall, with the details reported in his Ph.D. thesis (Segall, 1992). However, a brief summary of the thermal shock testing procedure and results will be reiterated here for completeness. The testing procedure involved the symmetric placement of each tube (152 mm long with an outside diameter of 43.9 mm and an inside diameter of 35.3 mm) in a furnace without restraints. Once positioned and appropriately instrumented, the furnace was closed and the tube was internally heated to 1000 °C and allowed to equilibrate for at least 15 min. After equilibration, the instrumentation was activated and a localized helium quench over a 10-mm segment (central portion of the tube) was allowed to flow to the surface of the tube as shown in figure 19. In the thermal fatigue portion of the study, when the 10-s quench (one thermal shock cycle) was completed, the tube was reheated and the process was repeated for up to five cycles. Acoustic emissions (AE) were continuously monitored in situ during the tests. In addition, transient internal surface temperature profiles at distances of 0, 2, 4, 6, 8, 10, 12, 14, 20, 30, 50, and 75 mm from the quench centerline were measured (fig. 20) using multiple thermocouples with temperature corrections (Segall, 1992). Error analysis indicated that a 1 to 3 °C error could have resulted from data-acquisition errors, and up to 2 °C from inherent thermocouple errors.

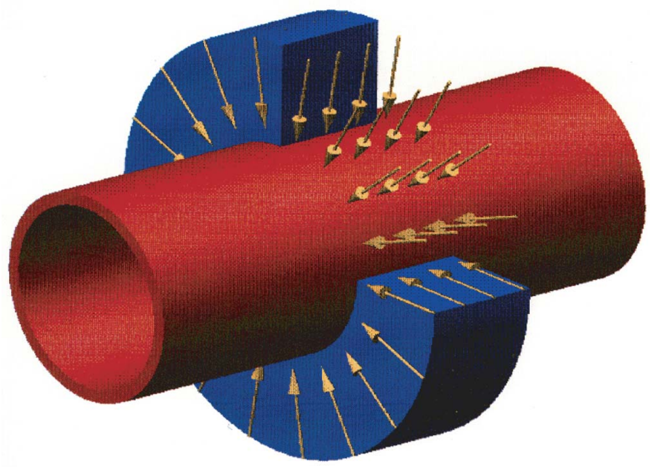

Figure 19.—Depiction of annular gas quench on the external surface of a tube.

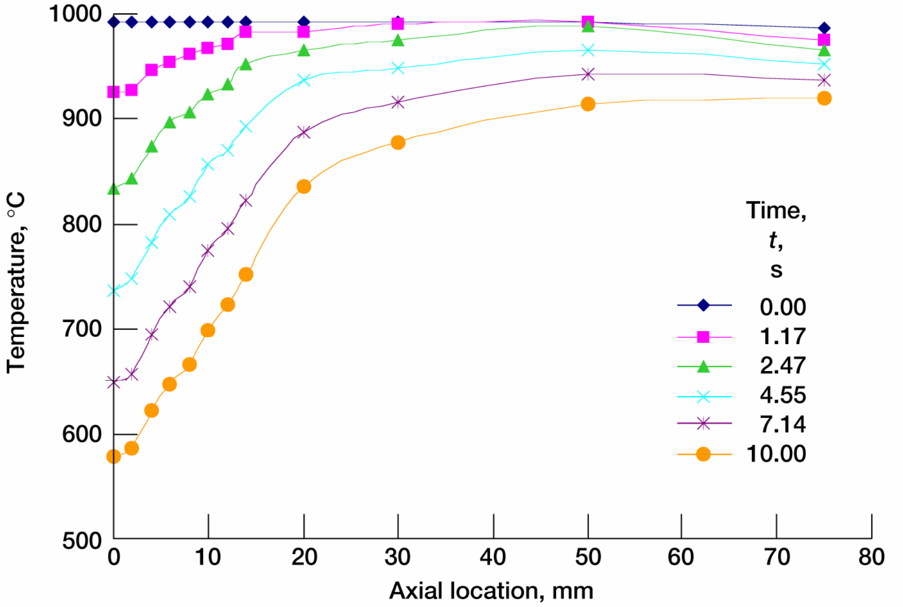

Figure 20.—Measured internal surface temperature distributions versus time for Hexoloy tubes quenched from 1000 °C.

The results of the SASC testing revealed a number of interesting behaviors. Post-thermal-shock fracture tests revealed a minimal propensity for SCG or fatigue after five cycles—either the specimens showed significant cracking with minimal retained strength or no damage at all. This behavior was corroborated by the in situ AE data, which indicated that most of the damage (if any) was incurred during the first cycle. An AE energy-versus-time plot (see fig. 21) showed that most of the damage took place during the first cycle, indicating minimal crack extension during the last four thermal shock cycles. All tubes with high AE histories showed extensive axial-to-circumferential crack paths with no discernible differences in the crack densities or patterns between the singly and multiply cycled tubes. Fractography conducted on the failed tubes indicated that the majority of failures were due to relatively large axial defects remaining from the extrusion process used to fabricate the tubes and that failures could originate at both internal and external surfaces.

To perform the transient reliability analysis, one must know the Weibull (m, σ_0) and SCG (N, B) parameters for the SASC material. When a reliability analysis is performed, these parameters are obtained from simple specimens. These simple specimens when loaded to failure should sample similar flaw populations to those existing in the tube. Hence, C-ring and O-ring specimens cut from as-received Hexoloy tubes were tested in fast fracture (Weibull parameters) and dynamic fatigue (SCG parameters) modes (Shelleman et al., 1991; Jadaan, 1990; Jadaan et al., 1991 and 1994; and Jadaan and Tressler, 1993). The C-ring specimen, with maximum tensile stress existing at its outer surface, samples flaws at the external surface of the tube; whereas the O-ring specimen, with maximum tensile stress existing at its internal surface, samples flaws at the inner surface of the tube. Hence, when the reliability of the tubes was modeled, the C-ring Weibull and SCG parameters were used to compute the transient probability of failure due to external surface defects, and the O-ring Weibull and SCG parameters were used to compute the transient probability of failure due to internal surface defects. The C-ring data were also used to compute the failure probability due to volume defects. Table IV lists the Weibull and SCG parameters for Hexoloy SiC at ambient temperature and 1200 °C on the basis of both volume and surface area analysis.

The ANSYS FEA program was used to compute the transient temperature and thermoelastic stresses for the thermally shocked tube. The tubular geometry combined with the axisymmetric nature of the quench allowed the tube to be modeled with two-dimensional axisymmetric plane55 thermal elements and axisymmetric plane42 structural solid elements. A fine mesh of 5000 elements was used to model half the tube, from the quench centerline ($y = 0$) to the end of the tube ($y = 0.076$ m). In this mesh, the tube's wall thickness was divided into 20 elements and its length was divided into 250 elements.

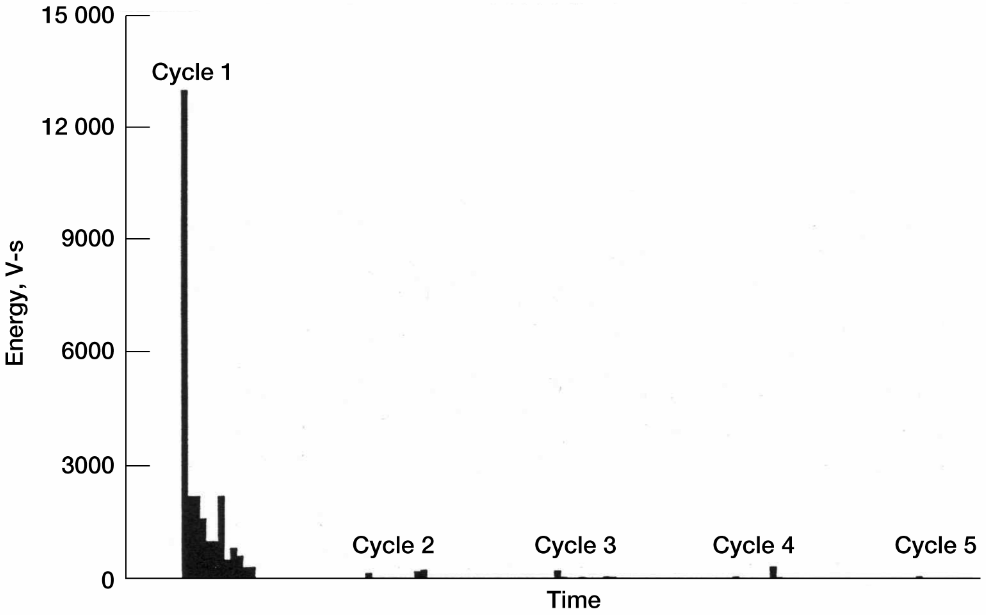

Figure 21.—Typical history of acoustic emission energy for a Hexoloy SiC tube quenched from 1000 °C.

The transient heat transfer analysis was conducted first. This involved circumferentially blasting a 5-mm-wide region of the tube's half length with cold air. Table V lists the thermal material properties as a function of temperature used in the thermal FEA. The temperature distributions throughout the tube as a function of time were needed in order to perform the transient thermoelastic stress analysis. Experimentally, only the internal temperature distributions as a function of time were known (fig. 20). An iterative inverse heat transfer analysis was conducted by prescribing appropriate convection film coefficients (representing thermal loads) on all surfaces for the entire quench period of 10 s. The FEA-computed transient temperature profiles closely matched the measured ones, especially within the critical quench zone. Figure 22 shows the FEA-calculated internal surface temperature profiles at the same six times that the temperatures were experimentally measured for figure 20. Adiabatic symmetry boundary conditions were imposed at the quench centerline. In addition, nonlinear and time-varying convective films, representing the continuous but changing thermal loading from the internal heating element as it cooled, were imposed on the internal surface. Changing, high-coefficient convective films within the 5-mm quenching zone (representing rapid heat loss due to quenching in that region) along with constant-convection films at the remainder of the external and edge surfaces of the tube were also prescribed. In addition, the temperature-dependent thermal conductivity and specific heat (table V) were tabulated within ANSYS for automatic interpolation. As can be seen from figures 20 and 22, the internal surface thermal profiles compare relatively well, especially within the critical quench zone.

Once the temperature profiles throughout the tube for the entire 10-s quench period were known, the transient thermoelastic stress analysis was conducted. The elastic properties of the Hexoloy material as functions of the temperature necessary for the structural analysis part of the study are listed in table V. Figures 23 and 24 display the hoop-stress distributions along the external and internal surfaces of the tube as a function of time during the 10-s quench period. Figure 25 shows the hoop-stress distributions within the tube at 0 and 10 s. It can be seen from these figures that the critical high tensile hoop stresses exist on both surfaces of the tube mainly within the 5-mm quench zone (based on one-half of the tube's length). The external hoop stresses were found to be higher than the internal hoop stresses since more rapid quenching takes place there. At the quench centerline of the external surface, the hoop stress spiked up to its maximum value of 187 MPa almost immediately (within 1 s) and then started to decay with time until it reached 127 MPa at the end of the quench test. At the internal surface, the hoop stress was initially compressive, but then it started to increase gradually until it reached a maximum of 106 MPa after approximately 7 s. Note that within the quench zone, almost the entire volume of material for almost the entire quench duration is in circumferential tension, while the rest of the tube is being subjected to either low tensile or compressive hoop stresses.

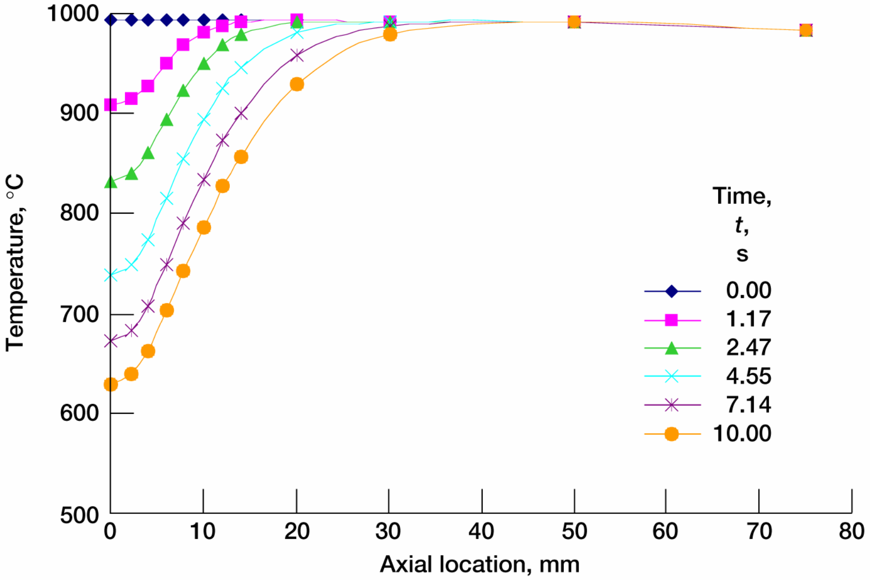

Figure 22.—Internal surface temperature distributions computed from finite element analysis versus time for Hexoloy tubes quenched from 1000 °C.

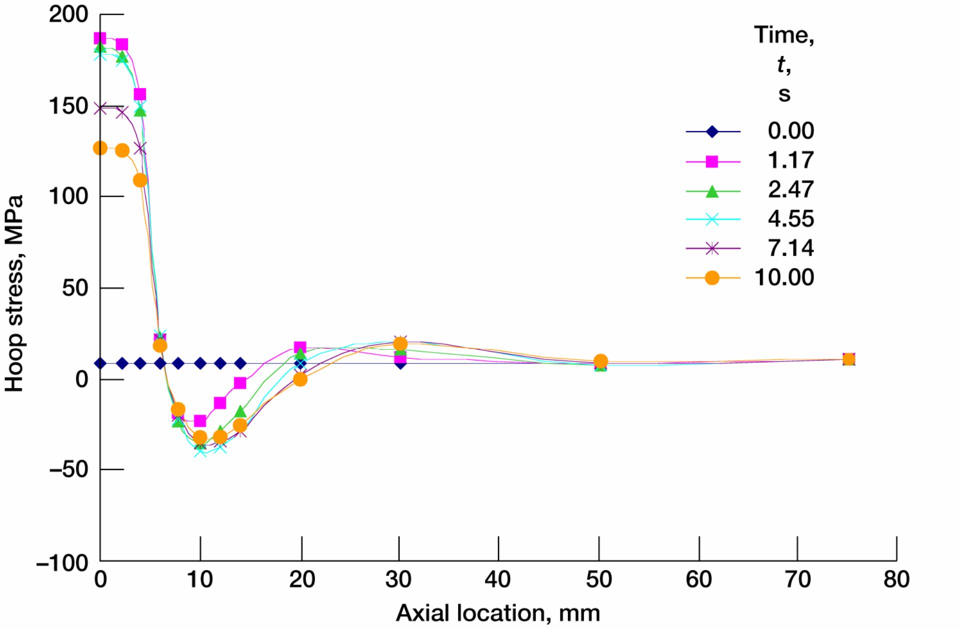

Figure 23.—External-tube-surface hoop stress distributions as function of time during the 10-s quench period.

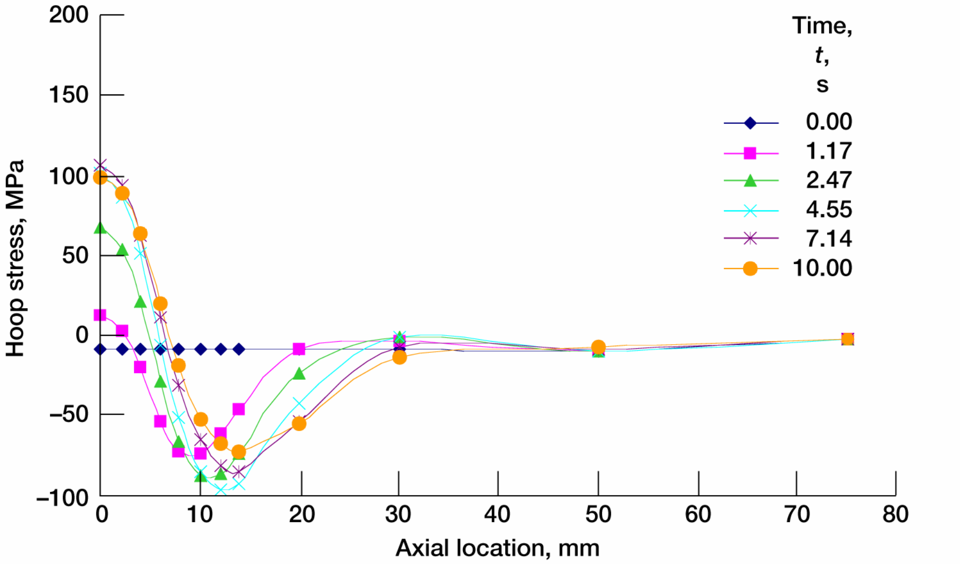

Figure 24.—Internal-tube-surface hoop stress distributions as function of time during the 10-s quench period.

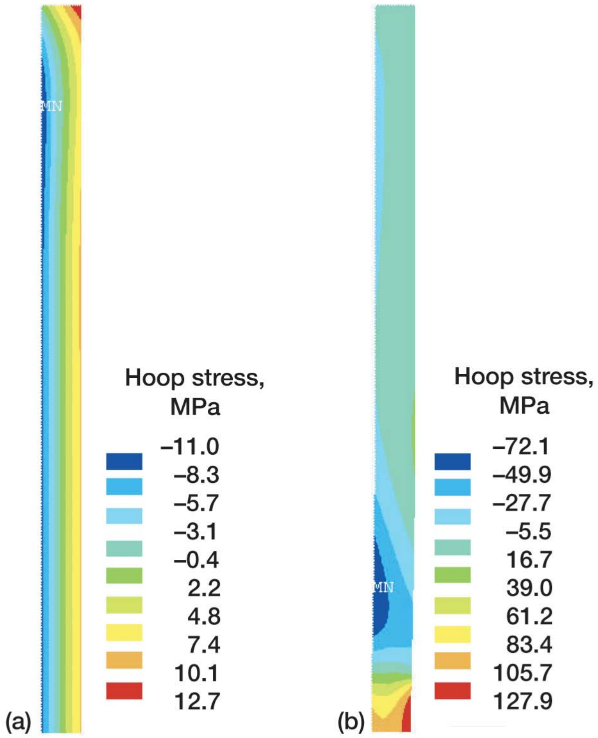

Figure 25.—Hoop-stress distributions in the quenched tube. (a) Time, 0 s; step 1. Maximum and minimum hoop stress, 12.7 and –11.0 MPa. (b) Time, 10 s; step 6. Maximum and minimum hoop stress, 127.9 and –72.2 MPa.

Figures 26 and 27 display the axial stress distributions along the external and internal surfaces of the tube as a function of time during the 10-s quench period. Figure 28 shows the axial stress distributions within the tube at 0 and 10 s. It can be seen from these figures that the critical high tensile axial stresses exist on both surfaces of the tube but within different regions. The external axial stresses were determined to be compressive within the quench zone and to be tensile within the central region of the tube between 10 and 50 mm. Within that central region, the tensile axial stress increased and shifted away from the quench plane as time elapsed. The maximum axial stress at the external surface was computed to be 125 MPa after approximately 7 s, 20 mm from the quench plane. At the internal surface of the tube, tensile axial stresses occurred within the quench zone and proved to be the highest of all stresses, reaching 265 MPa after 10 s. Figure 29 shows the transient axial stress distributions along the wall thickness at the quench centerline. In this case, approximately half of the internal volume of material was subjected to tensile axial stress while the external half was being axially compressed. This axial stress distribution within the quench plane is similar to that of a flexural specimen.

By combining these observations for both the hoop and axial stress distributions, one can note that within the quench zone the internal surface of the tube is being subjected to a biaxial tensile stress state (with the axial stress being the absolute highest), while the external surface of the tube is being subjected to tensile hoop and compressive axial stresses. Hence, it would be expected that the internal surface would be the most critical area and that it would contribute significantly to the failure probability of the tube.

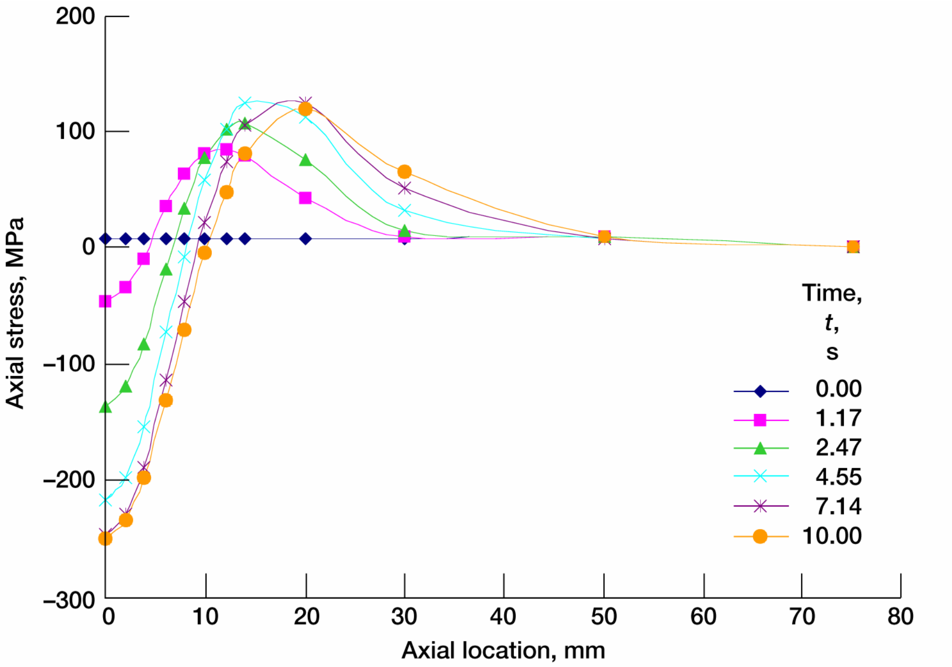

Figure 26.—External-tube-surface axial stress distributions as a function of time during the 10-s quench period.

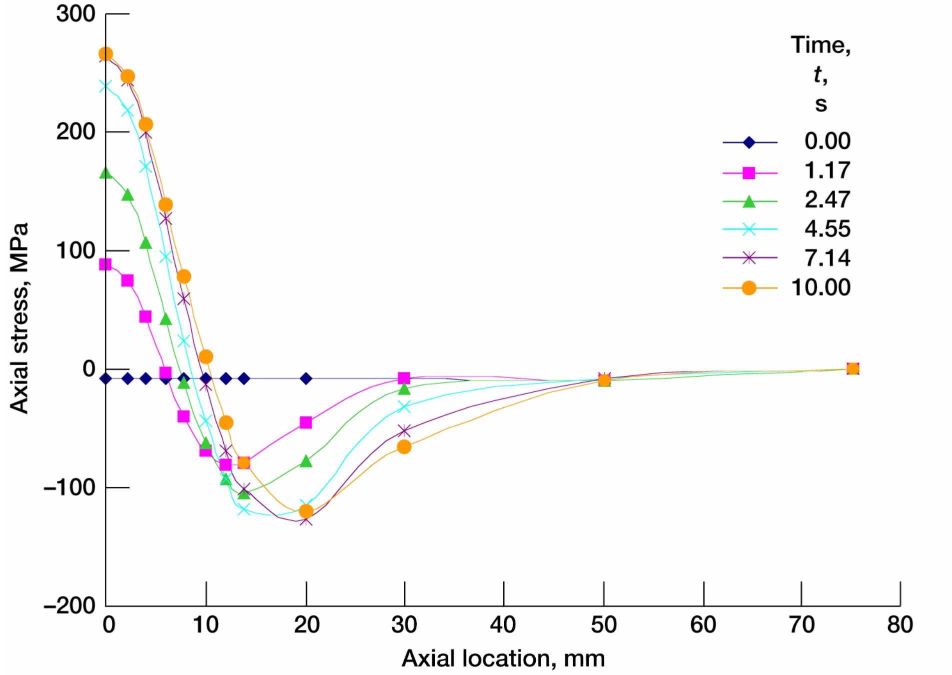

Figure 27.—Internal-tube-surface axial stress distributions as function of time during the 10-s quench period.

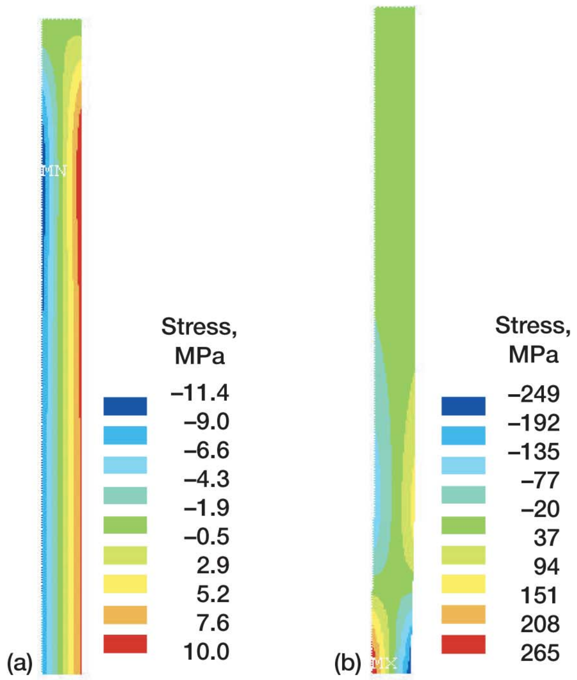

Figure 28.—Axial stress distributions in the quenched tube. (a) Time, 0 s. Maximum and minimum stress, 10.0 and –11.4 MPa. (b) Time, 10 s. Maximum and minimum stress, 265.3 and –248.8 MPa.

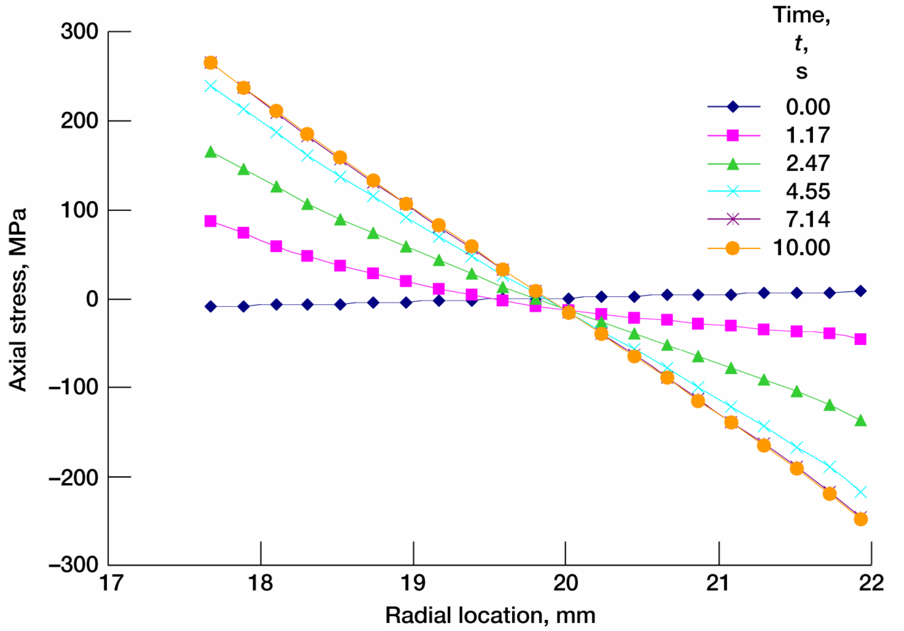

Figure 29.—Axial stress distribution through the tube's wall at the quench plane as a function of time.

The CARES/*Life* code was used to compute the SASC tube failure probabilities on the basis of the volume, internal surface, external surface, and total surface (internal and external surfaces combined) analyses. Three types of transient reliability analyses were conducted:

(1) Transient reliability with SCG during a one-cycle shock. Because of the lack of Hexoloy material properties in tubular form between room temperature and 1000 °C, the Weibull parameters between room temperature and 800 °C were assumed to remain constant and to be equal to the room temperature values. Between 800 and 1000 °C, the parameters were also assumed to remain constant but to be equal to the 1200 °C values. It was assumed that no SCG would take place between room temperature and 800 °C (this was done by setting the SCG coefficient B equal to an arbitrarily large number, $B = 1.0\times10^{15}$). Between 800 and 1000 °C, the SCG parameters were assumed to remain constant and to be equal to the 1200 °C values. The Hexoloy material is resistant to SCG below 1000 °C, but little data exist to quantify that behavior. In this thermal shock test, the temperature distribution for the entire duration remained below 1000 °C. So that the capability of the methodology described earlier could be demonstrated, it was assumed that some SCG does occur between 800 and 1000 °C.

(2) Transient reliability without SCG for one-cycle thermal shock (fast fracture). Of course, since in this analysis no SCG damage takes place during the load history, multiple-cycle thermal shock analysis would yield the same failure probability as it would that for one cycle.

(3) Transient reliability with SCG after five cycles of repeated quenching. In this analysis, reversible behavior was assumed. In other words, the Weibull modulus was assumed to vary with the temperature as cyclic quenching took place. The scale and SCG parameters were also allowed to vary with temperature during the five-cycle thermal fatigue load history.

Figures 30 to 33 display the transient P_f based on volume flaw analysis, internal surface flaw analysis, external surface flaw analysis, and total surface flaw analysis (for both the internal and external surfaces), respectively. The transient reliability analysis was performed by dividing the stress history into six time steps and assuming the stress and temperature within each time step would remain constant. These figures include the results for all three types of analyses just outlined. Obviously, the five cycles of tube-quenching fatigue analysis span over 50 s rather than the 10 s shown in these plots. However, for plot clarity and comparison to the P_f after one cycle, the P_f at the end of the five-cycle quench period was plotted arbitrarily to the right of 10 s.

It can be seen from figures 30 to 33 that, with the exception of external surface analysis, the probabilities of failure based on fast fracture (no SCG) and time-dependent behavior (with SCG) after one and five cycles were essentially equal and ranged between 92- and 95-percent probability of failure. Initially, 14 tubes were tested experimentally and three were found to be damaged after one quench cycle, resulting in $P_f = 3/14 = 21.4$ percent. Then, another set of 11 pristine tubes were tested, and six were found to be damaged after five quench cycles, resulting in $P_f = 6/11 = 54.5$ percent. As stated earlier, the AE study showed very little crack propagation within the last four cycles of the quench test. All damage either occurred in the first cycle or not at all. Hence, the results of the five-cycle test were the same as for a single-cycle test. The relatively large difference between the failure rates, the inherent scatter of flaws within SASC, and the seemingly low propensity for fatigue suggests that a greater number of tubes should be tested to accurately capture the failure rate for the tests conducted. Pooling the experimental results for the one- and five-cycle quench tests gives $P_f = 9/25 = 36.0$ percent.

Two potential sources of error could help explain why the failure probabilities were conservatively predicted compared with the experimental data: (1) heat transfer coefficients are notoriously difficult to measure, and hence, the absolute accuracy of the stress analysis would be in question, and (2) fractography of fractured tubes showed that the flaw population had a preferential orientation, which implies that the material strength was anisotropic. As previously mentioned, fractography indicated that the majority of failures were due to relatively large axial defects remaining from the extrusion process used to fabricate the tubes. The highest transient stresses were in the axial direction, as shown in figure 27. This means that the weakest material flaws were oriented parallel to the highest stresses. Hence, the weakest flaws could not fail from axial stresses. However, the transient reliability analysis did not take this orientation effect into account, and consequently, probably overpredicted the tube probability of failure. Note that specimen rupture data that tested the tube axial strength do not exist, and therefore, the degree of strength anisotropy is unknown.

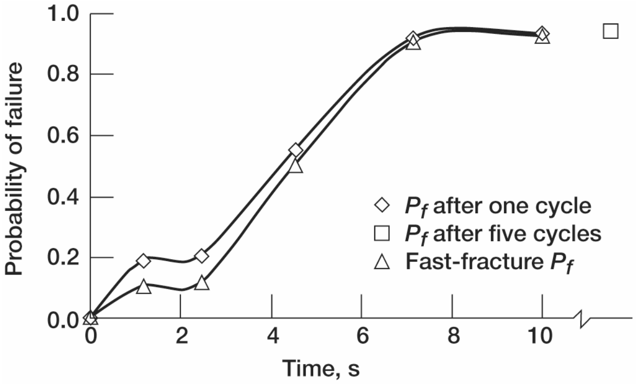

Figure 30.—Transient probability of failure, P_f, for thermally shocked Hexoloy tubes based on volume flaw analysis.

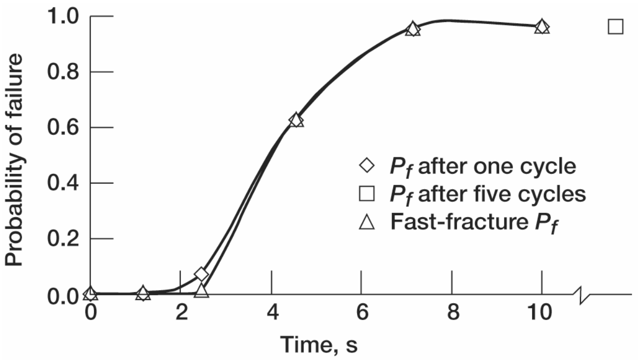

Figure 31.—Transient probability of failure, P_f, for thermally shocked Hexoloy tubes based on internal-surface flaw analysis.

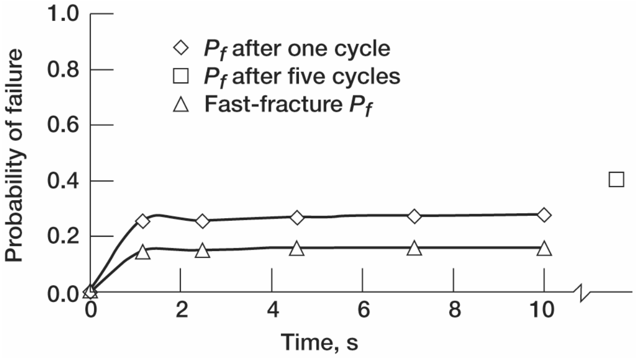

Figure 32.—Transient probability of failure, P_f, for thermally shocked Hexoloy tubes based on external-surface flaw analysis.

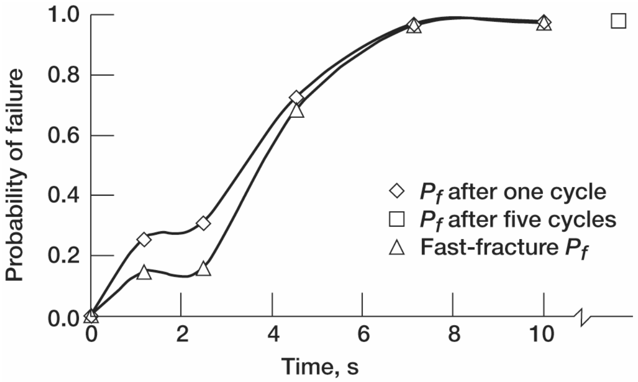

Figure 33.—Transient probability of failure, P_f, for thermally shocked Hexoloy tubes based on total-surface flaw analysis (for both the internal and external surfaces).

The effects of a global (hoop and axial) stress-reduction factor were examined to investigate the sensitivity of the predicted P_f to the variation in the stress (and strength) within the tube and the inverse heat-transfer analysis used to predict them. As can be seen from figure 34, a 10-percent reduction in stress magnitudes (corresponding to potential errors in the inverse heat transfer analysis and/or strength anisotropy) yielded a P_f of 55.3 percent, which matched the experimental observation for the five-cycle tube test. Given the potential for the material strength anisotropy and the degree of complexity for the inverse heat-transfer analysis to affect the accuracy of the predicted stresses, it can be argued that the predicted and measured probabilities of failure compare plausibly well.

As stated earlier, the transient reliability analysis for both volume and total surface area analyses showed no cyclic fatigue dependence after five quench cycles. There are mainly two reasons for that behavior. First, the Hexoloy material does not display significant SCG behavior below 1000 °C. In the current analysis, it was assumed that no SCG behavior occurred below 800 °C. Second, because of the rapid reduction in temperature after quenching and the short duration of the test cycle, the material was subjected to SCG conditions for only a few seconds, not long enough to induce significant SCG. So that this hypothesis could be tested, the transient failure probability of the quenched tube was computed as a function of the number of quench cycles. These computations were performed for stress levels reduced by 10 percent to reflect the 55-percent P_f measured after five quench cycles. Figure 35 shows how the transient P_f increased from 55 to 98 percent after 100 000 quench cycles when damage due to SCG was taken into account. Figure 35 also shows that when SCG was not taken into account, the P_f remained constant at 55 percent and did not increase with time. This indicates very clearly that, even for ceramics with minimal SCG behavior, ignoring the effect of crack propagation on the P_f could lead to premature failure and nonconservative designs.

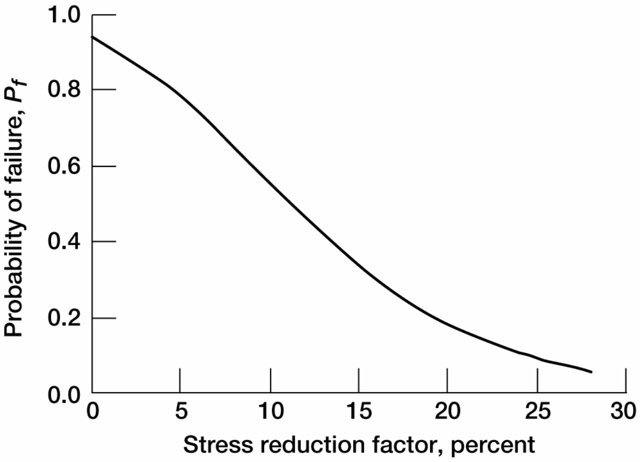

Figure 34.—Probability of failure versus stress reduction factor in Hexoloy tube quenched down from 1000 °C, based on volume flaw analysis.

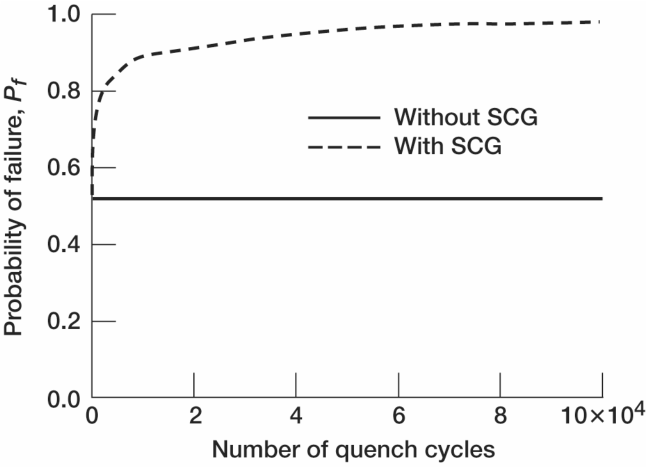

Figure 35.—Probability of failure, with and without SCG, as a function of the number of quench cycles in a thermally shocked Hexoloy tube.

4.0 Conclusions

A methodology for computing transient reliability in ceramic components subjected to fluctuating thermomechanical loading was developed and incorporated into the CARES/*Life* code. This enables CARES/*Life* to be used to predict component reliability for situations such as thermal shock, startup and shutdown conditions in heat engines, and cyclic loading. The methodology accounts for varying material response, whether due to temperature or environmental changes, by allowing Weibull and fatigue parameters to vary over the loading history. Examples demonstrating the viability of the technique for fast fracture, cyclic loading, and proof testing were presented.

Glenn Research Center
National Aeronautics and Space Administration
Cleveland, Ohio, September 17, 2004

Appendix A
Symbols

A	surface area
A_c	constant to fit experimental fatigue rupture data (eqs. (D193) and (D217))
A_d	constant to fit experimental dynamic fatigue rupture data (eq. (D205))
A_e	effective area (see app. D, section D.2.1.4, and eqs. (D70), (D71), and (D73) to (D75))
A_{ef}	modified effective area analogous to modified effective volume V_{ef} (see app. D, section D.2.2.3, and eqs. (D151), (D152), (D154), and (D155))
A_{elt}	area of an individual finite element (eqs. (D45) and (D113))
A_g	gauge area of a specimen (see section D.2.1.4; for example, the area of a tensile specimen under uniform uniaxial tension)
A_{isub}	area of an individual subelement
A_1	power-law crack-velocity parameter (eqs. (8) and (D93))
A_2	Walker-law crack-velocity parameter (eqs. (52), (55), and (D139))
A^2	Anderson-Darling goodness-of-fit test statistic (eq. (D90))
$\tilde{A}$	A_2/A_1 (eq. (E35))
$\mathcal{A}$, $\mathcal{B}$, $\mathcal{C}$	property sets (beginning of app. C)
a	crack half length; penny-shaped crack radius; radius of semicircular surface crack
$a(\Psi,t)$	crack length located at Ψ for time t
B	fatigue parameter; subcritical crack-growth parameter (eqs. (D98) and (D140))
B_B	subcritical crack-growth parameter for the Batdorf multiaxial equation (eq. (D150) and see app. D, section D.2.2.4)
B_{BS}	B_B for the surface-flaw failure mode
B_{BV}	B_B for the volume-flaw failure mode
B_{nw}	subcritical crack-growth parameter for the NSA criterion (see app. D, section D.2.2.4)
B_{nwS}	B_{nw} for the surface-flaw failure mode
B_{nwV}	B_{nw} for the volume-flaw failure mode
B_S	value of B for the surface-flaw failure mode
B_u	subcritical crack-growth parameter for specimen uniaxial Weibull distribution (eq. (D144) and see app. D, section D.2.2.4)
B_{uS}	B_u for the surface-flaw failure mode
B_{uV}	B_u for the volume-flaw failure mode

B_V	value of B for the volume-flaw failure mode
B_w	subcritical crack-growth parameter for uniaxial Weibull distribution (eq. (D145) and see app. D, section D.2.2.4)
B_{wS}	B_w for the surface-flaw failure mode
B_{wV}	B_w for the volume-flaw failure mode
$\bar{C}$	Shetty shear sensitivity constant; Shetty's constant in mixed-mode fracture criterion (eqs. (4), and (D30))
$\tilde{C}$	combined-law estimation parameter (eq. (E36))
c	the contour of a circle of unit radius in two-dimensional principal stress space (eq. (D37))
D	Kolmogorov-Smirnov goodness-of-fit test statistic defined as D^+ or D^-, whichever is the largest (eq. D89))
D^+, D^-	Kolmogorov-Smirnov goodness-of-fit test statistic (eq. D89))
det	determinant function
E	Young's modulus of elasticity; constant (see app. C)
e	scalar variable representing the random residual (eq. (E46))
$\exp(x)$	exponential function e^x
$F(\sigma_f)$	cumulative distribution function for argument σ_f (for example, see eqs. (D55) and (D89))
$F_n(\sigma_f)$	empirical distribution function for argument σ_f (eq. (D88))
$f(\alpha,\beta)$	function of the variables within the parentheses (for example, see eq. (D174))
f_c	cyclic frequency (in hertz); constant-amplitude frequency (eqs. (55) and (E1))
G	strain-energy release rate (eq. (D26))
G_c	critical strain-energy release rate (eq. (D26))
G_T	total strain-energy release rate (eq. (D26))
$G_{\mathrm{I}}, G_{\mathrm{II}}, G_{\mathrm{III}}$	strain-energy release rate for crack extension modes I, II, and III, respectively (eq. (D26))
g	g-factor (eqs. (57), (D130), (D133), (E6), and (E45), and table D.I)
H	Heaviside step function (examples include eqs. (82), (D19), (D43), (D238), and (E26))
h	total height of four-point bend bar with rectangular cross section (fig. D.4); base points or roots of Legendre polynominals (for example see eq. (D240))
$\mathbf{I}$	identity matrix (eq. (E51))
i	i^{th} value in a set (for example see eq. (D83))
$isub$	$isub^{th}$ value in a set of subelements (eqs. (21), (D34), (D46), (D106), and (D114))
$\mathbf{J}$	Jacobian operator, Jacobian matrix (eqs. (D33), (D45), (D105), and (D113))
$K(n)$	Kanofsky-Srinivasan confidence band factors (eq. (D91))
K_δ	dominant stress-intensity factor, either K_{II} or K_{III} (eq. (D30))

K_I	mode-I stress-intensity factor (eq. (1); also, for example, $K_\mathrm{I} = 1.366\sigma_n a^{1/2}$ (eq. (D54)) for a semicircular surface crack)
K_II	mode-II stress-intensity factor (for example $K_\mathrm{II} = 1.241\tau\, a^{1/2}$ (eq. (D54)) for a semicircular surface crack)
K_III	mode-III stress-intensity factor (for example $K_\mathrm{III} = 0.133\tau\, a^{1/2}$ (eq. (D54)) for a semicircular surface crack)
$K_{\mathrm{I}c}$	critical mode-I stress-intensity factor (fracture toughness)
$K_{\mathrm{I}eq}$	equivalent mode-I stress-intensity factor from applied multiaxial stress (eqs. (2) and (D92))
$\Delta K_{\mathrm{I}eq}(\Psi, n)$	range in equivalent mode-I stress-intensity factor for cycle n and location Ψ (eqs. (54) and (D139))
$K_{\mathrm{I}eq}(\Psi, t)$	equivalent mode-I stress-intensity factor at time t and location Ψ (eqs. (2), (D92), and (E4))
$K_{\mathrm{I}eq,\max}(\Psi, t)$	maximum mode-I equivalent stress-intensity factor over the load history (eqs. (53), (D139), and (E3))
$K_{\mathrm{I}eqc}(\Psi, t)$	critical equivalent mode-I stress-intensity factor from applied multiaxial stress at time t and location Ψ (eqs. (3) and (D95))
$K_{\mathrm{I}eqg}(\Psi, t)$	equivalent mode-I stress intensity factor associated with a g-factor for cyclic loading at time t and location Ψ (eqs. (E1), (E2), (E5), and (E6))
k	integer counter; number of time steps within (for example, see eq. (42))
k_B	Batdorf crack-density coefficient (eqs. (D18), (D42), and (E24))
k_{BS}	k_B for the surface-flaw failure mode
k_{BV}	k_B for the volume-flaw failure mode
k_w	Weibull crack-density coefficient (eqs. (D8) and (D35))
k_{wp}	Weibull polyaxial crack-density coefficient (eqs. (D11), (D12), (D37), (D38), and (E24))
k_{wpS}	k_{wp} for the surface-flaw failure mode
k_{wpV}	k_{wp} for the volume-flaw failure mode
k_{wS}	k_w for the surface-flaw failure mode
k_{wV}	k_w for the volume-flaw failure mode
$\bar{k}_B$	normalized Batdorf crack-density coefficient (eqs. (D63) and (D76))
$\bar{k}_{BS}$	$\bar{k}_B$ for the surface-flaw failure mode
$\bar{k}_{BV}$	$\bar{k}_B$ for the volume-flaw failure mode
L	likelihood function (eq. (D85))
L_1	length between outer loads in four-point bending (fig. D.4)
L_2	length between symmetrically applied inner loads in four-point bending (fig. D.4)
ln	natural logarithm

ℓ, m, n	direction cosines of normal to oblique plane in principal stress space for the Cauchy infinitesimal tetrahedron (figs. D.2, D.3, and D.6; and eqs. (D21) to (D23), (D47), (D48), (D101), and (D102))
MD	median deviation (see app. D, section D.2.2.5, and eqs. (D197), (D198), (D209), (D210), (D221), and (D222))
m	fast-fracture (inert strength) Weibull modulus (scatter parameter) (shape parameter) (eq. (D7))
m_S	m for the surface-flaw failure mode
m_V	m for the volume-flaw failure mode
$\tilde{m}$	time-dependent Weibull modulus (eq. (D144))
$\tilde{m}_S$	$\tilde{m}$ for the surface-flaw failure mode
$\tilde{m}_V$	$\tilde{m}$ for the volume-flaw failure mode
m'	estimated fast-fracture Weibull modulus estimated from fatigue data (eq. (D201))
m'_S	m' for the surface-flaw failure mode
m'_V	m' for the volume-flaw failure mode
N	crack-velocity exponent (for power law, eqs. (8) and (D93), and for Walker law, eq. (D139))
N_S	N for the surface-flaw failure mode
N_V	N for the volume-flaw failure mode
N_1, N_2	crack-velocity exponents for power law and Walker law, respectively, when both laws are superposed (eqs. (56) and (E1))
n	integer counter; total number of values in a set (for example, the total number of fractured specimens as shown in eq. (D83)); also, the number of loading cycles (for example, see eqs. (52) to (55) and (D139))
n_f	number of cycles to failure (eqs. (D158) and (D216))
n_{fin}	final number of cycles (eq. (65))
n_{gp}	number of gaussian integration points (for example, see eq. (D240))
n_{int}	initial number of cycles (eq. (65))
n_o	cycle-dependent scale parameter (eq. (D160))
n_{sub}	total number of subelements (eqs. (21), (D34), (D46), (D106), and (D114))
$n_{T,i}$	transformed i^{th} data number of cycles to failure at applied maximum (within the cycle) transformed stress level σ_T (eq. (D219))
$n_{T,0.50}$	the value of n_T when $P_f = 0.50$ (eq. (D221))
n_θ	characteristic number of cycles (eq. (D158))
$n_{\theta ST}$	$n_{\theta T}$ for the surface-flaw failure mode

$n_{\theta T}$	characteristic number of cycles at applied maximum (within the cycle) transformed stress level σ_T (eq. (D220))
$n_{\theta VT}$	$n_{\theta T}$ for the volume-flaw failure mode
$P(X=x)$	probability random variable X equals the value x (eq. (D3))
P_f	probability of failure ($P_f = 1 - P_s$)
ΔP_f	incremental probability of failure (eq. (D13))
$P_f(t)$	probability of failure at time t
$P_f(t_p)$	probability of failure from proof test at time t_p (eq. (D228))
$P_f(t_q)$	probability of failure from proof-test and service load at time t_q (eq. (D228))
$P_{fa}(t_q)$	attenuated probability of failure from proof-test and service load at time t_q (eqs. (72) and (D228))
$P_{faS}(t_q)$	$P_{fa}(t_q)$ for the surface-flaw failure mode
$P_{faV}(t_q)$	$P_{fa}(t_q)$ for the volume-flaw failure mode
$P_{f,i}$	ranked probability of failure for the i^{th} specimen (for example, see eqs. (D83) and (D198))
$P_{f,\mathrm{mean}}$	mean probability of failure (eq. (E44))
P_{fS}	P_f for the surface-flaw failure mode
ΔP_{fS}	ΔP_f for the surface-flaw failure mode
$P_{fS}(t)$	$P_f(t)$ for the surface-flaw failure mode
$P_{fS}(t_p)$	$P_f(t_p)$ for the surface-flaw failure mode
$P_{fS}(t_q)$	$P_f(t_q)$ for the surface-flaw failure mode
P_{fV}	P_f for the volume-flaw failure mode
ΔP_{fV}	ΔP_f for the volume-flaw failure mode
$P_{fV}(t)$	$P_f(t)$ for the volume-flaw failure mode
$P_{fV}(t_p)$	$P_f(t_p)$ for the volume-flaw failure mode
$P_{fV}(t_q)$	$P_f(t_q)$ for the volume-flaw failure mode
P_s	reliability or probability of survival ($P_s = 1 - P_f$)
$P_s(t)$	probability of survival at time t
$P_s(t_p)$	probability of survival from proof test at time t_p (eq. (72))
$P_s(t_q)$	probability of survival from proof-test and service load at time t_q (eq. (72))
$P_{sa}(t_q)$	attenuated probability of survival from proof-test and service load at time t_q (eq. (72))
$P_{saS}(t_q)$	$P_{sa}(t_q)$ for the surface-flaw failure mode
$P_{saV}(t_q)$	$P_{sa}(t_q)$ for the volume-flaw failure mode

P_{sS}	P_s for the surface-flaw failure mode
$P_{sS}(t)$	$P_s(t)$ for the surface-flaw failure mode
$P_{sS}(t_p)$	$P_s(t_p)$ for the surface-flaw failure mode
$P_{sS}(t_q)$	$P_s(t_q)$ for the surface-flaw failure mode
P_{sV}	P_s for the volume-flaw failure mode
$P_{sV}(t)$	$P_s(t)$ for the volume-flaw failure mode
$P_{sV}(t_p)$	$P_s(t_p)$ for the volume-flaw failure mode
$P_{sV}(t_q)$	$P_s(t_q)$ for the volume-flaw failure mode
ΔP_1	probability of existence of a crack with strength (or critical stress) between $\sigma_{\mathrm{I}eqc}$ and $\sigma_{\mathrm{I}eqc} + \Delta\sigma_{\mathrm{I}eqc}$ in an incremental volume or area (eqs. (D13), (D14), and (D40))
ΔP_{1S}	ΔP_1 for the surface-flaw failure mode
ΔP_{1V}	ΔP_1 for the volume-flaw failure mode
P_2	probability of a crack with strength $\sigma_{\mathrm{I}eqc}$ being so oriented that $\sigma_{\mathrm{I}eq} \geq \sigma_{\mathrm{I}eqc}$ (eqs. (D13), (D15), and (D41))
P_{2S}	P_2 for the surface-flaw failure mode
P_{2V}	P_2 for the volume-flaw failure mode
p	success probability (see paragraph above eq. (D4))
Q	Walker-law R-ratio sensitivity exponent (eqs. (52), (D139), and (E1))
$R(\Psi)$	R-ratio (ratio of minimum stress divided by maximum cyclic stress) at location Ψ where the R-ratio is assumed to be constant with time or cycles (eq. (E8))
$R(\Psi, n)$	R-ratio (ratio of minimum stress divided by maximum cyclic stress) at n cycles and location Ψ (eq. (D140))
$R(\Psi, t)$	R-ratio (ratio of minimum stress divided by maximum cyclic stress) at time t and location Ψ (eq. (59))
ROR	risk-of-rupture (eq. (D6))
r	number of remaining specimens in censored data analysis (eq. (D87))
r, s, t	finite element natural coordinates (eqs. (D33), (D45), (D105), and (D113))
$\mathbf{s}_c$	term in modified Levenberg-Marquardt algorithm (eqs. (E50) and (E51))
T	temperature
t	time
$\Delta t_{eq,j}$	equivalent (incremental) time for time step j including fatigue effects (eq. (69))
Δt_{es}	equivalent (incremental) time for an equivalent applied static stress (eqs. (D134) and (D135))
t_f	time to failure (eq. (D144)
$t_{f,i}$	i^{th} specimen time to failure (eqs. (D195) and (D207))

t_{fin}	final time
t_{int}	initial time
Δt_j	duration of time step j
t_{min}	service time after proof test before which no failure should occur (eq. (D235))
$t_{\mathrm{min},1,es}$	effective service time after proof test where no failure should occur for an applied static stress of $\sigma_{\mathrm{I}eq,1,T\mathrm{max},p}$ based on the properties of time step 1 (eqs. (91), (95), and (96))
t_o	time-dependent scale parameter (eqs. (D146), (D148), (D150), and (E32))
t_{od}	time-dependent scale parameter for dynamic fatigue (eq. (D157))
t_{odS}	t_{od} for the surface-flaw failure mode
t_{odV}	t_{od} for the volume-flaw failure mode
t_{oS}	t_o for the surface-flaw failure mode
t_{oV}	t_o for the volume-flaw failure mode
t_p	proof-test time (eqs. (72) and (D228))
$t_{p,1,es}$	effective proof-test time for an applied static stress of $\sigma_{\mathrm{I}eq,1,T\mathrm{max},p}$ based on the properties of time step 1 (see section 2.6 and eqs. (82), (88), and (92))
t_{per}	period of the cycle (eq. (D128))
t_q	total combined time in proof testing and service (eqs. (72) and (D228))
$t_{q,1,es}$	effective time for an applied static stress of $\sigma_{\mathrm{I}eq,1,T\mathrm{max},p}$ based on the properties of time step 1 for all time steps (service and proof test) (see section 2.6 and eq. (94))
$t_{T,i}$	transformed i^{th} specimen failure time at applied stress level σ_T (eqs. (D195) and (D207))
$t_{T,0.5}$	calculated value of t_T when $P_f = 0.50$ (eq. (D197))
t_ε	time in service (see section 2.6)
$t_{\varepsilon,1,es}$	effective service time for an applied static stress of $\sigma_{\mathrm{I}eq,1,T\mathrm{max},\varepsilon}$ based on the properties of time step 1 (see fig. 5 and section 2.6)
t_θ	characteristic time (eqs. (D144) and (D148))
$t_{\theta d}$	characteristic time for dynamic fatigue (eq. (D156))
$t_{\theta dS}$	$t_{\theta d}$ for the surface-flaw failure mode
$t_{\theta dST}$	$t_{\theta dT}$ for the surface-flaw failure mode
$t_{\theta dT}$	characteristic time for transformed applied stress rate (eq. (D208))
$t_{\theta dV}$	$t_{\theta d}$ for the volume-flaw failure mode
$t_{\theta dVT}$	$t_{\theta dT}$ for the volume-flaw failure mode
$t_{\theta S}$	t_θ for the surface-flaw failure mode

$t_{\theta ST}$	$t_{\theta T}$ for the surface-flaw failure mode
$t_{\theta T}$	characteristic time for transformed applied stress level (eq. (D196))
$t_{\theta V}$	t_{θ} for the volume-flaw failure mode
$t_{\theta VT}$	$t_{\theta T}$ for the volume-flaw failure mode
U_j	fatigue effect multiplier (eqs. (68) and (69))
V	volume
V_e	effective volume (see app. D, section D.2.1.4, and eqs. (D56) to (D58) and (D60) to (D62))
V_{ef}	modified effective volume (see app. D, section D.2.2.3, and eqs. (D146) to (D150), (E31), and (E33))
V_{elt}	volume of an individual finite element (eqs. (D33) and (D105))
V_{isub}	volume of an individual subelement
V_g	gauge volume of a specimen (see section D.2.1.4; for example, the volume of a tensile specimen under uniform uniaxial tension)
w	total width of four-point bend bar with rectangular cross section (after eq. (D59)); gaussian weight function (for example, see eq. (D240))
X	discrete real-valued random variable (eq. (D3))
X_1	transient reliability term; for example, see equations (33), (40), and (42)
X_{1p}	value of X_1 for proof test (eqs. (76) and (77))
X_{1q}	value of X_1 for combined proof test and service load condition (eqs. (79) and (80))
x	specific value of X (eq. (D3)); any variable (for example, see eq. (46))
x, y, z	location in the body of the structure; Cartesian coordinate directions
$\mathbf{x}$	k-dimensional vector of independent variables (eq. (E46))
Y	crack geometry correction factor or shape factor (eqs. (1), (D92), and (E2) to (E4))
y	$h/2$ (see fig. D.4 and eq. (D59)); scalar response or dependent variable (eq. (E46)); any variable (for example, see eq. (46))
Z	number of load cycles—a load cycle could consist of a collection of cycles with various amplitudes, peak loads, frequencies, wave forms, and other parameters. Z is associated with the power-law model for crack growth.
$Z_{\varepsilon,\mathrm{total}}$	total number of service load cycles (see section 2.6 and eq. (74))
$Z_{p,\mathrm{total}}$	total number of proof-test load cycles (see section 2.6 and eq. (73))
α	angle between σ_n and the stress σ_1 (or σ_x) on a unit radius sphere (figs. D.2 and D.6) or unit radius circle (fig. D.3)
(α, β)	arguments or function of orientation angles of a flaw (figs. D.2, D.3, and D.6)
β	angle between the σ_n projection and the stress σ_2 (or σ_y) in a plane perpendicular to σ_1 (or σ_x); azimuthal angle on the unit radius sphere (figs. D.2 and D.6)

Γ	gamma function
γ	total number of load blocks (see section 2.6 and eq. (74))
δ	applied load (fig. D.4); counter (eq. (74))
δ_c	step bound (app. E2)
Σ	summation function; applied multiaxial stress state (for example, see eq. (D13))
ζ	ζ–κ number of time steps in a service load cycle (see section 2.6 and eqs. (80) and (81))
$\eta(\sigma)$	Weibull crack-density function (eq. (D2)); number of flaws per unit volume or area with strength $\leq \sigma$
$\eta(\sigma_{\mathrm{I}eqc})$	Batdorf crack-density function (eqs. (D18) and (D42)); number of flaws per unit volume or area with strength $\leq \sigma_{\mathrm{I}eqc}$
$\eta_S(\sigma)$	$\eta(\sigma)$ for surface-distributed flaws
$\eta_S(\sigma_{\mathrm{I}eqc})$	$\eta(\sigma_{\mathrm{I}eqc})$ for surface-distributed flaws
$\eta_V(\sigma)$	$\eta(\sigma)$ for volume-distributed flaws
$\eta_V(\sigma_{\mathrm{I}eqc})$	$\eta(\sigma_{\mathrm{I}eqc})$ for volume-distributed flaws
$\boldsymbol{\theta}$	vector of regression parameters (eq. (E46))
$\boldsymbol{\theta}_c$	current estimate of vector $\boldsymbol{\theta}$ (eq. (E50))
$\boldsymbol{\theta}_n$	new estimate of vector $\boldsymbol{\theta}$ (eq. (E50))
κ	number of proof-test time steps in the first cycle of loading (see section 2.6 and eqs. (76) and (77))
λ	number of load blocks (for example, see eq. (48)); argument in Poisson distribution (eq. (D3))
μ	term in binomial series expansion (eq. (46))
μ_c	scalar control variable (eq. (E51))
ν	material Poisson's ratio
ξ	total number of time steps (see app. C)
ρ	integer smaller than i (see eq. (C23))
σ	applied uniaxial stress (for example, see eq. (D9))
$\sigma(t)$	far-field uniaxial stress applied normal to a crack at time t
$\sigma_{ch}(\Psi)$	characteristic value $\sigma_{\mathrm{I}eq}(\Psi,t)$ located at Ψ (eqs. (D127) and (D129))
σ_f	value of the peak stress in a component at failure (determined from experimental rupture data of simple specimen geometries such as flexure specimens or tensile specimens). Used to characterize the Weibull parameters m and σ_θ from the experimental rupture data of simple specimens (eq. (D55))
$\sigma_{f,i}$	i^{th} ranked value of n specimens of σ_f (for example, see eq. (D83)); applied stress level associated with the i^{th} failed specimen with failure time $t_{f,i}$ (eq. (D195))

$\sigma_{f,0}$	specimen fracture stress σ_f at time t transformed back to $t = 0$ (eq. (D144))
$\sigma_{f\mathrm{I},i}$	i^{th} transformed fast-fracture (inert) strength of the specimen (eq. (D203))
$\sigma_{i,0}$	i^{th} principal stress ($i = 1$, 2, or 3) applied at time t transformed back to $t = 0$ (eq. (D104))
$\sigma_{iq,0}(x, y, z)$	i^{th} principal far-field stress (for $i = 1, 2, 3$) at location x, y, z transformed to time $t = 0$ from the combined effect of the static applied multiaxial proof-test load to time t_p and the static applied multiaxial service load from time t_p until time t_q (eq. (D233))
σ_n	applied far-field stress component normal to a crack face (figs. D.2, D.3, and D.6; eqs. (D11), (D22), (D48), (D101), and (D109))
$\sigma_{n,0}(\Psi)$	normal stress σ_n located at Ψ transformed to $t = 0$. This symbol is associated with the NSA method (see app. D, section D.2.2.4, and explanation for eq. (D182))
$\sigma_{np}(\Psi)$	applied far-field static proof-test stress component normal to a crack face until time t_p and located at Ψ (eq. (D231))
$\sigma_{np,0}(\Psi)$	applied far-field static proof-test stress component normal to a crack face until time t_p and located at Ψ that is transformed to time $t = 0$ (eq. (D231))
$\sigma_{nq,0}(\Psi)$	applied far-field static normal stress located at Ψ transformed to time $t = 0$ from the combined effect of proof-test and service loading. The static proof-test load is applied until time t_p and the static service load is applied from time t_p until time t_q (eq. (D234)
σ_o	Weibull scale parameter (eqs. (D7), (D35), (D58), and (D71))
$\sigma_{oB,j}$	Weibull scale parameter for time step j incorporating the effect of $\bar{k}_B$ (for example, see eq. (28))
$\sigma_{oBS,j}$	$\sigma_{oB,j}$ for the surface-flaw failure mode
$\sigma_{oBV,j}$	$\sigma_{oB,j}$ for the volume-flaw failure mode
σ_{oS}	Weibull scale parameter for the surface-flaw failure mode
σ_{oV}	Weibull scale parameter for the volume-flaw failure mode
σ_T	specified level of stress for which equivalent failure times are computed (eqs. (D195) and (D219))
σ_u	threshold stress (strength) parameter (eq. (D7))
σ_{uS}	σ_u for the surface-flaw failure mode
σ_{uV}	σ_u for the volume-flaw failure mode
σ_x, σ_y, σ_z	global coordinate system tensile/compressive stress components (fig. D.6, and eqs. (D101) and (D102))
σ_1, σ_2, σ_3	principal stresses ($\sigma_1 \geq \sigma_2 \geq \sigma_3$)
$\sigma_{1,\,\max}(\Psi)$	maximum principal stress within the cycle located at Ψ (eq. (E33)); eq. (D145) shows Ψ as x, y, z

$\sigma_{1,0}(\Psi)$	1st principal stress or applied uniaxial stress at time t transformed back to $t = 0$ located at Ψ (eq. (E30); eq. (D145) shows Ψ as x, y, z
$\sigma_{1q,0}(x, y, z)$	see $\sigma_{iq,0}(x, y, z)$ for $i = 1$: the first principal stress
$\sigma_{2q,\,0}(x, y, z)$	see $\sigma_{iq,\,0}(x, y, z)$ for $i = 2$: the second principal stress
$\sigma_{3q,\,0}(x, y, z)$	see $\sigma_{iq,\,0}(x, y, z)$ for $i = 3$: the third principal stress
$\sigma_{\mathrm{I}eq}$	equivalent (or effective) mode-I far-field stress on a crack from applied multiaxial stress that results in modes I, II, and III crack surface displacements
$\sigma_{\mathrm{I}eq}(\Psi,\mathrm{t})$	equivalent mode-I far-field stress on a crack from applied multiaxial stress at time t and location Ψ
$\sigma_{\mathrm{I}eq,j}$	equivalent mode-I far-field stress during time step j
$\sigma_{\mathrm{I}eq,j,k}$	transformed stress during time step j using the material properties of time step k (eq. (44))
$\sigma_{\mathrm{I}eq,k,T\mathrm{max}}$	maximum transformed stress over k time steps (using the properties of step k) (eq. (43))
$\sigma_{\mathrm{I}eq,\mathrm{max}}$	maximum value of $\sigma_{\mathrm{I}eq}$ for all values of Ψ (eqs. (D16), (D17), and (D39))
$\sigma_{\mathrm{I}eq,\mathrm{max}}(\Psi)$	maximum equivalent (effective) mode-I far-field stress over a defined time interval or number of cycles located at Ψ (mean stress and amplitude assumed to be constant over time or cycles) (eqs. (D131), (E3), and (E4))
$\sigma_{\mathrm{I}eq,\mathrm{max}}(\Psi,(n \text{ or } t))$	maximum equivalent (effective) mode-I far-field stress over a particular loading cycle or at a defined time (over the period of the cycle at that time) located at Ψ (eqs. (53), (54), and (D139))
$\sigma_{\mathrm{I}eq,\mathrm{min}}(\Psi)$	minimum equivalent (effective) mode-I far-field stress over a defined time interval or number of cycles located at Ψ (mean stress and amplitude assumed to be constant over time or cycles) (eq. (E4))
$\sigma_{\mathrm{I}eq,\mathrm{min}}(\Psi,(n \text{ or } t))$	minimum equivalent (effective) mode-I far-field stress over a particular loading cycle or at a defined time (over the period of the cycle at that time) located at Ψ (eqs. (54) and (D139))
$\sigma_{\mathrm{I}eq,\zeta,T\mathrm{max}}$	maximum transformed stress over ζ time steps (using the properties of step ζ) for the proof-test and service load time steps (see section 2.6 and eqs. (79) and (80))
$\sigma_{\mathrm{I}eq,\kappa,T\mathrm{max}}$	maximum transformed stress over κ steps (using the properties of step κ) for the proof test (see section 2.6 and eqs. (76), (77), and (83))
$\sigma_{\mathrm{I}eq,0}(\Psi)$	equivalent mode-I far-field strength of a flaw located at Ψ transformed to $t = 0$. This can also be considered as a transformed equivalent stress to $t = 0$ located at Ψ (for example, see eqs. (19), (D97), and (E15))
$\sigma_{\mathrm{I}eq,0,\mathrm{max}}$	maximum value of $\sigma_{\mathrm{I}eq,0}$ for all values of Ψ (eq. (E23))
$\sigma_{\mathrm{I}eq,1,T\mathrm{max},p}$	maximum transformed stress over the proof-test time steps (using the properties of step 1) (see section 2.6 and eq. (84))
$\sigma_{\mathrm{I}eq,1,T\mathrm{max},\varepsilon}$	maximum transformed stress over the service load time steps (using the properties of step 1) (see section 2.6 and eq. (86))

$\sigma_{\mathrm{I}eqc}$	equivalent mode-I far-field strength of a flaw; equivalent (or effective) critical mode-I stress of a flaw—$\sigma_{\mathrm{I}eqc}$ is the threshold value of $\sigma_{\mathrm{I}eq}$ where unstable catastrophic crack growth occurs (eq. (D13))
$\sigma_{\mathrm{I}eqc}(\Psi, t)$	equivalent critical stress $\sigma_{\mathrm{I}eqc}$ at time t and located at Ψ (for example, see eqs. (3), (D95), and (E9))
$\sigma_{\mathrm{I}eqc,j}(t)$	equivalent mode-I far-field strength of a flaw at some time t that occurs over the interval of time step j ($t_{j-1} < t \leq t_j$) (for example, see eqs. (25), (26), (28), and (37))
$\sigma_{\mathrm{I}eqg}$	far-field equivalent static stress (eqs. (D127) to (D129), (D131), and (E5))
$\sigma_{\mathrm{I}eqp}(\Psi)$	equivalent mode-I far-field stress on a crack from the static applied multiaxial proof-test load to time t_p at location Ψ (eq. (D229))
$\sigma_{\mathrm{I}eqp,0}(\Psi)$	equivalent mode-I far-field stress on a crack from the static applied multiaxial proof-test load to time t_p at location Ψ transformed to time $t = 0$ (eq. (D229)
$\sigma_{\mathrm{I}eqq,0}(\Psi)$	equivalent mode-I far-field stress at location Ψ and transformed to time $t = 0$ on a crack from the combined effect of the static applied multiaxial proof-test load to time t_p and the static applied multiaxial service load from time t_p until time t_q (eq. (D232)
σ_θ	Weibull fast-fracture (inert strength) characteristic strength—the value of σ_f where 63.21 percent of experimental rupture specimens fail; it is determined from the regression of experimental rupture data of simple specimen geometries, such as flexure specimens or tensile specimens, by using the Weibull distribution (eq. (D55))
$\sigma_{\theta S}$	σ_θ for the surface-flaw failure mode
$\sigma_{\theta V}$	σ_θ for the volume-flaw failure mode
$\overline{\sigma}_n$	average normal stress (eqs. (D11) and (D37)); this symbol is associated with the NSA method
$\overline{\sigma}_{np,0}(x,y,z)$	averaged normal proof-test stress transformed to time $t = 0$ (eq. (D231))
$\overline{\sigma}_{nq,0}(x,y,z)$	averaged normal test stress transformed to time $t = 0$ from the combined effect of the proof-test and service load (eq. (D234))
σ'_θ	Weibull fast-fracture (inert strength) characteristic strength σ_θ estimated from fatigue data (eq. (D202))
$\sigma'_{\theta S}$	σ'_θ for the surface-flaw failure mode
$\sigma'_{\theta V}$	σ'_θ for the volume-flaw failure mode
$\dot{\sigma}$	applied constant uniaxial stress rate (eq. (D120))
$\dot{\sigma}_f$	stress rate at the point of maximum stress σ_f (eq. (D156))
$\dot{\sigma}_i$	applied stress rate associated with the i^{th} failed specimen with fracture time $t_{f,i}$ (eq. (D207))
$\dot{\sigma}_T$	specified level of stress rate for which equivalent failure times are computed (eq. (D207))

τ	applied far-field shear stress on a crack face; shear stress acting on the oblique plane whose normal is determined by angles α and β (figs. D.2, D.3, and D.6; and eqs. (D23), (D49), (D102), and (D110))
τ_{xy}, τ_{yz}, τ_{zx}	global coordinate system shear stress components (fig. D.6, and eqs. (D101) and (D102))
Ψ	represents a location (x, y, z) and (for the Batdorf method) a crack orientation (α, β); vector representing the location and/or orientation of the crack (see eq. (D92) for further explanation)
Ψ_0	spatial coordinates of Ψ where σ_f occurs (eq. (D144))
Ω	solid angle in three-dimensional stress space for which $\sigma_{\mathrm{I}eq} \geq \sigma_{\mathrm{I}eqc}$ (eq. (D15); area of a solid angle projected onto a unit radius sphere in a stress space containing all crack orientations for which the effective stress is greater than or equal to the critical equivalent mode-I strength $\sigma_{\mathrm{I}eqc}$ (eq. (E25))
$d\Omega$	$\sin \alpha \, d\alpha \, d\beta$ (incremental area on the surface of a unit radius sphere) where $\sigma_{\mathrm{I}eq} \geq \sigma_{\mathrm{I}eqc}$ (figs. D.2 and D.6)
$\Omega(\Sigma,\sigma_{\mathrm{I}eqc})$	Ω for applied multiaxial stress state Σ and critical stress $\sigma_{\mathrm{I}eqc}$
ω	arc length of an angle α projected onto a unit radius semicircle in stress space containing all the crack orientations for which $\sigma_{\mathrm{I}eq} \geq \sigma_{\mathrm{I}eqc}$ (eqs. (D39) and (D41)))

Subscripts

a	attenuated quantity (for example, see P_{fa}); applied or service load
B	Batdorf (for example, see $\bar{k}_B$); Batdorf
c	critical (for example, see $\sigma_{\mathrm{I}eqc}$); parameter (for example, see A_c)
ch	characteristic
d	dynamic fatigue
e	effective
ef	modified effective
elt	element (eq. (D113))
eq	equivalent (for example, see $\sigma_{\mathrm{I}eq}$)
es	equivalent static (for example, see t_{es})
f	failure or fracture (for example, see σ_f or P_f)
fin	final (for example, see t_{fin})
g	gauge
i	i^{th} value or i^{th} term
i, j, k	subscript for time step number ($i \leq j \leq k$); i^{th} value, j^{th} value, k^{th} value

int	initial (for example, see t_{int})
$isub$	individual subelement
max	maximum (for example, see $\sigma_{\mathrm{I}eq,\max}$)
min	minimum (for example, see $\sigma_{\mathrm{I}eq,\min}$)
n	normal stress (see σ_n); n^{th} value
o	scale parameter
p	proof test (for example, see t_p); polyaxial (for example, see k_{wpV})
q	combined proof-test and service load (for example, see t_q)
S	surface-based property
s	survival (for example, see P_s)
T	transformed value (for example, see $\sigma_{\mathrm{I}eq,k,T\max}$)
u	uniaxial; threshold
V	volume or a volume-based property (e.g., indicates volume-flaw analysis); volume (eqs. (D1), (D2), (D4) to (D18), (D20), (D34), (D56) to (D58), etc.)
w	Weibull
x	x coordinate direction
θ	characteristic (for example, see σ_θ)
0	value transformed to $t = 0$
I	mode I—crack opening mode (for example, see K_{I})
II	mode II—crack sliding mode (for example, see K_{II})
III	mode III—crack tearing mode (for example, see K_{III})

Superscripts

T	matrix transpose operation (eq. (E51))
·	rate (eq. (D120))
′	inert distribution parameter estimated from fatigue data (eqs. (D202), (D203), (D213) to (D215), and (D225) to (D227))
^	estimated parameter (eqs. (D86) and (D87))
~	modified parameter (eqs. (D144), (D147), (D149) to (D156), etc.)
–	normalized quantity (for example, see $\bar{k}_B$ and eq. (D62))

Definitions

Batdorf	component reliability model using the Weibull distribution and fracture mechanics principles to account for the effect of multiaxial stress states on reliability (see app. D) from Nemeth et al., 2003; Batdorf and Crose, 1974; and Batdorf and Heinisch, 1978a, for details)
extreme fiber stress	the location (point) in the body of the component where the stress is maximum (see σ_f)
fast-fracture	component rupture in the absence of SCG where strength is strictly controlled by the fracture toughness and the size, distribution, and orientation of inherent flaws (app. D from Nemeth et al., 2003).
mode I	crack opening mode
mode II	crack sliding mode (in-plane shear)
mode III	crack tearing mode (out-of-plane shear)
R-curve	where fracture toughness $K_{\mathrm{I}c}$ varies with crack size—typically increasing with crack size (see Broek, 1982, for introductory information)
transient reliability analysis	predicting the probability of survival of a component while accounting for loads and temperatures that can vary over time
Weibull distribution	see equation (16) and Weibull (1939a and 1939b)

Acronyms and Initialisms

AD	Anderson Darling (goodness-of-fit statistic) (eq. (D90))
CARES	Ceramics Analysis and Reliability Evaluation of Structures
EDF	empirical distribution function (eq. (D88))
FEA	finite element analysis
KS	Kolmogorov-Smirnov (goodness-of-fit statistic) (eqs. (D88) and (D89))
LEFM	linear elastic fracture mechanics
MEMS	microelectromechanical systems
MLE	maximum likelihood estimate
MOR	modulus of rupture
NDE	nondestructive evaluation
NSA	normal stress averaging (Weibull, 1939a, and eqs. (D11) and (D37))
PIA	principle of independent action—a component reliability model based on the Weibull distribution that accounts for multiaxial stress states by using principal stresses applied independently of one another (see app. D from Nemeth et al., 2003; Barnett et al., 1967; and Freudenthal, 1968)

SASC	form of silicon carbide made by Carborundum
SCG	slow crack growth
SIF	stress intensity factor
SL	significance level

Appendix B
Numerical Method for Transient Reliability Analysis (Weibull Technique for a Simple Uniaxial Stress State)

The numerical algorithm for transient reliability analysis follows for an applied uniform uniaxial tensile stress and a unit volume (or area). Because of its relative simplicity, the Weibull methodology (see eq. (16)) for an incremental volume under a uniform uniaxial stress state that varies over time and that is described with *k* discrete time steps is shown here for illustration purposes. The Batdorf methodology (for transient reliability analysis) is similar except for the additional complexity of accounting for the orientation of the flaw.

B.1 Initialize the Numerical Algorithm (for the last time step, *k*)

$$m_{k+1} = m_k \qquad N_{k+1} = 3 \qquad X_{k+1} = \frac{\sigma_{k,T\,\max}}{\sigma_{o,k}} \tag{B1}$$

B.2 Do-Loop Algorithm

Do *i* = (*k* + 1), 2, –1 (increment in decreasing order from (*k* + 1) to 2), where *k* is the total number of time steps)

$$X_{i-1} = X_i^{\frac{m_i(N_{i-1}-2)}{m_{i-1}(N_i-2)}} + \frac{\sigma_{i-1}^{N_{i-1}}\,\Delta t_{i-1}}{\sigma_{o,(i-1)}^{(N_{i-1}-2)}\,B_{i-1}} \tag{B2}$$

where the subscript numbers indicate the time step numbers.

B.3 End Do (Loop)

The risk of rupture *ROR* is calculated as

$$ROR = X_1^{\frac{m_1}{N_1-2}}\,V \tag{B3}$$

where *V* is the volume (*V* = 1 for a unit volume). The failure probability is

$$P_{fV} = 1 - \exp(-ROR) \tag{B4}$$

Appendix C
Efficient Numerical Computation for Transient Reliability Analysis With Cyclic Loading

A computationally efficient method has been developed to perform transient reliability analysis for (constant amplitude and frequency) cyclic loading (see eq. (50)). The technique allows for a tradeoff between solution accuracy and numerical efficiency. This appendix shows how it was developed.

The following reasoning is based on an example using a three-time-step (per cycle) loading problem. The basis for this formulation is the observation that a truncated binomial series expansion can be used to approximate the contribution of successive time steps. The numerical method described in appendix B for uniaxial stress transient reliability analysis is used here because of its simplicity.

To begin, consider a unit volume specimen being subjected to repeated transient load cycles, where each cycle can be divided into three time steps. Over each time step, the stress and material properties are assumed to remain constant, however stress and material properties (Weibull and SCG parameters) could vary between time steps within the cycle. These stresses and material properties are designated by specifying three time steps to define a single cycle:

Property set $\mathcal{A}$, time step 1—$\sigma_{\mathrm{I}eq,a}$, Δt_a, m_a, $\sigma_{o,a}$, N_a, B_a

Property set $\mathcal{B}$, time step 2—$\sigma_{\mathrm{I}eq,b}$, Δt_b, m_{b}, $\sigma_{o,b}$, N_b, B_b

Property set $\mathcal{C}$, time step 3—$\sigma_{\mathrm{I}eq,\mathrm{c}}$, Δt_c, m_c, $\sigma_{o,c}$, N_c, B_c

Set

$$a = \frac{\sigma_{\mathrm{I}eq,a}^{N_a} \Delta t_a}{\sigma_{o,a}^{N_a - 2} B_a} \qquad \begin{aligned} u &= m_a (N_b - 2) \\ v &= m_b (N_a - 2) \end{aligned}$$

$$b = \frac{\sigma_{\mathrm{I}eq,b}^{N_b} \Delta t_b}{\sigma_{o,b}^{N_b - 2} B_b} \qquad \begin{aligned} w &= m_b (N_c - 2) \\ x &= m_c (N_b - 2) \end{aligned}$$

$$c = \frac{\sigma_{\mathrm{I}eq,c}^{N_c} \Delta t_c}{\sigma_{o,c}^{N_c - 2} B_c} \qquad \begin{aligned} y &= m_c (N_a - 2) \\ z &= m_a (N_c - 2) \end{aligned}$$

The repeated cyclic loading and the three time steps making up each cycle follow the pattern in table C.I. The numerical algorithm described in appendix B for ξ total time steps encompassing ξ/3 total loading cycles is used to determine the risk of rupture. Now, perform the numerical algorithm in appendix B (see eq. (B2)) for overall step $i - 1$, where step $i - 1$ has the material properties of $\mathcal{A}$ from equation (B2) of the Do-Loop algorithm.

TABLE C.I.—CYCLIC LOADING PATTERN SHOWN FOR THREE CYCLES AND THREE TIME STEPS PER CYCLE

Property set associated with the time step	$\mathcal{A}$	$\mathcal{B}$	$\mathcal{C}$	$\mathcal{A}$	$\mathcal{B}$	$\mathcal{C}$	$\mathcal{A}$	$\mathcal{B}$	$\mathcal{C}$
Time step number within the cycle	1	2	3	1	2	3	1	2	3
Overall time step number	1	2	3	4	5	6	7	8	9
Cycle number	1	1	1	2	2	2	3	3	3

$$X_{i-1} = X_i^{v/u} + a \tag{C1}$$

Set $E = X_i^{y/u}$ and assume that $(\xi - i) >> 1$ such that $\xi - i$ is at least 3×100 (100 load cycles). In this case for the repeated cyclic load, $E >> a$, $E >> b$, and $E >> c$. This is because E already represents a summation of terms a, b, and c for $[\xi - (i - 1)]/3$ loading cycles. Because E is large relative to the terms a, b, and c, the exponentiation performed on X in the numerical algorithm can be approximated by a binomial series expansion truncated to two terms. That is, for a binomial series of the form

$$(x + y)^{\mu} = x^{\mu} + \mu x^{\mu - 1} y + \frac{\mu(\mu - 1)}{2!} x^{\mu - 2} y^2 + \frac{\mu(\mu - 1)(\mu - 2)}{3!} x^{\mu - 3} y^3 + \ldots \tag{C2}$$

where $(x^2 > y^2)$. When $x >> y$, the higher order terms in the series become negligible and we can approximate the series as a two-term expression:

$$(x + y)^{\mu} \approx x^{\mu} + \mu x^{\mu - 1}\,\mathrm{y} \qquad \text{when } x >> y \tag{C3}$$

For the $i - 1$ time step,

$$X_{i-1} = E + a \tag{C4}$$

and for the $i - 2$ time step in the solution algorithm in appendix B,

$$X_{i-2} = (E + a)^{z/y} + c \tag{C5}$$

Rewriting this using the two-term binomial expansion approximation of equation (C3) yields

$$X_{i-2} \approx E^{z/y} + \frac{E^{z/y}}{E} a\left(\frac{z}{y}\right) + c \tag{C6}$$

For the time step $i - 3$ then,

$$X_{i-3} = \left\{ E^{z/y} + \left[\frac{E^{z/y}}{E} a\left(\frac{z}{y}\right) + c \right] \right\}^{x/w} + b \tag{C7}$$

Because $E >> a$, then $E^{z/y} >> (E^{z/y}/E)\, a(z/y) + c$; so using the two-term binomial expansion again yields

$$X_{i-3} = \left(E^{z/y}\right)^{x/w} + \frac{\left(E^{z/y}\right)^{x/w}}{E^{z/y}} \frac{E^{z/y}}{E} a\left(\frac{z}{y}\right)\left(\frac{x}{w}\right) + \frac{\left(E^{z/y}\right)^{x/w}}{E^{z/y}} c\left(\frac{x}{w}\right) + b \tag{C8}$$

For the $i - 4$ time step,

$$X_{i-4} = \left\{ E^{(z/y)(x/w)} + \left[\frac{E^{(z/y)(x/w)}}{E} a\left(\frac{z}{y}\right)\left(\frac{x}{w}\right) + \frac{E^{(z/y)(x/w)}}{E^{z/y}} c\left(\frac{x}{w}\right) + b \right] \right\}^{v/u} + a \tag{C9}$$

and again, if we assume that the term in parenthesis in equation (C9) is small relative to $E^{(z/y)(x/w)}$, then using the two-term binomial expansion yields

$$X_{i-4} = E^{(z/y)(x/w)(v/u)} + \left[\frac{E^{(z/y)(x/w)(v/u)}}{E^{(z/y)(x/w)}}\right]\frac{E^{(z/y)(x/w)}}{E}a\left(\frac{z}{y}\right)\left(\frac{x}{w}\right)\left(\frac{v}{u}\right)$$

$$+\left[\frac{E^{(z/y)(x/w)(v/u)}}{E^{(z/y)(x/w)}}\right]\frac{E^{(z/y)(x/w)}}{E^{(z/y)}}c\left(\frac{x}{w}\right)\left(\frac{v}{u}\right) \qquad \text{(C10)}$$

$$+\left[\frac{E^{(z/y)(x/w)(v/u)}}{E^{(z/y)(x/w)}}\right]b\left(\frac{v}{u}\right)+a$$

Now, from the definition of the terms *u*, *v*, *w*, *x*, *y*, and *z*,

$$E^{(z/y)(x/w)(v/u)} = E^{\frac{m_a(N_c-2)}{m_c(N_a-2)}\,\frac{m_c(N_b-2)}{m_b(N_c-2)}\,\frac{m_b(N_a-2)}{m_a(N_b-2)}}$$

$$= E \qquad \text{(C11)}$$

So X_{i-4} can be simplified as

$$X_{i-4} = E + 2a + \frac{E}{E^{z/y}}c\left(\frac{x}{w}\right)\left(\frac{v}{u}\right) + \frac{E}{E^{(z/y)(x/w)}}b\left(\frac{v}{u}\right) \qquad \text{(C12)}$$

Note that the two steps involving property $\mathcal{A}$, steps $i-1$ and $i-4$, simplify to a simple sum of $2a$. This is useful because it indicates that the cumulative effect of similar time steps (same time step number within the cycle as shown in table C.I) can be described by a simple summation. Following the process further for the sake of illustration, for the $i-5$ time step, we obtain

$$X_{i-5} = X_{i-4}^{z/y} + c \qquad \text{(C13)}$$

$$X_{i-5} = \left\{E + \left[2a + \frac{E}{E^{z/y}}c\left(\frac{x}{w}\right)\left(\frac{v}{u}\right) + \frac{E}{E^{(z/y)(x/w)}}b\left(\frac{v}{u}\right)\right]\right\}^{z/y} + c \qquad \text{(C14)}$$

Using the two-term binomial expansion then gives

$$X_{i-5} = \left\{E^{(z/y)} + \left[\frac{E^{(z/y)}}{E}\right]2a\left(\frac{z}{y}\right) + \left[\frac{E^{(z/y)}}{E}\right]\frac{E}{E^{(z/y)}}c\left(\frac{x}{w}\right)\left(\frac{v}{u}\right)\left(\frac{z}{y}\right) + \left[\frac{E^{(z/y)}}{E}\right]\frac{E}{E^{(z/y)(x/w)}}b\left(\frac{v}{u}\right)\left(\frac{z}{y}\right)\right\} + c \qquad \text{(C15)}$$

Simplifying yields

$$X_{i-5} = \left(E^{(z/y)} + \left\{\left[\frac{E^{(z/y)}}{E}\right]2a\left(\frac{z}{y}\right) + 2c + \left[\frac{E^{(z/y)}}{E}\right]\frac{E}{E^{(z/y)(x/w)}}b\left(\frac{v}{u}\right)\left(\frac{z}{y}\right)\right\}\right) \qquad \text{(C16)}$$

Again note the direct summation of the properties for $\mathcal{C}$ denoted by the term $2c$. Also, note that the term associated with property $\mathcal{A}$ represents a value transformed from that associated with the property for $\mathcal{C}$. For time step $i - 6$,

$$X_{i-6} = X_{i-5}^{x/w} + b \tag{C17}$$

Using the two-term binomial expansion gives

$$\begin{aligned} X_{i-6} = \Bigg\{ E^{(z/y)(x/w)} & + \left[\frac{E^{(z/y)(x/w)}}{E^{(z/y)}}\right]\frac{E^{(z/y)}}{E}2a\left(\frac{z}{y}\right)\left(\frac{x}{w}\right) \\ & + \left[\frac{E^{(z/y)(x/w)}}{E^{(z/y)}}\right]2c\left(\frac{x}{w}\right) \\ & + \left[\frac{E^{(z/y)(x/w)}}{E^{(z/y)}}\right]\frac{E^{(z/y)}}{E}\frac{E}{E^{(z/y)(x/w)}}b\left(\frac{v}{u}\right)\left(\frac{z}{y}\right)\left(\frac{x}{w}\right) + b \Bigg\} \end{aligned} \tag{C18}$$

or

$$X_{i-6} = \left(E^{(z/y)(x/w)} + \left\{\left[\frac{E^{(z/y)(x/w)}}{E^{(z/y)}}\right]\frac{E^{(z/y)}}{E}2a\left(\frac{z}{y}\right)\left(\frac{x}{w}\right) + \left[\frac{E^{(z/y)(x/w)}}{E^{(z/y)}}\right]2c\left(\frac{x}{w}\right) + 2b\right\}\right) \tag{C19}$$

For time step $i - 7$,

$$X_{i-7} = X_{i-6}^{v/u} + a \tag{C20}$$

Then using the two-term binomial expansion gives

$$\begin{aligned} X_{i-7} = \Bigg\{ E^{(z/y)(x/w)(v/u)} & + \left[\frac{E^{(z/y)(x/w)(v/u)}}{E^{(z/y)(x/w)}}\right]\frac{E^{(z/y)(x/w)}}{E^{(z/y)}}\frac{E^{(z/y)}}{E}2a\left(\frac{z}{y}\right)\left(\frac{x}{w}\right)\left(\frac{v}{u}\right) \\ & + \left[\frac{E^{(z/y)(x/w)(v/u)}}{E^{(z/y)(x/w)}}\right]\frac{E^{(z/y)(x/w)}}{E^{(z/y)}}2c\left(\frac{x}{w}\right)\left(\frac{v}{u}\right) \\ & + \left[\frac{E^{(z/y)(x/w)(v/u)}}{E^{(z/y)(x/w)}}\right]2b\left(\frac{v}{u}\right) + a \Bigg\} \end{aligned} \tag{C21}$$

Simplifying gives

$$X_{i-7} = \left\{ E + \left[3a + \frac{E}{E^{z/y}}2c\left(\frac{x}{w}\right)\left(\frac{v}{u}\right) + \frac{E}{E^{(z/y)(x/w)}}2b\left(\frac{v}{u}\right)\right]\right]\right\} \tag{C22}$$

It is important to note that as the term in brackets [ ] gets large relative to X_{i-7} (and to smaller indices of X), the two-term binomial approximation becomes increasingly inaccurate. Also note the obvious similarities between expressions X_{i-4} and X_{i-7}. Therefore, for the $i - \rho$ time step,

$$X_{i-\rho} = \left\{E + \left[\frac{(\rho-1)}{3}a + \frac{E}{E^{z/y}}\frac{(\rho-1)}{3}c\left(\frac{x}{w}\right)\left(\frac{v}{u}\right)\right] + \frac{E}{E^{(z/y)(x/w)}}\frac{(\rho-1)}{3}b\left(\frac{v}{u}\right)\right\} + a \tag{C23}$$

In this case, $(i-\rho)/3$ is the number of cycles between the $i-1$ and $i-\rho$ time step. If $Z_\iota = (i-\rho)/3$ is set for the number of cycles in the interval, then

$$X_{i-\rho} = \left\{E + \left[Z_\iota a + \frac{E}{E^{z/y}}Z_\iota c\left(\frac{x}{w}\right)\left(\frac{v}{u}\right) + \frac{E}{E^{(z/y)(x/w)}}Z_\iota b\left(\frac{v}{u}\right)\right]\right\} + a \tag{C24}$$

If we use the two-term binomial expansion equation (eq. (C3)), equation (C25) below can be shown to be equivalent to equation (C24):

$$X_{i-\rho} = \left\{\left[\left(X_i^{v/u} + Z_\iota a\right)^{z/y} + Z_\iota c\right]^{x/w} + Z_\iota b\right\}^{v/u} + a \tag{C25}$$

or

$$X_{i-\rho} = \left\{\left[\left[X_i^{\frac{m_b(N_a-2)}{m_a(N_b-2)}} + \frac{\sigma_{\mathrm{I}eq,a}^{N_a} Z_\iota \Delta t_a}{\sigma_{o,a}^{N_a-2} B_a}\right]^{\frac{m_a(N_c-2)}{m_c(N_a-2)}} + \frac{\sigma_{\mathrm{I}eq,c}^{N_c} Z_\iota \Delta t_c}{\sigma_{o,c}^{N_c-2} B_c}\right]^{\frac{m_c(N_b-2)}{m_b(N_c-2)}} + \frac{\sigma_{\mathrm{I}eq,b}^{N_b} Z_\iota \Delta t_b}{\sigma_{o,b}^{N_b-2} B_b}\right\}^{\frac{m_b(N_a-2)}{m_a(N_b-2)}} + \frac{\sigma_{\mathrm{I}eq,a}^{N_a} Z_\iota \Delta t_a}{\sigma_{o,a}^{N_a-2} B_a} \tag{C26}$$

By an inductive argument for a cycle that contains *k* time steps, then

$$X_{i-\rho} = \left\{\ldots\left[\left[X_i^{\frac{m_{V,2}[N_{V,1}-2]}{m_{V,1}[N_{V,2}-2]}} + \frac{\sigma_{\mathrm{I}eq,1}^{N_{V,1}} Z_\iota \Delta t_1}{\sigma_{oBV,1}^{N_{V,1}-2} B_{V,1}}\right]_1^{\frac{m_{V,1}[N_{V,k}-2]}{m_{V,k}[N_{V,1}-2]}} + \frac{\sigma_{\mathrm{I}eq,k}^{N_{V,k}} Z_\iota \Delta t_k}{\sigma_{oBV,k}^{N_{V,k}-2} B_{V,k}}\right]_k^{\frac{m_{V,k}[N_{V,(k-1)}-2]}{m_{V,(k-1)}[N_{V,k}-2]}} + \ldots + \frac{\sigma_{\mathrm{I}eq,2}^{N_{V,2}} Z_\iota \Delta t_2}{\sigma_{oBV,2}^{N_{V,2}-2} B_{V,2}}\right\}_2^{\frac{m_{V,2}[N_{V,1}-2]}{m_{V,1}[N_{V,2}-2]}} + \frac{\sigma_{\mathrm{I}eq,1}^{N_{V,1}} \Delta t_1}{\sigma_{oBV,1}^{N_{V,1}-2} B_{V,1}} \tag{C27}$$

For a more convenient expression (similar to eq. (C27)), the indices can be adjusted so that, for $j = i-1$ and $\varphi = \rho - 1$,

$$X_{j-\varphi} = \Bigg\{ \cdots \Bigg[\Bigg[X_j^{\frac{m_{V,1}\left[N_{V,k}-2\right]}{m_{V,k}\left[N_{V,1}-2\right]}} + \frac{\sigma_{\mathrm{I}eq,k}^{N_{V,k}} Z_\iota \Delta t_k}{\sigma_{oBV,k}^{N_{V,k}-2} B_{V,k}} \Bigg]_k^{\frac{m_{V,k}\left[N_{V,(k-1)}-2\right]}{m_{V,(k-1)}\left[N_{V,k}-2\right]}} + \frac{\sigma_{\mathrm{I}eq,(k-1)}^{N_{V,(k-1)}} Z_\iota \Delta t_{(k-1)}}{\sigma_{oBV,(k-1)}^{N_{V,(k-1)}-2} B_{V,(k-1)}} \Bigg]_{k-1}^{\frac{m_{V,(k-1)}\left[N_{V,(k-2)}-2\right]}{m_{V,(k-2)}\left[N_{V,(k-1)}-2\right]}} + \cdots + \frac{\sigma_{\mathrm{I}eq,1}^{N_{V,1}} Z_\iota \Delta t_1}{\sigma_{oBV,1}^{N_{V,1}-2} B_{V,1}} \Bigg\}_1^{\frac{m_{V,1}\left[N_{V,k}-2\right]}{m_{V,k}\left[N_{V,1}-2\right]}} + \frac{\sigma_{\mathrm{I}eq,k}^{N_{V,k}} \Delta t_k}{\sigma_{oBV,k}^{N_{V,k}-2} B_{V,k}} \tag{C28}$$

Equations (C25), (C26), (C27), and (C28) were shown to be true on the basis of equation (C3)—a two-term truncation of the binomial series. When the value of $j - \varphi$ or $i - \rho$ becomes sufficiently large relative to the total (overall) number of time steps processed in the algorithm, equation (C3) loses accuracy. In other words, more terms of the binomial series are needed to maintain a level of accuracy as $j - \varphi$ or $i - \rho$ becomes sufficiently large. However, using more than two terms in the series would destroy the computational simplicity and efficiency of the methodology shown thus far. Therefore, to maintain accuracy, $j - \varphi$ or $i - \rho$ should be sufficiently small relative to the total number of time steps. To obtain a complete reliability solution, we discretize the load history into λ load blocks, with each block containing Z_ι cycles such that

$$Z_{\mathrm{total}} = \sum_{\iota=1}^{\lambda} Z_\iota \tag{C29}$$

where Z_{total} is the total number of cycles and each load block (see eq. (B28)) consists of Z_ι cycles, with each cycle containing k time steps. Equation (C28) describes the contribution to reliability for each load block. Using the numerical algorithm shown in equations (B1), (B2), and (B3), we can express the total contribution to reliability as from which the risk-of-rupture is computed from equation (B3) and failure probability is calculated from equation (B4) for the Weibull distribution and an incremental volume. Equation (C30) also plugs directly into the Batdorf formulation, as shown in equations (48), (49), and (50).

$$
\begin{aligned}
X_1 = \Bigg\{ [[\ldots [[\ldots \Bigg\{ [\ldots [[\Bigg\{ [\ldots \Bigg[\Bigg[& \left(\frac{\sigma_{\mathrm{I}eq,k,T\max}}{\sigma_{oBV,k}} \right)^{N_{V,k}-2} \\
& + \frac{\sigma_{\mathrm{I}eq,k}^{N_{V,k}} Z_{\lambda} \Delta t_k}{\sigma_{oBV,k}^{N_{V,k}-2} B_{V,k}} \Bigg]_k^{\frac{m_{V,k}[N_{V,(k-1)}-2]}{m_{V,(k-1)}[N_{V,k}-2]}} + \frac{\sigma_{\mathrm{I}eq,(k-1)}^{N_{V,(k-1)}} Z_{\lambda} \Delta t(k-1)}{\sigma_{oBV,(k-1)}^{N_{V(k-1)}-2} B_{V,(k-1)}} \Bigg]_{k-1}^{\frac{m_{V,(k-1)}[N_{V,(k-2)}-2]}{m_{V,(k-2)}[N_{V,(k-1)}-2]}} + \ldots + \frac{\sigma_{\mathrm{I}eq,1}^{N_{V,1}} Z_{\lambda} \Delta t_1}{\sigma_{oBV,1}^{N_{V,1}-2} B_{V,1}} \Bigg]_1^{\frac{m_{V,1}[N_{V,k}-2]}{m_{V,k}[N_{V,1}-2]}} \Bigg\}_{\lambda} \\
& + \frac{\sigma_{\mathrm{I}eq,k}^{N_{V,k}} Z_{(\lambda-1)} \Delta t_k}{\sigma_{oBV,k}^{N_{V,k}-2} B_{V,k}} \Bigg]_k^{\frac{m_{V,k}[N_{V,(k-1)}-2]}{m_{V,(k-1)}[N_{V,k}-2]}} + \frac{\sigma_{\mathrm{I}eq,(k-1)}^{N_{V,(k-1)}} Z_{(\lambda-1)} \Delta t(k-1)}{\sigma_{oBV,(k-1)}^{N_{V,(k-1)}-2} B_{V,(k-1)}} \Bigg]_{k-1}^{\frac{m_{V,(k-1)}[N_{V,(k-2)}-2]}{m_{V,(k-2)}[N_{V,(k-1)}-2]}} + \ldots + \frac{\sigma_{\mathrm{I}eq,1}^{N_{V,1}} Z_{(\lambda-1)} \Delta t_1}{\sigma_{oBV,1}^{N_{V,1}-2} B_{V,1}} \Bigg]_1^{\frac{m_{V,1}[N_{V,k}-2]}{m_{V,k}[N_{V,1}-2]}} \Bigg\}_{\lambda-1} \\
& + \ldots + \frac{\sigma_{\mathrm{I}eq,k}^{N_{V,k}} Z_1 \Delta t_k}{\sigma_{oBV,k}^{N_{V,k}-2} B_{V,k}} \Bigg]_k^{\frac{m_{V,k}[N_{V,(k-1)}-2]}{m_{V,(k-1)}[N_{V,k}-2]}} + \frac{\sigma_{\mathrm{I}eq,(k-1)}^{N_{V,(k-1)}} Z_1 \Delta t(k-1)}{\sigma_{oBV,(k-1)}^{N_{V,(k-1)}-2} B_{V,(k-1)}} \Bigg]_{k-1}^{\frac{m_{V,(k-1)}[N_{V,(k-2)}-2]}{m_{V,(k-2)}[N_{V,(k-1)}-2]}} + \ldots + \frac{\sigma_{\mathrm{I}eq,2}^{N_{V,2}} Z_1 \Delta t_2}{\sigma_{oBV,2}^{N_{V,2}-2} B_{V,2}} \Bigg]_2^{\frac{m_{V,2}[N_{V,1}-2]}{m_{V,1}[N_{V,2}-2]}} + \frac{\sigma_{\mathrm{I}eq,1}^{N_{V,1}} Z_1 \Delta t_1}{\sigma_{oBV,1}^{N_{V,1}-2} B_{V,1}} \Bigg]_1 \Bigg\}_1
\end{aligned}
\qquad \text{(C30)}
$$

In equation (C30), the logic of the two-term binomial approximation was applied for all solution segments and time steps, including the final steps (where use of the two-term binomial approximation is less accurate). This is acceptable for problems where larger cycle counts will be solved for because the contribution of the final 100 cycles (thereabouts) to the overall reliability will be small, and therefore the error introduced using equation (C30) should be small. The expression for X_1 in equation (C30) is convenient because it allows a tradeoff between computational efficiency and numerical accuracy. As more load blocks λ are used, the error should be reduced. However, as λ gets larger, more computational steps occur. As can be seen in equation (C30), the number of computational steps required is the number of load blocks λ times the number of time steps for each load cycle, k. Whereas, for the exact solution of equation (42), the number of computational steps is the total number of cycles n times the number of time steps for each cycle. In other words, nk computational steps are required instead of λk computational steps, where $n \geq \lambda$. When $\lambda = 1$, equation (C30) is most computationally efficient; whereas when $\lambda = n$, equation (C30) becomes equivalent to equation (42) for nk total time steps. The exact answer (eq. (42)) is asymptotically approached as the number of solution segments λ approaches n.

As the number of solution increments λ gets smaller, the computational efficiency increases, but at the cost of some loss of accuracy. For $\lambda = 1$, $Z = Z_1 = Z_{\text{total}}$ and equation (C30) simplifies to

$$X_1 = \Bigg\{ \Bigg[\cdots \Bigg[\Bigg[\left(\frac{\sigma_{\mathrm{I}eq,k,T_{\max}}}{\sigma_{oBV,k}} \right)^{N_{V,k}-2} + \frac{\sigma_{\mathrm{I}eq,k}^{N_{V,k}} Z_{\text{total}} \Delta t_k}{\sigma_{oBV,k}^{N_{V,k}-2} B_{V,k}} \Bigg]_k^{\frac{m_{V,k}\left[N_{V,(k-1)}-2\right]}{m_{V,(k-1)}\left[N_{V,k}-2\right]}} + \frac{\sigma_{\mathrm{I}eq,(k-1)}^{N_{V,(k-1)}} Z_{\text{total}} \Delta t_{(k-1)}}{\sigma_{oBV,(k-1)}^{N_{V,(k-1)}-2} B_{V,(k-1)}} \Bigg]_{(k-1)}^{\frac{m_{V,(k-1)}\left[N_{V,(k-2)}-2\right]}{m_{V,(k-2)}\left[N_{V,(k-1)}-2\right]}} + \ldots + \frac{\sigma_{\mathrm{I}eq,2}^{N_{V,2}} Z_{\text{total}} \Delta t_2}{\sigma_{oBV,2}^{N_{V,2}-2} B_{V,2}} \Bigg]_2^{\frac{m_{V,2}\left[N_{V,1}-2\right]}{m_{V,1}\left[N_{V,2}-2\right]}} + \frac{\sigma_{\mathrm{I}eq,1}^{N_{V,1}} Z_{\text{total}} \Delta t_1}{\sigma_{oBV,1}^{N_{V,1}-2} B_{V,1}} \Bigg\}_1 \tag{C31}$$

Equation (C31) represents the most computationally efficient solution for repeated block (or cyclic) loading. It is up to users to determine if the error associated with equation (C31) is acceptable (see the following numerical example).

An example of the methodology shown in equations (C30) and (C31) is provided in tables C.II to C.V to illustrate the tradeoff between computational efficiency and numerical accuracy using this methodology. In this example, a 10-time-step loading sequence was used. A unit volume was assumed, and the loading was uniaxial and uniform throughout the volume. The loading varied over each time step, and a temperature was associated with each time step. Table C.II shows the loading sequence, and table C.III shows how the Weibull and SCG parameters varied with temperature. These parameters were linearly interpolated at intermediate temperatures. Table C.IV contrasts the percent error between the exact numerical solution of equation (42) with that of equation (C31) for various cycle counts. It is interesting to note that the error was relatively small at the lower cycle counts ($n = 10$ and $n = 100$) and higher cycle counts ($n \geq 10\,000$). The error was as large as –11.6 percent in this example.

TABLE C.II.—TEN-STEP TRANSIENT UNIAXIAL LOAD HISTORY FOR A SINGLE LOAD CYCLE

Time step number	Time, s	Equivalent mode-I far-field stress, $\sigma_{\mathrm{I}eq}$, MPa	Temperature, °C
1	25	100	100
2	50	90	200
3	75	80	300
4	100	70	400
5	125	60	500
6	150	70	600
7	175	80	700
8	200	90	800
9	225	95	900
10	250	100	1000

TABLE C.III.—TEMPERATURE-DEPENDENT MATERIAL PROPERTIES

[Material properties are linearly interpolated between temperature levels for this example.]

Temperature	Volume Weibull modulus, m_V	Volume Weibull scale parameter, σ_{oV}	Volume crack velocity exponent, N_V	Volume SCG material parameter, B_V
100	5	230	40	0.0021
500	9	226	36	0.021
1000	14	221	31	0.21

TABLE C.IV.—EXAMPLE OF THE EXACT SOLUTION (EQS. (41) and (42)) VERSUS THE CYCLIC APPROXIMATION METHOD (EQ. (C31))

[The results for one load block represent the least accurate but most computationally efficient answer.]

Number of cycles, n	Volume probability of failure, P_{fV},		Error, percent
	Exact solution (eq. (41))	Cyclic approximation method (eq. (C31))	
10^0	0.16428	0.16428	0
10^1	.21701	.21571	−.6
10^2	.28955	.28037	−3.2
10^3	.41831	.36997	−11.6
10^4	.70425	.68330	−3.0
10^5	.96954	.96850	−.1
10^6	.99997	.99997	-1.0×10^{-4}

TABLE C.V.—EXAMPLE OF CYCLIC APPROXIMATION METHOD FOR VARIOUS NUMBERS OF LOAD BLOCKS USING EQUATIONS (C29) AND (C30)

[Each load block has the same number of cycles ($Z_\iota = Z_{\text{total}}/\lambda$).]

Number of cycles, n	Volume probability of failure, P_{fV}							
	Exact solution (eq. (41))	Number of load blocks, λ						
		1	2	5	10	100	500	1000
10^3	0.41831	0.36997	0.39447	0.40958	0.41420	0.41796	0.41827	0.41831
10^5	0.96954	0.96850	0.96864	0.96877	0.96884	0.96924	0.96948	0.96951

Table C.V shows the difference in failure probability between the exact solution (eq. (42)) and the approximate solution (eq. (C30)) for various numbers of load blocks λ. From table C.V it can be observed that the solution accuracy improves as λ gets larger. Figure C.1 shows the reduction in error as λ gets larger for 1000-cycle predicttions (the number of blocks approaches the number of cycles). At λ = 100, the error becomes relatively negligible. This still represents a 10-fold reduction in computational effort versus the exact solution. This example illustrates the level of error that may be encountered using the cyclic approximation method. The authors are not aware of a method to systematically specify what level of error could be expected for a given problem. It is, therefore, up to users to perform these tradeoff comparisons to determine an acceptable level of error versus computational effort.

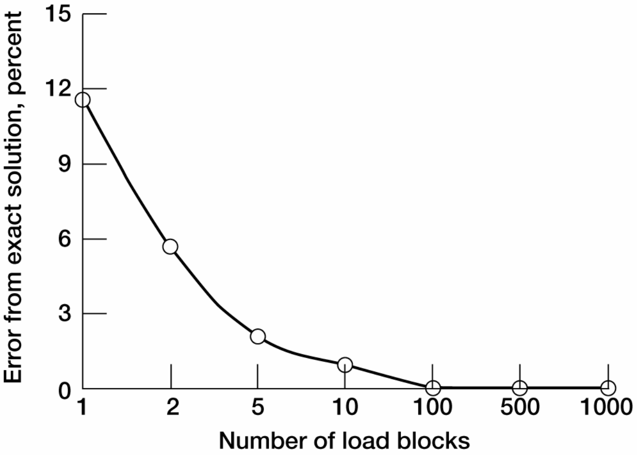

Figure C.1.—Percent error for 1000 cycles from the exact solution (eq. (42)) compared with the cyclic approximation method (eq. (C30)) for various numbers of load blocks λ.

Appendix D
Excerpted Introduction and Theory Section—CARES/*Life* Ceramics Analysis and Reliability Evaluation of Structures Life Prediction Program[2]

D.1 Introduction

Advanced ceramics have several inherent properties that must be considered in the design procedure. The most deleterious of these properties is that ceramics are brittle materials. This lack of ductility and yielding capability leads to low strain tolerance, low fracture toughness, and large variations in observed fracture strength. When a load is applied, the absence of significant plastic deformation or microcracking causes large stress concentrations to occur at microscopic flaws, which are unavoidably present as a result of materials processing operations or inservice environmental factors. The observed scatter in component strength is caused by the variable severity of these flaws and by the behavior of sudden catastrophic crack growth, which occurs when the crack driving force or energy release rate reaches a critical value. In addition, the ability of a ceramic component to sustain a load degrades over time because of a variety of effects such as oxidation, creep, stress corrosion, and cyclic fatigue. Stress corrosion and cyclic fatigue result in a phenomenon called subcritical crack growth (SCG). SCG initiates at a preexisting flaw and continues until a critical length is reached, causing catastrophic propagation. The SCG failure mechanism is a load-induced phenomenon over time. It can also be a function of chemical reaction, environment, debris wedging near the crack tip, and deterioration of bridging ligaments.

Once the factors that contribute to material failure have been identified and characterized, ceramic components can be designed for service applications using an appropriate brittle material design methodology. For this purpose, NASA's integrated design computer program CARES/*Life* (Ceramics Analysis and Reliability Evaluation of Structures/*Life*) has been developed to predict the fast-fracture and/or lifetime reliability of monolithic structural ceramic components subjected to thermomechanical and/or proof-test loading. This design methodology combines the statistical nature of strength-controlling flaws with fracture mechanics to allow for multiaxial stress states, concurrent flaw populations, and SCG. CARES/*Life* is an extension of the CARES program (Powers et al., 1992; Nemeth et al., 1990; Pai and Gyekenyesi, 1988; Gyekenyesi and Nemeth, 1987; and Gyekenyesi, 1986), which predicts the fast-fracture reliability of monolithic ceramic components. The fundamental subsets of the program include (1) fast-fracture reliability analysis, (2) inert (fast-fracture) statistical material parameter estimation, (3) crack-growth laws to account for static and cyclic fatigue, (4) static, dynamic, and cyclic fatigue parameter estimation, and (5) the effect of proof testing on component service probability of failure.

Because the presence of microscopic flaws causes ceramics to fail, examination of fracture surfaces can reveal the nature of failure. Fractography of broken samples has shown that these flaws can be characterized into two general categories: (1) defects internal or intrinsic to the material volume (volume flaws) and (2) defects extrinsic to the material volume (surface flaws). Intrinsic defects are the result of materials processing. Extrinsic flaws can result from grinding or other finishing operations, from chemical reaction with the environment, or from the internal defects intersecting the external surface. The different physical nature of these flaws results in dissimilar failure response to identical loading situations. Consequently, separate criteria must be employed to describe the effects of the applied loads on the component surface and volume.

Because of the statistical nature of these flaw populations, the size of the stressed material surface area and volume (known as the size effect) affects the strength. By increasing component size, the average strength is reduced because of the increased probability of having a weaker flaw. Generally, for metals, the variation of strength is small, and thus the scaling effect is negligible. However, for materials that display large variations of strength, this effect is not trivial. Hence, if a ceramic design is based on material parameters obtained from smaller size test pieces, then the effects of scaling must be taken into account, otherwise a nonconservative design will result.

---

[2] This is a revised version of a section of Nemeth et al. (2003). Note that in this appendix some variables were renamed and some text was edited to be more consistent with the main text of this report.

Another consequence of the random distribution of flaws is that failure of a complex component might not be initiated at the point of highest nominal stress. A particularly severe flaw may be located at a region of relatively low stress, yet still be the cause of component failure. For this reason, the entire field solution of the stresses should be considered. Clearly, it is not adequate to predict reliability only on the basis of the most highly stressed point.

Traditional analysis of the failure of materials uses a deterministic approach, where failure is assumed to occur when some allowable stress level or equivalent stress is exceeded. The most widely used of these theories are the maximum normal stress, maximum normal strain, maximum shear stress, and maximum distortional energy criteria of failure. These phenomenological failure theories have been reasonably successful when applied to ductile materials such as metals. However, these methods do not account for observed variations in ceramic component fracture stress. Therefore, to assure high reliability in brittle material design, large factors of safety are required. This does not allow for optimization of design since the physical phenomena that determine fracture response are not properly modeled.

Because of its lack of a proper physical basis, the traditional approach to design is not adequate to predict the failure of brittle materials. Consequently, Griffith (1921 and 1925) proposed a fracture theory where failure was due to the presence of cracks of specified size and shape distributed randomly throughout the material. He assumed that no interaction takes place between adjacent cracks and that failure occurs at the flaw with the least favorable orientation relative to the macroscopic loading. The Griffith energy balance criterion for fracture states that crack growth will occur if the energy release rate reaches a critical value. Griffith's theory provides a sound physical basis to describe the rupture process in an isotropic brittle continuum. However, it omits the effect of component size on strength because the crack length is not treated as a probabilistic quantity.

Reliability analysis is essential for accurate failure prediction and efficient structural utilization of brittle materials subjected to arbitrary stress states. When coupled with the weakest-link model (Weibull, 1939a), this approach takes into account not only the size effect and loading system, but also the variability in strength due to defect distributions. A statistical theory of failure can be readily incorporated into the finite element method of structural analysis since each element can be made arbitrarily small such that the element stress gradient is negligible. Component integrity is computed by calculating element-by-element reliability and then determining the component survivability as the product of the individual element reliabilities.

For fast-fracture reliability analysis, the first probabilistic approach used to account for the scatter in fracture strength and the size effect of brittle materials was introduced by Weibull (1939a, 1939b, and 1951). This approach is based on the previously developed weakest-link theory (WLT) (Peirce, 1926), which is primarily attributed to Peirce, who proposed it while modeling yarn failure. The WLT is analogous to pulling a chain, where catastrophic failure occurs when the weakest link in the chain is broken. Unlike Peirce, who assumed a gaussian distribution of strength, Weibull assumed a unique probability density function known as the Weibull distribution. It has been shown (Shih, 1980) that the three-parameter Weibull distribution is a more accurate approximation of ceramic material behavior than the gaussian or other distributions. Since three-parameter behavior is rarely observed in as-processed monolithic ceramics, the CARES/*Life* program uses the two-parameter Weibull model in which the threshold stress (the value of applied stress below which the failure probability is zero) is taken as zero. The reliability predictions obtained using the two-parameter model are more conservative than those obtained with the three-parameter model.

To predict the fast-fracture material response under multiaxial stress states by using statistical parameters obtained from flexural or uniaxial test specimens, Weibull proposed calculating the risk of rupture by averaging the tensile normal stress raised to an exponent in all directions over the area of a unit radius sphere (volume flaws; Weibull, 1939a) or over the contour of a unit radius circle (surface flaws; Gross and Gyekenyesi, 1989). Although this approach is intuitively plausible, it is somewhat arbitrary. In addition, it lacks a closed-form solution, and therefore, requires computationally intensive numerical modeling. Subsequently, Barnett et al. (1967) and Freudenthal (1968) proposed an alternative approach usually referred to as the principle of independent action (PIA) model for finding the failure probability in multidimensional stress fields. This principle states that the Weibull survival probability of a uniformly stressed material element experiencing multiaxial loading is equal to the product of the survival probabilities for each of the tensile principal stresses applied individually.

The PIA fracture theory is the weakest-link statistical equivalent of the maximum stress failure theory. The Weibull method of averaging the tensile normal stress and the PIA model have been the most popular methods for polyaxial stress-state analysis, and they have been widely applied in brittle material design (Margetson, 1976; Paluszny and Wu, 1977; DeSalvo, 1970; Wertz and Heitman, 1980; and Dukes, 1971). However, the Weibull and PIA hypotheses do not specify the nature of the defect-causing failure, so there is no foundation for extrapolating to conditions different from the original test specimen configuration. Consequently, the accuracy of these theories has been questioned, and other statistical models have been introduced (Batdorf and Crose, 1974; Evans and Jones, 1978; and Batdorf, 1978). The ideas developed by Batdorf and Crose (1974) are important because they provide a physical basis for incorporating the effect of multiaxial stresses into the WLT. They describe material volume and surface imperfections as randomly oriented, noninteracting discontinuities (cracks) with an assumed regular geometry. This enables the contributions of shear and normal forces to the fracture process to be explicitly treated. Failure is assumed to occur when the effective stress on the weakest flaw reaches a critical level. The effective stress is a combination of normal and shear stresses acting on the flaw. It is a function of the assumed crack configuration, the existing stress state, and the fracture criterion employed. Accounting for the presence of shear on the crack plane reduces the normal stress needed for fracture, yielding a more accurate reliability analysis than that of the shear-insensitive crack model (Weibull's method). Unlike in the deterministic Griffith failure criterion, the size of the crack in the probabilistic approach need not be considered because it is associated with the strength of the material.

The search for an accurate fracture criterion to predict fast-fracture response to monotonically increasing loads leads to the field of fracture mechanics. Many authors have discussed the stress distribution around cavities of various types under different loading conditions, and numerous criteria have been proposed to describe impending failure. Paul and Mirandy (1976) extended Griffith's maximum tensile stress criterion for biaxial loadings to include three-dimensional effects due to Poisson's ratio and flaw geometry, which could not be accounted for in Griffith's previous two-dimensional analysis. Other investigators (Giovan and Sines, 1979; Batdorf, 1980; Stout and Petrovic, 1984; and Petrovic and Stout, 1984) have compared results from the most widely accepted mixed-mode fracture criteria with each other and with selected experimental data. No prevailing consensus has emerged regarding a best theory. Also, most of the criteria predict somewhat similar results, despite the divergence of initial assumptions. Therefore, the authors of this report concluded that several alternatives would be available for the sake of comparison but that the semiempirical equation developed by Palaniswamy and Knauss (1978) and Shetty (1987) provides the most flexibility to fit the available experimental data. In addition, Shetty's criterion can account for the out-of-plane flaw growth that is observed under mixed-mode loadings. Finally, several different flaw geometries are described, but the penny-shaped and semicircular crack configurations are recommended as the most accurate representations of volume and surface defects, respectively.

A wide variety of materials, including ceramics, exhibit the phenomenon of delayed fracture or fatigue. Under the application of a loading function of a magnitude smaller than that which induces short-term failure, there is a regime where SCG occurs and this can lead to eventual component failure in service. SCG is a complex process involving a combination of simultaneous and synergistic failure mechanisms. These can be grouped into two categories: (1) crack growth due to corrosion and (2) crack growth due to mechanical effects arising from cyclic loading. Stress corrosion is due to a stress-dependent chemical interaction between the material and its environment. Water, for example, has a pronounced deleterious effect on the strength of glass and alumina. Higher temperatures also tend to accelerate this process. Mechanically induced cyclic fatigue is dependent only on the number of load cycles and not on the duration of the cycles. This phenomenon can be caused by a variety of effects, such as debris wedging or the degradation of bridging ligaments, but essentially it is based on the accumulation of some type of irreversible damage that tends to enhance the crack growth. Service environment, material composition, and material microstructure determine if a brittle material will display one, none, or some combination of these fatigue mechanisms.

Because of the complex nature of SCG, models that have been developed tend to be semiempirical and to approximate the behavior of SCG phenomenologically. Theoretical and experimental work in this area has demonstrated that lifetime failure characteristics can be described by considering the crack-growth rate versus the stress-intensity factor (SIF) or the range in the SIF. This is graphically depicted as the logarithm of the rate of crack growth versus the logarithm of the mode-I SIF. Curves of experimental data show three distinct regimes, or regions, of growth. The first region includes the threshold behavior of the crack, where below a certain value of stress intensity the crack growth is zero. Above this threshold level there is an approximately linear relationship of stable crack growth. In this second region, the crack velocity is essentially constant versus the SIF. The third region indicates unstable crack growth as the crack velocity rapidly increases and the critical SIF is approached. For the stress corrosion failure mechanism, region I is controlled by the rate of reaction of the corrosive species; region II is controlled by the diffusion of the corrosive species; and region III is unstable crack propagation. These curves are material and environment sensitive. This model, using conventional fracture mechanics relationships, satisfactorily describes the failure mechanisms in materials where, at high temperatures, plastic deformations and creep behave in a linear viscoelastic manner (Evans and Wiederhorn, 1974a). In general, at high temperatures and low levels of stress, failure is best described by creep rupture that generates new cracks (Wiederhorn and Fuller, 1985). Creep and material healing mechanisms are not addressed in the CARES/*Life* code.

The most often cited models in the literature regarding SCG are based on power-law formulations. Other theories, most notably that of Wiederhorn et al. (1980), have not achieved such widespread usage, although they may also have a reasonable physical foundation. Power-law formulations are used to model both the stress corrosion phenomenon and the cyclic fatigue phenomenon. This modeling flexibility, coupled with their widespread acceptance, makes these formulations the most attractive candidates to incorporate into a design methodology. A power-law formulation is obtained by assuming that the second crack-growth region is linear and that it dominates over the other regions. Three power-law formulations are useful for modeling brittle materials: the power law, the Paris law, and the Walker law. The power law (Evans and Wiederhorn, 1974a; and Wiederhorn, 1974a, pp. 613–646) describes the crack velocity as a function of the SIF, and it implies that the crack growth is due to stress corrosion. For cyclic fatigue, either the Paris law (Paris and Erdogan, 1963) or Walker's modified formulation of the Paris law (Walker, 1970, p. 1; and Dauskardt et al., 1992) is used to model the SCG. The Paris law describes the crack growth per load cycle as a function of the range in the SIF. The Walker equation relates the crack growth per load cycle to both the range in the crack-tip SIF and the maximum applied crack-tip SIF. It is useful for predicting the effect of the R-ratio (the ratio of the minimum cyclic stress to the maximum cyclic stress) on the material strength degradation.

Because SCG operates on the preexisting flaws in the material, the fast-fracture statistical theories discussed previously are required to predict the time-dependent reliability for brittle materials. The SCG model is combined with the two-parameter Weibull cumulative distribution function to characterize the component failure probability as a function of service lifetime. The effects of multiaxial stresses are considered by using the PIA model, the Weibull normal stress-averaging (NSA) method, or the Batdorf theory.

Lifetime reliability analysis accounting for SCG under cyclic and/or sustained loads is essential for the safe and efficient utilization of brittle materials in structural design. Current life design methodology assumes that the SCG of mixed-mode loading is based on a power function relationship existing between the crack propagation rate and the equivalent mode-I SIF (Boehm, 1989; Hamanaka et al., 1990; Hamada and Teramae, 1990; Thiemeier, 1989; Sturmer, 1991; and Wittig et al., 1991). The literature is sparse regarding crack-velocity measurements for mixed-mode loadings of brittle materials. When a crack is subjected to a combined-mode loading, it extends in a curved or kinked path that reorients the crack to a pure mode-I coplanar extension at the crack tip (Shetty and Rosenfield, 1991). The models of Boehm, Hamanaka, Homada, Thiemeier, and Sturmer do not consider this more complex behavior because of the paucity of available data. The approach taken by these researchers is reasonable if the duration where mixed-mode loading exists at the crack tip is small in comparison to the duration where the crack tip is extending in pure mode I. In any event, the formulations they adopted tend to yield conservative results.

For corrosion-assisted SCG, time-dependent reliability analysis for a component subjected to various cyclic boundary load conditions can be simplified by transforming that type of loading to an equivalent static state. The conversion, through the use of a constant called the g-factor (Evans, 1980; and Mencik, 1984), satisfies the requirement that both systems will cause the same crack growth. Implicit in this conversion is the validity of the crack-growth power-law relationship. The probability of failure is then obtained with respect to the transformed equivalent static state.

Prior to placing a component in service, confidence that it will perform reliably is usually demonstrated through proof testing. To a great extent, this is the accepted way to assure the reliability of a component (Evans and Wiederhorn, 1974b; Wiederhorn, 1974b; Ritter et al., 1980; Fuller et al., 1980; and Srinivasan and Seshadri, 1982). Ideally, the boundary load conditions applied to a component under proof testing simulate those conditions a component would be subjected to in service, and the proof-test loads are appropriately greater in magnitude over some fixed time interval. The significance of proof testing is that it enables specimens with a certain minimum flaw size or larger to be eliminated from the strength distribution. Thus, an attenuated probability of failure is obtained, and the survived components can be placed in service with greater confidence in their integrity. In practice, however, it is often difficult, expensive, or impossible for the proof-test load conditions to exactly simulate the service load conditions: the loads can be misaligned, or the proof-test and the service load can have different multiaxial stress states. This situation can be accounted for when proof-testing design methodology is incorporated into the statistical fracture theories for polyaxial stress states (Service and Ritter, 1986; Hamanaka et al., 1990; and Brukner-Foit et al., 1994). An attenuated probability of failure is computed for the components that survive; however, a minimum life of assured reliability may no longer be relevant.

D.2 CARES/*Life* Computer Program

The CARES/*Life* computer program predicts the reliability and the failure probability of a monolithic ceramic component as a function of its service life. CARES/*Life* couples to commercially available finite element programs, such as ANSYS, via a neutral file interface. It accounts for material failure from the SCG of preexisting flaws and uses the Weibull distribution to describe the probabilistic distribution of strength. The computational algorithms are written in FORTRAN 77. Finite element heat transfer and linear-elastic stress analysis are used to determine the temperature and stress distributions in the component. Component reliability for volume (intrinsic) flaws is determined from the finite element stress, temperature, and volume output from two-dimensional, three-dimensional, or axisymmetric elements. Reliability for surface (extrinsic) flaws is calculated from the shell element (or simulated shell element) stress, temperature, and area data. CARES/*Life* produces an optional file containing risk-of-rupture intensities (a local measure of reliability) for graphical rendering of the structure's critical regions.

The phenomenon of SCG is modeled with the power law, the Paris law, and the Walker law. The power law (Evans and Wiederhorn, 1974a; and Wiederhorn, 1974a, pp. 613–646) describes the crack velocity as a function of the SIF. For cyclic fatigue, either the Paris law (Paris and Erdogan, 1963) or Walker's modified formulation of the Paris law (Walker, 1970, p. 1; and Dauskardt et al., 1992) is used to model the SCG. The Paris law relates the crack growth per load cycle to the range in the SIF. The Walker equation relates the crack growth per load cycle to both the range in the crack-tip SIF and the maximum applied crack-tip SIF. This formulation accounts for the effect of the *R*-ratio (minimum cycle stress to maximum cycle stress) on lifetime. The power law and the Paris law require two experimentally derived fatigue parameters—*N* and *B*—which depend on the material and environment. The Walker equation requires three material-environmental parameters—*N*, *B*, and *Q*. Steady-state cyclic loading is accounted for by using the Walker law, using the Paris law, or employing *g*-factors (Mencik, 1984) in conjunction with the power law. The *g*-factor approach equates variable cyclic loadings to equivalent static loadings. CARES/*Life* includes the sinusoidal, square, and sawtooth loading waveforms. Typically, the use of *g*-factors is appropriate for flat *R*-curve materials.

The probabilistic nature of material strength and the effects of multiaxial stresses are modeled by using either the PIA, the Weibull NSA method, or the Batdorf theory. The Batdorf theory combines linear elastic fracture mechanics with the weakest-link mechanism. It requires a user-selected flaw geometry and a mixed-mode fracture criterion to describe volume or surface strength-limiting defects. The combination of a particular flaw shape and fracture criterion results in an effective stress, which is a function of the far-field stresses, and acts on the crack plane. Figure D.1 shows the fracture criteria and flaw geometries available to users for both surface- and volume-flaw analysis. The simple PIA fracture theory does not use a crack geometry, and only tensile principal stresses contribute to failure. The Weibull NSA method is also independent of crack geometry. The mode-I (opening mode) crack growth is considered, and mode-II (sliding mode) and mode-III (tearing mode) effects are neglected. The combination of a particular flaw shape and fracture criterion results in an effective stress involving far-field

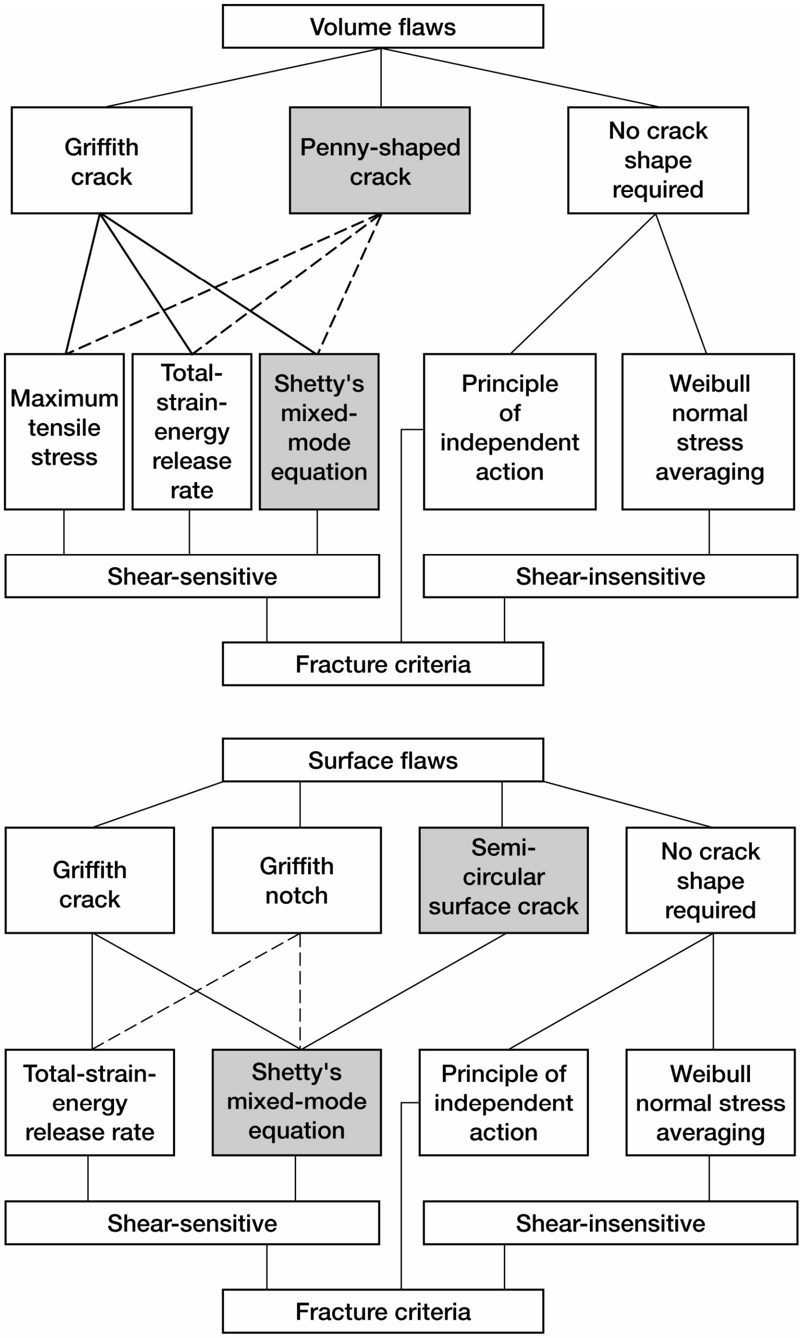

Figure D.1.—Available failure criteria and crack shapes.

principal stresses in terms of normal and shear stresses acting on the crack plane. CARES/*Life* includes the total strain-energy release rate theory (coplanar crack extensions) (Batdorf and Heinisch, 1978a). Out-of-plane crack-extension criteria are approximated by a simple semiempirical equation (Palaniswamy and Knauss, 1978; and Shetty, 1987). This equation involves a parameter that can be varied to model the maximum tangential stress theory (Erdogan and Sih, 1963), the minimum strain-energy-density criterion (Sih, 1974), the maximum strain-energy release rate theory (Hellen and Blackburn, 1975; and Ichikawa, 1991), or experimental results. For comparison, Griffith's maximum tensile stress analysis for volume flaws is also included. The highlighted boxes in figure D.1 show the recommended fracture criteria and flaw shapes. If the normal stress acting on the flaw plane is compressive, then no crack growth is assumed to occur with these models. Typically, brittle materials are much stronger in compression than in tension. It is assumed that the lower tensile strength limit will predominate over the higher compressive limit for a typical component design. If the compressive stresses are significant, they should be checked against limiting values from other methods.

For fast fracture, the probabilistic nature of material strength is described by the two-parameter Weibull cumulative distribution function, which incorporates WLT. This relation postulates that inherent material flaws in the component body (volume flaws) and on its surface (surface flaws) govern the strength response. The component reliability is determined by integrating the stress over the body. The Weibull stress-volume integral is a function of the scale parameter σ_o and the shape parameter m. The scale parameter corresponds to the stress level at which 63.21 percent of specimens with unit volume or area would fracture. The characteristic strength σ_θ is similar to the Weibull scale parameter except that it includes the effect of the specimen volume or area. The shape parameter (or Weibull modulus), denoted by m, is a dimensionless quantity that measures the degree of strength dispersion of the flaw distribution.

Weibull material parameters, the Batdorf crack-density coefficient k_B, and fatigue parameters are estimated from rupture strength data of naturally flawed specimens. The parameters are obtained from the fracture stresses of specimens whose geometry and loading configurations are held constant (30 or more specimens are recommended). A similar number is recommended for fatigue experiments. The CARES/*Life* program includes closed-form solutions for the three- and four-point modulus-of-rupture (MOR) bending bar (Baratta et al., 1987) and the pure tensile specimen (Liu and Brinkman, 1986) under isothermal conditions. For other conventional specimen geometries, material parameters can be estimated via effective volume and area calculations (a finite element model of the specimen geometry and loading is required).

Since the material parameters are a function of temperature, various constant-temperature data sets can be simultaneously input and the corresponding parameter estimates can be calculated and made available for component reliability analysis. Linear interpolation is performed to obtain values at intermediate temperatures. More sophisticated interpolation techniques are not used because of the potential of obtaining erroneous results. Each constant-temperature data set can consist of up to 999 specimens. In addition, each specimen can be identified by its mode of failure—either volume flaw, surface flaw, or some other mode—so that parameter estimates for competing failure modes can be obtained.

CARES/*Life* estimates fatigue parameters from naturally flawed specimens ruptured under static, cyclic, or dynamic loading. Cyclic fatigue parameter evaluation assumes steady-state loading and a constant R-ratio throughout the specimen. Fatigue parameters can be calculated using either the median-value technique (Jakus et al., 1978), a least-squares regression technique, or a median-deviation regression method, which is somewhat similar to trivariant regression (Jakus et al., 1978). The median-value technique is a well-known estimation procedure based on regression of the median values of the fatigue data at the various stress levels or rates. The least-squares regression technique involves a regression on all the fatigue data to establish the parameters. The median-deviation procedure involves minimizing the median deviation (MD) of the scatter in the data versus the crack-growth exponent N. In the CARES/*Life* code, this minimization is accomplished by maximizing the time-dependent Weibull modulus versus the crack-growth exponent N. The fast-fracture strength distribution Weibull modulus m and the characteristic strength σ_θ are optionally estimated from the fatigue data for a failure time of 1 s with constant stress-rate loading (or a lifetime of $1/(N+1)$ cycles). The fatigue data are transformed to an equivalent fast-fracture strength distribution. This enables goodness-of-fit testing and the use of an outlier test. The resulting goodness-of-fit statistics are applied to the original fatigue data. If inert strength fracture data are simultaneously input, then the Weibull parameters for these data override those calculated from time-dependent data.

For inert strength fracture (fast-fracture) data, parameter estimation of the biased Weibull modulus and characteristic strength σ_θ can be performed for unimodal (single failure mode) or concurrent surface and volume-flaw populations by using least-squares analysis (Johnson, 1964) or the maximum-likelihood method (Nelson, 1982). Because estimates of Weibull parameters are obtained from a finite amount of data, they contain an inherent uncertainty that can be characterized by the bounds in which the true parameters are likely to lie. Methods have been developed to evaluate confidence limits that quantify this range with a level of probability as a function of sample size. For the maximum-likelihood method with a complete sample, unbiasing factors for the shape parameter m, and 5- and 95-percent confidence limits for m and the characteristic strength σ_θ, are provided

(Thoman et al., 1969). For a censored sample, an asymptotic approximation of the 90-percent confidence limits is calculated. No unbiasing of parameters or estimation of confidence limits is given when the least-squares option is requested.

CARES/*Life* includes a test that identifies potential bad data (outliers) from the time-dependent or inert-strength fracture experiments. This test, known as the Stefansky outlier test (Stefansky, 1972; and Neal et al., 1987), is based on the normal distribution and, therefore, its application to the Weibull distribution is not rigorous. However, it serves as a useful guideline to users. Data detected as outliers are flagged with a warning message, and any further action is left to the discretion of users.

The ability of the hypothesized distribution to reasonably fit the empirical data is measured with the Kolmogorov-Smirnov (KS) and Anderson-Darling (AD) goodness-of-fit tests. These tests are extensively discussed by D'Agostino and Stephens (1986). The tests quantify discrepancies between the experimental data and the estimated Weibull distribution by a significance level associated with the hypothesis that the data were generated from the proposed distribution. The AD test is more sensitive than the KS test to discrepancies at low and high probabilities of failure. The calculated significance levels are based on the assumption that the Weibull parameters are chosen independently from the experimental data. For inert strength data, the Kanofsky-Srinivasan 90-percent confidence band values (Kanofsky and Srinivasan, 1972) about the Weibull line are given as an additional test of the goodness-of-fit of the data to the Weibull distribution.

CARES/*Life* automatically calculates the other material parameters necessary for the reliability analysis. The biased estimate of the shape parameter m and the estimated characteristic strength σ_θ are used along with the specimen geometry to calculate the Weibull scale parameter σ_o. The Batdorf normalized crack-density coefficient $\bar{k}_B$ is computed from the selected fracture criterion, crack geometry, and the biased estimate of the shape parameter.

The relationships between the fatigue parameters (N and B) and the various failure criteria have been established to ensure the compatibility of failure probabilities. From test specimen data (uniaxial tension, three-point bend bar, and four-point bend bar), compatibility is derived by equating the risk-of-rupture of the uniaxial Weibull model to the risk-of-rupture of the PIA, NSA, or Batdorf shear-sensitive, multiaxial models. This satisfies the requirement that for a uniaxial stress state, all multiaxial models produce the same probability of failure as the uniaxial Weibull model. The value of N is invariant, and the value of B is adjusted to satisfy this compatibility condition.

Finite element analysis is an ideal mechanism for obtaining the stress distribution needed to calculate the survival probability of a structure. Each element can be made arbitrarily small, such that the stresses can be taken as constant throughout each element (or subelement). In CARES/*Life*, the reliability calculations are performed at the gaussian integration points of the element. Use of the element integration points enables the element to be divided into subelements, where integration point subvolumes, subareas, and subtemperatures are calculated. The location of the gaussian integration point in the finite element and the corresponding weight functions are considered when the subelement volume and area are calculated. The number of subelements in each element depends on the integration order chosen and the element type. If the probability of survival for each element is assumed to be a mutually exclusive event, the overall component reliability is the product of all the calculated element (or subelement) survival probabilities.

The component reliability analysis module of the CARES/*Life* program uses the output from finite element elastostatic analysis to calculate time-dependent reliability for each element. This has been implemented for various commercial finite-element-analysis software packages—a complete list of which is not provided here because this list is subject to change. Volume-flaw-based reliability is calculated from the volume-flaw material strength parameters previously estimated from experimental data and the stresses, volumes, and temperatures for each solid element. Volume-flaw analysis can be performed using brick, wedge, and tetrahedron isoparametric solid elements, along with triangular (and optionally quadrilateral) axisymmetric isoparametric elements. Surface-flaw-based reliability is calculated from the surface-flaw material strength parameters and individual shell element output of the two-dimensional surface stresses, areas, and temperatures. Surface-flaw analysis can be performed using quadrilateral and triangular isoparametric shell elements. Modeling with axisymmetric elements generally is not enabled for surface-flaw reliability analysis. Shell elements (or simulated shell elements) are used to identify the external surfaces of solid elements that correspond to the component external surfaces important to the reliability analysis. Shell elements with exclusively membrane properties and negligible thickness (and hence stiffness) are used.

CARES/*Life* uses component symmetry to permit the use of the cyclic symmetry modeling option or similar mesh-reduction schemes. CARES/*Life* also permits the analysis of simultaneously occurring flaw populations in a given finite element model (multiple ceramic materials or multiple flaw population capability). Elements not designated as brittle materials are ignored in the reliability computations. Temperature-dependent statistical material properties are linearly interpolated at each individual element temperature. Element and nodal identification numbers can be arbitrary. The risk-of-rupture intensity is also calculated for each element, and these values are sorted to determine the maximum values. Element risk-of-rupture intensities are written to an importable data file to show the regions on the component where failure has the highest likelihood of occurring.

Proof-test methodology is incorporated into the PIA, the Weibull NSA method, and the Batdorf theories, accounting for the effect of multiaxial stresses. With the Weibull NSA and the Batdorf theory, the proof-test load need not closely simulate the actual service conditions on the component. This is important because it allows a reliability analysis to be performed when proof-test stresses have not been applied in the same direction and/or location as have the service load stresses.

D.2.1 Fast-Fracture Reliability Analysis

***D.2.1.1 Overview*.**—The use of advanced ceramic materials in structural applications requiring high component integrity has led to the development of a time-dependent probabilistic design methodology. This method combines three major elements: (1) linear elastic fracture mechanics theory that relates the strength of ceramics to the size, shape, orientation, and growth of critical flaws; (2) extreme value statistics to obtain the characteristic flaw size distribution function, which is a material property; and (3) material microstructure. Inherent to this design procedure is that the requirement of total safety must be relaxed and that an acceptable failure probability must be specified.

The statistical nature of fracture in engineering materials can be viewed from two distinct models (Tracy, 1982). The first was presented by Weibull and used the WLT as originally proposed by Peirce (1926). The second model was also analyzed by Peirce (1926) and by Daniels (1945). This second model is referred to as the “bundle” or “parallel” model. In the bundle model, a structure is viewed as a bundle of parallel fibers. Each fiber can support a load less than its breaking strength indefinitely but will break immediately under any load equal to or greater than its breaking strength. When a fiber fractures, a redistribution of load occurs and the structure may survive. Failure occurs when the remaining fibers can no longer support the increased load. The weakest-link model assumes that the structure is analogous to a chain with n links. Each link may have a different limiting strength. When a load is applied to the structure such that the weakest link fails, then the structure fails. Observations show that advanced monolithic ceramics closely follow the WLT. A component fails when an equivalent stress at a flaw reaches a critical value that depends on the fracture mechanics criterion, crack configuration, crack orientation, and the crack-density function of the material. In comparison with the bundle model, WLT is, in most cases, more conservative.

Weibull’s WLT model does not consider failure caused by purely compressive stress states. Phenomenological observations indicate that compressive stresses do not play a major role in the failure of ceramic structures since the compressive strength of brittle materials is significantly greater than their tensile strength. The effect of a predominant compression on failure is assumed to be negligible in the CARES/*Life* program.

One of the important features of WLT is that it predicts a size effect. The number and severity of flaws present in a structure depends on the material volume and surface area. The largest flaw in a big specimen is expected to be more severe than the largest flaw in a smaller specimen. Another consequence of WLT is that component failure might not be initiated at the point of highest nominal stress (Davies, 1973), as would be true for ductile materials. A large flaw might be located in a region far removed from the most highly stressed zone. Therefore, the complete stress solution of the component must be considered.

Classical WLT does not predict behavior in a multiaxial stress state. A number of concepts such as the PIA, Weibull’s NSA method, and Batdorf’s model have been applied to account for polyaxial stress-state response. Batdorf’s model (Batdorf and Crose, 1974) assumes the following: (1) microcracks in the material are the cause of fracture, (2) cracks do not interact, (3) each crack has a critical stress that is defined as the stress normal to the crack plane that will cause fracture, and (4) fracture occurs under combined stresses when an effective stress acting on the crack is equal to the critical stress. For an assumed crack shape, the effective stress can be obtained through the application of a fracture criterion. These concepts are used in conjunction with techniques to obtain the various statistical material parameters necessary for fast-fracture reliability analysis.

D.2.1.2 Volume-flaw reliability analysis.—Consider a stressed component containing many flaws, and assume that failure is due to any number of independent and mutually exclusive mechanisms (links). Each link involves an infinitesimal probability of failure. Discretize the component into n incremental links. The probability of survival $(P_{sV})_i$ of the i^{th} link is related to the probability of failure $(P_{fV})_i$ of the i^{th} link by $(P_{sV})_i = [1 - (P_{fV})_i]$, and the resultant probability of survival of the whole structure is the product of the individual probabilities of survival:

$$P_{sV} = \prod_{i=1}^{n} \left(P_{sV}\right)_i = \prod_{i=1}^{n} \left[1 - \left(P_{fV}\right)_i\right] \cong \prod_{i=1}^{n} \exp\left[-\left(P_{fV}\right)_i\right] = \exp\left[-\sum_{i=1}^{n} \left(P_{fV}\right)_i\right] \tag{D1}$$

where the subscript V denotes volume-dependent terms. Assume the existence of a function $\eta_V(\sigma)$, referred to as the crack-density function, representing the number of flaws per unit volume having a strength equal to or less than σ. Under a local tensile stress σ_i, the probability of failure of the i^{th} link, representing the incremental volume ΔV_i, is $(P_{fV})_i = [\eta_V(\sigma_i)\, \Delta V_i]$, where the incremental volume ΔV_i is arbitrarily small such that the value of the expression within the brackets is much less than one. Applying a uniform tensile stress σ, such that $\sigma = \sigma_i$ for all incremental volumes ΔV_i, then from equation (D1) the resultant probability of survival for material volume V, where V is the sum of all ΔV_i, is

$$P_{sV} = \exp\left[-\eta_V(\sigma)\, V\right] \tag{D2}$$

Equation (D2) can also be derived from the Poisson probability density function. The Poisson density function is described by (see Hoel et al., 1971, for example)

$$P(X = x) = f(x) = \begin{cases} \dfrac{\lambda^x \exp(-\lambda)}{x!} & x = 0, 1, 2, \ldots \\ 0 & \text{elsewhere} \end{cases} \tag{D3}$$

where λ is a positive number. The real-valued function $f(x)$ is the discrete density function of random variable X where $P(X = x)$ is the probability that a discrete real-valued random variable X equals a possible value x. The Poisson distribution approximates the binomial distribution for large values of n, where n is the number of Bernoulli trials with success probability $p = \lambda/n$ at each trial. Equation (D2) is obtained when $P(X = 0)$ is computed for $n = V$ and $p = \eta_V(\sigma)$, hence

$$P_{sV} = P(X = 0) = \frac{\lambda^0 \exp(-\lambda)}{0!} = \exp(-\lambda) = \exp\left[-\eta_V(\sigma)\, V\right] \tag{D4}$$

Equation (D4) calculates the probability of the event that no flaws of strength σ or less are present in the material volume V and, therefore, represents the survival probability of the material under applied load σ.

The probability of failure for the uniformly stressed volume V is

$$P_{fV} = 1 - P_{sV} = 1 - \exp\left[-\eta_V(\sigma)\, V\right] \tag{D5}$$

where V is the total volume. If the stress magnitude is a function of location, then

$$P_{fV} = 1 - \exp\left[-\int_V \eta_V(\sigma)\,\mathrm{d}V \right] = 1 - \exp - \left(ROR_V \right) \tag{D6}$$

A term called the risk-of-rupture by Weibull and denoted here by the symbol *ROR* is commonly used in reliability analysis. Equations similar to (D5) and (D6) are applicable to surface-distributed flaws where surface area replaces volume and the flaw density function is surface-area dependent.

Weibull introduced a three-parameter power function for the crack-density function $\eta_V(\sigma)$,

$$\eta_V(\sigma) = \left(\frac{\sigma - \sigma_{uV}}{\sigma_{oV}} \right)^{m_V} \tag{D7}$$

where σ_{uV} is the threshold stress parameter, which is usually taken as zero for ceramics. This parameter is the value of the applied stress below which the failure probability is zero. When this parameter is zero, the two-parameter Weibull model is obtained. The scale parameter σ_{oV} then corresponds to the stress level where 63.21 percent of tensile specimens with unit volumes would fracture. Note from equations (D5) and (D7) for a unit volume when $(\sigma - \sigma_{uV}) = \sigma_{oV}$ that a value of 0.6321 is obtained. The scale parameter σ_{oV} has dimensions of stress×(volume)$^{1/m_V}$, where m_V is the shape parameter (Weibull modulus), a dimensionless parameter that measures the degree of strength variability. As m_V increases, the dispersion is reduced. For large values of m_V (>40), such as those obtained for ductile metals, the magnitude of the scale parameter corresponds to the material ultimate strength. These three statistical parameters are material properties, and they are temperature and processing dependent.

Three-parameter behavior is not commonly observed in as-processed monolithic ceramics, and statistical estimation of the three material parameters is more involved than it is with the two-parameter model. The CARES/*Life* program uses the two-parameter model. The subsequent reliability predictions are more conservative than for the three-parameter model since we have taken the minimum strength of the material as zero.

The two-parameter crack-density function is expressed as

$$\eta_V(\sigma) = \left(\frac{\sigma}{\sigma_{oV}} \right)^{m_V} = k_{wV}\,\sigma^{m_V} \tag{D8}$$

and when equation (D8) is substituted into equation (D6), the failure probability becomes

$$P_{fV} = 1 - \exp\left(-k_{wV} \int_V \sigma^{m_V}\,\mathrm{d}V \right) \tag{D9}$$

where $k_{wV} = \left(\sigma_{oV}\right)^{-m_V}$ is the uniaxial Weibull crack-density coefficient. Various methods have been developed to calculate σ_{oV} and m_V for a given material by using fracture strength data from simple uniaxial specimen tests (Pai and Gyekenyesi, 1988).

The two most common techniques for using uniaxial data to calculate P_{fV} in polyaxial stress states are the PIA method (Barnett, et al., 1967, and Freudenthal, 1968) and the Weibull normal tensile stress-averaging method (Weibull, 1939a). In the PIA model, the principal stresses $\sigma_1 \geq \sigma_2 \geq \sigma_3$ are assumed to act independently. If all principal stresses are tensile, the probability of failure according to this approach is

$$P_{fV} = 1 - \exp\left[-k_{wV} \int_V \left(\sigma_1^{m_V} + \sigma_2^{m_V} + \sigma_3^{m_V} \right) \mathrm{d}V \right] \tag{D10}$$

Compressive principal stresses are assumed not to contribute to the failure probability. It has been shown that this equation yields nonconservative estimates of P_{fV} in comparison with the Weibull normal stress method (Batdorf, 1977a).

The failure probability using the Weibull normal tensile stress-averaging (NSA) method, which has been described through an integral formulation (Gross and Gyekenyesi, 1989), can be calculated from

$$P_{fV} = 1 - \exp\left(- \int_V k_{wpV} \, \overline{\sigma}_n^{\,m_V} \, \mathrm{d}V \right) \tag{D11}$$

where

$$\overline{\sigma}_n^{\,m_V} = \frac{\int_A \sigma_n^{m_V} \, \mathrm{d}A}{\int_A \mathrm{d}A}$$

The area integration is performed in principal stress space over the surface A of a sphere of unit radius for regions where σ_n, the projected normal stress on the surface, is tensile. The polyaxial Weibull crack-density coefficient is k_{wpV}. The relationship between k_{wpV} and k_{wV} is found by equating the failure probability for uniaxial loading to that obtained for the polyaxial stress state when the latter is reduced to a uniaxial condition. The result is

$$k_{wpV} = \left(2m_V + 1\right) k_{wV} \tag{D12}$$

Batdorf and Crose (1974) proposed a statistical theory in which attention is focused on cracks and their failure under stress. Flaws are taken to be uniformly distributed and randomly oriented in the material bulk. Fracture is assumed to depend only on the tensile stress acting normal to the crack plane; hence, shear insensitivity is inherent to the model. Subsequently, Batdorf and Heinisch (1978a) included the detrimental effects of shear traction on a flaw plane. Their method applies fracture mechanics concepts by combining a crack geometry and a mixed-mode fracture criterion to describe the condition for crack growth. Adopting this approach, the CARES/*Life* program contains several fracture criteria and flaw shapes for volume and surface analyses (fig. D.1).

Consider a small, uniformly stressed material element of volume ΔV. The incremental probability of failure under the applied multiaxial state of stress Σ can be written as the product of two probabilities,

$$\Delta P_{fV}\left(\Sigma, \sigma_{\mathrm{I}eqc}, \Delta V\right) = \Delta P_{1V} P_{2V} \tag{D13}$$

where ΔP_{1V} is the probability of the existence in ΔV of a crack having an equivilent critical stress between $\sigma_{\mathrm{I}eqc}$ and $\sigma_{\mathrm{I}eqc} + \Delta\sigma_{\mathrm{I}eqc}$. Critical stress is defined as the remote, uniaxial fracture strength of a given crack in mode-I loading. The term $\sigma_{\mathrm{I}eqc}$ denotes an effective (or equivalent) critical mode-I stress from applied multiaxial stresses. The second probability, P_{2V}, denotes the probability that a crack of critical stress $\sigma_{\mathrm{I}eqc}$ will be oriented in a direction such that an effective stress $\sigma_{\mathrm{I}eq}$ (which is a function of fracture criterion, stress state, and crack configuration) satisfies the condition $\sigma_{\mathrm{I}eq} \geq \sigma_{\mathrm{I}eqc}$. The effective stress $\sigma_{\mathrm{I}eq}$ is defined as the equivalent mode-I stress a flaw would experience when subjected to a multiaxial stress state that results in mode-I, -II, and -III crack surface displacements, and $\sigma_{\mathrm{I}eqc}$ is the threshold value of $\sigma_{\mathrm{I}eq}$ where unstable catastrophic crack growth ensues.

The strength of a component containing a flaw population is related to the critical flaw size, which is implicitly used in statistical fracture theories. Batdorf and Crose (1974) describe ΔP_{1V} as

$$\Delta P_{1V} = \Delta V \frac{\mathrm{d}\eta_V\left(\sigma_{\mathrm{I}eqc}\right)}{\mathrm{d}\,\sigma_{\mathrm{I}eqc}} \mathrm{d}\,\sigma_{\mathrm{I}eqc} \tag{D14}$$

and P_{2V} is expressed as

$$P_{2V} = \frac{\Omega\left(\Sigma, \sigma_{\mathrm{I}eqc}\right)}{4\pi} \tag{D15}$$

where $\eta_V(\sigma_{\mathrm{I}eqc})$ is the Batdorf crack-density function and $\Omega(\Sigma, \sigma_{\mathrm{I}eqc})$ is the area of the solid angle projected onto the unit radius sphere in principal stress space containing all the crack orientations for which $\sigma_{\mathrm{I}eq} \geq \sigma_{\mathrm{I}eqc}$. The constant 4π is the surface area of a unit radius sphere and corresponds to a solid angle containing all possible flaw orientations.

The probability of survival in a volume element ΔV_i is

$$\left(P_{sV}\right)_i = \exp\left\{-\Delta V\left[\int_0^{\sigma_{\mathrm{I}eq,\max}} \frac{\Omega\left(\Sigma, \sigma_{\mathrm{I}eqc}\right)}{4\pi} \frac{\mathrm{d}\,\eta_v\left(\sigma_{\mathrm{I}eqc}\right)}{\mathrm{d}\,\sigma_{\mathrm{I}eqc}} \mathrm{d}\,\sigma_{\mathrm{I}eqc}\right]\right\}_i \tag{D16}$$

where $\sigma_{\mathrm{I}eq,\max}$ is the maximum effective stress a randomly oriented flaw could experience from the given stress state. Hence, the component failure probability is

$$P_{fV} = 1 - \exp\left\{-\int_V \left[\int_0^{\sigma_{\mathrm{I}eq,\max}} \frac{\Omega\left(\Sigma, \sigma_{\mathrm{I}eqc}\right)}{4\pi} \frac{\mathrm{d}\,\eta_v\left(\sigma_{\mathrm{I}eqc}\right)}{\mathrm{d}\,\sigma_{\mathrm{I}eqc}} \mathrm{d}\,\sigma_{\mathrm{I}eqc}\right] \mathrm{d}V\right\} \tag{D17}$$

The Batdorf crack-density function $\eta_V(\sigma_{\mathrm{I}eqc})$ is a material property, independent of stress state, and is usually approximated by a power function (Batdorf and Heinisch, 1978a). This leads to the Batdorf crack-density function of the form

$$\eta_V\left(\sigma_{\mathrm{I}eqc}\right) = k_{BV}\sigma_{\mathrm{I}eqc}^{m_V} \tag{D18}$$

where the material Batdorf crack-density coefficient k_{BV} and the Weibull modulus m_V are evaluated from experimental inert strength fracture data. Batdorf and Crose (1974) initially proposed a Taylor series expansion for $\eta_V(\sigma_{\mathrm{I}eqc})$, but this method has computational difficulties. A more convenient integral equation approach was formulated and extended to the use of data from four-point MOR bar tests (Rufin et al., 1984). Note that $\eta_V(\sigma_{\mathrm{I}eqc})$ has units of inverse volume.

Although the Weibull (eq. (D8)) and Batdorf (eq. (D18)) crack-density functions are similar in form, they are not the same. The Weibull function simply depends on the applied uniaxial stress distribution σ and is the only term other than the volume necessary to calculate P_{fV}. The Batdorf function depends on the mode-I strength of the crack $\sigma_{\mathrm{I}eqc}$, which is probabilistic and must be integrated over a range of values for a given stress state. Furthermore, to obtain P_{fV}, a crack orientation function, P_{2V}, must be considered in addition to the density function and the volume. Finally, the Batdorf coefficient k_{BV} cannot be calculated from inert strength data until a fracture criterion and crack shape are chosen—in contrast to the Weibull coefficient k_{wV}, which depends only on the data.

To determine a component probability of failure, one must evaluate P_{2V} (eq. (D15)) for each elemental volume ΔV_i, within which a uniform multiaxial stress state Σ is assumed. The solid angle $\Omega(\Sigma, \sigma_{\mathrm{I}eqc})$ depends on the selected fracture criterion, the crack configuration, and the applied stress state. For multiaxial stress states, with few exceptions, $\Omega(\Sigma, \sigma_{Ieqc})$ must be determined numerically. For a sphere of unit radius (fig. D.2), an elemental surface area of the sphere is $dA = \sin\alpha \, d\beta \, d\alpha$. Project onto the spherical surface the equivalent (effective) stress $\sigma_{Ieq}(\Sigma, \alpha, \beta)$. The solid angle $\Omega(\Sigma, \sigma_{Ieqc})$ is the area of the sphere containing all the projected equivalent stresses satisfying $\sigma_{Ieq} \geq \sigma_{Ieqc}$. Note the symmetry of σ_{Ieq} in principal stress space, and address the first octant of the unit sphere, then

$$\Omega(\Sigma, \sigma_{Ieqc}) = \int_0^{\pi/2} \int_0^{\pi/2} H(\sigma_{Ieq}, \sigma_{Ieqc}) \sin\alpha \, d\alpha \, d\beta \tag{D19}$$

where

$$H(\sigma_{Ieq}, \sigma_{Ieqc}) = 1 \qquad \sigma_{Ieq} \geq \sigma_{Ieqc}$$

$$H(\sigma_{Ieq}, \sigma_{Ieqc}) = 0 \qquad \sigma_{Ieq} < \sigma_{Ieqc}$$

Substituting into equation (D17) and integrating with respect to σ_{Ieqc}, changes the component failure probability to (Batdorf, 1978)

$$P_{fV} = 1 - \exp\left[-\frac{2}{\pi} \int_V \int_0^{\pi/2} \int_0^{\pi/2} \eta_V(\sigma_{Ieq}) \sin\alpha \, d\alpha \, d\beta \, dV \right] \tag{D20}$$

where

$$\eta_V(\sigma_{Ieq}) = k_{BV} \, \sigma_{Ieq}^{m_V}(x, y, z, \alpha, \beta)$$

For a given element, $\sigma_{Ieq}(x, y, z, \alpha, \beta)$ is the projected equivalent stress over the unit radius sphere in principal stress space as shown in figure D.2.

Equation (D20) circumvents the involved numerical integration of $\Omega(\Sigma, \sigma_{Ieqc})$ as developed in the original CARES program (Nemeth et al., 1990). Equations (D17) and (D20) are equivalent formulations; however, equation (D20) is more convenient for computational purposes with few exceptions (Batdorf and Crose, 1974). Therefore, CARES/*Life* applies equation (D20) to obtain the component probability of failure.

Assuming a shear-insensitive condition, fracture occurs when $\sigma_n = \sigma_{Ieq} \geq \sigma_{Ieqc}$, where σ_n is the normal tensile stress on the flaw plane. However, it is known from fracture mechanics analysis that for a flat crack, a shear stress τ applied parallel to the crack plane (mode II or III) also contributes to fracture. Therefore, the effective stress σ_{Ieq} is a function of both σ_n and τ.

Selecting an arbitrary plane in principal stress space (fig. D.2) and imposing equilibrium conditions yields the following equations:

$$\sigma^2 = (\sigma_1 \ell)^2 + (\sigma_2 m)^2 + (\sigma_3 n)^2 \tag{D21}$$

$$\sigma_n = \sigma_1 \ell^2 + \sigma_2 m^2 + \sigma_3 n^2 \tag{D22}$$

and

$$\tau^2 = \sigma^2 - \sigma_n^2 \tag{D23}$$

where σ is the total traction vector acting on the crack plane and the direction cosines ℓ, m, and n are given in figure D.2 in terms of trigonometric functions of α and β.

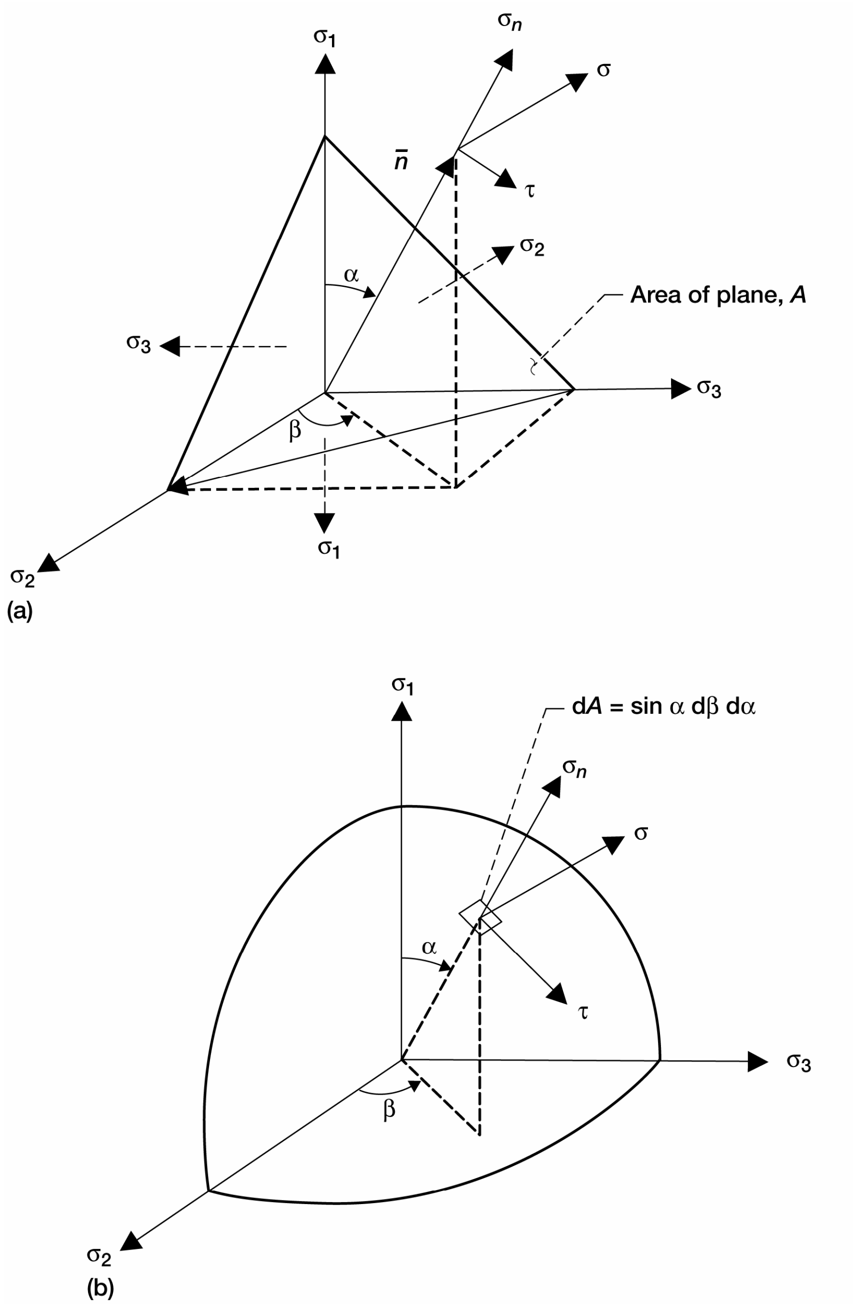

Figure D.2.—Stresses on Cauchy infinitesimal tetrahedron. (a) In principal stress space. Direction cosines: $\ell = \cos \alpha$, $m = \sin \alpha \cos \beta$, $n = \sin \alpha \sin \beta$. (b) Projected onto a plane tangent to the unit radius sphere.

From the selected fracture criterion and crack configuration, σ_{Ieq} is obtained as a function of Σ, α, and β. Batdorf and Heinisch (1978a) give effective stress expressions for two flaw shapes by using both Griffith's maximum tensile stress criterion and Griffith's total coplanar strain-energy release rate criterion G_T. Arranged in order of increasing shear sensitivity, for the maximum tensile stress criterion the effective stress equation for a Griffith flaw is

$$\sigma_{\mathrm{I}eq} = \frac{1}{2}\left(\sigma_n + \sqrt{\sigma_n^2 + \tau^2}\right) \tag{D24}$$

and for a penny-shaped flaw, where ν is Poisson's ratio, it is

$$\sigma_{\mathrm{I}eq} = \frac{1}{2}\left\{\sigma_n + \sqrt{\sigma_n^2 + \left[\frac{\tau}{(1-0.5\nu)}\right]^2}\right\} \tag{D25}$$

The total coplanar strain-energy release rate criterion is calculated from

$$G_T = G_{\mathrm{I}} + G_{\mathrm{II}} + G_{\mathrm{III}} \tag{D26}$$

where G is the energy release rate for various crack-extension modes. In terms of SIFs, the effective stress equation can be derived from (plane strain condition assumed) enforcing the condition $G_T = G_c$, where G_c is the critical strain-energy release rate. Thus,

$$K_{\mathrm{I}eqc}^2 = K_{\mathrm{I}}^2 + K_{\mathrm{II}}^2 + \frac{K_{\mathrm{III}}^2}{1-\nu} \tag{D27}$$

where $K_{\mathrm{I}eqc}$ denotes an equivalent $K_{\mathrm{I}c}$ from a multiaxial stress state.

For a Griffith crack, assuming that modes I and II dominate the response with $K_{\mathrm{I}} = \sigma_n\sqrt{\pi a}$ and $K_{\mathrm{II}} = \tau\sqrt{\pi a}$, where $2a$ is the crack length, we have from equation (D27)

$$\sigma_{\mathrm{I}eq} = \sqrt{\sigma_n^2 + \tau^2} \tag{D28}$$

For a penny-shaped crack at the critical point on the crack periphery, we have $K_{\mathrm{I}} = 2\sigma_n\sqrt{a/\pi}$ and $K_{\mathrm{II}} = [4\tau/(2-\nu)]\sqrt{a/\pi}$ (Sih, 1973), where a is now the crack radius. The resulting effective stress from equation (D28) is

$$\sigma_{\mathrm{I}eq} = \left\{\sigma_n^2 + \left[\frac{\tau}{(1-0.5\nu)}\right]^2\right\}^{1/2} \tag{D29}$$

The equations given by Batdorf and Heinisch consider only self-similar (coplanar) crack extension. However, a flaw experiencing a multiaxial stress state usually undergoes crack propagation initiated at some angle to the flaw plane (noncoplanar crack growth). Shetty (1987) performed experiments on polycrystalline ceramics and glass, where he investigated crack propagation as a function of an applied far-field multiaxial stress state. He modified an equation proposed by Palaniswamy and Knauss (1978) so that it would empirically fit experimental data. This multimodal interaction equation takes the form

$$\frac{K_{\mathrm{I}}}{K_{\mathrm{I}c}} + \left(\frac{K_\delta}{\bar{C}K_{\mathrm{I}c}}\right)^2 = 1 \tag{D30}$$

where K_δ is either K_{II} or K_{III}, whichever is dominant, and $\overline{C}$ is a constant adjusted to best fit the data. Shetty (1987) found a range of values of $0.80 \le \overline{C} \le 2.0$ for the materials he tested that contained large induced flaws. As $\overline{C}$ increases, the response becomes progressively more shear insensitive.

Using this relationship with assumed mode-I and -II dominance for the Griffith crack yields

$$\sigma_{\mathrm{I}eq} = \frac{1}{2}\left[\sigma_n + \sqrt{\sigma_n^2 + \left(\frac{2\tau}{\overline{C}}\right)^2}\right] \tag{D31}$$

and for a penny-shaped crack, we obtain

$$\sigma_{\mathrm{I}eq} = \frac{1}{2}\left\{\sigma_n + \sqrt{\sigma_n^2 + \left[\frac{4\tau}{\overline{C}(2-\nu)}\right]^2}\right\} \tag{D32}$$

For a Griffith crack when $\overline{C} = 0.80$, 0.85, 1.0, and 1.15, equation (D30) models, respectively, the following criteria: Ichikawa's maximum strain-energy release rate approximation (Ichikawa, 1991), the maximum tangential stress (Erdogan and Sih, 1963), Hellen and Blackburn's maximum strain-energy release rate formulation (Hellen and Blackburn, 1975), and colinear crack extension.

Similarly, for a penny-shaped crack with a material having a Poisson's ratio of about 0.22 and $\overline{C} = 0.80$, 0.85, 1.05, and 1.10, equation (D30) models, respectively, the following criteria: Ichikawa's maximum energy release rate approximation (Ichikawa, 1991), the maximum tangential stress (Erdogan and Sih, 1963), Hellen and Blackburn's maximum strain-energy release rate formulation (Hellen and Blackburn, 1975), and colinear crack extension.

For a stressed component, the probability of failure is calculated from equation (D20). The finite element method enables discretization of the component into incremental volume elements. CARES/*Life* evaluates the failure probability at the gaussian integration points of the element or optionally at the element centroid. Using the element integration points subdivides the element into subelements, hence each V_{isub} corresponds to the $isub^{\mathrm{th}}$ subelement volume. In the usual context of finite element methods, the volume of a three-dimensional element V_{elt} is calculated after transformation into the natural coordinate space (Bathe, 1982)

$$V_{elt} = \int_{-1}^{1}\int_{-1}^{1}\int_{-1}^{1} \det \mathbf{J}(r,s,t)\,\mathrm{d}r\,\mathrm{d}s\,\mathrm{d}t \tag{D33}$$

where $\mathbf{J}$ is the Jacobian operator and r, s, and t are the natural coordinates. The subelement volume is defined as the contribution of the integration point to the element volume in the course of the numerical integration procedure. This means that the volume of each subelement (corresponding to a Gauss integration point) is calculated using the shape functions inherent to the element type. The stress state in each subelement is assumed to be uniform. Powers et al. (1992) gives further details of the subelementing procedure as used in CARES/*Life.* The numerical solution of equation (D20) takes the following form:

$$P_{fV} = 1 - \exp\left\{-\frac{2\,k_{BV}}{\pi}\sum_{isub=1}^{n_{\mathrm{sub}}} V_{isub}\left[\int_A \sigma_{\mathrm{I}eq}^{m_V}(\alpha,\beta)\,\mathrm{d}A\right]_{isub}\right\} \tag{D34}$$

where n_{sub} is the total number of subelements. If k_{BV} is element dependent, it will appear inside the brackets. CARES/*Life* uses gaussian numerical integration to evaluate equation (D34). This is detailed further in section D.2.3.

D.2.1.3 Surface-flaw reliability analysis.—For surface-flaw analysis (Gyekenyesi and Nemeth, 1987), many of the equations from section D.2.1.2 remain the same, except that the statistical material parameters are a function of surface area instead of volume and the equivalent stresses are projected onto the contour of a circle of unit radius rather than onto the surface of a sphere of unit radius. The cracks are assumed to be randomly oriented in the plane of the external boundary with their planes normal to the surface (Batdorf and Heinisch, 1978b).

For surface-flaw-induced failure in ceramic structures, the probability of failure for the two-parameter Weibull distribution, which is analogous in form to equation (D9), is

$$P_{fS} = 1 - \exp\left(-k_{wS} \int_A \sigma^{m_S} \, \mathrm{d}A \right) \tag{D35}$$

where $k_{wS} = (1/\sigma_{oS})^{m_S}$ is the uniaxial Weibull surface crack-density coefficient. The subscript S denotes the terms that are surface-area dependent. Here σ_{oS} is the surface scale parameter with units of $\text{stress} \times (\text{area})^{1/m_S}$ and A is the stressed surface area. For biaxial stress states, the PIA model yields

$$P_{fS} = 1 - \exp\left[-k_{wS} \int_A \left(\sigma_1^{m_S} + \sigma_2^{m_S} \right) \mathrm{d}A \right] \tag{D36}$$

where σ_1 and σ_2 are the principal tensile in-plane stresses acting on the surface of the structure. For the Weibull NSA method, the failure probability is expressed as

$$P_{fS} = 1 - \exp\left(-k_{wpS} \int_A \overline{\sigma}_n^{m_S} \, \mathrm{d}A \right) \tag{D37}$$

where

$$\overline{\sigma}_n^{m_s} = \frac{\int_c \sigma_n^{m_s} \, \mathrm{d}c}{\int_c \mathrm{d}c}$$

Here k_{wpS} is the polyaxial Weibull crack-density coefficient for surface flaws. The line integration is performed over the contour c of a circle of unit radius where the projected normal stress σ_n is tensile. The relationship of k_{wpS} to k_{wS} is obtained by carrying out the integration in equation (D37) for a uniaxial stress and equating the resultant failure probability to that of equation (D35) (Pai and Gyekenyesi, 1988). This results in

$$k_{wpS} = \frac{m_S \, \Gamma(m_S) \sqrt{\pi}}{\Gamma\left(m_S + \frac{1}{2} \right)} k_{wS} \tag{D38}$$

where Γ is the gamma function. Equation (D37) is the shear-insensitive case of the more general Batdorf polyaxial model.

For mixed-mode fracture due to surface flaws, the Batdorf polyaxial failure probability equation (analogous to eq. (D17)) is

$$P_{fS} = 1 - \exp\left[\int_A \int_0^{\sigma_{\mathrm{I}eq,\max}} \frac{\omega\left(\Sigma, \sigma_{\mathrm{I}eqc}\right)}{2\pi} \frac{\mathrm{d}\eta_S\left(\sigma_{\mathrm{I}eqc}\right)}{\mathrm{d}\sigma_{\mathrm{I}eqc}} \mathrm{d}\sigma_{\mathrm{I}eqc}\, \mathrm{d}A\right] \tag{D39}$$

where, analogous to equations (D14) and (D15),

$$\Delta P_{1S} = \Delta A \frac{\mathrm{d}\,\eta_S\left(\sigma_{\mathrm{I}eqc}\right)}{\mathrm{d}\,\sigma_{\mathrm{I}eqc}}\, \mathrm{d}\sigma_{\mathrm{I}eqc} \tag{D40}$$

and

$$P_{2S} = \frac{\omega\,\left(\Sigma, \sigma_{\mathrm{I}eqc}\right)}{2\pi} \tag{D41}$$

For randomly oriented cracks, $\omega(\Sigma,\sigma_{\mathrm{I}eqc})$ is the total arc length on a circle of unit radius in principal stress space on which the projection of the equivalent stress satisfies $\sigma_{\mathrm{I}eq} \geq \sigma_{\mathrm{I}eqc}$, and 2π is the total arc length of the circle. Similar to cases with volume flaws, the Batdorf crack-density function is approximated by the power function,

$$\eta_S\left(\sigma_{\mathrm{I}eqc}\right) = k_{BS}\sigma_{\mathrm{I}eqc}^{m_S} \tag{D42}$$

where k_{BS} is the Batdorf surface crack-density coefficient.

A simplification of equation (D39) is obtained by noting the following:

$$\omega\left(\Sigma, \sigma_{\mathrm{I}eqc}\right) = \int_0^{2\pi} H\left(\sigma_{\mathrm{I}eq}, \sigma_{\mathrm{I}eqc}\right) \mathrm{d}\,\alpha \tag{D43}$$

where

$$H\left(\sigma_{\mathrm{I}eq}, \sigma_{\mathrm{I}eqc}\right) = 1 \qquad \sigma_{\mathrm{I}eq} \geq \sigma_{\mathrm{I}eqc}$$

$$H\left(\sigma_{\mathrm{I}eq}, \sigma_{\mathrm{I}eqc}\right) = 0 \qquad \sigma_{\mathrm{I}eq} < \sigma_{\mathrm{I}eqc}$$

Substituting into equation (D39) and noting symmetry (for principal stress space), we obtain

$$P_{fS} = 1 - \exp\left[-\frac{2}{\pi} \int_A \int_0^{\pi/2} \eta_S\left(\sigma_{\mathrm{I}eq}\right) \mathrm{d}\alpha\, \mathrm{d}A\right] \tag{D44}$$

where

$$\eta_S\left(\sigma_{\mathrm{I}eq}\right) = k_{BS}\sigma_{\mathrm{I}eq}^{m_S}\left(x, y, \alpha\right)$$

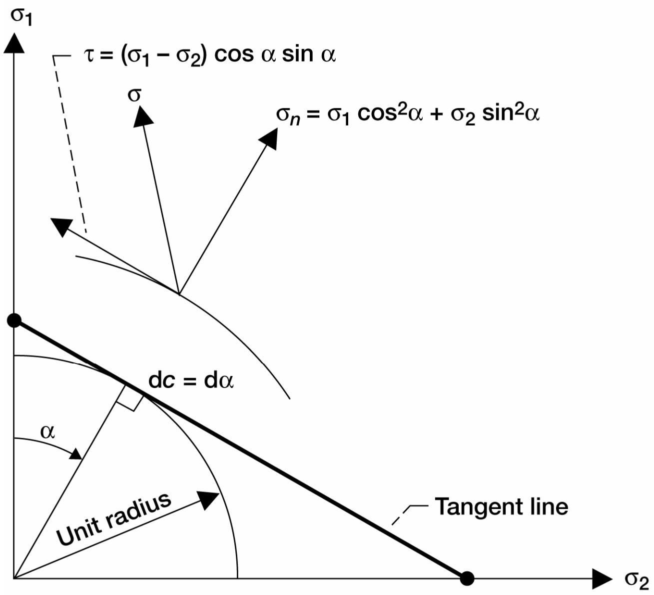

Figure D.3.—Normal and shear stress as a function of α projected onto a tangent line to a circle of unit radius (in principal stress space). Direction cosines: $\ell = \cos\alpha$, $m = \sin\alpha$.

For a given element, $\sigma_{\mathrm{I}eq}(x, y, \alpha)$ is the projected equivalent stress over the first quadrant of a circle of unit radius in principal stress space, as shown in figure D.3. Equation (D44) circumvents the computation of $\omega(\Sigma, \sigma_{\mathrm{I}eqc})$ and is used to obtain the component probability of failure in CARES/*Life*.

The finite element method enables discretization of the surface of the component into incremental area elements. CARES/*Life* evaluates the failure probability at the gaussian integration points of shell elements or optionally at the element centroid. Using the element integration points subdivides the element into subelements, where each A_{isub} corresponds to the $isub^{\mathrm{th}}$ subelement area. The element and subelement area of a two-dimensional element are calculated in similar fashion to the method outlined for equation (D33) except that the element area A_{elt} is calculated after transformation into a natural two-dimensional coordinate space:

$$A_{elt} = \int_{-1}^{1}\int_{-1}^{1} \det \mathbf{J}(r,s)\,\mathrm{d}r\,\mathrm{d}s \tag{D45}$$

Powers et al. (1992) gives further details of the subelementing procedure as used in CARES/*Life*.

The stress state in each subelement is assumed to be uniform, and the numerical formulation of equation (D44) is

$$P_{fS} = 1 - \exp\left\{-2\,\frac{k_{BS}}{\pi}\sum_{isub=1}^{n_{\mathrm{sub}}} A_{isub}\left[\int_0^{\pi/2} \sigma_{\mathrm{I}eq}^{m_S}(\alpha)\,\mathrm{d}\alpha\right]_{isub}\right\} \tag{D46}$$

where n_{sub} is the total number of subelements. If k_{BS} is element dependent, it will appear inside the brackets. CARES/*Life* uses gaussian numerical integration to evaluate equation (D46). This is detailed further in section D.2.3, beginning at equation (D246).

For the plane stress condition, selecting an arbitrary plane and imposing equilibrium conditions yields the following equations:

$$\sigma^2 = (\sigma_1 \ell)^2 + (\sigma_2 m)^2 \tag{D47}$$

and

$$\sigma_n = \sigma_1 \ell^2 + \sigma_2 m^2 \tag{D48}$$

$$\tau^2 = \sigma^2 - \sigma_n^2 \tag{D49}$$

where σ is the total traction vector acting on the crack plane and the direction cosines ℓ and m are given in figure D.3 in terms of trigonometric functions of α.

Fracture occurs when the equivalent stress $\sigma_{\mathrm{I}eq} \geq \sigma_{\mathrm{I}eqc}$. For the shear-insensitive case, fracture depends only on the value of the normal tensile stress such that $\sigma_{\mathrm{I}eq} = \sigma_n$. For shear-sensitive cracks and colinear crack extension, assuming a Griffith crack with $K_{\mathrm{I}} = \sigma_n \sqrt{\pi a}$ and $K_{\mathrm{II}} = \tau \sqrt{\pi a}$, we obtain as before

$$\sigma_{\mathrm{I}eq} = \sqrt{\sigma_n^2 + \tau^2} \tag{D50}$$

whereas for a Griffith notch subjected to plane strain conditions with $K_{\mathrm{I}} = 1.1215\, \sigma_n \sqrt{\pi a}$ and $K_{\mathrm{III}} = \tau \sqrt{\pi a}$ (Sih, 1973), we obtain

$$\sigma_{\mathrm{I}eq} = \sqrt{\sigma_n^2 + \frac{0.7951}{(1-\nu)}\tau^2} \tag{D51}$$

Note that the equivalent stress for the Griffith crack is dependent on modes I and II, whereas the equivalent stress for the Griffith notch is dependent on modes I and III (Gyekenyesi and Nemeth, 1987).

For noncoplanar crack growth, from equation (D30) the effective stress equation for the Griffith crack is

$$\sigma_{\mathrm{I}eq} = \frac{1}{2}\left[\sigma_n + \sqrt{\sigma_n^2 + 4\left(\frac{\tau}{\overline{C}}\right)^2}\,\right] \tag{D52}$$

and for the Griffith notch is

$$\sigma_{\mathrm{I}eq} = \frac{1}{2}\left[\sigma_n + \sqrt{\sigma_n^2 + 3.1803\left(\frac{\tau}{\overline{C}}\right)^2}\,\right] \tag{D53}$$

For a semicircular surface crack, $K_{\mathrm{I}} = 1.366\, \sigma_n \sqrt{a}$, $K_{\mathrm{II}} = 1.241\, \tau \sqrt{a}$, and $K_{\mathrm{III}} = 0.133\, \tau \sqrt{a}$ (Smith et al., 1967; and Smith and Sorensen, 1974). Since the contribution of K_{III} is small, it is neglected, and thus the effective stress for this case is

$$\sigma_{\mathrm{I}eq} = \frac{1}{2}\left[\sigma_n + \sqrt{\sigma_n^2 + 3.301\left(\frac{\tau}{\overline{C}}\right)^2}\,\right] \tag{D54}$$

For the same stress state and identical $\overline{C}$, the Griffith crack is the most shear sensitive, whereas the Griffith notch and the semicircular crack give almost identical predictions.

D.2.1.4 Material strength characterization.—Ceramic inert strength due to inherent flaws is described by the simple Weibull uniaxial cumulative distribution function. For brittle materials, tensile strength, compressive strength, shear strength, flexural strength, and theoretical strength all have unique meanings and different values. The theoretical strength is defined as the tensile stress required to break atomic bonds, which typically ranges from 1/10th to 1/5th of the elastic modulus for ceramic materials. Because of processing flaws, this strength is never obtained. In an inert environment, a much more meaningful strength measurement is the inert strength or ultimate tensile strength in uniaxial tension or flexural testing. In flexural strength testing, the bend strength σ_f of a ceramic is defined as the maximum tensile stress in the beam specimen (MOR), which in this situation occurs on the specimen surface. The main objective of the CARES/*Life* program is to characterize ceramic strength in terms of either the MOR or the pure uniaxial strength, and to use this information with appropriate analysis to predict component response under complex multiaxial stress states. This section deals with the calculation of the Weibull scale parameter σ_o and the Batdorf crack-density coefficient k_B. Closed-form solutions for σ_o are given for the uniaxial tensile, three-point bending, and four-point bending specimen geometries. Also, simplified Weibull equations are described that facilitate evaluation of Weibull parameters from experimental data. Procedures for obtaining Weibull parameters from experimental data are described in the following section (D.2.1.5).

Typically for brittle materials, the Weibull parameters are determined from simple specimen geometry and loading conditions, such as beams under flexure and either cylindrical or flat specimens under uniform uniaxial tension. For fast-fracture in an inert environment, the flexural test failure probability can be expressed in terms of the maximum stress (or extreme fiber stress) in the specimen σ_f at the moment of fracture by using the two-parameter Weibull form given in equations (D9) and (D35):

$$P_f = 1-\exp\left[-\left(\frac{\sigma_f}{\sigma_\theta}\right)^m\right] \tag{D55}$$

where m is the volume- or area-based fast-fracture Weibull modulus and σ_θ is the volume- or area-based specimen characteristic strength. The Weibull scale parameter σ_o (as defined in eqs. (D7) and (D35) for volume and surface cracks, respectively) is determined from σ_θ, m, the specimen geometry, and the loading configuration. The scale parameter σ_o is a material property, whereas σ_θ includes the effects of the specimen dimensions and stress distribution. The characteristic strength σ_θ is defined as the uniform stress or extreme fiber stress at which the probability of failure is 0.6321. The component failure behavior in fast-fracture, equation (D55), is only a function of σ_f and the empirically determined parameters m and σ_θ. Procedures such as the least-squares method or maximum-likelihood analysis are used to estimate m and σ_θ from experimental fracture data as described in the next section (D.2.1.5).

The uniaxial inert strength distribution for volume flaws (eq. (D9)) is expressed in terms of the extreme fiber fracture stress σ_f of the specimen by

$$P_{fV} = 1-\exp\left[-V_e\left(\frac{\sigma_f}{\sigma_{oV}}\right)^{m_V}\right] \tag{D56}$$

where an effective volume V_e is defined by equating the risk of rupture, equation (D9), with equation (D55).

$$V_e = \int_V \left(\frac{\sigma(x,y,z)}{\sigma_f}\right)^{m_V} \mathrm{d}V = \left(\frac{\sigma_{oV}}{\sigma_{\theta V}}\right)^{m_V} \tag{D57}$$

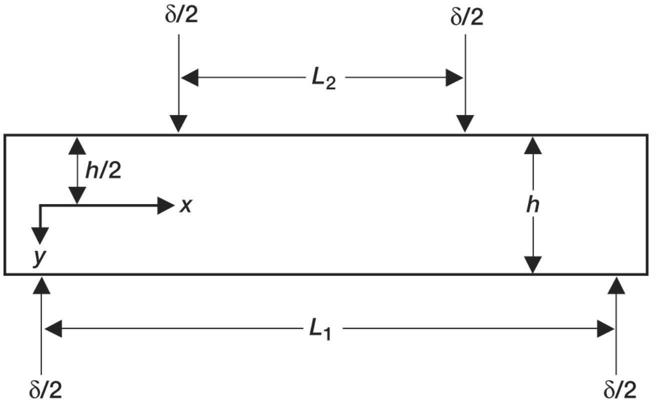

Figure D.4.—Four-point bend specimen geometry; *w*, beam width; δ, applied load.

The effective volume is the equivalent amount of volume under a uniform uniaxial tensile stress of magnitude σ_f that is needed to give an identical failure probability as the specimen. Comparing equations (D55) and (D56) we solve the volume-flaw scale parameter as

$$\sigma_{oV} = \sigma_{\theta V}\, V_e^{1/m_V} \tag{D58}$$

For the four-point bend specimen geometry shown in figure D.4, the tensile stress distribution in the specimen is

$$\begin{aligned} \sigma_x &= \frac{4xy\sigma_f}{(L_1 - L_2)h} & 0 \le x \le \frac{L_1 - L_2}{2} \\ \sigma_x &= \frac{2y\sigma_f}{h} & \frac{L_1 - L_2}{2} \le x \le \frac{L_1 + L_2}{2} \\ \sigma_x &= \frac{4(L_1 - x)y\sigma_f}{(L_1 - L_2)h} & \frac{L_1 + L_2}{2} \le x \le L_1 \end{aligned} \tag{D59}$$

where for the applied load δ the extreme fiber stress is $\sigma_f = (3/2)[\delta(L_1 - L_2)/wh^2]$.

Substituting equation (D59) into equation (D57) and solving for the effective volume, we obtain

$$V_e = \frac{wh}{2}\frac{(L_1 + m_V L_2)}{(m_V + 1)^2} \tag{D60}$$

The effective volume for the three-point bend specimen geometry is obtained when $L_2 = 0$ in equation (D60). For uniaxial tensile loading, the effective volume is equal to the gauge volume V_g, which is the uniformly stressed region where fracture is expected to occur.

When a specimen is subjected to multiaxial stresses, the PIA and Batdorf theories are used to equate the specimen strength to the uniaxial stress state. For the PIA theory, the effective volume used with equation (D56) is

$$V_e = \left(\frac{1}{\sigma_f}\right)^{m_V} \int_V \left(\sigma_1^{m_V} + \sigma_2^{m_V} + \sigma_3^{m_V}\right) \mathrm{d}V \tag{D61}$$

where $\sigma_1 \geq \sigma_2 \geq \sigma_3$ are functions of (x, y, z) and negative values are taken as zero. In this case, σ_f represents the maximum principal stress found in the component. For the Batdorf theory, the effective volume used with equation (D56) is defined as

$$V_e = \frac{2\bar{k}_{BV}}{\pi}\int_V \left\{ \int_0^{\pi/2}\int_0^{\pi/2} \left[\frac{\sigma_{\mathrm{I}eq}\left(x,y,z,\alpha,\beta\right)}{\sigma_f}\right]^{m_V} \sin\alpha \ \mathrm{d}\alpha \ \mathrm{d}\beta \right\} \mathrm{d}V \tag{D62}$$

where

$$\bar{k}_{BV} = \frac{k_{BV}}{k_{wV}} \tag{D63}$$

The term $\bar{k}_{BV}$ is the normalized Batdorf crack-density coefficient for volume flaws. It is obtained by equating the risks of rupture of equations (D9) and (D20), the polyaxial Batdorf theory to the uniaxial Weibull model, for an imposed uniaxial stress state or, equivalently, by equating the effective volumes in equations (D57) and (D62). Under a uniform uniaxial stress of magnitude σ_1, this yields

$$\bar{k}_{BV} = \frac{\pi}{2\int_0^{\pi/2}\int_0^{\pi/2}\left(\frac{\sigma_{\mathrm{I}eq}(\sigma_1,\alpha,\beta)}{\sigma_1}\right)^{m_V} \sin\alpha \ \mathrm{d}\alpha \ \mathrm{d}\beta} \tag{D64}$$

This equation is evaluated numerically except for two special cases where a closed-form solution is known to exist. For the shear-insensitive fracture criterion

$$\left[\frac{\sigma_{\mathrm{I}eq}(\sigma_1,\alpha,\beta)}{\sigma_1}\right] = \cos^2\alpha \tag{D65}$$

Substituting into equation (D64), then

$$\bar{k}_{BV} = 2m_V + 1 \tag{D66}$$

For the coplanar strain-energy release rate criterion and the Griffith crack geometry,

$$\left[\frac{\sigma_{\mathrm{I}eq}(\sigma_1,\alpha,\beta)}{\sigma_1}\right] = \cos\alpha \tag{D67}$$

Again, substituting into equation (D64) gives

$$\bar{k}_{BV} = m_V + 1 \tag{D68}$$

For surface flaws, the uniaxial inert strength distribution (eq. (D35)) is expressed in terms of the extreme fiber fracture stress σ_f of the specimen by

$$P_{fS} = 1 - \exp\left[-A_e\left(\frac{\sigma_f}{\sigma_{oS}}\right)^{m_S}\right] \tag{D69}$$

where an effective area A_e is defined:

$$A_e = \int_A \left(\frac{\sigma}{\sigma_f} \right)^{m_S} \mathrm{d}\,A \tag{D70}$$

Comparing equations (D55) and (D69), we solve the surface-flaw scale parameter as

$$\sigma_{oS} = \sigma_{\theta S}\; A_e^{1/m_S} \tag{D71}$$

Referring to equation (D59) for the four-point bend specimen geometry (fig. D.4), we see that the tensile stress on the beam surface, $y = h/2$, is

$$\begin{aligned}
&\sigma_x = \frac{2x\sigma_f}{(L_1 - L_2)} && 0 \le x \le \frac{L_1 - L_2}{2} \\
&\sigma_x = \sigma_f && \frac{L_1 - L_2}{2} \le x \le \frac{L_1 + L_2}{2} \\
&\sigma_x = \frac{2(L_1 - x)}{(L_1 - L_2)}\sigma_f && \frac{L_1 + L_2}{2} \le x \le L_1
\end{aligned} \tag{D72}$$

Substituting equation (D72) and equation (D59) for the side surface stress distributions into equation (D70) and performing the integration, we obtain the effective area as

$$A_e = \left[\frac{\left(\dfrac{L_2}{L_1}\right) m_S + 1}{(m_S + 1)^2} \right] \left(\frac{m_S\, w}{w + h} + 1 \right) (w + h) L_1 \tag{D73}$$

The effective area for the three-point bending specimen geometry is obtained when $L_2 = 0$ in equation (D73). For uniaxial tensile loading, the effective area is equal to the specimen gauge area A_g, which is the total specimen surface area of interest.

When a specimen is subjected to multiaxial stresses, the PIA and Batdorf model risks of rupture are equated to the uniaxial Weibull risk of rupture given by equation (D69). For the PIA model, the effective area used with equation (D69) is

$$A_e = \left(\frac{1}{\sigma_f} \right)^{m_S} \int_A \left[\sigma_1(x, y)^{m_S} + \sigma_2(x, y)^{m_S} \right] \mathrm{d}A \tag{D74}$$

and σ_f represents the maximum principal stress found on the component. For the Batdorf theory, the effective area used with equation (D69) is

$$A_e = \frac{2\bar{k}_{BS}}{\pi} \int_A \left\{ \int_0^{\pi/2} \left[\frac{\sigma_{\mathrm{I}eq}(x, y, \alpha)}{\sigma_f} \right]^{m_S} \mathrm{d}\alpha \right\} \mathrm{d}A \tag{D75}$$

where

$$\bar{k}_{BS} = \frac{k_{BS}}{k_{wS}} \tag{D76}$$

The term $\bar{k}_{BS}$ is the normalized Batdorf crack-density coefficient for surface flaws. In CARES/*Life*, the normalized Batdorf crack-density coefficient for surface flaws is found for a uniaxially loaded specimen by equating the risk-of-ruptures of equations (D35) and (D44), or equivalently by equating the effective areas in equations (D70) and (D75). For a uniform uniaxial stress of magnitude σ_1, this yields

$$\bar{k}_{BS} = \frac{\pi}{2\int_0^{\pi/2}\left[\dfrac{\sigma_{\mathrm{I}eq}(\sigma_1,\alpha)}{\sigma_1}\right]^{m_S} \mathrm{d}\alpha} \tag{D77}$$

This equation is evaluated numerically. A closed-form solution is known to exist for the shear-insensitive fracture criterion (Gross and Gyekenyesi, 1989). Since

$$\left[\frac{\sigma_{\mathrm{I}eq}(\sigma_1,\alpha)}{\sigma_1}\right] = \cos^2\alpha \tag{D78}$$

substituting into equation (D77) gives

$$\bar{k}_{BS} = \frac{\sqrt{\pi}\, m_S\, \Gamma(m_S)}{\Gamma\left(m_S + \dfrac{1}{2}\right)} \tag{D79}$$

For the shear-sensitive fracture criterion, Griffith crack geometry, and colinear crack extension,

$$\left[\frac{\sigma_{\mathrm{I}eq}(\sigma_1,\alpha)}{\sigma_1}\right] = \cos\alpha \tag{D80}$$

Again, substituting into equation (D77) gives

$$\bar{k}_{BS} = \frac{\sqrt{\pi}\, m_S\, \Gamma\left(\dfrac{m_S}{2}\right)}{2\,\Gamma\left(\dfrac{m_S+1}{2}\right)} \tag{D81}$$

D.2.1.5 Estimation of statistical material strength parameters.—Selected statistical theories and equations for Weibull parameter estimation are explained in detail in Pai and Gyekenyesi (1988). The following is a brief description of these methods and how they are used in the CARES/*Life* code. For brittle materials, the Weibull parameters are determined from repeated fracture experiments on nominally identical specimens. Typically this involves a simple geometry and loading condition, such as beams under flexure or specimens with either a round or rectangular cross section under uniform uniaxial tension. As a rule of thumb, a minimum of 30 specimens are required to obtain parameter estimates with a reasonably narrow standard deviation within which the true values of the parameters are likely to reside. Since each specimen carries a fixed cost, experimentalists desire to use analytical methods that maximize the information that can be gained from a data sample while using the fewest possible number of specimens. CARES/*Life* accomplishes this by including efficient parameter estimation schemes as well as statistical measures to quantify the quality of the data.

For fast-fracture, the flexural test failure probability can be expressed in terms of the extreme fiber fracture stress σ_f by using a simplified two-parameter Weibull form as described by equation (D55), where m is the volume or area Weibull modulus and σ_θ is the volume or area specimen characteristic strength. Although the statistical theories and parameter estimation methods outlined in the following discussion are expressed in terms of the fast-fracture strength distribution, these techniques are equally applicable to the time-dependent distribution.

Before computing the estimates of the statistical parameters, it is essential that we carefully examine the available specimen data to screen them for outliers. Very often, a data set may contain one or more values that may not belong to the overall population. The statistical procedure used to detect the outliers at different significance levels is explained in Pai and Gyekenyesi (1988) and Stefansky (1972). This outlier test assumes that the data are normally distributed and from a complete sample. Therefore, the application of this test to the Weibull distribution and censored statistics is only approximate. CARES/*Life* improves the original technique (Pai and Gyekenyesi, 1988) by numerically integrating the *t*-distribution to calculate the critical values for significance levels in the range of 0.0 to 10.0 percent with a resolution of 0.1 percent (polynomial approximating functions are no longer used).

Various methods are available to estimate the statistical material parameters from experimental data for the two-parameter Weibull distribution. The success of the statistical approach depends on how well the probability density function fits the data. Two popular techniques used to evaluate the characteristic strength and shape parameters (σ_θ and m) from inert strength data are least-squares analysis and the maximum-likelihood method. Least-squares analysis is a special case of the maximum-likelihood method, where the error is normally distributed and has a zero mean and constant variance. The least-squares method is not suitable for calculating confidence intervals and unbiasing factors, which quantify the statistical uncertainties in the available data.

Equation (D55) can be linearized by taking the natural logarithm twice, yielding

$$\ln\left[\ln\left(\frac{1}{P_s}\right)\right]=\ln\left[\ln\left(\frac{1}{1-P_f}\right)\right]=\ln\left(\frac{1}{\sigma_\theta}\right)^m+m\ln\sigma_f \tag{D82}$$

For the least-squares analysis, it is necessary to obtain the line of best fit with slope m and an intercept that, as seen in equation (D82), is equal to $\ln(1/\sigma_\theta)^m$. The failure probability P_f is determined by conducting fracture tests on n specimens. The fracture stresses are ranked such that $\sigma_{f,1} < \sigma_{f,2} <\ldots< \sigma_{f,i} <\ldots< \sigma_{f,n}$. For rank regression analysis, the probability of failure of a specimen with rank i is

$$P_{f,i}=P_f\left(\sigma_{f,i}\right)=\frac{i-0.3}{n+0.4} \tag{D83}$$

By taking the partial derivative of the sum of the squared residuals with respect to m and σ_θ, and by equating the derivatives to zero, values of m and σ_θ are calculated.

With censored data (competing failure modes), one cannot directly use the rank regression analysis as given in equation (D83). To take into account the influence of the suspended items, Johnson (1964) developed the rank increment technique. For this technique, all observed fracture stresses are arranged in ascending order, and rank increment values are calculated for each failure stress from the following equation:

$$\text{Rank increment}=\frac{(n+1)-\text{previous adjusted rank}}{1+\text{number of items beyond present suspended item}} \tag{D84}$$

The new adjusted rank values are obtained by adding the rank increment value to the previously adjusted rank. These adjusted rank values are then used to calculate the failure probability by using the median rank regression equation (D83). Finally, the estimated Weibull parameters for m and σ_θ are obtained.

Since the distribution of errors from the data is not normal, the maximum-likelihood method is often preferred in Weibull analysis. This method has certain inherent properties. The likelihood equation from which the maximum-likelihood estimates (MLEs) are obtained will have a unique solution. In addition, as the sample size increases, the solution converges to the true values of the parameters. Another feature of the maximum-likelihood method is that there are no ranking functions or linear regression analysis when complete or censored samples are analyzed. The likelihood equation for a complete sample is given by

$$L = \prod_{i=1}^{n} \left(\frac{m}{\sigma_\theta} \right) \left(\frac{\sigma_{f,i}}{\sigma_\theta} \right)^{m-1} \exp\left[-\left(\frac{\sigma_{f,i}}{\sigma_\theta} \right)^{m} \right] \tag{D85}$$

The values of m and σ_θ that maximize the likelihood function L are determined by taking the partial derivative of the logarithm of the likelihood function with respect to m and σ_θ. The estimated values, $\hat{m}$ and $\hat{\sigma}_\theta$, are obtained by equating the resulting expressions to zero and solving the simultaneous equations with the Newton-Raphson iterative technique. The MLEs of m and σ_θ are designated by $\hat{m}_V$ and $\hat{\sigma}_{\theta V}$ and by $\hat{m}_S$ and $\hat{\sigma}_{\theta S}$ for volume-flaw analysis and surface-flaw analysis, respectively. For censored statistics, we have

$$\frac{\sum_{i=1}^{n} \left(\sigma_{f,i}\right)^{\hat{m}} \ln\left(\sigma_{f,i}\right)}{\sum_{i=1}^{n} \left(\sigma_{f,i}\right)^{\hat{m}}} - \frac{1}{r} \sum_{i=1}^{r} \ln\left(\sigma_{f,i}\right) - \frac{1}{\hat{m}} = 0 \tag{D86}$$

and

$$\hat{\sigma}_\theta = \left(\frac{\sum_{i=1}^{n} \sigma_{f,i}^{\hat{m}}}{r} \right)^{1/\hat{m}} \tag{D87}$$

where r is the number of remaining specimens failed by the flaw mode for which parameters are being calculated. For a complete (uncensored) sample, r is replaced by n, which is the total size of the sample.

The MLE of the shape parameter is always a biased estimate that depends on the number of specimens in the sample. Unbiasing of the shape parameter estimate is desired to minimize the deviation between the sample and the true population. The unbiased estimate of m is obtained by multiplying the biased estimate with an unbiasing factor (Thoman et al., 1969). The confidence intervals for complete samples also can be obtained (Thoman et al., 1969). For censored samples, a rigorous method for obtaining confidence intervals has not been developed because of the complexity of competing failure modes. Confidence bounds for censored statistics are instead estimated in the CARES/*Life* code from the factors obtained from complete samples (Pai and Gyekenyesi, 1988). Confidence bounds enable users to estimate the uncertainty in the parameters as a function of the number of specimens. Bounds at a 90-percent confidence level (and therefore at 5 and 95 percentage points of distribution of the MLEs of the parameters) have been incorporated into the CARES/*Life* program, with data taken from Thoman et al. (1969).

Subjective judgement is needed to test the goodness of fit of the data to the assumed distribution. When graphical techniques are used, it can be very difficult to decide if the hypothesized distribution is valid, especially for small sample sizes. Therefore, many statistical tests have been developed to quantify the degree of correlation of the experimental data to the proposed distribution. In general, a statistic is a numerical value computed from a random sample of the total population. The difference between an empirical distribution function (EDF) and a hypothesized distribution function is called an EDF statistic. There are two major classes of EDF statistics, and they differ in the manner in which the functional (vertical) difference between the EDF and the proposed distribution function is considered. The KS goodness-of-fit statistic D belongs to the supremum class and is very effective for small samples. It uses the largest vertical difference between the two distribution functions to determine the goodness of fit. For the KS test, the sample is arranged in ascending order, and the EDF denoted by $F_n(\sigma_f)$ is a step function obtained from the following expressions:

$$\left.\begin{aligned} &F_n(\sigma_f) = 0 \quad \sigma_f < \sigma_{f,1} \\ &F_n(\sigma_f) = \frac{i}{n} \quad \sigma_{f,i} \le \sigma_f < \sigma_{f,(i+1)} \quad \text{and} \quad i = 1, 2, 3 \ldots, n-1 \\ &F_n(\sigma_f) = 1 \quad \sigma_{f,n} \le \sigma_f \end{aligned}\right\} \tag{D88}$$

where $\sigma_{f,1} < \sigma_{f,2} < \ldots \sigma_{f,i} \ldots < \sigma_{f,n}$ are the ordered fracture stresses from a sample of size n. The statistic D is obtained by initially evaluating two other statistics, D^+ and D^- (the largest vertical difference when $F_n(\sigma_f)$ is greater than the distribution function $F(\sigma_f)$, where $F(\sigma_f) = P_f$ in eq. (D55), and the largest vertical difference when $F_n(\sigma_f)$ is smaller than $F(\sigma_f)$, respectively). All three statistics are calculated by using the following expressions:

$$\begin{aligned} D^+ &= \left| \frac{i}{n} - F(\sigma_{f,i}) \right| \\ D^- &= \left| F(\sigma_{f,i}) - \frac{i-1}{n} \right| \qquad i = 1, 2, \ldots, n \\ D &= \max(D^+, D^-) \end{aligned} \tag{D89}$$

For ceramics design, the $F(\sigma_{f,i})$'s are equal to P_f's and are calculated from equation (D55).

On the other hand, the AD statistic A^2 belongs to the quadratic class and is a more powerful goodness-of-fit statistic. It evaluates the discrepancy between the two distributions through squared differences and the use of an appropriate weighting function. The statistic A^2 is given by

$$A^2 = -n - \left(\frac{1}{n}\right) \sum_{i=1}^{n} (2i-1) \left\{ \ln F(\sigma_{f,i}) + \ln\left[1 - F(\sigma_{f,(n+1-i)})\right] \right\} \tag{D90}$$

and again, $F(\sigma_{f,i})$ are the predicted failure probabilities obtained from equation (D55).

Corresponding significance levels SL are calculated from the D and A^2 statistics. From previous surveys (Pai and Gyekenyesi, 1988), there is no specific mention of an absolute accepted significance level. Therefore, users must be subjective, using their own judgment in either accepting or rejecting the hypothesis that the data fit a Weibull distribution. However, a higher value of SL indicates that the data fit the distribution more closely. In CARES/*Life*, the significance level is calculated with the assumption that the Weibull parameters are calculated independent of the observed strength data. However, the Weibull parameters are actually estimates based on the experimental data, and hence the assumption of independence is violated. We recommend that the significance level be viewed as a relative measure of goodness of fit and not as an absolute measure.

For complete samples, the 90-percent Kanofsky-Srinivasan confidence band values about the proposed distribution are also calculated to ascertain the fit of the data. These values are similar to the KS statistic D centered around the EDF. The bands are generated by

$$\text{Confidence bands} = \left[F\left(\sigma_f\right) - K(n), F\left(\sigma_f\right) + K(n)\right] \tag{D91}$$

where $F(\sigma_f)$ is the failure probability obtained by substituting the Weibull parameters in equation (D55). The Kanofsky functions, denoted by $K(n)$, are described in Abernethy et al. (1983).

Some limitations are intrinsic to a purely statistical approach to design. One problem occurs when the design stress is well below the range of experimental data, as shown in figure D.5. Extrapolation of the Weibull distribution into this regime may yield erroneous results if other phenomena are present. When two flaw populations exist concurrently, but only one (population *A*) is active in the strength regime tested, the predicted failure probability may be incorrect. Furthermore, if the threshold strength is not zero, the strength may be underestimated. Finally, an approach based only on statistics can allow for stress-state effects only in an empirical fashion.

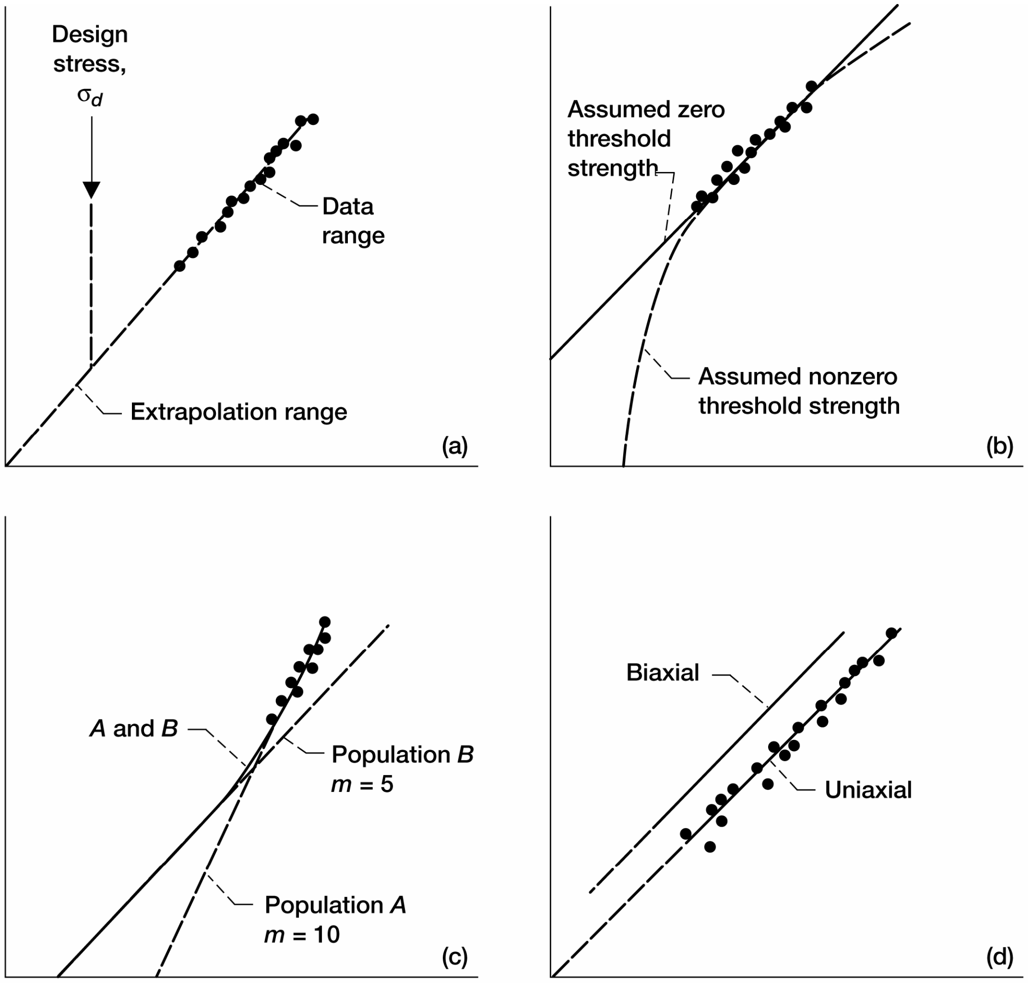

Figure D.5.—Limitations of experimental data extrapolation and statistical approach to design. (a) Basic data. (b) Nonzero threshold strength. (c) Undetected flaw populations. (d) Stress state effects.

D.2.2 Time-Dependent Reliability Analysis

D.2.2.1 Overview.—For ceramics and glasses, the ability to sustain a load degrades over time because of a variety of possible effects, such as oxidation, creep, stress corrosion, and cyclic fatigue. Stress corrosion and cyclic fatigue are representatives of a phenomenon called SCG, which initiates on a preexisting flaw and continues until a critical length is reached, causing catastrophic propagation. This occurs when the equivalent mode-I SIF $K_{\mathrm{I}eq}$ equals the fracture toughness $K_{\mathrm{I}c}$. The SCG failure mechanism is load induced over time. It can also be a function of the chemical reaction with the environment, debris wedging near the crack tip, the progressive deterioration of bridging ligaments, and other factors. Because of this complexity, the models that have been developed tend to be semiempirical and approximate the phenomenological behavior of SCG.

The previous equations in this appendix assumed that no SCG occurred prior to failure, and all failures were assumed to be independent of the time and history of previous thermal-mechanical loadings. The effects of time-dependent SCG on component reliability will now be addressed. Creep and material healing mechanisms are not addressed. Proof testing (Evans and Wiederhorn, 1974b) will improve the reliability of a survived component. This form of testing results in an attenuated probability of failure and a predicted minimum life expectancy of the survived components under the service load. This subject is discussed in section D.2.2.6.

For the analysis of time-dependent reliability, in addition to the Weibull shape and scale parameters, the material-environmental fatigue parameters (N and B) are required. The derivations that follow develop the time-dependent probability of failure based on the mode-I equivalent stress distribution due to thermal-mechanical loading at time t_f, transformed to its equivalent stress distribution at time $t = 0$. Determination of the fatigue parameters is discussed in section D.2.2.5.

Investigations in the area of mode-I crack extension (Paris and Sih, 1965) have resulted in the following relationship:

$$K_{\mathrm{I}eq}(\Psi,t) = \sigma_{\mathrm{I}eq}(\Psi,t)\, Y \sqrt{a(\Psi,t)} \tag{D92}$$

where $K_{\mathrm{I}eq}$ is the equivalent mode-I SIF and $\sigma_{\mathrm{I}eq}$ is the equivalent mode-I far-field stress normal to a crack. The parameter Y is a function of crack geometry and can vary with SCG; however, we assume that Y is a fixed geometric constant, $a(\Psi,t)$ is the appropriate crack length at time t, and Ψ represents a location (x, y, z) within the body and the orientation (α, β) of the crack. In some models, such as the Weibull and PIA, Ψ represents a location (x, y, z) only. The equations presented in this section are based on the Batdorf theory and the PIA model. For the Batdorf theory, $\Psi = (x, y, z, \alpha, \beta)$ for volume-flaw analysis and $\Psi = (x, y, \alpha)$ for surface-flaw analysis. For the PIA model, $\Psi = (x, y, z)$ for volume-flaw analysis and $\Psi = (x, y)$ for surface-flaw analysis.

The crack growth as a function of the equivalent mode-I SIF is assumed to follow a power-law relationship:

$$\frac{\mathrm{d}\,a(\Psi,t)}{\mathrm{d}t} = A_1\, K_{\mathrm{I}eq}^{N}(\Psi,t) \tag{D93}$$

where A_1 and N are material and environmental parameters. Parameters A_1 and N are typically temperature dependent, and hence for a nonuniform temperature distribution, they are a function of location (x, y, z). In the following equations, A_1 and N are shown for isothermal conditions. Substituting equation (D92) into equation (D93) yields

$$\frac{\mathrm{d}\,a(\Psi,t)}{\mathrm{d}t} = A_1\, \sigma_{\mathrm{I}eq}^{N}(\Psi,t)\, Y^N a^{N/2}(\Psi,t) \tag{D94}$$

The relationship at time t between $a(\Psi,t)$ and a mode-I critical effective stress $\sigma_{\mathrm{I}eqc}(\Psi,t)$ is

$$a(\Psi,t)=\left(\frac{K_{\mathrm{I}eqc}}{Y}\right)^{2}\sigma_{\mathrm{I}eqc}^{-2}(\Psi,t) \tag{D95}$$

Differentiating equation (D95) and substituting into equation (D94) results in

$$\int_{\sigma_{\mathrm{I}eqc}(\Psi,t=0)}^{\sigma_{\mathrm{I}eqc}(\Psi,t_f)}\sigma_{\mathrm{I}eqc}^{N-3}(\Psi,t)\,\mathrm{d}\sigma_{\mathrm{I}eqc}=-A_1Y^2\,\frac{K_{\mathrm{I}eqc}^{N-2}}{2}\int_0^{t_f}\sigma_{\mathrm{I}eq}^{N}(\Psi,t)\,\mathrm{d}t \tag{D96}$$

where $\sigma_{\mathrm{I}eqc,0}(\Psi, t = 0)$ is the transformed critical equivalent stress distribution at $t = 0$, and $\sigma_{\mathrm{I}eqc}(\Psi, t_f)$ is the critical equivalent stress distribution in the component at time $t = t_f$. At the time of failure $t = t_f$, the critical equivalent stress (strength) of the crack $\sigma_{\mathrm{I}eqc}(\Psi, t_f)$ just equals the equivalent applied stress $\sigma_{\mathrm{I}eq}(\Psi, t_f)$. With this condition, an expression can be obtained for a transformed equivalent stress at time $t = 0$, henceforth denoted by $\sigma_{\mathrm{I}eq,0}(\Psi)$, where $\sigma_{\mathrm{I}eq,0}(\Psi) = \sigma_{\mathrm{I}eq}(\Psi, t = 0) = \sigma_{\mathrm{I}eqc}(\Psi, t = 0)$. The transformed equivalent stress (Thiemeier, 1989, and Wittig et al., 1991) is

$$\sigma_{\mathrm{I}eq,0}(\Psi)=\left[\frac{\int_0^{t_f}\sigma_{\mathrm{I}eq}^{N}(\Psi,t)\,\mathrm{d}t}{B}+\sigma_{\mathrm{I}eq}^{N-2}(\Psi,t_f)\right]^{\frac{1}{(N-2)}} \tag{D97}$$

where

$$B=\frac{2}{A_1\,Y^2\,K_{\mathrm{I}eqc}^{N-2}\,(N-2)} \tag{D98}$$

and N and B are the material and environmental fatigue parameters. The dimensionless fatigue parameter N is independent of the fracture criterion, and the parameter B has units of stress^2 × time. In CARES/*Life*, the value of B is adjusted to satisfy the requirement that for a uniaxial stress state, all models produce the same probability of failure. The determination of these parameters is addressed in section D.2.2.5.

D.2.2.1.1 Time-dependent volume-flaw reliability analysis: CARES/*Life* computes the time-dependent reliability of a ceramic component, assuming a crack-density distribution that is a function of the critical effective stress distribution. The crack-density coefficient is now time dependent. For volume-flaw analysis, the crack-density function is expressed as

$$\eta_v[\sigma(\Psi)]=k_{BV}\,\sigma_{\mathrm{I}eq,0}^{m_V}(\Psi) \tag{D99}$$

where k_{BV} and m_V are material constants and the transformed effective stress $\sigma_{\mathrm{I}eq,0}(\Psi)$ is expressed as

$$\sigma_{\mathrm{I}eq,0}(\Psi)=\left[\frac{\int_0^{t_f}\sigma_{\mathrm{I}eq}^{N_V}(\Psi,t)\,\mathrm{d}t}{B_{BV}}+\sigma_{\mathrm{I}eq}^{N_V-2}(\Psi,t_f)\right]^{\frac{1}{(N_V-2)}} \tag{D100}$$

where N_V and B_{BV} are material fatigue parameters. Note that the parameters m_V, σ_{0V}, N_V, and B_{BV} are not shown as functions of location (x, y, z), which they potentially are if the temperature distribution throughout the body is nonuniform. Based on a probability-of-failure model, a subscripted fatigue parameter, such as B_{BV} for the Batdorf model, is computed. The parameter B_{BV} is directly proportional to B. The various model-dependent subscripted fatigue parameters are all directly proportional to B. They are evaluated by satisfying the requirement that for a uniaxial stress state, all models produce the same probability of failure. For large values of N, all model fatigue parameters tend to B. The relationship between the B subscripted parameters is discussed in section D.2.2.4.

If the boundary load direction and/or location changes with time, the principal stress vectors change direction with respect to a fixed global coordinate system. If this occurs, the permanent reference axis becomes the fixed global coordinate system. The normal and shear stresses are computed with respect to the global coordinate system. The normal stress is

$$\sigma_n = \ell^2\sigma_x + m^2\sigma_y + n^2\sigma_z + 2\left(\ell m\,\tau_{xy} + mn\,\tau_{yz} + n\ell\,\tau_{zx}\right) \tag{D101}$$

and the shear stress is

$$\tau^2 = \left(\ell\,\sigma_x + m\,\tau_{yx} + n\,\tau_{zx}\right)^2 + \left(\ell\tau_{xy} + m\,\sigma_y + n\,\tau_{zy}\right)^2 + \left(\ell\,\tau_{xz} + m\,\tau_{yz} + n\,\sigma_z\right)^2 - \sigma_n^2 \tag{D102}$$

where ℓ, m, and n are the direction cosines defined in figure D.6. Symmetry conditions permit the integration of the equivalent mode-I stress projection over the upper half of the spherical surface as shown in figure D.6.

The time-dependent probability of failure for the Batdorf model is

$$P_{fV}\left(t_f\right) = 1 - \exp\left[-\frac{k_{BV}}{2\pi}\int_V \int_0^{2\pi}\int_0^{\pi/2} \sigma_{\mathrm{I}eq,0}^{m_V}(\Psi)\sin\alpha\ \mathrm{d}\alpha\ \mathrm{d}\beta\ \mathrm{dV}\right] \tag{D103}$$

where $\sigma_{\mathrm{I}eq,0}(\Psi)$ is the transformed effective stress distribution as given in equation (D100), and $\sigma_{\mathrm{I}eq,0}(\Psi)$ is dependent on the appropriate fracture criterion, crack shape, and time to failure t_f. The fracture criteria and crack shapes available for time-dependent analysis are identical to those used for fast fracture analysis. The available fracture criteria are the Weibull NSA criterion (a shear-insensitive case of the Batdorf theory), the maximum tensile stress criterion, the total coplanar strain-energy release rate criterion, and the noncoplanar crack-extension (Shetty) criterion.

For the PIA model, the probability of failure is

$$P_{fV}\left(t_f\right) = 1 - \exp\left\{-k_{wV}\int_V \left[\sigma_{1,0}^{m_V}(\Psi) + \sigma_{2,0}^{m_V}(\Psi) + \sigma_{3,0}^{m_V}(\Psi)\right]\mathrm{d}V\right\} \tag{D104}$$

where

$$\sigma_{i,0}(\Psi) = \left[\frac{\int_0^{t_f}\sigma_i^{N_V}\left(x,y,z,t\right)\mathrm{d}t}{B_{wV}} + \sigma_i^{N_V-2}\left(x,y,z,t_f\right)\right]^{\frac{1}{N_V-2}}$$

and $i = 1, 2, 3$. The principal tensile stress distributions are $\sigma_1(x, y, z, t)$, $\sigma_2(x, y, z, t)$, and $\sigma_3(x, y, z, t)$.

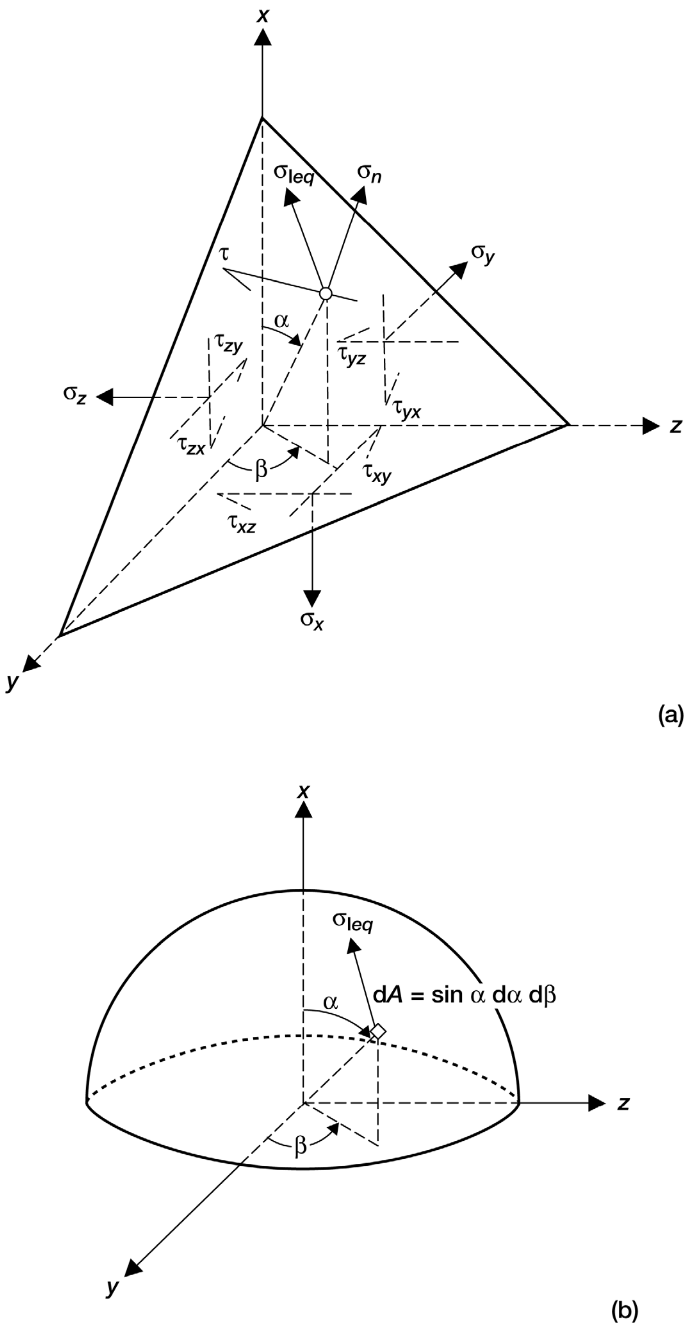

Figure D.6.—Projection of equivalent stress onto the upper half of a unit radius sphere in the global coordinate system. (a) Cauchy stress components on an infinitesimal tetrahedron. Direction cosines: $\ell = \cos\alpha$, $m = \sin\alpha\cos\beta$, $n = \sin\alpha\sin\beta$; $\sigma_n = \ell^2\sigma_x + m^2\sigma_y + n^2\sigma_z + 2(\ell m\tau_{xy} + mn\tau_{yz} + n\ell\tau_{zx})$; $\tau = \sqrt{(\ell\sigma_x + m\tau_{yx} + n\tau_{zx})^2 + (\ell\tau_{xy} + m\sigma_y + n\tau_{zy})^2 + (\ell\tau_{xz} + m\tau_{yz} + n\sigma_z)^2 - \sigma_n^2}$. (b) Global coordinate system.

For a stressed component, the probability of failure for volume-flaw analysis is calculated from equation (D103). The finite element method enables discretization of the component into incremental volume elements. CARES/*Life* evaluates the reliability at the gaussian integration points of the element or, optionally, at the element centroid. Using the element integration points subdivides the element into subelements, hence each

V_{isub} corresponds to the $isub^{\text{th}}$ subelement volume. In the usual context of finite element methods, the volume of a three-dimensional element V_{elt} is calculated after transformation into the natural coordinate space (Bathe, 1982):

$$V_{elt} = \int_{-1}^{1}\int_{-1}^{1}\int_{-1}^{1} \det \mathbf{J}(r,s,t)\,\mathrm{d}r\,\mathrm{d}s\,\mathrm{d}t \tag{D105}$$

where **J** is the Jacobian operator and *r*, *s*, and *t* are the natural coordinates. The subelement volume is defined as the contribution of the integration point to the element volume in the course of the numerical integration procedure. The volume of each subelement (corresponding to a Gauss integration point) is calculated using the shape functions inherent to the element type. The stress state in each subelement is assumed to be uniform. Powers et al. (1992) gives further details of the subelementing procedure as used in CARES/*Life*. The numerical solution of equation (D103) takes the following form:

$$P_{fV}(t_f) = 1 - \exp\left[-\frac{k_{BV}}{2\pi}\sum_{isub=1}^{n_{\text{sub}}} V_{isub}\left(\int_0^{2\pi}\int_0^{\pi/2} \sigma_{\mathrm{I}eq,0}^{m_V}(\Psi)\sin\alpha\,\mathrm{d}\alpha\,\mathrm{d}\beta\right)_{isub}\right] \tag{D106}$$

where n_{sub} is the total number of subelements. If k_{BV} is element dependent, it would appear inside the brackets. CARES/*Life* uses gaussian numerical integration to evaluate equation (D106). This is detailed further in section D.2.3, except that in this case the integration is performed over one-half of the unit radius sphere since a global coordinate system reference frame is used.

D.2.2.1.2 Time-dependent surface-flaw reliability analysis: CARES/*Life* computes the time-dependent reliability of a ceramic component assuming a crack-density distribution that is a function of the critical effective stress distribution. The crack-density coefficient is now time-dependent. For surface-flaw analysis, the crack-density function is expressed as

$$\eta_S[\sigma(\Psi)] = k_{BS}\,\sigma_{\mathrm{I}eq,0}^{m_S}(\Psi) \tag{D107}$$

where k_{BS} and m_S are material parameters and the transformed effective stress, $\sigma_{\mathrm{I}eq,0}$, is expressed as

$$\sigma_{\mathrm{I}eq,0}(\Psi) = \left[\frac{\int_0^{t_f}\sigma_{\mathrm{I}eq}^{N_S}(\Psi,t)\,\mathrm{d}t}{B_{BS}} + \sigma_{\mathrm{I}eq}^{N_S-2}(\Psi,t_f)\right]^{\frac{1}{N_S-2}} \tag{D108}$$

where N_S and B_{BS} are material fatigue parameters. Note that the parameters m_S, σ_{oS}, N_S, and B_{BS} are not shown as a function of location (*x*, *y*), which they potentially are if the temperature distribution on the surface is nonuniform. On the basis of a probability-of-failure model, a subscripted fatigue parameter, such as B_{BS} for the Batdorf model, is computed. The parameter B_{BS} is directly proportional to *B*. The various model-dependent subscripted fatigue parameters are all directly proportional to *B*. They are evaluated by satisfying the requirement that for a uniaxial stress state, all models produce the same probability of failure. For large values of *N*, all model fatigue parameters tend to *B*. The relationship between the *B* subscripted parameters is discussed in section D.2.2.4.

If the boundary load direction and/or location changes with time, the principal stress vectors change direction with respect to a fixed global coordinate system. If this occurs, the permanent reference axis becomes the fixed global coordinate system. The normal and shear stresses are computed with respect to the global coordinate system. The normal stress is

$$\sigma_n = \ell^2 \sigma_x + m^2 \sigma_y + 2\,\ell m\, \tau_{xy} \tag{D109}$$

and the shear stress is

$$\tau^2 = \left(\ell\, \sigma_x + m\, \tau_{yx}\right)^2 + \left(\ell\, \tau_{xy} + m\, \sigma_y\right)^2 - \sigma_n^2 \tag{D110}$$

where ℓ and m are the direction cosines. Symmetry conditions permit the projection of the equivalent mode-I stress over half of the perimeter of the unit radius circle.

The probability of failure for the Batdorf model is

$$P_{fS}\left(t_f\right) = 1 - \exp\left[-\frac{k_{BS}}{\pi} \int_A \int_0^{\pi} \sigma_{\mathrm{I}eq,0}^{m_S}\left(\Psi\right) \mathrm{d}\alpha\, \mathrm{d}A \right] \tag{D111}$$

where $\sigma_{\mathrm{I}eq,0}(\Psi)$ is the transformed effective stress distribution as given in equation (D108). The distribution $\sigma_{\mathrm{I}eq,0}(\Psi)$ is dependent on the appropriate fracture criterion, crack shape, and time to failure t_f. The criteria and crack shapes available for time-dependent analysis are identical to those used for fast fracture. The fracture criteria are the Weibull NSA criterion (a shear-insensitive case of the Batdorf theory), the total coplanar strain-energy release rate criterion, and the noncoplanar crack-extension (Shetty) criterion.

For the PIA model, the probability of failure is

$$P_{fS}\left(t_f\right) = 1 - \exp\left\{ -k_{wS} \int_A \left[\sigma_{1,0}^{m_S}\left(\Psi\right) + \sigma_{2,0}^{m_S}\left(\Psi\right) \right] \mathrm{d}A \right\} \tag{D112}$$

where

$$\sigma_{i,0}\left(\Psi\right) = \left[\frac{\int_0^{t_f} \sigma_i^{N_S}\left(x,y,t\right) \mathrm{d}t}{B_{wS}} + \sigma_i^{N_S-2}\left(x,y,t_f\right) \right]^{\frac{1}{N_S-2}}$$

$i = 1, 2$; and $\sigma_1(x, y, t)$ and $\sigma_2(x, y, t)$ are the principal tensile stress distributions.

The finite element method enables discretization of the surface of the component into incremental area elements. CARES/*Life* evaluates the reliability at the gaussian integration points of shell elements or, optionally, at the element centroids. Using the element integration points subdivides the element into subelements, where each A_{isub} corresponds to the $isub^{\text{th}}$ subelement area. The area of a two-dimensional element and subelement are calculated in similar fashion to the method outlined for equation (D105) except that the element area A_{elt} is calculated after transformation into a natural two-dimensional coordinate space:

$$A_{elt} = \int_{-1}^{1} \int_{-1}^{1} \det \mathbf{J}\left(r,s\right) \mathrm{d}r\, \mathrm{d}s \tag{D113}$$

Powers et al. (1992) gives further details of the subelementing procedure as used in CARES/*Life*.

The stress state in each subelement is assumed to be uniform, and the numerical formulation of equation (D111) is

$$P_{fS}\left(t_f\right)=1-\exp\left\{-\frac{k_{BS}}{\pi}\sum_{isub=1}^{n_{\text{sub}}} A_{isub}\left[\int_0^{\pi}\sigma_{\mathrm{I}eq,0}^{m_S}(\Psi)\,\mathrm{d}\alpha\right]_{isub}\right\} \tag{D114}$$

where n_{sub} is the total of number of subelements. If k_{BS} is element dependent, it appears inside the brackets. CARES/*Life* uses gaussian numerical integration to evaluate equation (D114). This is detailed further in section D.2.3, except that in this case the integration is performed over one-half of the unit radius circle since a global coordinate system reference frame is used.

D.2.2.1.3 Static fatigue: Static fatigue is defined as the application of a constant load over a period of time. For static fatigue, the mode-I equivalent stress is independent of time, and from equation (D97),

$$\sigma_{\mathrm{I}eq,0}(\Psi)=\sigma_{\mathrm{I}eq}(\Psi)\left[\frac{t_f\,\sigma_{\mathrm{I}eq}^2(\Psi)}{B}+1\right]^{\frac{1}{N-2}} \tag{D115}$$

For volume-flaw analysis (by symmetry, integrating over one octant of the unit radius sphere), the probability of failure for the Batdorf model is

$$P_{fV}\left(t_f\right)=1-\exp\left[\frac{-2k_{BV}}{\pi}\int_V\int_0^{\pi/2}\int_0^{\pi/2}\sigma_{\mathrm{I}eq,0}^{m_V}(\Psi)\sin\alpha\,\mathrm{d}\alpha\,\mathrm{d}\beta\,\mathrm{d}V\right] \tag{D116}$$

For the PIA model, the probability of failure is

$$P_{fV}\left(t_f\right)=1-\exp\left\{-k_{wV}\int_V\left[\sigma_{1,0}^{m_V}(\Psi)+\sigma_{2,0}^{m_V}(\Psi)+\sigma_{3,0}^{m_V}(\Psi)\right]\mathrm{d}V\right\} \tag{D117}$$

where

$$\sigma_{i,0}(\Psi)=\left[\frac{\sigma_i^{N_V}(x,y,z)\,t_f}{B_{wV}}+\sigma_i^{N_V-2}(x,y,z)\right]^{\frac{1}{N_V-2}}$$

for the principal stresses denoted by $i = 1, 2, 3$.

The probability of failure for surface flaws is analogous to that for volume flaws. For the Batdorf model, the probability of failure is expressed as

$$P_{fS}\left(t_f\right)=1-\exp\left[\frac{-2k_{BS}}{\pi}\int_A\int_0^{\pi/2}\sigma_{\mathrm{I}eq,0}^{m_S}(\Psi)\mathrm{d}\alpha\,\mathrm{d}A\right] \tag{D118}$$

For the PIA model, the probability of failure is

$$P_{fS}\left(t_f\right)=1-\exp\left\{-k_{wS}\int_A\left[\sigma_{1,0}^{m_S}(\Psi)+\sigma_{2,0}^{m_S}(\Psi)\right]\mathrm{d}A\right\} \tag{D119}$$

where

$$\sigma_{i,0}(\Psi) = \left[\frac{\sigma_i^{N_S}(x,y)\,t_f}{B_{wS}} + \sigma_i^{N_S-2}(x,y) \right]^{\frac{1}{N_S-2}}$$

for the principal stresses $i = 1, 2$.

D.2.2.1.4 Dynamic fatigue: Dynamic fatigue is defined as the application of a constant stress rate $\dot{\sigma}(\Psi)$ over a period of time t. Assuming the applied stress is zero at time $t = 0$, then

$$\sigma_{\mathrm{I}eq}(\Psi, t) = \dot{\sigma}(\Psi)\,t \tag{D120}$$

Substituting equation (D120) into equation (D97) results in

$$\sigma_{\mathrm{I}eq,0}(\Psi) = \left\{ \frac{\int_0^{t_f} \left[\dot{\sigma}(\Psi)t\right]^N \mathrm{d}t}{B} + \left[\dot{\sigma}(\Psi)t_f\right]^{N-2} \right\}^{\frac{1}{N-2}} \tag{D121}$$

At the time of failure $t = t_f$, equation (D120) can be restated as $\sigma_{\mathrm{I}eq}(\Psi, t_f) = \dot{\sigma}(\Psi)\,t_f$. Substituting this expression into equation (D97) results in

$$\sigma_{\mathrm{I}eq,0}(\Psi) = \left[\frac{\sigma_{\mathrm{I}eq}^{N}(\Psi, t_f)\,t_f}{(N+1)B} + \sigma_{\mathrm{I}eq}^{N-2}(\Psi, t_f) \right]^{\frac{1}{N-2}} \tag{D122}$$

For volume flaws, the Batdorf probability-of-failure equation is

$$P_{fV}(t_f) = 1 - \exp\left[-\frac{2\,k_{BV}}{\pi} \int_V \int_0^{\pi/2} \int_0^{\pi/2} \sigma_{\mathrm{I}eq,0}^{m_V}(\Psi) \sin\alpha \;\, \mathrm{d}\alpha\, \mathrm{d}\beta\, \mathrm{d}V \right] \tag{D123}$$

For the PIA model, the probability of failure is

$$P_{fV}(t_f) = 1 - \exp\left\{ -k_{wV} \int_V \left[\sigma_{1,0}^{m_V}(\Psi) + \sigma_{2,0}^{m_V}(\Psi) + \sigma_{3,0}^{m_V}(\Psi) \right] \mathrm{d}V \right\} \tag{D124}$$

where

$$\sigma_{i,0}(\Psi) = \left[\frac{\sigma_i^{N_V}(x,y,z,t_f)\,t_f}{(N_V+1)B_{wV}} + \sigma_i^{N_V-2}(x,y,z,t_f) \right]^{\frac{1}{N_V-2}}$$

for the principal stresses where $i = 1, 2, 3$.

For surface flaws, the Batdorf model probability of failure is

$$P_{fS}\left(t_f\right)=1-\exp\left[-\frac{2\,k_{BS}}{\pi}\int_A\int_0^{\pi/2}\sigma_{\mathrm{I}eq,0}^{m_S}\left(\Psi\right)\mathrm{d}\alpha\,\mathrm{d}A\right] \tag{D125}$$

For the PIA model, the probability of failure is

$$P_{fS}\left(t_f\right)=1-\exp\left\{-k_{wS}\int_A\left[\sigma_{1,0}^{m_S}\left(\Psi\right)+\sigma_{2,0}^{m_S}\left(\Psi\right)\right]\mathrm{d}A\right\} \tag{D126}$$

where

$$\sigma_{i,0}\left(\Psi\right)=\left[\frac{\sigma_i^{N_S}\left(x,y,t_f\right)t_f}{\left(N_S+1\right)B_{wS}}+\sigma_i^{N_S-2}\left(x,y,t_f\right)\right]^{\frac{1}{N_S-2}}$$

for the principal stresses where $i = 1, 2$.

D.2.2.1.5 Cyclic fatigue: Cyclic fatigue is the repeated application of a loading sequence. Analysis of the time-dependent probability of failure for a component subjected to various cyclic boundary load conditions is simplified by transforming that type of loading to an equivalent static state. The conversion satisfies the requirement that both systems will cause the same crack growth (Mencik, 1984). Implicit in this conversion is the validity of the crack-growth equation (D93). The probability of failure is obtained with respect to the transformed static state.

The fatigue parameters can also be determined from cyclic loaded specimens via transformation to an equivalent static state. Since static and cyclic tests can yield different results when the fatigue parameters are being determined, the type of loading used should simulate as closely as possible the service conditions. This is discussed in more detail in section D.2.2.5.

Evans (1980) and Mencik (1984) defined *g*-factors $g(\Psi)$, for various types of cyclic loading, that are used to convert the cyclic load pattern to an equivalent static state. For periodic loading, t_{per} is the time interval of one cycle, and $\sigma_{\mathrm{I}eqg}(\Psi)$ is the equivalent static stress acting over the same time interval, t_{per}, as the applied cyclic stress $\sigma_{\mathrm{I}eq}(\Psi, t)$. The equivalent static stress is defined as

$$\sigma_{\mathrm{I}eqg}\left(\Psi\right)=g\left(\Psi\right)^{1/N}\,\sigma_{ch}\left(\Psi\right) \tag{D127}$$

where $\sigma_{ch}(\Psi)$ is a characteristic value of $\sigma_{\mathrm{I}eq}(\Psi, t)$. Over one cycle where both load systems cause the same crack growth,

$$\sigma_{\mathrm{I}eqg}^N\left(\Psi\right)t_{\mathrm{per}}=\int_0^{t_{\mathrm{per}}}\sigma_{\mathrm{I}eq}^N\left(\Psi,t\right)\mathrm{d}t \tag{D128}$$

where

$$\sigma_{\mathrm{I}eqg}^N\left(\Psi\right)=\left[\frac{\int_0^{t_{\mathrm{per}}}\sigma_{\mathrm{I}eq}^N\left(\Psi,t\right)\mathrm{d}t}{t_{\mathrm{per}}}\right]=\sigma_{ch}^N\left(\Psi\right)g\left(\Psi\right) \tag{D129}$$

and the g-factor is

$$g(\Psi)=\left\{\frac{\int_0^{t_{\text{per}}}\left[\frac{\sigma_{\text{I}eq}(\Psi,t)}{\sigma_{ch}(\Psi)}\right]^N \mathrm{d}t}{t_{\text{per}}}\right\} \tag{D130}$$

In CARES/*Life*, the characteristic value $\sigma_{ch}(\Psi)$ of $\sigma_{\text{I}eq}(\Psi, t)$ is taken as $\sigma_{\text{I}eq,\max}(\Psi)$, the maximum stress of the periodic load over the cycle time interval t_{per}. For a periodic load over an extended time t_1,

$$\sigma_{\text{I}eqg}^N(\Psi)t_1=\int_0^{t_1}\sigma_{\text{I}eq}^N(\Psi,t)\,\mathrm{d}t= t_1\left[\frac{\int_0^{t_{\text{per}}}\sigma_{\text{I}eq}^N(\Psi,t)\,\mathrm{d}t}{t_{\text{per}}}\right]=g(\Psi)\sigma_{\text{I}eq,\max}^N(\Psi)t_1 \tag{D131}$$

When more than one type of loading is applied to a component, such as a periodic cyclic load and a static load, the g-factor is based on the effective variation of the combined loading. The g-factor can vary from element to element, and the stress-volume integration is performed over the hemisphere of the unit radius sphere for volume flaws and on the perimeter of the unit radius semicircle for surface flaws.

For n multiple, but different, cyclic loadings over an interval of time $t_n = t_f$,

$$\sigma_{\text{I}eqg}^N(\Psi)t_f=\int_0^{t_1}\sigma_{\text{I}eq}^N(\Psi,t)\,\mathrm{d}t+\int_{t_1}^{t_2}\sigma_{\text{I}eq}^N(\Psi,t)\,\mathrm{d}t+....+\int_{t_{n-1}}^{t_n}\sigma_{\text{I}eq}^N(\Psi,t)\,\mathrm{d}t \tag{D132}$$

Thus,

$$\sigma_{\text{I}eqg}^N(\Psi)t_f=\sum_{i=1}^{n}\sigma_{\text{I}eq,\max,i}^N(\Psi)g_i(\Psi)\Delta t_i \tag{D133}$$

where

$$\Delta t_i = t_i - t_{i-1}$$

and

$$g_i(\Psi)=\left\{\frac{\int_{t_{i-1}}^{t_i}\left[\frac{\sigma_{\text{I}eq,i}(\Psi,t)}{\sigma_{\text{I}eq,\max,i}(\Psi)}\right]^N \mathrm{d}t}{\Delta t_i}\right\}$$

where $\sigma_{\text{I}eq,\max,i}(\Psi)$ is the maximum value of $\sigma_{\text{I}eq}(\Psi)$ over Δt_i.

Another approach by Mencik is to define an equivalent static time t_{es} during which a characteristic stress (σ_{ch} is chosen as the maximum stress $\sigma_{\mathrm{I}eq,\max}(\Psi)$) would cause the same crack growth as the applied cyclic stress $\sigma_{\mathrm{I}eq}(\Psi, t)$ during time Δt. Thus,

$$\sigma_{\mathrm{I}eq,\max}^{N}(\Psi)\Delta t_{es}(\Psi) = \frac{\Delta t}{t_{\mathrm{per}}}\int_{0}^{t_{\mathrm{per}}}\sigma_{\mathrm{I}eq}^{N}(\Psi,t)\,\mathrm{d}t = \sigma_{\mathrm{I}eq,\max}^{N}(\Psi)\,g(\Psi)\,\Delta t \tag{D134}$$

or

$$\Delta t_{es}(\Psi) = g(\Psi)\Delta t \tag{D135}$$

For multiple, but different, cyclic loading over an interval of time $t_f = \Delta t_1 + \Delta t_2 + ... + \Delta t_n$

$$\begin{aligned}\sigma_{\mathrm{I}eq,\max}^{N}(\Psi)\left[\Delta t_{es,1}(\Psi) + \Delta t_{es,2}(\Psi) + ... + \Delta t_{es,n}(\Psi)\right] = \\ \sigma_{\mathrm{I}eq,\max}^{N}(\Psi)\left[g_1(\Psi)\Delta t_1 + g_2(\Psi)\Delta t_2 + ... + g_n(\Psi)\Delta t_n\right]\end{aligned} \tag{D136}$$

or

$$\sum_{i=1}^{\mathrm{n}} \Delta t_{es,i}(\Psi) = \sum_{i=1}^{\mathrm{n}} g_i(\Psi)\Delta t_i \tag{D137}$$

In this case, $\sigma_{\mathrm{I}eq,\max}$ is the maximum value of $\sigma_{\mathrm{I}eq}$ over t_n and $\sigma_{\mathrm{I}eq,\max}$ replaces $\sigma_{\mathrm{I}eq,\max,i}$ in the calculation of $g_i(\Psi)$.

Mencik (1984) lists g-factors for a variety of waveforms. Table D.I lists the g-factors for various loadings and waveforms supported by CARES/*Life*. A simple closed-form expression for the sine wave is not available, and consequently, a numerical evaluation is required.

CARES/*Life* adopts the approach of equation (D131) to compute the time-dependent reliability. Equation (D131), the static equivalent stress distribution, is substituted into equation (D97) where the time t_1 is replaced by t_f. Hence,

$$\sigma_{\mathrm{I}eq,0}(\Psi) = \sigma_{\mathrm{I}eq,\max}(\Psi)\left[\frac{g(\Psi)\sigma_{\mathrm{I}eq,\max}^{2}(\Psi)t_f}{B} + 1\right]^{\frac{1}{N-2}} \tag{D138}$$

Formulations for other failure models are developed analogously.

TABLE D.I.—g-FACTORS FOR WAVEFORMS WITH VARIOUS LOADINGS
$[H(t,C)=1 \text{ for } t \geq C;\ H(t,C)=0 \text{ for } t < C;\ \sigma_{11} \geq 0.]$

Loading function, $\sigma_{leq}(t)$	g-factor, $g=\frac{1}{t_{per}}\int_0^{t_{per}}\left(\frac{\sigma_{Ieq}(t_{\mathrm{per}})}{\sigma_{Ieq,\max}}\right)^N \mathrm{d}t$	Waveform
Static fatigue $\sigma_{leq}=$ constant	1	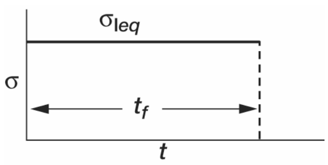
Dynamic fatigue $\sigma_{leq}(t)=\dot{\sigma}t$	$\frac{1}{N+1}$	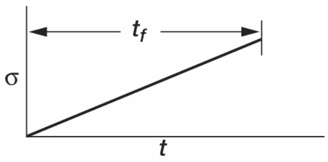
Cyclic square wave $\sigma_{Ieq}=\sigma_1[H(t,0)-H(t,t_1)]+\sigma_{11}[H(t,t_1)-H(t,t_{per})]$	$\frac{t_1+\left(\frac{\sigma_{11}}{\sigma_1}\right)^N t_{11}}{t_1+t_{11}}$	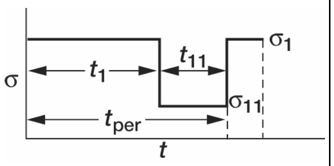
Sine wave $\sigma_{Ieq}(t)=\left(\frac{\sigma_1-\sigma_{11}}{2}\right)\sin\left(\frac{2\pi t}{t_{\mathrm{per}}}\right)+\left(\frac{\sigma_1+\sigma_{11}}{2}\right)$	$\frac{1}{t_{\mathrm{per}}}\int_0^{t_{\mathrm{per}}}\left[\frac{\sigma_1+\sigma_{11}+(\sigma_1-\sigma_{11})\sin\left(\frac{2\pi t}{t_{\mathrm{per}}}\right)}{2\sigma_1}\right]^N \mathrm{d}t$	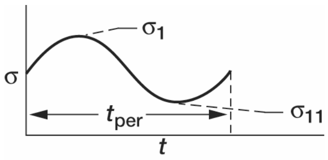
Cyclic saw-tooth wave $\sigma_{leq}(t)=\left(\frac{2(\sigma_1-\sigma_{11})t}{t_{\mathrm{per}}}+\sigma_{11}\right)\left[H(t,0)-H\left(t,\frac{t_{\mathrm{per}}}{2}\right)\right]$ $+\left(\frac{-2(\sigma_1-\sigma_{11})t}{t_{\mathrm{per}}}+2\sigma_1-\sigma_{11}\right)\left[H\left(t,\frac{t_{\mathrm{per}}}{2}\right)-H(t,t_{\mathrm{per}})\right]$	$\frac{\sigma_1-\sigma_{11}\left(\frac{\sigma_{11}}{\sigma_1}\right)^N}{(N+1)(\sigma_1-\sigma_{11})}$	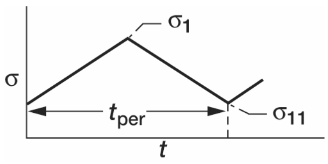
Positive half pulse of sine wave $\sigma_{Ieq}(t)=\left(\sigma_1\sin\left(\frac{2\pi t}{t_{per}}\right)\right)\left[H(t,0)-H\left(t,\frac{t_{\mathrm{per}}}{2}\right)\right]$	$\frac{\Gamma\left(\frac{N+1}{2}\right)}{\sqrt{\pi}\,N\,\Gamma\left(\frac{N}{2}\right)}$	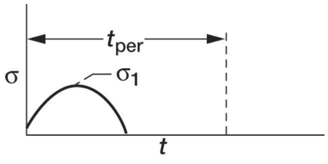

D.2.2.2 Application of the Paris and Walker laws.—This section considers the more general case of reliability modeling where the applied loading varies as a function of time. SCG is a complex phenomenon involving a combination of simultaneous and synergistic failure mechanisms. These can be grouped into two classes: static effects and cyclic effects. Static effects refer to the slow propagation of cracks under cyclic stresses and may be explained by the same environmental and corrosive processes responsible for SCG under static loads. Cyclic effects are functionally dependent on the number of cycles and on the duration of each cycle. The SCG phenomenon can be caused by a variety of effects, such as debris wedging or the degradation of bridging ligaments, but essentially it is based on the accumulation of some type of irreversible damage that tends to enhance the crack growth. Not all materials display cyclic effects. Glasses seem to show only static effects, whereas polycrystalline materials are more susceptible to cyclic effects. Modeling for cyclic effects is based on phenomenological criteria (Paris law and Walker law) traditionally used for metal fatigue.

Using *g*-factors with the power-law formulation to predict component life is an unconservative practice for materials prone to cyclic damage. To empirically model cyclic effects in ceramic materials, Dauskardt et al. (1990a and 1992) suggest the use of the Paris power-law expression (Paris and Erdogan, 1963), which has traditionally been used in metals design. Dauskardt et al. (1992) use the Walker modification of the Paris law (Walker, 1970, p. 1) to describe the crack-growth increment per cycle as

$$\frac{\mathrm{d}\,a(\Psi,n)}{\mathrm{d}n} = A_2\, K_{\mathrm{I}eq,\max}^{N-Q}(\Psi,n)\,\Delta K_{\mathrm{I}eq}^{Q}(\Psi,n) \tag{D139}$$

where n is the number of cycles,

$$K_{\mathrm{I}eq,\max}(\Psi,n) = \sigma_{\mathrm{I}eq,\max}(\Psi,n)\,Y\sqrt{a(\Psi,n)}$$

and $\Delta K_{\mathrm{I}eq}(\Psi, n)$ represents the range of the equivalent SIF over the load cycle.

$$\Delta K_{\mathrm{I}eq}(\Psi,n) = \Delta\sigma_{\mathrm{I}eq}(\Psi,n)\,Y\sqrt{a(\Psi,n)} = \left[\sigma_{\mathrm{I}eq,\max}(\Psi,n) - \sigma_{\mathrm{I}eq,\min}(\Psi,n)\right]Y\sqrt{a(\Psi,n)}$$

and A_2, N, and Q are the cyclic fatigue parameters determined from experiments. The Paris law is obtained when N and Q are equal in value. The subscripts “max” and “min” indicate the maximum and minimum cycle stress, respectively. The integration of equation (D139) parallels that of equation (D93), yielding

$$\sigma_{\mathrm{I}eq,0}(\Psi,n_f) = \left\{\frac{\int_{n=0}^{n_f}\left[1-R(\Psi,n)\right]^{Q}\sigma_{\mathrm{I}eq,\max}^{N}(\Psi,n)\,\mathrm{d}n}{B} + \sigma_{\mathrm{I}eq,\max}^{N-2}(\Psi,n_f)\right\}^{\frac{1}{N-2}} \tag{D140}$$

where

$$B = \frac{2}{A_2\, Y^2\, K_{\mathrm{I}eqc}^{N-2}\,(N-2)}$$

where n_f denotes the number of cycles to failure, B is now expressed in units of stress^2 × cycle (B is determined from cyclic data), and the R-ratio (defined as the ratio of the minimum to maximum cyclic stress) is

$$R(\Psi,n) = \frac{\sigma_{\mathrm{I}eq,\min}(\Psi,n)}{\sigma_{\mathrm{I}eq,\max}(\Psi,n)}$$

For a periodic cyclic stress, $R(\Psi,n)$ and $\sigma_{\mathrm{I}eq,\min}(\Psi, n)$ are independent of n, hence

$$\sigma_{\mathrm{I}eq,0}\left(\Psi, n_f\right) = \sigma_{\mathrm{I}eq,\max}\left(\Psi\right)\left\{\frac{\sigma^2_{\mathrm{I}eq,\max}\left(\Psi\right)\left[1-R\left(\Psi\right)\right]^{Q} n_f}{B} + 1\right\}^{\frac{1}{N-2}} \tag{D141}$$

When $R = 1$ (the static fatigue case), there is no time-dependent degradation of material strength due to cyclic effects. When $R < 0$, compressive stresses are present, which depending on the material, may or may not further degrade the strength. If no further degradation of strength occurs when $R < 0$, R should be set to zero in equation (D141). The probability of failure for cyclic fatigue using the Batdorf model for volume-flaw analysis is

$$P_{fV}\left(n_f\right) = 1 - \exp\left[\frac{-2\,k_{BV}}{\pi}\int_V \int_0^{\pi/2}\int_0^{\pi/2} \sigma^{m_V}_{\mathrm{I}eq,0}\left(\Psi, n_f\right) \sin\alpha \, \mathrm{d}\alpha \, \mathrm{d}\beta \, \mathrm{d}V\right] \tag{D142}$$

Analogously, equations may be derived for the PIA model or for surface-flaw analysis.

The Paris law should be used with prudence. Assuming that the static effects and cyclic effects are mutually exclusive events, the component reliability can be described as the product of the reliabilities calculated for each of these phenomena:

$$P_{S_{\text{combined}}} = P_{S_{\text{static effects}}} \, P_{S_{\text{cyclic effects}}} \tag{D143}$$

thus when $R = 1$, degradation due to static fatigue is accounted for.

D.2.2.3 Material failure characterization for static, cyclic, or dynamic loading.—For time-dependent fracture under static or cyclic fatigue loading, failure probability can be expressed in terms of the specimen time to failure t_f by using the two-parameter specimen uniaxial Weibull model (Paluszny and Nicholls, 1978)

$$P_f\left(t_f\right) = 1 - \exp\left[-\left(\frac{\sigma_{f,0}}{\sigma_\theta}\right)^m\right] = 1 - \exp\left\{-\left[\frac{\sigma_f^N\left(\Psi_0\right)g\left(\Psi_0\right)t_f}{B_u\,\sigma_\theta^{N-2}}\right]^{\tilde{m}}\right\} = 1 - \exp\left[-\left(\frac{t_f}{t_\theta}\right)^{\tilde{m}}\right] \tag{D144}$$

where

$$\tilde{m} = \frac{m}{\left(N-2\right)} \qquad t_\theta = \frac{B_u\,\sigma_\theta^{N-2}}{\sigma_f^N\left(\Psi_0\right)g\left(\Psi_0\right)}$$

and

$$\frac{\sigma_f^2\left(\Psi_0\right)g\left(\Psi_0\right)t_f}{B_u} >> 1$$

For static loading, $g(\Psi) = 1$. At location Ψ_o, $\sigma_f(\Psi_o)$ is the maximum static or cyclic failure stress in the specimen, $g(\Psi_o)$ is the g-factor at that location, σ_θ is the characteristic strength, $\sigma_{f,0}$ is the transformed static inert strength, $\tilde{m}$ is a modified Weibull modulus, and t_θ is the volume or area specimen characteristic time. Henceforth, $\sigma_f(\Psi_o)$ is replaced by σ_f, where location at Ψ_o is implied. The characteristic time is analogous to the characteristic strength. Equation (D144) allows the specimen time-dependent failure response to be described with a simple Weibull equation that is a function only of t_f and the empirically determined parameters $\tilde{m}$ and t_θ. Procedures such as the least-squares method or maximum-likelihood analysis can be used to estimate these parameters from experimental fracture data as described in section D.2.1.5.

For static or cyclic fatigue, if we use the uniaxial time-dependent Weibull distribution for volume flaws with the g-factor approach of equation (D130), and for

$$\frac{\sigma_{1,\max}^{2}(x,y,z)\,g(x,y,z)\,t_f}{B_{wV}} >> 1$$

then

$$P_{fV}(t_f) = 1 - \exp\left[\frac{-1}{\sigma_{oV}^{m_V}}\int_V \sigma_{1,0}^{m_V}(x,y,z)\,\mathrm{d}V\right] \tag{D145}$$

where

$$\sigma_{1,0}(x,y,z) = \left[\frac{\sigma_{1,\max}^{N_V}(x,y,z)\,g(x,y,z)\,t_f}{B_{wV}}\right]^{\frac{1}{N_V-2}}$$

and σ_1 indicates the first principal stress. For the case when the g-factor is constant throughout the specimen, henceforth denoted by g, equation (D145) can be expressed in terms of the maximum static or cyclic failure stress σ_f in the specimen by multiplying the numerator and denominator by $\sigma_f^{\tilde{m}_V N_V}$. Thus,

$$P_{fV}(t_f) = 1 - \exp\left[-V_{ef}\left(\frac{t_f}{t_{oV}}\right)^{\tilde{m}_V}\right] \tag{D146}$$

where

$$t_{oV} = \frac{B_{wV}\,\sigma_{oV}^{N_V-2}}{g\,\sigma_f^{N_V}}$$

and

$$V_{ef} = \int_V \left[\frac{\sigma_{1,\max}(x,y,z)}{\sigma_f}\right]^{\tilde{m}_V N_V} \mathrm{d}V \tag{D147}$$

The term V_{ef} is the modified effective volume when the applied stress distribution is normalized with respect to σ_f. All expressions previously derived for V_e are still applicable for V_{ef} with the exception that $\tilde{m}_V N_V$ should be substituted for m_V (see section D.2.2.4). For a constant g-factor, comparing equations (D144) and (D146) yields the time-dependent scale parameter relationship:

$$t_{oV} = t_{\theta V} \, V_{ef}^{1/\tilde{m}_V} \tag{D148}$$

The modified effective volume that is used with equation (D146) and the PIA model is

$$V_{ef} = \left(\frac{1}{\sigma_f}\right)^{\tilde{m}_V N_V} \int_V \left[\sigma_{1,\max}^{\tilde{m}_V N_V}(x,y,z) + \sigma_{2,\max}^{\tilde{m}_V N_V}(x,y,z) + \sigma_{3,\max}^{\tilde{m}_V N_V}(x,y,z)\right] \mathrm{d}V \tag{D149}$$

where the principal stresses are

$$\sigma_{1,\max}(x,y,z) \geq \sigma_{2,\max}(x,y,z) \geq \sigma_{3,\max}(x,y,z) \geq 0$$

For the Batdorf theory, the modified effective volume analogous with equation (D146) is defined as

$$V_{ef} = \frac{2\bar{k}_{BV}}{\pi} \int_V \left\{ \int_0^{\pi/2} \int_0^{\pi/2} \left[\frac{\sigma_{Ieq,\max}(\Psi)}{\sigma_f}\right]^{\tilde{m}_V N_V} \sin\alpha \; \mathrm{d}\alpha \; \mathrm{d}\beta \right\} \mathrm{d}V \tag{D150}$$

and

$$t_{oV} = \frac{B_{BV} \, \sigma_{oV}^{N_V - 2}}{g \, \sigma_f^{N_V}}$$

For surface flaws, the resulting equations are similar to those equations previously derived. Integration is performed over the specimen surface, and the modified effective area A_{ef} is obtained.

$$P_{fS}(t_f) = 1 - \exp\left[-A_{ef}\left(\frac{t_f}{t_{oS}}\right)^{\tilde{m}_S}\right] \tag{D151}$$

where

$$t_{oS} = \frac{B_{wS} \, \sigma_{oS}^{N_S - 2}}{g \, \sigma_f^{N_S}}$$

For the uniaxial Weibull distribution

$$A_{ef} = \int_A \left[\frac{\sigma_{1,\max}(x,y)}{\sigma_f}\right]^{\tilde{m}_S N_S} \mathrm{d}A \tag{D152}$$

The time-dependent scale parameter is

$$t_{oS} = t_{\theta S} \, A_{ef}^{1/\tilde{m}_S} \tag{D153}$$

The modified effective area for the PIA model is

$$A_{ef} = \left(\frac{1}{\sigma_f}\right)^{\tilde{m}_S N_S} \int_A \left[\sigma_{1,\max}^{\tilde{m}_S N_S}(x,y) + \sigma_{2,\max}^{\tilde{m}_S N_S}(x,y)\right] \mathrm{d}A \tag{D154}$$

For the Batdorf theory, the modified effective area is

$$A_{ef} = \frac{2\bar{k}_{BS}}{\pi} \int_A \left\{ \int_0^{\pi/2} \left[\frac{\sigma_{Ieq,\max}(\Psi)}{\sigma_f}\right]^{\tilde{m}_S N_S} \mathrm{d}\alpha \right\} \mathrm{d}A \tag{D155}$$

and

$$t_{oS} = \frac{B_{BS}\, \sigma_{oS}^{N_S-2}}{g\, \sigma_f^{N_S}}$$

Similar to cyclic fatigue, for dynamic fatigue the specimen time to failure can be expressed using the two-parameter Weibull form as

$$P_f = 1 - \exp\left[-\left(\frac{t_f}{t_{\theta d}}\right)^{\tilde{m}(N+1)}\right] \tag{D156}$$

where

$$t_{\theta d} = \left[\frac{(N+1) B_u\, \sigma_\theta^{N-2}}{\dot{\sigma}_f^N}\right]^{1/(N+1)}$$

t_f is the time to failure, and $t_{\theta d}$ is the characteristic time (the subscript d indicates dynamic fatigue). Note that for dynamic fatigue (constant stress-rate loading) the g-factor has a value of $1/(N + 1)$. For volume flaws, substituting $1/(N_V + 1)$ for the g-factor and rearranging equation (D146) gives

$$P_{fV}(t_f) = 1 - \exp\left[-V_{ef}\left(\frac{t_f}{t_{odV}}\right)^{\tilde{m}_V (N_V+1)}\right] \tag{D157}$$

where

$$t_{odV} = \left[\frac{(N_V+1) B_{wV}\, \sigma_{oV}^{N_V-2}}{\dot{\sigma}_f^{N_V}}\right]^{1/(N_V+1)} = t_{\theta dV} V_{ef}^{1/\tilde{m}_V}$$

Note that in equation (D157), σ_f denotes the maximum stress in the specimen and $\dot{\sigma}$ is the stressing rate at that location. The derivation for surface flaws follows a similar line of reasoning.

For the Paris law, the relation analogous to equation (D144) is

$$P_f = 1 - \exp\left[-\left(\frac{n_f}{n_\theta} \right)^{\tilde{m}} \right] \tag{D158}$$

where n_f is the cycles to failure and n_θ is a characteristic number of cycles. Similar to equation (D145)

$$P_{fV}\left(n_f\right) = 1 - \exp\left[\frac{-1}{\sigma_{oV}^{m_V}} \int_V \sigma_{1,0}^{m_V}\left(x,y,z\right) \mathrm{d}V \right] \tag{D159}$$

where

$$\sigma_{1,0}\left(x,y,z\right) = \left[\frac{\sigma_{1,\max}^{N_V}\left(x,y,z\right)\left(1-R\right)^{N_V} n_f}{B_{wV}} \right]^{\frac{1}{N_V - 2}}$$

Similar to equation (D146) then,

$$P_{fV}\left(n_f\right) = 1 - \exp\left[-V_{ef} \left(\frac{n_f}{n_{oV}} \right)^{\tilde{m}_V} \right] \tag{D160}$$

where

$$n_{oV} = \frac{B_{wV}\, \sigma_{oV}^{N_V - 2}}{\left(1-R\right)^{N_V} \sigma_f^{N_V}} = n_{\theta V}\, V_{ef}^{1/\tilde{m}_V}$$

The derivation for surface flaws follows a similar line of reasoning.

***D.2.2.4 Fatigue parameter risk-of-rupture compatibility*.**—To ensure compatibility of failure probabilities, one must establish the relationships between the fatigue parameters (N and B) and the various failure criteria. From uniaxial test specimen data (simple tension, three-point bend, or four-point bend), compatibility is derived by equating the risk of rupture of the specimen uniaxial Weibull equation to the uniaxial Weibull model, the PIA model, the Weibull NSA, or the Batdorf shear-sensitive formulation.

For volume-flaw analysis, the probabilities of failure for the various approaches mentioned previously are

Specimen uniaxial Weibull

$$P_f = 1 - \exp\left[-\left(\frac{\sigma_{f,0}}{\sigma_{\theta V}} \right)^{m_V} \right]$$

Uniaxial Weibull

$$P_f = 1 - \exp\left[-k_{wV} \int_V \sigma_{1,0}^{m_V}\left(x,y,z\right) \mathrm{d}V \right]$$

PIA model

$$P_f = 1 - \exp\left\{ -k_{wV} \int_V \left[\sum_{i=1}^{3} \sigma_{i,0}^{m_V}\left(x,y,z\right) \right] \mathrm{d}V \right\}$$

NSA

$$P_f = 1 - \exp\left[-k_{wpV} \int_V \overline{\sigma}_{n,0}^{m_V}(x, y, z)\,\mathrm{d}V \right]$$

Batdorf model

$$P_f = 1 - \exp\left[-\frac{2}{\pi} k_{BV} \int_V \int_0^{\pi/2} \int_0^{\pi/2} \sigma_{\mathrm{I}eq,0}^{m_V}(\Psi) \sin\alpha \;\mathrm{d}\alpha \;\mathrm{d}\beta \;\mathrm{d}V \right]$$

The subscript 0 denotes the transformed stress to time $t = 0$.

The basis for compatibility-of-failure probabilities is the requirement that all expressions produce the same probability of failure for a uniaxial stress state as that obtained from the specimen uniaxial Weibull equation. The value of N remains invariant, whereas the value of B is adjusted to satisfy this requirement. The approach is similar to that used to obtain the relationships of the crack-density coefficients for fast-fracture reliability analysis. The most common experimental test specimens used in the evaluation of the fatigue parameters are the uniaxial tension, three-point bend, and four-point bend geometries. The fatigue parameters N and B are obtained from the data based solely on the maximum stress in the specimen at fracture σ_f and the time to failure t_f.

For the specimen uniaxial Weibull equation, the time-dependent transformation equations are

Static fatigue

$$\sigma_{f,0} = \left(\frac{\sigma_f^{N_V}\, t_f}{B_{uV}} \right)^{\frac{1}{N_V - 2}}$$

Dynamic fatigue

$$\sigma_{f,0} = \left(\frac{\sigma_f^{N_V}\, t_f}{B_{uV}\,(N_V + 1)} \right)^{\frac{1}{N_V - 2}}$$

Cyclic fatigue

$$\sigma_{f,0} = \left(\frac{\sigma_f^{N_V}\, g\, t_f}{B_{uV}} \right)^{\frac{1}{N_V - 2}}$$

if it is assumed that $\sigma^2 t_f / B >> 1$, where t_f is the time to fracture, g is the g-factor used with cyclic loading, σ_f is the maximum tensile stress in the specimen at fracture, and B_{uV} is the fatigue parameter obtained from the specimen uniaxial Weibull equation. Equating the risk of rupture of the specimen uniaxial Weibull model with the uniaxial Weibull model risk of rupture gives

$$\left(\frac{\sigma_f^{N_V}\, t_f}{\sigma_{\theta V}^{N_V - 2}\, B_{uV}} \right)^{\tilde{m}_V} = \int_V \left[\frac{\sigma_1^{N_V}(x, y, z)\, t_f}{B_{wV}\, \sigma_{oV}^{N_V - 2}} \right]^{\tilde{m}_V} \mathrm{d}V \qquad \text{(D161)}$$

then

$$\left(\frac{B_{wV}}{B_{uV}} \right)^{\tilde{m}_V} = \frac{1}{V_e} \int_V \left[\frac{\sigma_1(x, y, z)}{\sigma_f} \right]^{\tilde{m}_V N_V} \mathrm{d}V = \frac{V_{ef}}{V_e} \qquad \text{(D162)}$$

where

$$V_e = \left(\frac{\sigma_{oV}}{\sigma_{\theta V}}\right)^{m_V} = \int_V \left[\frac{\sigma_1(x,y,z)}{\sigma_f}\right]^{m_V} \mathrm{d}V \tag{D163}$$

For V_{ef}, the static equivalent stress distribution $\sigma_1(x, y, z)$ is normalized with respect to the maximum equivalent static tensile stress σ_f at t_f. Thus, V_{ef} for a given specimen configuration is similar to V_e for the same specimen, with the exception that the exponent associated with V_{ef} is $\tilde{m}_V N_V$, whereas the exponent associated with V_e is m_V. When there is no stress gradient in the specimen, then V_e and V_{ef} are equivalent. When stress gradients exist throughout the specimen, then these terms are not equal. For the three- and four-point bend specimens (for three-point bend, the inner span L_2 is set equal to zero), equating the risk of rupture of the specimen uniaxial Weibull equation with that of the uniaxial Weibull expression yields

$$B_{wV} = B_{uV}\left[\frac{\frac{wh}{2}\left(L_1 + \tilde{m}_V N_V L_2\right)}{V_e\left(1+\tilde{m}_V N_V\right)^2}\right]^{1/\tilde{m}_V} = B_{uV}\left(\frac{V_{ef}}{V_e}\right)^{1/\tilde{m}_V} \tag{D164}$$

where

$$V_e = \left[\frac{wh}{2}\,\frac{\left(L_1 + m_V L_2\right)}{\left(1+m_V\right)^2}\right]$$

and

$$V_{ef} = \left[\frac{wh}{2}\,\frac{\left(L_1 + \tilde{m}_V N_V L_2\right)}{\left(1+\tilde{m}_V N_V\right)^2}\right]$$

For the PIA model, the relationship between B_{wV} and B_{uV} is

$$\left(\frac{B_{wV}}{B_{uV}}\right)^{\tilde{m}_V} = \frac{1}{V_e}\int_V \left\{\left[\frac{\sigma_1(x,y,z)}{\sigma_f}\right]^{\tilde{m}_V N_V} + \left[\frac{\sigma_2(x,y,z)}{\sigma_f}\right]^{\tilde{m}_V N_V} + \left[\frac{\sigma_3(x,y,z)}{\sigma_f}\right]^{\tilde{m}_V N_V}\right\}\mathrm{d}V = \frac{V_{ef}}{V_e} \tag{D165}$$

Equating the risk of rupture of the specimen uniaxial Weibull to the Batdorf risk of rupture yields the relationship between B_{BV} and B_{uV}:

$$\left(\frac{B_{BV}}{B_{uV}}\right)^{\tilde{m}_V} = \frac{1}{V_e}\left\{\frac{2\bar{k}_{BV}}{\pi}\int_V \int_0^{\pi/2}\int_0^{\pi/2}\left[\frac{\sigma_{\mathrm{I}eq}(\Psi)}{\sigma_f}\right]^{\tilde{m}_V N_V} \sin\alpha\ \mathrm{d}\alpha\ \mathrm{d}\beta\ \mathrm{d}V\right\} \tag{D166}$$

where $\sigma_{\mathrm{I}eq}(\Psi)$ represents the static equivalent stress distribution. For the Weibull NSA method, B_{nwV} is substituted for B_{BV}, and $\sigma_{\mathrm{I}n,0}(\Psi)$ is substituted for $\sigma_{\mathrm{I}eq,0}(\Psi)$.

The relationship between B_{wV} and B_{BV} is established by equating the risk of ruptures for the uniaxial Weibull model and the Batdorf model:

$$\left(\frac{B_{wV}}{B_{BV}}\right)^{\tilde{m}_V} = \frac{\displaystyle\int_V \left[\frac{\sigma_{\mathrm{I}eq}(x,y,z)}{\sigma_f}\right]^{\tilde{m}_V N_V} \mathrm{d}V}{\displaystyle\frac{2\bar{k}_{BV}}{\pi}\int_V \left\{\int_0^{\pi/2}\int_0^{\pi/2}\left[\frac{\sigma_{\mathrm{I}eq}(\Psi)}{\sigma_f}\right]^{\tilde{m}_V N_V} \sin\alpha \,\mathrm{d}\alpha\,\mathrm{d}\beta\right\}\mathrm{d}V} \tag{D167}$$

For the uniaxial stress state, this expression becomes strictly a function of the fracture criterion. This can be demonstrated with a shear-insensitive fracture criterion (equivalent to the Weibull NSA method), where

$$\sigma_{\mathrm{I}eq}(\Psi) = \sigma_{\mathrm{I}eq}(x,y,z)\cos^2\alpha \tag{D168}$$

so that

$$\left(\frac{B_{wV}}{B_{BV}}\right)^{\tilde{m}_V} = \frac{\displaystyle\int_V \left[\frac{\sigma_{\mathrm{I}eq}(x,y,z)}{\sigma_f}\right]^{\tilde{m}_V N_V} \mathrm{d}V}{\displaystyle\frac{2\bar{k}_{BV}}{\pi}\int_V \left[\frac{\sigma_{\mathrm{I}eq}(x,y,z)}{\sigma_f}\right]^{\tilde{m}_V N_V}\left(\int_0^{\pi/2}\int_0^{\pi/2}\cos^{2\tilde{m}_V N_V}\alpha \,\sin\alpha \,\mathrm{d}\alpha\,\mathrm{d}\beta\right)\mathrm{d}V} \tag{D169}$$

combined with equation (D66) then

$$\left(\frac{B_{wV}}{B_{BV}}\right)^{\tilde{m}_V} = \frac{2\tilde{m}_V N_V + 1}{2m_V + 1} \tag{D170}$$

For colinear crack extension with a Griffith crack,

$$\sigma_{\mathrm{I}eq}(\Psi) = \sigma_{\mathrm{I}eq}(x,y,z)\cos\alpha \tag{D171}$$

so that

$$\left(\frac{B_{wV}}{B_{BV}}\right)^{\tilde{m}_V} = \frac{\displaystyle\int_V \left[\frac{\sigma_{\mathrm{I}eq}(x,y,z)}{\sigma_f}\right]^{\tilde{m}_V N_V} \mathrm{d}V}{\displaystyle\frac{2\bar{k}_{BV}}{\pi}\int_V \left[\frac{\sigma_{\mathrm{I}eq}(x,y,z)}{\sigma_f}\right]^{\tilde{m}_V N_V}\left(\int_0^{\pi/2}\int_0^{\pi/2}\cos^{\tilde{m}_V N_V}\alpha \,\sin\alpha \,\mathrm{d}\alpha\,\mathrm{d}\beta\right)\mathrm{d}V} \tag{D172}$$

combined with equation (D68) then

$$\left(\frac{B_{wV}}{B_{BV}}\right)^{\tilde{m}_V} = \frac{\tilde{m}_V N_V + 1}{m_V + 1} \tag{D173}$$

For an arbitrary fracture criterion expressed as some function of the flaw orientation,

$$\sigma_{\mathrm{I}eq}(\Psi) = \sigma_{\mathrm{I}eq}(x, y, z)\, f(\alpha, \beta) \tag{D174}$$

then

$$\left(\frac{B_{wV}}{B_{BV}}\right)^{\tilde{m}_V} = \frac{\pi}{2\bar{k}_{BV}\left(\int_0^{\pi/2}\int_0^{\pi/2} f^{\,\tilde{m}_V N_V}(\alpha, \beta) \sin\alpha \;\mathrm{d}\alpha\;\mathrm{d}\beta\right)} \tag{D175}$$

For surface-flaw analysis, the relationship between the specimen uniaxial Weibull fatigue parameter B_{uS} and the uniaxial Weibull parameter B_{wS}, the Weibull NSA parameter B_{nwS}, and the Batdorf parameter B_{BS} is obtained in a similar manner to that used for the volume-flaw analysis. Equating the risk of rupture of the specimen uniaxial Weibull equation to the uniaxial Weibull equation yields

$$\left(\frac{\sigma_f^{\,N_S} t_f}{\sigma_{\theta S}^{N_S-2} B_{uS}}\right)^{\tilde{m}_S} = \int_A \left[\frac{\sigma_1^{N_S}(x, y)\, t_f}{B_{wS}\, \sigma_{oS}^{N_S-2}}\right]^{\tilde{m}_S} \mathrm{d}A \tag{D176}$$

then

$$\left(\frac{B_{wS}}{B_{uS}}\right)^{\tilde{m}_S} = \frac{1}{A_e}\int_A \left[\frac{\sigma_1(x, y)}{\sigma_f}\right]^{\tilde{m}_S N_S} \mathrm{d}A = \frac{A_{ef}}{A_e} \tag{D177}$$

where

$$A_e = \left(\frac{\sigma_{oS}}{\sigma_{\theta S}}\right)^{m_S} = \int_A \left[\frac{\sigma_1(x, y)}{\sigma_f}\right]^{m_S} \mathrm{d}A \tag{D178}$$

For A_{ef}, the static equivalent stress distribution $\sigma_1(x, y)$ is normalized with respect to the maximum equivalent static tensile stress σ_f at t_f. Thus, A_{ef} for a given specimen configuration is similar to A_e for the same specimen with the exception that the exponent associated with A_{ef} is $\tilde{m}_S N_S$, whereas the exponent associated with A_e is m_S. When there is no stress gradient on the specimen, then A_e and A_{ef} are equivalent. When stress gradients exist throughout the specimen, then these terms are not equal.

For the four-point bend specimen ($L_2 = 0$ for the three-point bend solution),

$$A_e = \frac{(L_1 + m_S L_2)(h + w + m_S w)}{(1 + m_S)^2} \tag{D179}$$

Equating the risk of rupture of the specimen uniaxial Weibull equation to the uniaxial Weibull formulation yields

$$B_{wS} = B_{uS}\left[\frac{(L_1 + \tilde{m}_S N_S L_2)(h + w + w\tilde{m}_S N_S)}{A_e\,(1 + \tilde{m}_S N_S)^2}\right]^{1/\tilde{m}_S} = B_{uS}\left(\frac{A_{ef}}{A_e}\right)^{1/\tilde{m}_S} \tag{D180}$$

For the PIA model, the relationship between B_{wS} and B_{uS} is

$$\left(\frac{B_{wS}}{B_{uS}}\right)^{\tilde{m}_S} = \frac{1}{A_e}\int_A \left\{ \left[\frac{\sigma_1(x,z)}{\sigma_f}\right]^{\tilde{m}_S N_S} + \left[\frac{\sigma_2(x,z)}{\sigma_f}\right]^{\tilde{m}_S N_S} \right\} dA = \frac{A_{ef}}{A_e} \tag{D181}$$

Equating the risk of rupture of the specimen uniaxial Weibull equation to the Batdorf risk of rupture yields the relationship between B_{BS} and B_{uS}

$$\left(\frac{B_{BS}}{B_{uS}}\right)^{\tilde{m}_S} = \frac{1}{A_e}\left\{ \frac{2\bar{k}_{BS}}{\pi}\int_A\int_0^{\pi/2} \left[\frac{\sigma_{\mathrm{I}eq}(\Psi)}{\sigma_f}\right]^{\tilde{m}_S N_S} \mathrm{d}\alpha\ \mathrm{d}A \right\} \tag{D182}$$

where $\sigma_{\mathrm{I}eq}(\Psi)$ represents the static equivalent stress distribution. For the Weibull NSA method, B_{nwV} is substituted for B_{BV} and $\sigma_{n,0}(\Psi)$ is substituted for $\sigma_{\mathrm{I}eq,0}(\Psi)$.

The relationship between B_{wS} and B_{BS} is established by equating the risk of ruptures of the uniaxial Weibull model and the Batdorf model

$$\left(\frac{B_{wS}}{B_{BS}}\right)^{\tilde{m}_S} = \frac{\displaystyle\int_A \left[\frac{\sigma_{\mathrm{I}eq}(x,y)}{\sigma_f}\right]^{\tilde{m}_S N_S} \mathrm{d}A}{\displaystyle\frac{2\bar{k}_{BS}}{\pi}\int_A \left[\int_0^{\pi/2}\left(\frac{\sigma_{\mathrm{I}eq}(\Psi)}{\sigma_f}\right)^{\tilde{m}_S N_S} \mathrm{d}\alpha\right]\mathrm{d}A} \tag{D183}$$

For the uniaxial stress state, this expression becomes strictly a function of the fracture criterion. This can be demonstrated with a shear-insensitive fracture criterion (equivalent to the Weibull NSA method), where

$$\sigma_{\mathrm{I}eq}(\Psi) = \sigma_{\mathrm{I}eq}(x,y)\cos^2\alpha \tag{D184}$$

so that

$$\left(\frac{B_{wS}}{B_{BS}}\right)^{\tilde{m}_S} = \frac{\displaystyle\int_A \left[\frac{\sigma_{\mathrm{I}eq}(x,y)}{\sigma_f}\right]^{\tilde{m}_S N_S} \mathrm{d}A}{\displaystyle\frac{2\bar{k}_{BS}}{\pi}\int_A \left[\frac{\sigma_{\mathrm{I}eq}(x,y)}{\sigma_f}\right]^{\tilde{m}_S N_S}\left(\int_0^{\pi/2}\cos^{2\tilde{m}_S N_S}\alpha\ \mathrm{d}\alpha\right)\mathrm{d}A} \tag{D185}$$

combined with equation (D79) then

$$\left(\frac{B_{wS}}{B_{BS}}\right)^{\tilde{m}_S} = \frac{N_S\,\Gamma(\tilde{m}_S N_S)\,\Gamma\left(m_S + \frac{1}{2}\right)}{(N_S - 2)\,\Gamma\left(\tilde{m}_S N_S + \frac{1}{2}\right)\Gamma(m_S)} \tag{D186}$$

For colinear crack extension with a Griffith crack

$$\sigma_{\mathrm{I}eq}(\Psi) = \sigma_{\mathrm{I}eq}(x,y)\cos\alpha \tag{D187}$$

so that

$$\left(\frac{B_{wS}}{B_{BS}}\right)^{\widetilde{m}_S} = \frac{\int_A \left(\frac{\sigma_{\mathrm{I}eq}(x,y)}{\sigma_f}\right)^{\widetilde{m}_S N_S} \mathrm{d}A}{\frac{2\bar{k}_{BS}}{\pi}\int_A \left(\frac{\sigma_{\mathrm{I}eq}(x,y)}{\sigma_f}\right)^{\widetilde{m}_S N_S} \left[\int_0^{\pi/2} \cos^{\widetilde{m}_S N_S}\alpha \,\mathrm{d}\alpha\right]\mathrm{d}A} \tag{D188}$$

combined with equation (D81) then

$$\left(\frac{B_{wS}}{B_{BS}}\right)^{\widetilde{m}_S} = \frac{N_S\,\Gamma\left(\frac{\widetilde{m}_S N_S}{2}\right)\Gamma\left(\frac{m_S+1}{2}\right)}{\left(N_S-2\right)\Gamma\left(\frac{\widetilde{m}_S N_S+1}{2}\right)\Gamma\left(\frac{m_S}{2}\right)} \tag{D189}$$

For an arbitrary fracture criterion expressed as some function of the flaw orientation,

$$\sigma_{\mathrm{I}eq}(\Psi) = \sigma_{\mathrm{I}eq}(x,y)\, f(\alpha) \tag{D190}$$

then

$$\left(\frac{B_{wS}}{B_{BS}}\right)^{\widetilde{m}_S} = \frac{\pi}{2\bar{k}_{BS}\left[\int_0^{\pi/2} f^{\widetilde{m}_S N_S}(\alpha)\,\mathrm{d}\alpha\right]} \tag{D191}$$

D.2.2.5 Evaluation of fatigue parameters from inherently flawed specimens.—The lifetime reliability of structural ceramic components depends on the history of the loading, the component geometry, the distribution of preexisting flaws, and the parameters that characterize SCG. These crack-growth parameters must be measured under conditions representative of the service environment. When determining fatigue parameters from the rupture data of naturally flawed specimens, the statistical effects of the flaw distribution must be considered along with the strength degradation effects of SCG. A more direct approach is to calculate fatigue parameters from velocity measurements of an induced crack of known configuration, thereby eliminating the statistical aspects of the flaw population from the experiment. The weakness of this approach, however, is the difficulty of getting a notched or indented specimen to behave in a manner identical to that of the naturally flawed specimen. CARES/*Life* was developed on the basis that fatigue parameters are most accurately obtained from naturally flawed specimens. In the following discussion, three methods are described to estimate these parameters from fatigue data: the median-value technique, a least-squares regression technique, and the median-deviation (MD) technique, a modification to a method from Jakus et al. (1978). These methods are described in terms of volume-flaw analysis for static (or constant amplitude and frequency cyclic) fatigue. Only the MD technique is discussed for dynamic (constant stressing rate) fatigue using the power-law formulation and the Paris law methodology for constant amplitude and frequency cyclic loading. Analogous relations for surface flaws are easily developed by replacing the effective volume with the effective area.

D.2.2.5.1 Static and cyclic fatigue parameter evaluation: When equation (D146) is rearranged for static fatigue or constant amplitude and frequency cyclic loading at a fixed level of reliability, the specimen time to failure for volume flaws is expressed as a function of the maximum stress σ_f in the specimen (for cyclic loading this corresponds to $\sigma_{1eq,\max}$ at the highest stressed point in the specimen)

$$t_f = \left\{ \frac{B_{wV}\,\sigma_{oV}^{N_V-2}}{\left[g \left[\frac{V_{ef}}{\ln\left(\frac{1}{1-P_{fV}}\right)} \right] \right]^{1/\tilde{m}_V}} \right\} \sigma_f^{\,-N_V} \tag{D192}$$

The *g*-factor is assumed to be constant throughout the specimen and for all loading levels. The terms between the brackets are simplified by replacing them with a constant, yielding

$$t_f = A_c\,\sigma_f^{-N_V} \tag{D193}$$

Equation (D193) is a convenient expression from which to fit experimental data, thus A_c and N_V can be considered as material-environmental parameters. Taking the logarithm of equation (D193) yields

$$\ln t_f = \ln A_c - N_V \ln \sigma_f \tag{D194}$$

Linear regression analysis of the experimental data is used to solve equation (D194) for the slope $-N_V$ and the intercept ln A_c. The fatigue parameter estimation techniques in CARES/*Life* estimate A_c and N_V for a probability of failure fixed at 50 percent ($P_{fV} = 0.50$).

For the median-value technique, CARES/*Life* uses the median value at each individual stress level as the data points. Using equation (D194) and performing a least-squares linear regression on the set of median values estimates the line corresponding to a failure probability of 50 percent with slope $-N_V$ and intercept ln A_c. Details of the least-squares solution technique are given in Pai and Gyekenyesi (1988). The median-value estimation method is the least efficient fatigue parameter estimation technique in CARES/*Life* (i.e., the estimated parameter has the largest confidence interval for a given sample size).

Another fatigue parameter estimation method incorporated in CARES/*Life* is the least-squares regression technique. This method is similar to the median-value technique except that linear regression using equation (D194) is performed with all the fatigue data points (instead of only the median values). The fatigue parameter N_V is obtained from the slope of the regression line. Assuming that the experimental data are at a sufficient number of discrete levels of applied stress, CARES/*Life* transforms all the data failure times $t_{f,i}$ to an equivalent failure time $t_{T,i}$ at an equivalent single level of stress, σ_T. Equating the failure probabilities calculated from equation (D146) for data number *i* yields

$$t_{T,i} = t_{f,i}\left(\frac{\sigma_{f,i}}{\sigma_T}\right)^{N_V} \tag{D195}$$

where the subscript T indicates a transformed value. In CARES/*Life*, the value of σ_T is the lowest level of applied stress in the data set. With all the data transformed to the various values $t_{T,i}$, CARES/*Life* performs a Weibull parameter estimation as described in section D.2.1.5, solving equation (D144) for $\tilde{m}_V$ and $t_{\theta VT}$. Substituting into equation (D193) for a time to failure corresponding to a 50-percent probability of failure yields

$$A_c = t_{\theta VT}\,\sigma_T^{N_V}\left[\ln\left(\frac{1}{1-0.50}\right)\right]^{1/\tilde{m}_V} = \frac{B_{wV}\,\sigma_{oV}^{N_V-2}}{g}\left[\frac{\ln\left(\frac{1}{1-0.50}\right)}{V_{ef}}\right]^{1/\tilde{m}_V} \tag{D196}$$

where

$$t_{\theta VT} = \frac{B_{wV}\,\sigma_{oV}^{N_V-2}}{g\,\sigma_T^{N_V}\,V_{ef}^{1/\tilde{m}_V}}$$

The third option in CARES/*Life* for estimating fatigue parameters is a modification to a method used by Jakus et al. (1978). This estimation technique is referred to as the MD procedure. In this procedure, the fatigue parameters and Weibull modulus are determined by minimizing the median deviation of the logarithm of the time. The characteristic strength $\sigma_{\theta V}$ is assumed to be known. From equation (D195), the fatigue data are transformed to a single stress level for an assumed value of N_V. Using equation (D144) and the previously mentioned least-squares or maximum-likelihood estimation methods, we obtain the Weibull parameters $\tilde{m}_V$ and $t_{\theta VT}$. With these parameters, the median value ($t_{T,0.5}$) is calculated (i.e., the value for t_T when $P_{fV} = 0.50$). Using the transformed fatigue data as a discrete variable, we can define the median deviation (using absolute values) as

$$MD = \frac{1}{k}\sum_{i=1}^{k}\left|\ln t_{T,i} - \ln\left[t_{\theta VT}\left(\ln\frac{1}{1-0.50}\right)^{1/\tilde{m}_V}\right]\right| = \frac{1}{k}\sum_{i=1}^{k}\left|\ln t_{T,i} - \ln t_{T,0.50}\right| \tag{D197}$$

for the k data points. The *MD* is a measure of dispersion or scatter about the median. It can also be obtained for the continuous variable defined by the Weibull parameters $\tilde{m}_V$ and $t_{\theta VT}$ for ranked probabilities of failure $P_{f,i}$.

$$MD = \frac{1}{k}\sum_{i=1}^{k}\left|\ln\left[t_{\theta VT}\left(\ln\frac{1}{1-P_{f,i}}\right)^{1/\tilde{m}_V}\right] - \ln t_{T,0.5}\right| = \frac{1}{\tilde{m}_V}\left[\frac{1}{k}\sum_{i=1}^{k}\left|\ln\left(\frac{\ln\frac{1}{1-P_{f,i}}}{\ln\frac{1}{1-0.5}}\right)\right|\right] \tag{D198}$$

The value of N_V for which the *MD* is a minimum establishes the solution. The scatter of the distribution is measured with the Weibull modulus $\tilde{m}_V$ since for a fixed value of k the expression inside the brackets of equation (D198) is a constant. CARES/*Life* minimizes equation (D198) by maximizing $\tilde{m}_V$ versus N_V. This process is iterative, covering an appropriate range of values of N_V. After a solution for N_V is obtained, equation (D196) is used to calculate A_c.

The MD procedure was investigated with Monte-Carlo simulations of static fatigue data. For sample sizes of 20 and 30 specimens each, 10 000 simulations were run where the fast-fracture Weibull modulus m randomly varied between 2.0 and 30.0, N randomly varied between 10.0 and 60.0, and the number of stress levels randomly varied between 2 and the sample size. The parameters σ_{oV} and B_U were fixed at 100.0 and 10 000.0/(N + 1), respectively. The results of the simulations were compared with estimates calculated using the median-value technique for the same fracture data. Examination of the 90-percent confidence intervals indicated that the MD procedure yielded better results than the median-value technique. Using MLE gave better results than using least-squares estimation with the MD procedure. For the crack-growth exponent N, the 90-percent confidence interval from the MD procedure (with MLE) was about 70 percent of the range of the median-value 90-percent confidence interval, with no bias indicated with either estimator. For the crack-growth constant B_U, the 90-percent confidence interval for the MD procedure was dramatically smaller than the median-value 90-percent confidence interval—with negligible bias indicated with the MD method and significant negative bias indicated with the median-value method.

The fatigue parameter B_{wV} can be obtained by comparing equations (D192) and (D193) for a 50-percent probability of failure

$$B_{wV} = \frac{A_c\, g}{\sigma_{oV}^{N_V-2}} \left[\frac{V_{ef}}{\ln\left(\dfrac{1}{1-0.50} \right)} \right]^{1/\tilde{m}_V} \tag{D199}$$

Alternatively, B_{wV} can be obtained by equating equations (D144) and (D145):

$$B_{wV} = \frac{t_{\theta V}\; g\, \sigma_f^{N_V}\; V_{ef}^{1/\tilde{m}_V}}{\sigma_{oV}^{N_V-2}} \tag{D200}$$

Information on the underlying inert strength distribution also can be obtained from the fatigue data. Using equation (D195) to transform all the fatigue data to a single Weibull distribution and performing least-squares or maximum-likelihood analysis establishes the parameters $\tilde{m}_V$ and $t_{\theta VT}$. The fast-fracture Weibull modulus is then solved as

$$m_V' = \tilde{m}_V \left(N_V - 2 \right) \tag{D201}$$

where the superscript ′ denotes a fast-fracture parameter estimated from fatigue data. The fast-fracture characteristic strength $\sigma_{\theta V}$ cannot be estimated from the fatigue data. CARES/*Life* calculates a characteristic strength, $\sigma_{\theta V}'$, on the basis of an extrapolation of the fatigue data to a specific failure time. This time is arbitrarily fixed at 1/(N + 1) seconds for static loading (equivalent to 1.0 s for dynamic loading). From equation (D195) then,

$$\sigma_{\theta V}' = \sigma_T \left[t_{\theta VT} \left(N_V + 1 \right) \right]^{1/N_V} \tag{D202}$$

Much more statistical uncertainty is associated with the determination of the Weibull modulus than with the characteristic strength for fast-fracture testing.

With the calculated quantities $\sigma_{\theta V}'$ and m_V', the fatigue data can be transformed to an equivalent inert strength distribution by equating the risk of rupture of equations (D55) and (D144) for the various transformed fatigue data values

$$\sigma'_{f\,\mathrm{I},i} = \sigma_{\theta V}' \left(\frac{t_{T,i}}{t_{\theta VT}} \right)^{\frac{1}{N_V-2}} \tag{D203}$$

where $\sigma'_{f1,i}$ represents the i^{th} transformed inert fracture strength of the specimen. Plotting the ranked values $\sigma'_{f1,i}$, for ln ln (1/1 $-P_{fV}$) versus ln σ, gives useful visual information for the analyst. With $\sigma'_{\theta V}$, m'_V, and the various $\sigma'_{f1,i}$ values, CARES/*Life* performs the outlier test and determines the KS and AD goodness-of-fit statistics, as explained in section D.2.1.5. The outlier test and goodness-of-fit statistics in this case are also valid for the transformed fatigue data (denoted with the subscript *T*) and the original fatigue data. Hence, the calculated goodness-of-fit significance levels measure the hypothesis that fatigue data were generated from the parameters N_V, A_c, and m'_V.

D.2.2.5.2 Dynamic fatigue parameter evaluation: The fatigue parameter estimation methodology for dynamic fatigue is similar to the power-law formulation for static and cyclic fatigue. When equation (D157) is rearranged for a fixed level of reliability, the specimen failure stress σ_f for volume flaws is expressed as a function of the stress rate $\dot{\sigma}$ at the highest stressed point in the component:

$$\sigma_f = \left\{ \frac{(N_V + 1)\, B_{wV}\, \sigma_{oV}^{N_V - 2}}{\left[\dfrac{V_{ef}}{\ln\left(\dfrac{1}{1 - P_{fV}} \right)} \right]^{1/\tilde{m}_V}} \right\}^{1/(N_V+1)} \dot{\sigma}^{1/(N_V+1)} \tag{D204}$$

The terms between the brackets are simplified by replacing them with a constant, yielding

$$\sigma_f = A_d\, \dot{\sigma}^{1/(N_V+1)} \tag{D205}$$

Equation (D205) is a convenient expression from which to fit experimental data, thus A_d and N_V can be considered as material-environmental parameters. Taking the logarithm of equation (D205) yields

$$\ln \sigma_f = \ln A_d + \frac{1}{N_V + 1} \ln \dot{\sigma} \tag{D206}$$

The median-value, least-squares, and MD techniques are used to solve equation (D206) as previously discussed for static and cyclic loadings.

Assuming that experimental data are at a sufficient number of discrete levels of stress rates, CARES/*Life* transforms all the data failure times $t_{f,i}$ to equivalent failure times $t_{T,i}$ at a fixed stress rate $\dot{\sigma}_T$. Equating the failure probabilities calculated from equation (D156) for data number *i* yields

$$t_{T,i} = t_{f,i} \left(\frac{\dot{\sigma}_i}{\dot{\sigma}_T} \right)^{N_V/(N_V+1)} \tag{D207}$$

where the subscript *T* indicates a transformed value and $t_{f,i} = \sigma_{f,i} / \dot{\sigma}_i$. In CARES/*Life*, the value of $\dot{\sigma}_T$ is the lowest stress rate in the data set. With all the data transformed to the various values $t_{T,i}$ (and thus, able to be characterized by a single Weibull distribution), CARES/*Life* performs Weibull parameter estimation as described in section D.2.1.5, solving equation (D156) for $\tilde{m}_V(N_V+1)$ and $t_{\theta VT}$. Substituting into equation (D205) for a time to failure corresponding to a 50-percent probability of failure yields

$$A_d = t_{\theta dVT}\left\{\dot{\sigma}_T^{N_V}\left[\ln\left(\frac{1}{1-0.50}\right)\right]^{1/\tilde{m}_V}\right\}^{1/(N_V+1)} = \left\{(N_V+1)\,B_{wV}\,\sigma_{oV}^{N_V-2}\left[\frac{\ln\left(\frac{1}{1-0.50}\right)}{V_{ef}}\right]^{1/\tilde{m}_V}\right\}^{1/(N_V+1)} \tag{D208}$$

where

$$t_{\theta dVT} = \left[\frac{(N_V+1)B_{wV}\,\sigma_{oV}^{N_V-2}}{\dot{\sigma}_T^{N_V}\,V_{ef}^{1/\tilde{m}_V}}\right]^{1/(N_V+1)}$$

The MD method for estimating fatigue parameters minimizes the median deviation of the logarithm of the time to failure. From equation (D207), the fatigue data are transformed to a single stress rate for an assumed value of N_V. Equation (D156) and the previously mentioned least-squares or maximum-likelihood estimation methods are used to obtain the Weibull parameters $\tilde{m}_V(N_V+1)$ and $t_{\theta dVT}$. With these parameters, the median value ($t_{T,0.5}$) is calculated (i.e., the value for t_T when $P_{fV} = 0.50$). When the transformed fatigue data are used as discrete variables, *MD* is defined as

$$MD = \frac{1}{k}\sum_{i=1}^{k}\left|\ln t_{T,i} - \ln\left[t_{\theta dVT}\left(\ln\frac{1}{1-0.50}\right)^{\frac{1}{\tilde{m}_V(N_V+1)}}\right]\right| = \frac{1}{k}\sum_{i=1}^{k}\left|\ln t_{T,i} - \ln t_{T,0.50}\right| \tag{D209}$$

for the k data points. The *MD* is a measure of dispersion or scatter about the median. It can also be obtained for the continuous variable defined by the Weibull parameters $\tilde{m}_V(N_V+1)$ and $t_{\theta dVT}$ for ranked probabilities of failure $P_{f,i}$.

$$MD = \frac{1}{k}\sum_{i=1}^{k}\left|\ln\left[t_{\theta dVT}\left(\ln\frac{1}{1-P_{f,i}}\right)^{\frac{1}{\tilde{m}_V(N_V+1)}}\right] - \ln t_{T,0.05}\right| = \frac{1}{\tilde{m}_V(N_V+1)}\left[\frac{1}{k}\sum_{i=1}^{k}\left|\ln\left(\frac{\ln\frac{1}{1-P_{f,i}}}{\ln\frac{1}{1-0.5}}\right)\right|\right] \tag{D210}$$

The value of N_V for which the *MD* is a minimum establishes the solution. The scatter of the distribution is measured with the Weibull modulus $\tilde{m}_V(N_V+1)$ since for a fixed value of k the expression inside the brackets of equation (D210) is a constant. CARES/*Life* minimizes equation (D210) by maximizing $\tilde{m}_V(N_V+1)$ versus N_V. This process is iterative, covering an appropriate range of values of N_V. After a solution for N_V is obtained, equation (D208) is used to calculate A_d.

The MD procedure was investigated with Monte-Carlo simulations of dynamic fatigue data. For sample sizes of 20 and 30 specimens each, 10 000 simulations were run where the fast-fracture Weibull modulus m randomly varied between 2.0 and 30.0, N randomly varied between 10.0 and 60.0, and the number of stress rates randomly varied between 2 and the sample size. The parameters σ_{oV} and B were fixed at 100.0 and 10 000.0/(N + 1), respectively.

The results of the simulations were compared with estimates calculated using the median-value technique for the same fracture data. The conclusions reached with dynamic fatigue simulations were identical to those obtained with the static fatigue simulations.

The fatigue parameter B_{wV} can be obtained by comparing equations (D204) and (D205) for a 50-percent probability of failure

$$B_{wV} = \frac{A_d^{N_V+1}}{\left(N_V+1\right)\sigma_{oV}^{N_V-2}} \left[\frac{V_{ef}}{\ln\left(\frac{1}{1-0.50}\right)} \right]^{1/\tilde{m}_V} \tag{D211}$$

Alternatively, B_{wV} can be obtained by equating equations (D156) and (D157):

$$B_{wV} = \frac{t_{\theta dV}^{N_V+1}\,\dot{\sigma}^{N_V}\,V_{ef}^{1/\tilde{m}_V}}{\left(N_V+1\right)\sigma_{oV}^{N_V-2}} \tag{D212}$$

Information on the underlying inert strength distribution can also be obtained from the fatigue data. Using equation (D207) to transform all the fatigue data to a single Weibull distribution and performing least-squares or maximum-likelihood analysis establishes the parameters $\tilde{m}_V\left(N_V+1\right)$ and $t_{\theta VT}$. The fast-fracture Weibull modulus is then solved as

$$m'_V = \tilde{m}_V\left(N_V-2\right) \tag{D213}$$

where the superscript ′ denotes a fast-fracture parameter estimated from fatigue data. The fast-fracture characteristic strength $\sigma_{\theta V}$ cannot be estimated from the fatigue data. CARES/*Life* calculates a characteristic strength, $\sigma'_{\theta V}$, based on extrapolation of the dynamic fatigue data to a specific time. This time is arbitrarily fixed at 1.0 s. From equation (D207)

$$\sigma'_{\theta V} = \dot{\sigma}\, t_{\theta dVT}^{\left(N_V+1\right)/N_V} \tag{D214}$$

Much more statistical uncertainty is associated with the determination of the Weibull modulus than with the characteristic strength for fast-fracture testing.

With the calculated quantities $\sigma'_{\theta V}$ and m'_V, the fatigue data can be transformed to an equivalent inert strength distribution by equating the risk of rupture of equations (D55) and (D156) for the various data values,

$$\sigma'_{f\,\mathrm{I},i} = \sigma'_{\theta V}\left(\frac{t_{T,i}}{t_{\theta dVT}}\right)^{\frac{N_V+1}{N_V-2}} \tag{D215}$$

where $\sigma'_{f\mathrm{I},i}$ represents the i^{th} transformed inert fracture strength of the specimen. Plotting the ranked values $\sigma'_{f\mathrm{I},i}$, for ln ln(1/1 −P_{fV}) versus ln σ, gives useful visual information for the analyst. With $\sigma'_{\theta V}$, m'_V, and the various $\sigma'_{f\mathrm{I},i}$ values, CARES/*Life* performs the outlier test and determines the KS and AD goodness-of-fit statistics, as explained in section D.2.1.5. The outlier test and goodness-of-fit statistics in this case are also valid for the transformed fatigue data (denoted with subscript T) and the original fatigue data. Hence the calculated goodness-of-fit significance levels measure the hypothesis that fatigue data were generated from the parameters N_V, A_d, and m'_V.

D.2.2.5.3 Cyclic fatigue parameter evaluation: Fatigue parameter estimation for the Paris law is identical to the power-law formulation for cyclic fatigue except that time is replaced with cycles and the *g*-factor is replaced with $(1-R)^N$. Note that this section does not address Walker-law parameter estimation. For this parameter estimation technique, cyclic data are required at two or more applied loading levels and the *R* ratio must be held constant for all the data. Equation (D158) is rearranged for steady-state cyclic loading at a fixed level of reliability, and the specimen number of cycles to failure n_f for volume flaws is expressed as a function of the maximum static equivalent stress σ_f in the specimen ($\sigma_f = \sigma_{\mathrm{I}eq,\max}$) at the highest stressed point in the component.

$$n_f = \left\{ \frac{B_{wV}\,\sigma_{oV}^{N_V-2}}{(1-R)^{N_V}\left[\dfrac{V_{ef}}{\ln\left(\dfrac{1}{1-P_{fV}}\right)}\right]^{1/\tilde{m}_V}} \right\} \sigma_f^{-N_V} \tag{D216}$$

The terms between the brackets are simplified by replacing them with a constant, yielding

$$n_f = A_c\,\sigma_f^{-N_V} \tag{D217}$$

Equation (D217) is a convenient expression from which to fit experimental data; thus, A_c and N_V can be considered as material-environmental parameters. Taking the logarithm of equation (D217) yields

$$\ln n_f = \ln A_c - N_V \ln \sigma_f \tag{D218}$$

The median-value, least-squares, and MD techniques are used to solve equation (D218) as previously discussed for the power-law methodology.

Assuming that the experimental data are at a sufficient number of discrete levels of applied stress, all the data cycles to failure $n_{f,i}$ are transformed to an equivalent number of cycles $n_{T,i}$ at an equivalent single level of (maximum within the cycle) stress σ_T. Equating the failure probabilities calculated from equation (D160) for data number *i* yields

$$n_{T,i} = n_{f,i}\left(\frac{\sigma_{f,i}}{\sigma_T}\right)^{N_V} \tag{D219}$$

where the subscript *T* indicates a transformed value. In CARES/*Life*, the value of σ_T is the lowest level of applied (maximum within the cycle) stress in the data set. With all the data transformed to the various values $n_{T,i}$, CARES/*Life* performs Weibull parameter estimation as described in section D.2.1.5, solving equation (D158) for $\tilde{m}_V$ and $n_{\theta VT}$. Substituting into equation (D217) for the number of cycles corresponding to a 50-percent probability of failure yields

$$A_c = n_{\theta VT}\,\sigma_T^{N_V}\left[\ln\left(\frac{1}{1-0.50}\right)\right]^{1/\tilde{m}_V} = \frac{B_{wV}\,\sigma_{oV}^{N_V-2}}{(1-R)^{N_V}}\left[\frac{\ln\left(\frac{1}{1-0.50}\right)}{V_{ef}}\right]^{1/\tilde{m}_V} \qquad \text{(D220)}$$

where

$$n_{\theta VT} = \frac{B_{wV}\ \sigma_{oV}^{N_V-2}}{(1-\mathrm{R})^{N_V}\ \sigma_T^{N_V}\ V_{ef}^{1/\tilde{m}_V}}$$

The MD method for estimating fatigue parameters minimizes the *MD* of the logarithm of the number of cycles. From equation (D219), the fatigue data are transformed to a single stress level for an assumed value of N_V. Equation (D158) and the previously mentioned least-squares or maximum-likelihood estimation methods are used to obtain the Weibull parameters $\tilde{m}_V$ and $n_{\theta VT}$. With these parameters, the median value $n_{T,0.50}$, is calculated (i.e., the value for n_T when $P_{fV} = 0.50$). Using the transformed fatigue data as a discrete variable yields a definition of *MD* as

$$MD = \frac{1}{k}\sum_{i=1}^{k}\left|\ln n_{T,i} - \ln\left[n_{\theta VT}\left(\ln\frac{1}{1-0.50}\right)^{1/\tilde{m}_V}\right]\right| = \frac{1}{k}\sum_{i=1}^{k}\left|\ln n_{T,i} - \ln n_{T,0.50}\right| \qquad \text{(D221)}$$

for the *k* data points, where *MD* is a measure of dispersion, or scatter, about the median. It can also be obtained for the continuous variable defined by the Weibull parameters $\tilde{m}_V$ and $n_{\theta VT}$ for ranked probabilities of failure $P_{f,i}$.

$$MD = \frac{1}{k}\sum_{i=1}^{k}\left|\ln\left[n_{\theta VT}\left(\ln\frac{1}{1-P_{f,i}}\right)^{1/\tilde{m}_V}\right] - \ln n_{T,0.50}\right| = \frac{1}{\tilde{m}_V}\left[\frac{1}{k}\sum_{i=1}^{k}\left|\ln\left(\frac{\ln\frac{1}{1-P_{f,i}}}{\ln\frac{1}{1-0.5}}\right)\right|\right] \qquad \text{(D222)}$$

The value of N_V for which the *MD* is a minimum establishes the solution. The scatter of the distribution is measured with the Weibull modulus $\tilde{m}_V$ since for a fixed value of *k* the expression inside the brackets of equation (D222) is a constant. CARES/*Life* minimizes equation (D222) by maximizing $\tilde{m}_V$ versus N_V. This process is iterative, covering an appropriate range of values of N_V. After a solution for N_V is obtained, equation (D220) is used to calculate A_c.

The fatigue parameter B_{wV} can be obtained by comparing equations (D216) and (D217) for a 50-percent probability of failure:

$$B_{wV} = \frac{A_c(1-R)^{N_V}}{\sigma_{oV}^{N_V-2}}\left[\frac{V_{ef}}{\ln\left(\frac{1}{1-0.50}\right)}\right]^{1/\tilde{m}_V} \qquad \text{(D223)}$$

Alternatively, B_{wV} can be obtained by equating equations (D158) and (D160):

$$B_{wV} = \frac{n_{\theta V} \left(1-R\right)^{N_V} \sigma_f^{N_V} \; V_{ef}^{1/\tilde{m}_V}}{\sigma_{oV}^{N_V-2}} \qquad \text{(D224)}$$

Information on the underlying inert strength distribution can also be obtained from the fatigue data. Using equation (D219) to transform all the fatigue data to a single Weibull distribution and performing least-squares or maximum-likelihood analysis establishes the parameters $\tilde{m}_V$ and $n_{\theta VT}$. The fast-fracture Weibull modulus is then solved as

$$m'_V = \tilde{m}_V \left(N_V - 2\right) \qquad \text{(D225)}$$

where the superscript ′ denotes a fast-fracture parameter estimated from fatigue data. The fast-fracture characteristic strength $\sigma_{\theta V}$ cannot be estimated from the fatigue data. CARES/*Life* calculates a characteristic strength $\sigma'_{\theta V}$ based on extrapolation of the fatigue data to a specific number of cycles. This number is arbitrarily fixed at $1/(N+1)$ cycles.

$$\sigma'_{\theta V} = \sigma_T \left[n_{\theta VT} \left(N_V + 1\right)\right]^{1/N_V} \qquad \text{(D226)}$$

Much more statistical uncertainty is associated with the determination of the Weibull modulus than with the characteristic strength for fast-fracture testing.

With the calculated quantities $\sigma'_{\theta V}$ and m'_V, the fatigue data can be transformed to an equivalent inert strength distribution by equating the risk of rupture of equations (D55) and (D158) for the various data values

$$\sigma'_{f1,i} = \sigma'_{\theta V} \left(\frac{n_{T,i}}{n_{\theta VT}} \right)^{\frac{1}{N_V - 2}} \qquad \text{(D227)}$$

where $\sigma'_{f1,i}$ represents the i^{th} transformed inert fracture strength of the specimen. Plotting the ranked values $\sigma'_{f1,i}$, for $\ln \ln(1/1 - P_{fV})$ versus $\ln \sigma$ gives useful visual information for the analyst. With $\sigma'_{\theta V}$, m'_V, and the various $\sigma'_{f1,i}$ values, CARES/*Life* performs the outlier test and determines the KS and AD goodness-of-fit statistics, as explained in section D.2.1.5. The outlier test and goodness-of-fit statistics in this case are also valid for the transformed fatigue data (denoted with the subscript T) and the original fatigue data. Hence, the calculated goodness-of-fit significance levels measure the hypothesis that fatigue data were generated from the parameters N_V, A_c, and m'_V.

D.2.2.6 Proof-testing effect on component service probability of failure.—Prior to placing a component in service, confidence that it will perform reliably is usually demonstrated through proof testing. Another method, nondestructive evaluation (NDE), is used to remove components with discernable but unacceptable flaw sizes (Wiederhorn and Fuller, 1985). Ideally, the boundary conditions applied to a component under proof testing simulate those conditions the component would be subjected to in service, and the proof-test loads are appropriately greater in magnitude over a fixed time interval t_p. After proof testing, the survived component is placed in service with greater confidence in its integrity and a predictable minimum service life $t_{\min}$ with reliability equal to one.

The objective of the following analysis is to predict the attenuated probability of failure of a component in service after proof testing and the minimum life expectancy of the proof-tested component. This concept will then be extended to predict the component reliability for off-axis proof testing (misaligned and dissimilar multiaxial loads). All derivations in this section are for static fatigue and volume flaws. If the proof-test and service stress distributions are cyclic, the *g*-factor approach is required to transform the stresses to their equivalent static stresses. Analogous relationships may be developed for the surface-flaw solution.

The attenuated probability of failure P_{faV} of a component surviving proof testing for time t_p and subjected to an in-service equivalent static stress distribution $\sigma_{Ieq}(\Psi)$ over a time interval $(t_q - t_p)$ is (Weibull, 1939b, Evans and Wiederhorn, 1974b)

$$P_{faV}\left(t_q\right)=\frac{P_{fV}\left(t_q\right)-P_{fV}\left(t_p\right)}{1-P_{fV}\left(t_p\right)} \tag{D228}$$

The term $P_{fV}(t_p)$ is the probability of failure of a survived component subjected to a proof-test static equivalent stress distribution, $\sigma_{Ieqp}(\Psi)$, over a time interval denoted by t_p. The term $P_{fV}(t_q)$ is the probability of failure of a survived component subjected to a proof-test static equivalent stress distribution $\sigma_{Ieqp}(\Psi)$ over time interval t_p and an in-service static equivalent stress distribution $\sigma_{Ieq}(\Psi)$ over time interval $t_q - t_p$. The reliability of the survived component increases as the ratio of the proof-test stress to the service stress increases.

For the Batdorf model, the probability of failure of a given component over time interval t_p is

$$P_{fV}\left(t_p\right)=1-\exp\left[-\frac{2\,k_{BV}}{\pi}\int_V\int_0^{\pi/2}\int_0^{\pi/2}\sigma_{Ieqp,0}^{m_V}\left(\Psi\right)\sin\alpha\,\mathrm{d}\alpha\,\mathrm{d}\beta\,\mathrm{d}V\right] \tag{D229}$$

where, from equation (D97), the transformed proof-test stress distribution over time interval t_p is

$$\sigma_{Ieqp,0}\left(\Psi\right)=\left[\frac{\sigma_{Ieqp}^{N_V}\left(\Psi\right)t_p}{B_{BV}}+\sigma_{Ieqp}^{N_V-2}\left(\Psi\right)\right]^{\frac{1}{N_V-2}}$$

For the PIA model,

$$P_{fV}\left(t_p\right)=1-\exp\left[-k_{wV}\int_V\left(\sigma_{1p,0}^{m_V}+\sigma_{2p,0}^{m_V}+\sigma_{3p,0}^{m_V}\right)\mathrm{d}V\right] \tag{D230}$$

where

$$\sigma_{ip,0}\left(\Psi\right)=\left[\frac{\sigma_{ip}^{N_V}\left(x,y,z\right)t_p}{B_{wV}}+\sigma_{ip}^{N_V-2}\left(x,y,z\right)\right]^{\frac{1}{N_V-2}}$$

for principal stresses $i = 1, 2, 3$, where $\sigma_{1p}(x, y, z)$, $\sigma_{2p}(x, y, z)$, and $\sigma_{3p}(x, y, z)$ are the proof-test principal tensile stress distributions.

Alternatively, the probability of failure based on the Weibull NSA method is

$$P_{fV}\left(t_p\right)=1-\exp\left[-k_{wpV}\int_V\overline{\sigma}_{np,0}^{m_V}\left(x,y,z\right)\mathrm{d}V\right] \tag{D231}$$

where

$$\overline{\sigma}^{m_V}_{np,0}(x,y,z)=\frac{\int_A \sigma^{m_V}_{np,0}(\Psi)\,\mathrm{d}A}{\int_A \mathrm{d}A}$$

and

$$\sigma_{np,0}(\Psi)=\left[\frac{\sigma^{N_V}_{np}(\Psi)\,t_p}{B_{nwV}}+\sigma^{N_V-2}_{np}(\Psi)\right]^{\frac{1}{N_V-2}}$$

The term $\overline{\sigma}^{m_V}_{np,0}(x,y,z)$ is the proof-test average normal stress from the projection of $\sigma_{np}(\Psi)$, the normal stress, over the surface area of a unit radius sphere (eq. (D11)).

The probability of failure of a given component over time interval t_q is calculated as follows for the Batdorf model

$$P_{fV}(t_q)=1-\exp\left[\frac{-2\,k_{BV}}{\pi}\int_V\int_0^{\pi/2}\int_0^{\pi/2}\sigma^{m_V}_{\mathrm{I}eqq,0}(\Psi)\sin\alpha\,\mathrm{d}\alpha\,\mathrm{d}\beta\,\mathrm{d}V\right] \tag{D232}$$

where

$$\sigma_{\mathrm{I}eqq,0}(\Psi)=\left[\frac{\sigma^{N_V}_{\mathrm{I}eq}(\Psi)\left(t_q-t_p\right)+\sigma^{N_V}_{\mathrm{I}eqp}(\Psi)\,t_p}{B_{BV}}+\sigma^{N_V-2}_{\mathrm{I}eq}(\Psi)\right]^{\frac{1}{N_V-2}}$$

For the PIA model,

$$P_{fV}(t_q)=1-\exp\left[-k_{wV}\int_V\left(\sigma^{m_V}_{1q,0}+\sigma^{m_V}_{2q,0}+\sigma^{m_V}_{3q,0}\right)\mathrm{d}V\right] \tag{D233}$$

where

$$\sigma_{iq,0}(\Psi)=\left[\frac{\sigma^{N_V}_{i}(x,y,z)\left(t_q-t_p\right)+\sigma^{N_V}_{ip}(x,y,z)\,t_p}{B_{wV}}+\sigma^{N_V-2}_{i}(x,y,z)\right]^{\frac{1}{N_V-2}}$$

for principal stresses i = 1, 2, 3, where $\sigma_1(x, y, z)$, $\sigma_2(x, y, z)$, and $\sigma_3(x, y, z)$ are the principal tensile stress distributions. For the Weibull NSA method,

$$P_{fV}(t_q)=1-\exp\left[-k_{wpV}\int_V\overline{\sigma}^{m_V}_{nq,0}(x,y,z)\,\mathrm{d}V\right] \tag{D234}$$

where

$$\overline{\sigma}^{m_V}_{nq,0}(x,y,z)=\frac{\int_A \sigma^{m_V}_{nq,0}(\Psi)\,\mathrm{d}A}{\int_A \mathrm{d}A}$$

and

$$\sigma_{nq,0}(\Psi)=\left(\frac{\sigma_n^{N_V}(\Psi)(t_q-t_p)+\sigma_{np}^{N_V}(\Psi)\,t_p}{B_{nwV}}+\sigma_n^{N_V-2}(\Psi)\right)^{\frac{1}{N_V-2}}$$

where $\overline{\sigma}^{m_V}_{nq,0}(x,y,z)$ is the average transformed normal stress from the projection of the transformed normal stress distribution $\sigma_{nq,0}(\Psi)$ over a unit radius sphere. After determining the values of $P_{fV}(t_q)$ and $P_{fV}(t_p)$, the service-component-attenuated probability of failure $P_{faV}(t_q)$ is computed. Depending on the magnitude of the service load and time of application, $P_{fV}(t_q)$ can be less than $P_{fV}(t_p)$. For this case, the attenuated probability of failure P_{faV} is 0.

The minimum life expectancy of a survived component for a static equivalent stress distribution is obtained by satisfying the condition $P_{fV}(t_q) = P_{fV}(t_p)$. For the Batdorf model, equating equations (D232) and (D229) results in

$$t_{\min}=\left(\frac{B_{BV}}{\sigma^2_{\mathrm{I}eq}(\Psi)}\left\{\left[\left[\frac{\sigma_{\mathrm{I}eqp}(\Psi)}{\sigma_{\mathrm{I}eq}(\Psi)}\right]^{N_V-2}-1\right]\right\}\right)_{\min} \tag{D235}$$

where the subscript “min” denotes the smallest value of the term in equation (D235) for all Ψ throughout the component. If at any location the component proof-test stress level is less than the service stress level, then an assured minimum lifetime $t_{\min}$ does not exist and the component cannot be guaranteed to survive for any given time during service loading. When the proof-test loading is identical to the service loading, except for the magnitude of the loads, then the minimum value for equation (D235) occurs at the maximum stress point in the component. Analogous relations for $t_{\min}$ may be obtained for the PIA model and the Weibull NSA method.

D.2.2.7 Proof testing—off-axis loading.—Often, the proof-test loading does not exactly simulate the service loading. In such cases, the component stress distribution during testing differs from that during service, resulting in what is known as off-axis loading (misaligned and dissimilar loadings). Equation (D228) must then be applied locally at Ψ to calculate the attenuated failure probability, and the Batdorf model or Weibull’s NSA method are applied. Regions where the service stress is compressive are assumed not to fail.

For off-axis loading, the load direction and/or load boundary differ from the service load condition, and modeling is now with respect to a global coordinate system (see eqs. (D101), (D102), (D109), and (D110)). For the Batdorf model, the probability of failure for a given component over time interval t_p is then

$$P_{fV}(t_p)=1-\exp\left[\frac{-k_{BV}}{2\pi}\int_V\int_0^{2\pi}\int_0^{\pi/2}\sigma^{m_V}_{\mathrm{I}eqp,0}(\Psi)\sin\alpha\,\mathrm{d}\alpha\,\mathrm{d}\beta\,\mathrm{d}V\right] \tag{D236}$$

and the probability of failure over time interval t_q is

$$P_{fV}(t_q)=1-\exp\left[\frac{-k_{BV}}{2\pi}\int_V\int_0^{2\pi}\int_0^{\pi/2}\sigma^{m_V}_{\mathrm{I}eqq,0}(\Psi)\sin\alpha\,\mathrm{d}\alpha\,\mathrm{d}\beta\,\mathrm{d}V\right] \tag{D237}$$

where $\sigma_{\mathrm{I}eqp,0}(\Psi)$ and $\sigma_{\mathrm{I}eqq,0}(\Psi)$ are the previously defined transformed stress distributions. Substituting equations (D236) and (D237) into equation (D228) and simplifying yields the expression for the attenuated failure probability

$$P_{faV}\left(t_q\right)=1-\exp\left\{-\frac{k_{BV}}{2\pi}\int_V\int_0^{2\pi}\int_0^{\pi/2}\left[\sigma_{\mathrm{I}eqq,0}^{m_V}(\Psi)-\sigma_{\mathrm{I}eqp,0}^{m_V}(\Psi)\right]H(\Psi)\sin\alpha\,\mathrm{d}\alpha\,\mathrm{d}\beta\,\mathrm{d}V\right\} \tag{D238}$$

where

$$H(\Psi)=1 \quad \sigma_{\mathrm{I}eq}(\Psi)\geq\sigma_{\mathrm{I}eqp}(\Psi)$$

If

$$\sigma_{\mathrm{I}eq}(\Psi)<\sigma_{\mathrm{I}eqp}(\Psi)$$

then

$$H(\Psi)=1 \quad t_{\min}(\Psi)<t_q-t_p$$

$$H(\Psi)=0 \quad t_{\min}(\Psi)\geq t_q-t_p$$

The Heaviside function is introduced to account for $t_{\min}$, which is now evaluated locally at Ψ.

D.2.3 Gaussian Numerical Integration Procedure for the Batdorf Theory

For volume flaws integrating over one-eighth of the unit sphere,

$$P_{fV}\left(t_f\right)=1-\exp\left[-\frac{2k_{BV}}{\pi}\sum_{isub=1}^{n_{\mathrm{sub}}}V_{isub}\left(\int_0^{\pi/2}\int_0^{\pi/2}\sigma_{\mathrm{I}eq,0}^{m_V}(\Psi)\sin\alpha\,\mathrm{d}\alpha\,\mathrm{d}\beta\right)_{isub}\right] \tag{D239}$$

Refer to figure D.2 (also fig. D.6) for the definitions of angles α and β. The integration of the unit sphere of equation (D239) can be performed using gaussian numerical integration or Legendre-Gauss quadrature. The gaussian numerical integration formula is

$$\int_{\chi_1}^{\chi_2}f(\chi)\mathrm{d}\chi=\frac{(\chi_2-\chi_1)}{2}\sum_{j=1}^{n_{gp}}w_j\;f\left[\frac{h_j(\chi_2-\chi_1)+\chi_2+\chi_1}{2}\right] \tag{D240}$$

where w_j are the gaussian weights and h_j are the base points or roots of Legendre polynomials, the values of which are obtained from standard mathematical tables for a given n_{gp} number of points. For a constant angle α,

$$\mathrm{d}\alpha\int_0^{\pi/2}\sigma_{\mathrm{I}eq,0}^{m_V}(\alpha,\beta)\sin\alpha\,\mathrm{d}\beta=\mathrm{d}\alpha\left(\frac{\pi/2-0}{2}\right)\sum_{j=1}^{n_{gp}}w_j\,\sigma_{\mathrm{I}eq,0}^{m_V}(\alpha,z_j)\sin\alpha=\mathrm{d}\alpha\left(\frac{\pi}{4}\right)\sum_{j=1}^{n_{gp}}w_j\,\sigma_{\mathrm{I}eq,0}^{m_V}(\alpha,z_j)\sin\alpha \tag{D241}$$

where z_j is a transformed value for angle β defined as

$$z_j = \frac{h_j(\pi/2-0)+\pi/2+0}{2} = \frac{\pi(h_j+1)}{4} \tag{D242}$$

Then,

$$\begin{aligned}\int_0^{\pi/2}\int_0^{\pi/2}\sigma_{\mathrm{I}eq,0}^{m_V}(\Psi)\sin\alpha\,\mathrm{d}\alpha\,\mathrm{d}\beta &= \left(\frac{\pi/2-0}{2}\right)\sum_{k=1}^{n_{gp}} w_k\ \sin(u_k)\left[\left(\frac{\pi}{4}\right)\sum_{j=1}^{n_{gp}} w_j\,\sigma_{\mathrm{I}eq,0}^{m_V}(u_k,z_j)\right] \\ &= \frac{\pi^2}{16}\sum_{k=1}^{n_{gp}}\sum_{j=1}^{n_{gp}}(w_k w_j)\sin(u_k)\sigma_{\mathrm{I}eq,0}^{m_V}(u_k,z_j)\end{aligned} \tag{D243}$$

where u_k is a transformed value for angle α defined by

$$u_k = \frac{h_k(\pi/2-0)+\pi/2+0}{2} = \frac{\pi(h_k+1)}{4} \tag{D244}$$

and again, w_k are the gaussian weights and h_k are the base points or roots of Legendre polynomials obtained from standard mathematical tables. Consequently, combining equation (D239) with equation (D243) results in a numerical algorithm for volume-flaw failure probability of

$$\begin{aligned}P_{fV}(t_f) &= 1-\exp\left\{-\frac{\pi k_{BV}}{8}\sum_{isub=1}^{n_{\mathrm{sub}}} V_{isub}\left[\sum_{k=1}^{n_{gp}}\sum_{j=1}^{n_{gp}}(w_k w_j)\sin(u_k)\sigma_{\mathrm{I}eq,0}^{m_V}(u_k,z_j)\right]_{isub}\right\} \\ z_j &= \frac{\pi(h_j+1)}{4} \\ u_k &= \frac{\pi(h_k+1)}{4}\end{aligned} \tag{D245}$$

Likewise, for surface-distributed flaws for one-fourth of the unit circle (see fig. D.3),

$$P_{fS}(t_f) = 1-\exp\left\{-\frac{2k_{BS}}{\pi}\sum_{isub=1}^{n_{\mathrm{sub}}} A_{isub}\left[\int_0^{\pi/2}\sigma_{\mathrm{I}eq,0}^{m_S}(\Psi)\,\mathrm{d}\alpha\right]_{isub}\right\} \tag{D246}$$

$$\int_0^{\pi/2}\sigma_{\mathrm{I}eq,0}^{m_S}(\alpha)\,\mathrm{d}\alpha = \left(\frac{\pi/2-0}{2}\right)\sum_{j=1}^{n_{gp}} w_j\,\sigma_{\mathrm{I}eq,0}^{m_V}(z_j) = \left(\frac{\pi}{4}\right)\sum_{j=1}^{n_{gp}} w_j\,\sigma_{\mathrm{I}eq,0}^{m_V}(z_j) \tag{D247}$$

where z_j is a transformed value for angle α defined by

$$z_j = \frac{h_j(\pi/2-0)+\pi/2+0}{2} = \frac{\pi(h_j+1)}{4} \tag{D248}$$

Consequently, combining equation (D246) with equation (D247) results in a numerical algorithm for surface-flaw failure probability of

$$P_{fS}\left(t_f\right)=1-\exp\left\{-\frac{k_{BS}}{2}\sum_{isub=1}^{n_{sub}} A_{isub}\left[\sum_{j=1}^{n_{gp}} w_j\,\sigma_{\mathrm{I}eq,0}^{m_V}\left(z_j\right)\right]_{isub}\right\}$$

$$z_j=\frac{\pi\left(h_j+1\right)}{4} \tag{D249}$$

CARES/*Life* defaults to n_{gp} = 15, although values for 30 and 50 points are available for increased sampling precision.

Appendix E
Revised Version of Life Prediction and Reliability Analysis of Ceramic Structures Under Combined Static and Cyclic Fatigue[3]

Sharif Rahman
The University of Iowa
Iowa City, Iowa 52242

Noel N. Nemeth and John P. Gyekenyesi
National Aeronautics and Space Administration
Glenn Research Center
Cleveland, Ohio 44135

E.1 Summary

This appendix presents a computational methodology for life prediction and time-dependent reliability analysis of ceramic structures under combined effects of static and cyclic fatigue. It involves (1) a crack-growth equation representing damage contributions from both static and cyclic fatigue, (2) a multivariate nonlinear regression model for performing parameter estimation from fatigue data generated by small specimens, and (3) the Batdorf model for structural reliability analysis. A linear superposition of crack-growth rates obtained from the power-law and Walker-law equations was used. The model assumes that the time-dependent and cycle-dependent crack-growth formulation exponents are identical, and that loading frequency and amplitude do not vary over time. For the parameter estimation, the regression was performed using a nonlinear least-squares method and a modified Levenberg-Marquardt algorithm. A numerical example is presented to illustrate the parameter estimation component of this methodology. The results suggest that the predicted stress-life curves based on the proposed model can correlate better with experimental data when compared with either the power-law or the Walker-law models individually.

E.2 Introduction

The catastrophic failure of ceramic materials can be caused by subcritical crack growth (SCG) of preexisting natural flaws. In other words, under the action of a load, a flaw can grow in a stable manner until a critical dimension is reached, then uncontrolled and catastrophic crack propagation ensues. Hence, understanding SCG behavior under static, dynamic, and cyclic loads is important for the reliable design of ceramic structures. The SCG phenomenon may arise from a variety of physical processes. For example, the crack growth may occur because of the interaction of the environment with the high stress fields near the crack tip (static fatigue) or because of mechanically induced degradation from cyclic fatigue loading (cyclic fatigue). Until about 1990, the general perception was that ceramic materials are largely insensitive to mechanical degradation under cyclic loads (Evans, 1980; Evans and Fuller, 1974; and Evans and Linzer, 1976). Hence, the SCG rate and lifetime for cyclic loading were predicted from the results of static fatigue. This was substantiated by cyclic experiments on glass and porcelain materials (Evans and Fuller, 1974). However, several studies suggest that polycrystalline ceramics and ceramic composites can be susceptible to cyclic fatigue degradation (Ritchie and Dauskardt, 1991; Kishimoto, 1991; and Suresh, 1990). Such degradation cannot be explained by environmental interaction alone, but rather is due to a mechanically induced effect associated with the repeated loading and unloading of the applied forces.

---

[3] This is a revised version of Rahman et al. (1998). Note that in this appendix some variables were renamed and some text was edited to be more consistent with the main text of this report.

Under these conditions, the experimentally measured lifetimes, as observed for alumina, are shorter by several orders of magnitude than can be predicted from static tests (Chen and Knapp, 1974; Pabst et al., 1980; and Fett et al., 1991 and 1993). A dependency of lifetime on cyclic loading frequency was observed that is in contrast to the predictions of static tests (Fett et al., 1993; and Krohn and Hasselman, 1972). Test data verifying enhanced crack-growth rate under cyclic loading compared with static loading now exist for other brittle monolithic ceramics (e.g., silicon nitride—Hoshide et al., 1988; Kawakubo and Komeya, 1987; Horibe, 1988; Masuda et al., 1988; Ueno, 1990; and Mutoh et al., 1991), toughened ceramics (e.g., magnesia-partially-stabilized zirconia—Dauskardt et al., 1987, 1990a, and 1990b; Swain and Zelizko, 1986; Zelizko et al., 1988; Zelizko and Swain, 1988; Suresh and Brockenbrough, 1988; Jensen et al., 1989; Sylva and Suresh, 1989; Steffen et al., 1990; and Bowman et al., 1987), sintered zirconia (e.g., yttria-stabilized zirconia—Liu and Chen, 1991a, 1991b, and 1992), and reinforced alumina (Dauskardt et al., 1993).

To predict the susceptibility of a load-bearing ceramic part to catastrophic failure, simple phenomenological models are used that are calibrated to experimental results involving many specimens. The variability in strength observed from nominally identical parts is described with the Weibull distribution. For static fatigue, a power-law relationship (Evans and Wiederhorn, 1974a) is typically employed to characterize the crack-growth rate as a function of the stress-intensity factor (SIF). For cyclic fatigue, either the Paris law (Paris and Erdogan, 1963) or Walker law (Walker, 1970, pp. 1–14) is used to define the kinetics of SCG. Integration of such a relationship (either power law, Paris law, or Walker law) with the Weibull distribution is used to calculate the time-dependent reliability of a component.

Although much has been learned about the individual mechanisms of SCG, not enough research has been performed on the combined effects of static and cyclic fatigue. For a real component in service, SCG is a complex phenomenon that may involve simultaneous and synergistic failure mechanisms. Hence, material strength degradation due to SCG may be a combination of damage from both time-dependent and cycle-dependent crack growth. Currently, methods are available only to characterize static or cyclic fatigue working independently. Under these conditions, the inert and fatigue parameters can be easily calculated using the aforementioned laws and standard parameter estimation techniques. However, not many models exist to characterize SCG under the combined effects of static and cyclic fatigue. Consequently, the reliability of ceramic structures is not well understood when there are damage contributions from both types of fatigue.

This report proposes a computational methodology for time-dependent reliability analysis of ceramic structures under the combined effects of static and cyclic fatigue. It is based on (1) a crack-growth equation including damage contributions from both static and cyclic fatigue, (2) a multivariate nonlinear regression model for performing parameter estimation from fatigue data generated by small simply loaded specimens, and (3) the Batdorf model for structural reliability analysis. A linear superposition of crack-growth rates obtained from the power-law and Walker-law equations was used to model fatigue effects. For the parameter estimation, the regression was performed using a nonlinear least-squares method and a modified Levenberg-Marquardt algorithm to calculate the optimized parameters. The model was tested with experimental data available in the literature. Finally, a closed-form expression was derived for the transformed inert strength, which can be used for fatigue reliability analysis. A numerical example is presented to illustrate the parameter estimation component of this methodology.

E.3 Combined Static and Cyclic Fatigue

E.3.1 Crack-Growth Equation

Traditionally, the power law (Evans and Wiederhorn, 1974a) has been used to characterize crack growth under static and cyclic loading, and more recently, the Walker law (Walker, 1970, pp. 1–14) has been used to characterize crack growth under cyclic (fatigue) loading. For combined static and cyclic fatigue, assume that the crack-growth rates by each of these two growth mechanisms can be superposed linearly to yield

$$\frac{\mathrm{d}a(\Psi,t)}{\mathrm{d}t} = A_1 K_{\mathrm{I}eqg}^{N_1}(\Psi,t) + f_c A_2 K_{\mathrm{I}eq,\max}^{N_2-Q}(\Psi,t)\Delta K_{\mathrm{I}eq}(\Psi,t)^{Q} \tag{E1}$$

where t is time; Ψ is a vector representing the location and/or orientation of the crack in the body; a is the appropriate crack length at time t and Ψ; f_c is constant-amplitude frequency; A_1, A_2, N_1, N_2, and Q are material parameters that depend on temperature and environment; $K_{\mathrm{I}eq}(\Psi, t)$ is the mode-I equivalent SIF at time t and Ψ; $K_{\mathrm{I}eq,\max}$ is the maximum mode-I equivalent SIF (i.e., when the stress reaches maximum over the cycle); and $\Delta K_{\mathrm{I}eq}(\Psi, t)$ is the range of the mode-I equivalent SIF over the cycle. From linear-elastic fracture mechanics, these SIFs can be expressed as

$$K_{\mathrm{I}eqg}(\Psi,t) = \sigma_{\mathrm{I}eqg}(\Psi) Y \sqrt{a(\Psi,t)} \tag{E2}$$

$$K_{\mathrm{I}eq,\max}(\Psi,t) = \sigma_{\mathrm{I}eq,\max}(\Psi) Y \sqrt{a(\Psi,t)} \tag{E3}$$

$$\Delta K_{\mathrm{I}eq}(\Psi,t) = \left[\sigma_{\mathrm{I}eq,\max}(\Psi) - \sigma_{\mathrm{I}eq,\min}(\Psi)\right] Y \sqrt{a(\Psi,t)} \tag{E4}$$

where $\sigma_{\mathrm{I}eq,\max}(\Psi)$ is the far-field equivalent maximum normal stress, $\sigma_{\mathrm{I}eq,\min}(\Psi)$ is the far-field equivalent minimum normal stress, Y is a geometric factor, and $\sigma_{\mathrm{I}eqg}(\Psi)$ is the far-field equivalent static stress given by

$$\sigma_{\mathrm{I}eqg}(\Psi) = g^{1/N_1}(\Psi)\sigma_{\mathrm{I}eq,\max}(\Psi) \tag{E5}$$

with the g-factor defined as

$$g(\Psi) = \frac{1}{t_{\mathrm{per}}} \int_0^{t_{\mathrm{per}}} \left[\frac{\sigma_{\mathrm{I}eq}(\Psi,t)}{\sigma_{\mathrm{I}eq,\max}(\Psi)}\right]^{N_1} \mathrm{d}t \tag{E6}$$

where $\sigma_{\mathrm{I}eq}(\Psi, t)$ is the time-dependent cyclic load. In equation (E5), it is assumed that the equivalent static stress distribution $\sigma_{\mathrm{I}eqg}(\Psi)$ produces the same amount of crack growth as the periodic cyclic stress distribution over the time interval (period) t_{per} (Mencik, 1984). See table D.1 from Nemeth et al. (2003), Mencik (1984), and Gross et al. (1996) for a list of g-factors for various types of loading conditions. Equations (E2) to (E4) are used to express the crack-growth rate in equation (E1) as

$$\frac{\mathrm{d}a(\Psi,t)}{\mathrm{d}t} = A_1 g(\Psi) K_{\mathrm{I}eq,\max}(\Psi,t)^{N_1} + f_c A_2 [1 - R(\Psi)]^Q K_{\mathrm{I}eq,\max}(\Psi,t)^{N_2} \tag{E7}$$

where

$$R(\Psi) = \frac{\sigma_{\mathrm{I}eq,\min}(\Psi)}{\sigma_{\mathrm{I}eq,\max}(\Psi)} \tag{E8}$$

is known as the stress ratio.

E.3.2 Inert Strength

To predict the time-dependent failure probability under fatigue loading, one must calculate the inert strength $\sigma_{\mathrm{I}eq,0}(\Psi)$: that is, the effective (equivalent applied) stress at time $t = 0$. Given a crack-growth equation (such as eq. (E7)), the critical equivalent stress $\sigma_{\mathrm{I}eqc}(\Psi, t_f)$ at time to failure t_f can be transformed to its equivalent effective stress $\sigma_{\mathrm{I}eq,0}(\Psi)$ for $t = 0$. Let $\sigma_{\mathrm{I}eqc}(\Psi, t)$ denote the critical stress (or strength) at time t when the SIF reaches the equivalent mode-I plane strain fracture toughness of the material at crack initiation $K_{\mathrm{I}eqc}$. Using equation (E2) gives

$$K_{\mathrm{I}eqc} = \sigma_{\mathrm{I}eqc}(\Psi,t)Y\sqrt{a(\Psi,t)} \tag{E9}$$

On inversion,

$$a(\Psi,t) = \left(\frac{K_{\mathrm{I}eqc}}{Y}\right)^2 \frac{1}{\sigma_{\mathrm{I}eqc}^2(\Psi,t)} \tag{E10}$$

and subsequent differentiation with time gives

$$\frac{\mathrm{d}a(\Psi,t)}{\mathrm{d}t} = -2\left(\frac{K_{\mathrm{I}eqc}}{Y}\right)^2 \frac{1}{\sigma_{\mathrm{I}eqc}^3(\Psi,t)} \frac{\mathrm{d}\sigma_{\mathrm{I}eqc}(\Psi,t)}{\mathrm{d}t} \tag{E11}$$

Comparing equations (E7) and (E11) and noting that

$$\frac{K_{\mathrm{I}eq,\max}(\Psi,t)}{K_{\mathrm{I}eqc}} = \frac{\sigma_{\mathrm{I}eq,\max}(\Psi,t)}{\sigma_{\mathrm{I}eqc}(\Psi,t)} \tag{E12}$$

we can show that

$$\begin{gathered} -2\left(\frac{K_{\mathrm{I}eqc}}{Y}\right)^2 \frac{1}{\sigma_{\mathrm{I}eqc}^3(\Psi,t)} \frac{\mathrm{d}\sigma_{\mathrm{I}eqc}(\Psi,t)}{\mathrm{d}t} = \\ A_1 g(\Psi) K_{\mathrm{I}eqc}^{N_1} \left[\frac{\sigma_{\mathrm{I}eq,\max}(\Psi,t)}{\sigma_{\mathrm{I}eqc}(\Psi,t)}\right]^{N_1} + f_c A_2 [1-R(\Psi)]^Q K_{\mathrm{I}eqc}^{N_2} \left[\frac{\sigma_{\mathrm{I}eq,\max}(\Psi,t)}{\sigma_{\mathrm{I}eqc}(\Psi,t)}\right]^{N_2} \end{gathered} \tag{E13}$$

If one follows the separation of variables ($\sigma_{\mathrm{I}eqc}(\Psi, t)$ and t) in equation (E13), it is theoretically possible to calculate the inert strength $\sigma_{\mathrm{I}eqc,0}$ (Ψ), but no closed-form explicit solution exists using equation (E13) directly. A closed-form solution is desired in order to minimize the amount of computation involved with reliability analysis—especially with large finite element models. However, if it is assumed that the fatigue exponents for static and cyclic fatigue are identical, a relatively simple closed-form expression can be obtained. For example, if $N_1 = N_2 = N$, equation (E13) becomes

$$\int_{\sigma_{\mathrm{I}eqc}(\Psi,t=0)}^{\sigma_{\mathrm{I}eqc}(\Psi,t_f)} \sigma_{\mathrm{I}eqc(\Psi,t)}^{N-3} \mathrm{d}\sigma_{\mathrm{I}eqc} = -\frac{1}{2}\left\{A_1 g(\Psi) + f_c A_2 [1-R(\Psi)]^Q\right\} Y^2 K_{\mathrm{I}eqc}^{N-2} \sigma_{\mathrm{I}eq,\max}^N(\Psi) \int_0^{t_f} \mathrm{d}t \tag{E14}$$

which can be solved for the inert strength as

$$\sigma_{\mathrm{I}eq,0}\left(\Psi\right)=\left(\frac{\sigma_{\mathrm{I}eq,\max}^{N}\left(\Psi\right)\left\{g\left(\Psi\right)+f_c\,\frac{A_2}{A_1}\left[1-R\left(\Psi\right)\right]^{Q}\right\}t_f}{B}+\sigma_{\mathrm{I}eqc}^{N-2}\left(\Psi,t_f\right)\right)^{\frac{1}{N-2}} \tag{E15}$$

where $\sigma_{\mathrm{I}eq,0}(\Psi) = \sigma_{\mathrm{I}eqc}(\Psi, t = 0)$ and

$$B=\frac{2}{A_1 Y^2 K_{\mathrm{I}eqc}^{N-2}\left(N-2\right)} \tag{E16}$$

It must be emphasized that equations (E15) and (E16) impose a single value of fatigue exponent over all conditions of static and cyclic fatigue. Although this is a significant limitation imposed on the proposed methodology, it can be argued that it, nonetheless, represents an improvement over the previous practice of using either a pure power-law or Walker-law formulation. Also, the convenient form of equation (E15) considerably simplifies the task of estimating the model parameters from cyclic fatigue specimen rupture data.

For

$$\frac{\sigma_{\mathrm{I}eq,\max}^{2}\left(\Psi\right)\left\{g\left(\Psi\right)+f_c\,\frac{A_2}{A_1}\left[1-R\left(\Psi\right)\right]^{Q}\right\}t_f}{B}>>1 \tag{E17}$$

Equation (E15) can be further approximated by

$$\sigma_{\mathrm{I}eq,0}\left(\Psi\right)=\left\{\frac{\sigma_{\mathrm{I}eq,\max}^{N}\left(\Psi\right)\left\{g\left(\Psi\right)+f_c\,\frac{A_2}{A_1}\left[1-R\left(\Psi\right)\right]^{Q}\right\}t_f}{B}\right\}^{\frac{1}{N-2}} \tag{E18}$$

Equation (E18) neglects the strength of the material (at $t = t_f$), but the simplified equation is very useful for parameter estimation as described later.

By setting either $A_2 = 0$ or $A_1 = 0$ in equation (E1), one can easily check that equation (E18) reduces to

$$\sigma_{\mathrm{I}eq,0}\left(\Psi\right)=\left[\frac{\sigma_{\mathrm{I}eq,\max}^{N}\left(\Psi\right)g\left(\Psi\right)t_f}{B}\right]^{\frac{1}{N-2}} \tag{E19}$$

$$B=\frac{2}{A_1 Y^2 K_{\mathrm{I}eqc}^{N-2}\left(N-2\right)} \tag{E20}$$

and

$$\sigma_{\mathrm{I}eq,0}\left(\Psi\right)=\left\{\frac{\sigma_{\mathrm{I}eq,\max}^{N}\left(\Psi\right)f_c\left[1-R\left(\Psi\right)\right]^{Q}t_f}{B}\right\}^{\frac{1}{N-2}} \tag{E21}$$

$$B = \frac{2}{A_2 Y^2 K_{\mathrm{I}eqc}^{N-2}(N-2)} \tag{E22}$$

for crack growth under pure static fatigue and pure cyclic fatigue, respectively. Equations (E19) to (E22) match the existing solutions (see app. D, reproduced from Nemeth et al., 2003) for the power-law and Walker-law models for static and cyclic fatigue, respectively.

E.4 Time-Dependent Reliability Analysis

Time-dependent reliability is based on the mode-I equivalent stress distribution transformed to its equivalent stress distribution at time $t = 0$. In this study, a closed-form expression for the transformed stress (inert stress) under the combined effects of static and cyclic fatigue crack growth was developed (see eq. (E18)). It involves various fatigue parameters, such as A_1, A_2, B, N, and Q, that must be estimated from the fatigue data generated by small, simply loaded specimens. Details of parameter estimation are given later. In this section, the reliability model is briefly described with the assumption of first volume flaws and then surface flaws in ceramic structures.

E.4.1 Volume-Flaw Analysis

The probability of failure for a ceramic component using the Batdorf model for volume flaws is (Batdorf and Crose, 1974; Batdorf and Heinisch, 1978a; and Batdorf, 1977b)

$$P_f(t) = 1 - \exp\left\{ -\int_V \left[\int_0^{\sigma_{\mathrm{I}eq,0,\max}} \frac{\Omega}{4\pi} \frac{\mathrm{d}\eta(\sigma_{\mathrm{I}eqc})}{\mathrm{d}\sigma_{\mathrm{I}eqc}} \mathrm{d}\sigma_{\mathrm{I}eqc} \right] \mathrm{d}V \right\} \tag{E23}$$

where V is the volume, η is the crack-density function, $\sigma_{\mathrm{I}eq,0,\max}$ is the maximum value of $\sigma_{\mathrm{I}eq,0}$ (Ψ) for all values of Ψ, and Ω is the area of a solid angle projected onto a unit radius sphere in principal stress space containing all crack orientations for which the effective stress is greater than or equal to the critical equivalent mode-I strength $\sigma_{\mathrm{I}eqc}$. The crack-density distribution is a function of the critical effective stress distribution. For volume-flaw analysis, the crack-density function is expressed as

$$\eta(\sigma_{\mathrm{I}eqc}) = k_B \sigma_{\mathrm{I}eqc}^m \tag{E24}$$

where k_B and m are material constants. The solid angle Ω is expressed as

$$\Omega = \int_0^{2\pi} \int_0^{\pi} H(\sigma_{\mathrm{I}eq,0}, \sigma_{\mathrm{I}eqc}) \sin\alpha \, \mathrm{d}\alpha \, \mathrm{d}\beta \tag{E25}$$

where

$$H(\sigma_{\mathrm{I}eq,0}, \sigma_{\mathrm{I}eqc}) = \begin{cases} 0 & \sigma_{\mathrm{I}eq,0} < \sigma_{\mathrm{I}eqc} \\ 1 & \sigma_{\mathrm{I}eq,0} \geq \sigma_{\mathrm{I}eqc} \end{cases} \tag{E26}$$

and α and β are the radial and azimuthal angles, respectively, on the unit radius sphere. The transformed equivalent stress $\sigma_{\mathrm{I}eq,0}$ (Ψ) is dependent on the appropriate fracture criterion, crack shape, and time to failure t_f. Equation (E23) can be simplified by integrating $\sigma_{\mathrm{I}eqc}$, yielding the time-dependent probability of failure for volume-flaw analysis, and is given by Batdorf (1977b):

$$P_f = 1 - \exp\left[-\frac{k_B}{2\pi} \int_V \int_0^{2\pi} \int_0^{\pi} \sigma_{\mathrm{I}eq,0}(\Psi)^m \sin\alpha \, \mathrm{d}\alpha \, \mathrm{d}\beta \, \mathrm{d}V \right] \tag{E27}$$

E.4.2 Surface-Flaw Analysis

The probability of failure for a ceramic component using the Batdorf model for surface flaws is (Batdorf and Crose, 1974; Batdorf and Heinisch, 1978a; and Batdorf, 1977b)

$$P_f(t) = 1 - \exp\left\{ -\int_A \left[\int_0^{\sigma_{\mathrm{I}eq,0,\max}} \frac{\omega}{\pi} \frac{\mathrm{d}\eta(\sigma_{cr})}{\mathrm{d}\sigma_{cr}} \mathrm{d}\sigma_{cr} \right] \mathrm{d}A \right\} \tag{E28}$$

where A is the surface area and ω is the arc length of an angle α projected onto a unit radius semicircle in principal stress space containing all of the crack orientations for which the effective stress is greater than or equal to the critical stress. Analogous to the argument for volume flaws, equation (E28) can be reformulated, yielding (Batdorf, 1978)

$$P_f(t) = 1 - \exp\left[-\frac{k_B}{\pi} \int_A \int_0^{\pi} \sigma_{\mathrm{I}eq,0}(\Psi)^m \, \mathrm{d}\alpha \, \mathrm{d}A \right] \tag{E29}$$

For both volume and surface-flaw analyses, the fracture criteria and crack shapes available for time-dependent analysis are identical to those used for fast-fracture analysis in CARES/*Life* (Ceramics Analysis and Reliability Evaluation of Structures/*Life*; see app. D, reproduced from Nemeth et al., 2003). These fracture criteria include Weibull normal stress averaging (Weibull, 1939a; a shear-insensitive case of the Batdorf theory), the total coplanar strain-energy release rate (Batdorf and Heinisch, 1978a), and the noncoplanar crack-extension (Shetty) criterion (Shetty, 1987).

For a stressed component, the probability of failure can be calculated by equation (E27) or (E29), depending on the type of flaws. The finite element method enables discretization of the component into incremental volume elements (volume flaws) and area elements (surface flaws). CARES/*Life* evaluates the reliability at the gaussian integration points of the element. The subelement volume is defined as the contribution of the numerical integration procedure. The volume or area of each subelement (corresponding to a gaussian integration point) is calculated using shape functions inherent to the element type (Powers et al., 1992). If it is assumed that the probability of survival for each element is a mutually exclusive event, the overall component reliability is then the product of all the calculated element (or subelement) survival probabilities.

E.5 Estimation of Fatigue Parameters

Lifetime reliability of structural ceramic components depends on the loading history, the component geometry, the distribution of preexisting flaws, and the parameters that characterize SCG. These crack-growth parameters must be measured under conditions representative of the service environment. When fatigue parameters are being determined from the rupture data of naturally flawed small specimens, the statistical effects of flaw distribution must be considered along with the strength degradation effects of SCG. In this study, a multivariate nonlinear least-squares method was developed to estimate the fatigue parameters. This method is described in terms of volume-flaw analysis. An analogous formulation can easily be developed for surface flaws by replacing the effective volume with the effective area.

For combined static and cyclic fatigue, using the uniaxial time-dependent Weibull distribution for volume flaws, the failure probability P_f is (see app. D, reproduced from Nemeth et al., 2003)

$$P_f = 1 - \exp\left[-\frac{1}{\sigma_o^m}\int_V \sigma_{1,0}^m(\Psi)\,\mathrm{d}V\right] \tag{E30}$$

where $\sigma_{1,0}$ is the transformed principal stress back to time $t = 0$, V is the volume, and m and σ_0 are the shape and scale parameters of the Weibull distribution. For the case when the g-factor is constant throughout the specimen, henceforth denoted by g, equation (E30) can be expressed in terms of the maximum failure stress σ_f in the specimen by multiplying the numerator and denominator by $\sigma_f{}^{mN/N-2}$. Thus,

$$P_f = 1 - \exp\left[-V_{ef}\left(\frac{t_f}{t_o}\right)^{\frac{m}{N-2}}\right] \tag{E31}$$

where

$$t_o = \frac{B\sigma_o^{N-2}}{\left[g + f_c\frac{A_2}{A_1}(1-R)^Q\right]\sigma_f{}^N} \tag{E32}$$

where

$$V_{ef} = \int_V \left[\frac{\sigma_{1,\max}(\Psi)}{\sigma_f}\right]^{\frac{mN}{N-2}}\mathrm{d}V \tag{E33}$$

is the modified effective volume when the applied stress distribution is normalized with respect to σ_f, and where $\sigma_{1,\max}(\Psi)$ is the maximum principal stress within the cycle located at Ψ. (Note that g, f_c, and R are assumed to be constant throughout the specimen. Rearranging equation (E31) yields

$$t_f = \frac{B\sigma_o^{N-2}}{\left[g + f_c\frac{A_2}{A_1}(1-R)^Q\right]\left[\frac{V_{ef}}{\ln\left(\frac{1}{1-P_f}\right)}\right]^{\frac{m}{N-2}}\sigma_f{}^N} \tag{E34}$$

which represents an equation for specimen time to failure as a function of failure stress for a fixed value of failure probability. On simplifying this expression,

$$t_f = \frac{\tilde{C}}{\left[g + f_c \tilde{A}(1-R)^Q\right]\sigma_f{}^N} \tag{E35}$$

where $\tilde{A} = A_2/A_1$ and $\tilde{C}$ are constants with

$$\tilde{C} = \frac{B\sigma_o^{N-2}}{\left[\dfrac{V_{ef}}{\ln\left(\dfrac{1}{1-P_f}\right)}\right]^{\frac{m}{N-2}}} \tag{E36}$$

Equation (E35) is a convenient stress-life equation that can be used to fit experimental data from specimens under combined static and cyclic fatigue. For pure time-dependent crack growth and pure cycle-dependent crack growth, respectively, the corresponding equations become

$$t_f = \frac{\tilde{C}}{g\sigma_f{}^N} \tag{E37}$$

and

$$t_f = \frac{\tilde{C}}{\left[f_c(1-R)^Q\right]\sigma_f{}^N} \tag{E38}$$

which correspond to power-law and Walker-law equations for crack-growth rate, respectively. Regardless of what equation is used, a multiple regression analysis is needed to estimate the model parameters. Table E.I summarizes the independent and dependent variables for various fatigue mechanisms and corresponding parameters that can be estimated from equations (E35), (E37), and (E38). The term $\tilde{C}_{\text{mean}}$ in table E.I indicates a parameter for a best-fit regression line through the data for the mean probability of failure $P_{f,\text{mean}}$ in equation (E36). In this study, both a linear least-squares method (for the first iteration) and a nonlinear least-squares method (for subsequent iterations) were used to estimate these fatigue parameters. For the nonlinear problem, a modified Levenberg-Marquardt algorithm (Levenberg, 1944; Marquardt, 1963; and Dennis and Schnabel, 1983) was used to calculate the parameters. An IMSL software version of this algorithm (Visual Numerics, 2004) was subsequently used with the CARES/*Life* program to perform the parameter estimation.

TABLE E.I.—REGRESSION VARIABLES AND PARAMETERS FOR VARIOUS DAMAGE MECHANISMS

Damage mechanism	Crack-growth model	Independent variables	Dependent variable	Model parameters
Time-dependent	Power law	σ_f, R	t_f	$\tilde{C}_{\text{mean}}, N$
Cycle-dependent	Walker law	σ_f, R, f_c	t_f	$\tilde{C}_{\text{mean}}, N, Q$
Combined methodology	Proposed law (eq. (E1)) [a]	σ_f, R, f_c	t_f	$\tilde{C}_{\text{mean}}, N, Q, \tilde{A}$

[a] Proposed methodology is limited to the case where N_1 and N_2 are identical in value.

The methodology developed for the parameter estimation is based on using the natural log expression of equation (E35). This was done to decrease the sensitivity of the model to certain numerical conditions. Additional relations were added to estimate the inert-strength Weibull modulus as well as to consider the effect of runout data (unfailed specimens) on the parameter estimates. The inert-strength Weibull modulus can be estimated from the fatigue data by transforming all the data to a single R-ratio and applied stress. Equating the probabilities of failure in equation (E34) for a transformed data point at the lowest applied peak cyclic stress and $R = 1.0$ (static fatigue), with the untransformed point, gives

$$t_{Ti} = \left[g_i + f_{ci}\widetilde{A}(1-R_i)^Q\right] t_{fi}\left(\frac{\sigma_{fi}}{\sigma_T}\right)^N \tag{E39}$$

where T is used to denote the transformed data for the i^{th} specimen number. The transformed data are (in theory) Weibull distributed as shown by equation (E31). A least-squares or maximum-likelihood Weibull parameter estimation (as employed in the CARES/*Life* code) can then be performed to obtain an estimate of the Weibull exponent $m/(N-2)$. The inert-strength Weibull modulus m can be calculated since the estimates of N and $m/(N-2)$ are determined from the solution algorithm.

Runout (i.e., censored or suspended) data can be accounted for by using the method of Johnson (Johnson, 1964; and Abernethy, 1993). This method requires ranking the data from lowest to highest probability of failure. Equation (E39) can be used to rank data from lowest to highest transformed time to failure, which is analogous to ranking by probability. The median rank formula is

$$P_f\left(t_{Ti}\right) = \frac{i-0.3}{n+0.4} \tag{E40}$$

which is used in conjunction with Johnson's adjusted rank increment formula,

$$\text{Rank increment} = \frac{(n+1)-(\text{previous adjusted rank})}{1+(\text{number of items beyond present suspended item})} \tag{E41}$$

to adjust the ranked probability of failure of the i^{th} lowest transformed failure time for the n total number of specimens. Equations (E39), (E40), and (E41) enable a failure probability to be assigned to each ruptured specimen. On this basis, equation (E36) can be used to calculate $\widetilde{C}_i$ for each data point relative to the mean (average) line parameter estimate $\widetilde{C}_{\text{mean}}$ obtained from the Levenberg-Marquardt algorithm. This is necessary in order to determine the residual of each data point, as explained in section E.8. The following summarizes the steps taken to obtain a convergent solution. This process is iterative.

Step 1.—Use a multiple linear regression routine with the Walker law (eq. (E38)) to obtain a set of initial parameter estimates.

Step 2.—Use the results from step 1 as seed values for the Levenberg-Marquardt algorithm for the combined fatigue model (eqs. (E35) and (E36)). Table E.I shows the parameters obtained for the combined model from the Levenberg-Marquardt algorithm. The residual term for this step is the difference between the natural log of the time to failure of the discrete data point and the natural log of the predicted value for the mean line ($\widetilde{C}_{\text{mean}}$, $P_{f,\text{mean}}$) time to failure t_{mean}.

Step 3.—Obtain the inert-strength Weibull modulus m using equation (E39) in conjunction with either the least-squares method or maximum-likelihood regression for the following Weibull form:

$$P_f = 1-\exp\left[-\left(\frac{t_{T,f}}{t_{T,\theta}}\right)^{\frac{m}{N-2}}\right] \tag{E42}$$

This step also uses equation (E40) to establish the order of the transformed data (from lowest to highest).

Step 4.—Determine the value of $P_{f,\mathrm{mean}}$ using the transformed data from equation (E39) and the Weibull mean value formula:

$$t_{T,\mathrm{mean}} = t_{T,\theta}\Gamma\left(1+\frac{N-2}{m}\right) \tag{E43}$$

where Γ is the gamma function. Substitute $t_{T,\mathrm{mean}}$ for $t_{T,f}$ in equation (E42) and calculate $P_{f,\mathrm{mean}}$.

Step 5.—Associate a probability of failure $P_{f,i}$ for each data point *i* using the median and/or adjusted rank formulas outlined in equations (E40) and (E41). Note that runout data do not have a probability of failure associated with them (the residuals for runouts are not calculated); however, the runout data do affect the rank increment adjustment (eq. (E41)) for failed specimens.

Step 6.—Determine $\widetilde{C}_i$ for each data point *i* using $P_{f,i}$, $\widetilde{C}_{\mathrm{mean}}$, $P_{f,\mathrm{mean}}$, and equation (E36):

$$\widetilde{C}_i = \widetilde{C}_{\mathrm{mean}}\left[\frac{\ln\left(\dfrac{1}{\left(1-P_{f,i}\right)}\right)}{\ln\left(\dfrac{1}{\left(1-P_{f,\mathrm{mean}}\right)}\right)}\right]^{\frac{N-2}{m}} \tag{E44}$$

Step 7.—Employ the Levenberg-Marquardt algorithm to obtain a new set of parameter estimates. The residual term (see section E.8) for this step is the difference between the natural log of the time to failure of the discrete data point *i* versus the natural log of the predicted value of the time to failure using $\widetilde{C}_i$ with equation (E35).

Step 8.—Repeat steps 3 to 7 until parameter estimates converge (the difference between the previous estimates and the new estimates reaches a sufficiently small tolerance).

The parameter estimation methodology and the theoretical formulation of the reliability model presented in this report has been implemented into CARES/*Life*. Commercial finite element programs, such as ANSYS, can be used with CARES/*Life*. Using these new capabilities, one can perform durability and reliability analyses of ceramic structures under the combined effects of static and fatigue damage. All of the results presented in this report were obtained by using CARES/*Life*.

E.6 Numerical Example

This example demonstrates the estimation of fatigue parameters from rupture data generated by cyclically loaded specimens. The experimental data were originally produced and analyzed by Liu and Chen (1991a and 1991b) and later used as an example problem with CARES/*Life* (Nemeth et al., 1993 and 2003). These data are reexamined herein using the proposed fatigue model and parameter estimation capability. Furthermore, this reexamination demonstrates parameter estimation capability for the Walker law and power law for multiple levels of *R*-ratio.

The material used in the experiments was 3-mol%-yttria-stabilized tetragonal zirconia (3Y–TZP) with a grain size of about 0.38 μm. Cyclic fatigue experiments for various levels of *R*-ratio were performed on smooth-surfaced uniaxial tensile specimens. Five specimens each were tested at *R*-ratios of 0.8, 0.5, and 0.0; and six specimens were tested at an *R*-ratio of −1.0. A triangular cyclic stress wave form was used at a frequency of 1 Hz for 10^5 cycles or until failure occurred. The tensile specimens had a 16-mm-gauge length and 6-mm-gauge diameter. Fractographic examination showed that failure most frequently occurred at or near the surface and that the failure origins were pore-type flaws.

Table E.II shows 21 test data sets of time to failure for various combinations of failure stress and *R*-ratio. There were three specimens that did not fail in 10^5 s or cycles (runout data). These runout data were included in the parameter estimation analysis. Further details on these experimental data can be obtained from Liu and Chen (1991a and 1991b).

Table E.III shows the fatigue parameters estimated with CARES/*Life* assuming three stress-life relations represented by equations (E35), (E37), and (E38). These equations are based on the crack-growth rate modeled by the combined law, the power law, and the Walker law, respectively. The *g*-factor used for the power law and the combined law formulations with the triangular waveform is (see table D.1)

$$g = \begin{cases} \dfrac{1}{(1-R)(N+1)} & R \le 0 \\[2ex] \dfrac{1-R^{N+1}}{(1-R)(N+1)} & R \ge 0 \end{cases} \tag{E45}$$

TABLE E.II.—EXPERIMENTAL FATIGUE DATA FOR YTTRIA-STABILIZED ZIRCONIA
[Liu and Chen, 1991a. Frequency, 1 Hz.]

R-ratio	Time to failure, s	Maximum failure stress, MPa
–1	87	500
	79	500
	1 391	450
	1 026	450
	5 447	400
	29 658	400
0	2 954	500
	2 713	500
	73	500
	11 690	400
	[a]100 000	400
0.5	250	600
	1 665	600
	19 945	500
	54 824	500
	[a]100 000	400
0.8	15	600
	284	600
	3 206	500
	10 523	500
	[a]100 000	400

[a]Runout data were used in the analysis.

TABLE E.III.—ESTIMATED MULTIVARIATE REGRESSION PARAMETERS FOR YTTRIA-STABILIZED ZIRCONIA

Crack-growth model	Regression parameter				
	Parameter estimation constant, $\tilde{C}_{\text{mean}}$ (see eq. (E36))	Material or environmental fatigue exponent, N	R-ratio sensitivity exponent, Q	A_2/A_1 ratio, $\tilde{A}$	Weibull modulus, m
Power law	64.2	9.3	(a)	(a)	3.2
Power law[b]	147.1	22.4	(a)	(a)	22.8
Walker law	80.7	11.8	1.2	(a)	6.3
Walker law[c]	130.8	20.0	2.5	(a)	18.6
Proposed law (eq. (E1))	111.9	16.8	3.2	0.65	13.6
Fast fracture[d]	(a)	(a)	(a)	(a)	14.0

[a] Not applicable.

[b] For R = 0.8 and 0.5 data only.

[c] For R = 0.0 and –1.0 data only.

[d] Four-point bending bar inert strength results from Nemeth et al. (1993).

Table E.III also shows the estimated Weibull modulus m obtained from the fatigue data. These values can be compared with the inert-strength Weibull modulus obtained from four-point bending bar experiments (Liu and Chen, 1991a and 1991b; and Nemeth et al., 1993).

Figure E.1 compares the life (at a failure probability of $P_{f,\text{mean}}$) predicted using the power-law model (eq. (E37)) with the experimental data for various stresses and R-ratios. A visual inspection reveals that the quality of fit to the data does not appear to be very good. The slope (which represents the fatigue exponent) appears to be too steep, yielding a low value for the fatigue exponent N. Also, as the R-ratio becomes smaller, the deviation from the data tends to increase. This trend is not apparent for R = 0.5, but it is apparent when R = 0 and –1. In this case, the deviation from the data progresses in a nonconservative manner (life is overpredicted for a given stress level). These experimental results for R = 0 and –1 seem to indicate that some cyclic degradation is present.

Figure E.2 compares the life predicted using the Walker-law model (eq. (E38)) with the same experimental data as in figure E.1. The visual fit to the data is somewhat improved relative to figure E.1, although the slope still appears too steep. As the R-ratio becomes smaller, the Walker law predicts that the damage increases. This prediction is consistent with the trends of this particular set of data, except for the R = 0.5 data.

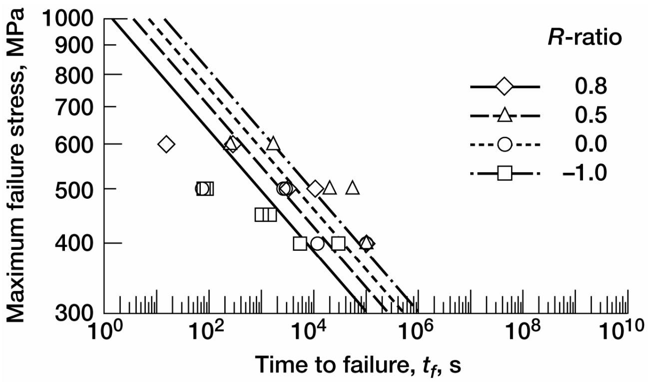

Figure E.1.—Stress-life curves for 3Y–TZP using the power-law model (eq. (E37)); parameter estimation constant, ln $\tilde{C}$ (see eq. (36)), 64.2; fatigue exponent, N, 9.3; constant-amplitude frequency, f_c, 1 Hz.

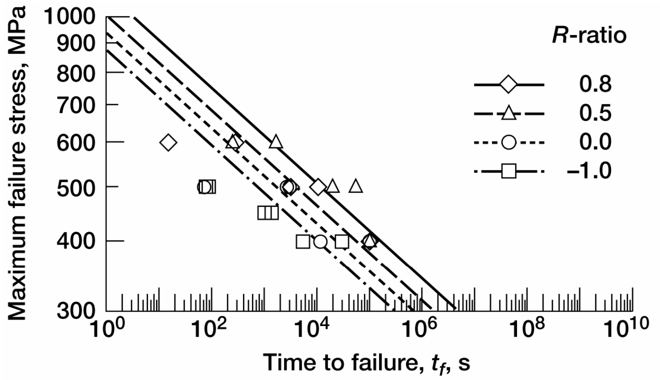

Figure E.2.—Stress-life curves for 3Y–TZP using the Walker-law model (eq. (E38)); parameter estimation constant, ln $\tilde{C}$ (see eq. (36)), 80.7; fatigue exponent, N, 11.8; R-ratio sensitivity exponent, Q, 1.2; constant-amplitude frequency, f_c, 1 Hz.

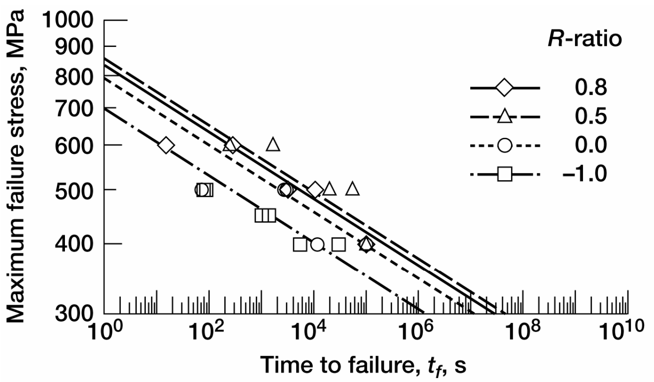

Figure E.3.—Stress-life curves for 3Y–TZP using the proposed combined-law model (eq. (E35)); parameter estimation constant, ln $\tilde{C}$ (see eq. (36)), 111.9; fatigue exponent, N, 16.8; R-ratio sensitivity factor $\tilde{A}$, 0.65; R-ratio sensitivity exponent, Q, 3.2; constant-amplitude frequency, f_c, 1 Hz.

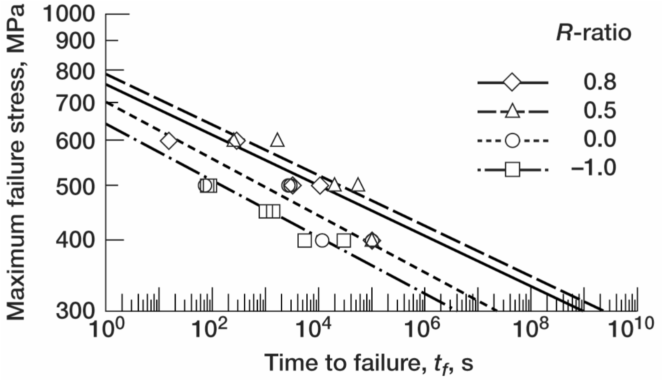

Figure E.4.—Stress-life curves for 3Y–TZP using separate models: (1) power law—eq. (37); parameter estimation constant, ln $\tilde{C}$ (eq. (36)), 147.1; fatigue exponent, N, 22.4 for R–ratios of 0.8 and 0.5, and (2) Walker law—eq. (38); ln $\tilde{C}$, 130.8; fatigue exponent, N, 20.0; R-ratio sensitivity exponent, Q, 2.5 for R-ratios of 0.0 and –1.0. Constant-amplitude frequency, f_c, 1 Hz.

Contrasting figures E.1 and E.2 shows the difference between the power and Walker models. As the *R*-ratio becomes smaller, the amount of cumulative damage for the power law is less than that for the Walker law. In other words, the two laws have opposite trends in predicting the effect of *R*-ratio on the strength of the material. It is interesting to note that the fatigue data oscillated some on this shift pattern when the *R*-ratio increased from –1 to 0.8. Hence, both models failed to capture this experimental behavior completely.

Figure E.3 compares the life predicted using the proposed combined model (eq. (E35)) with the fatigue data. The predicted stress-life curves are in better agreement with the experimental data regardless of the *R*-ratio; also, the slope of the lines appears to be significantly improved. Although the predictions are similar to those for the Walker-law model for *R*-ratios of –1 and 0 (as expected), they are in better agreement with the data for *R*-ratios of 0.5 and 0.8 when compared with the previous models. This is obviously due to the inclusion of crack-growth rates contributed by both static and cyclic fatigue mechanisms in equation (E1). In addition, the predicted stress-life curves were able to show the oscillatory trend with respect to the *R*-ratio exhibited by the experimental data. This is an encouraging result, but more fatigue data involving various frequencies and *R*-ratios need to be analyzed in order to make a substantial claim on the accuracy of the proposed model.

Figure E.4 shows the mean regression lines for both the power and Walker models when they are used separately. In this case, the Levenberg-Marquardt algorithm was used twice to estimate parameters (see table E.III). The power-law model was used for data with *R*-ratios of 0.8 and 0.5, whereas the Walker-law model was used for data with *R*-ratios of 0.0 and –1.0. This was done to test the ability of either model to fit to better-behaved data (better behaved in terms of the ability of the model to account for the *R*-ratio effect). In other words, the lack of fit to data shown in figures E.1 and E.2 was more likely due to the limitations of the models than to shortcomings or errors in implementing the Levenberg-Marquardt algorithm.

Regarding the data itself, figure E.4 indicates that the fatigue exponents are approximately equivalent for the power-law- and Walker-law-analyzed data, although the data are too few to draw any firm conclusions regarding this observation. Also, from table E.III, the Weibull modulus obtained from the fatigue data varied widely from model to model. It is interesting to note that the cases of poor fit to the fatigue data (figs. E.1 and E.2) gave the lowest estimated Weibull modulus. The Weibull modulus estimated from the combined model correlated well with that of the four-point bending bar inert strength data in Nemeth et al. (1993). Finally, figure E.4 may lend some credence to the assertion in Nemeth et al. (2003) that taking the product of a power-law reliability model and a Walker-law reliability model could yield acceptable results in combined cyclic and static fatigue loading situations.

E.7 Summary and Conclusions

A computational methodology was developed for the life prediction and time-dependent reliability analysis of ceramic structures under the combined effects of static and cyclic fatigue. It is based on (1) a crack-growth equation involving damage contributions from both static and cyclic fatigue, (2) a multivariate nonlinear regression analysis of fatigue data for parameter estimation, and (3) the Batdorf model for predicting structural reliability. For the parameter estimation, the regression was performed using the nonlinear least-squares method and a modified Levenberg-Marquardt algorithm to calculate the optimized model parameters. A numerical example was presented to illustrate the parameter estimation component of this methodology. The results show that the predicted stress-life curves based on the proposed model agree better with the experimental data than the predictions of existing models do. However, the proposed model assumes that the fatigue exponents due to static and cyclic fatigue are the same. Hence, a potential enhancement to this methodology may include further generalization to account for dissimilar fatigue exponents.

E.8 Appendix—Nonlinear Least-Squares Method by Levenberg-Marquardt Algorithm

Consider a nonlinear regression model given by

$$y = f(\mathbf{x};\, \theta) + e \tag{E46}$$

where f is a nonlinear function, $\mathbf{x} \in \Re^k$ is a k-dimensional vector of independent variables, $y \in \Re$ is a scalar response or dependent variable, $\theta \in \Re^p$ is a p-dimensional vector of regression parameters, and $e \in \Re$ is a scalar variable representing a random residual. Let y_i and $\mathbf{x}_i$ denote the i^{th} values of y and $\mathbf{x}$ for $i = 1, 2, \ldots, n$, where n is the total number of independent observations (data). Given a parameter vector θ, let $\mathbf{e}(\theta) = [e_1(\theta), e_2\, \theta), \ldots, e_n(\theta)]$ denote an n-dimensional vector of residuals in which the i^{th} residual is

$$e_i = y_i - f(\mathbf{x}_i;\, \theta) \tag{E47}$$

Define a norm of the vector $\mathbf{e}(\theta)$ given by

$$\left\|\mathbf{e}(\boldsymbol{\theta})\right\| = \sum_{i=1}^{n} e_i(\boldsymbol{\theta})^2 \tag{E48}$$

which represents a sum of the square of all residuals. A value of θ that minimizes $\left\|\mathbf{e}(\boldsymbol{\theta})\right\|$ is known as the least-squares estimate of θ. This can be mathematically stated as

$$\min_{\boldsymbol{\theta}} \left\|\mathbf{e}(\boldsymbol{\theta})\right\| \qquad \text{or} \qquad \min_{\boldsymbol{\theta}} \sum_{i=1}^{n} e_i(\boldsymbol{\theta})^2 \tag{E49}$$

The minimization problem defined by equation (E49) can be solved by a modified Levenberg-Marquardt algorithm. In this algorithm, given a current estimate θ_c, a new estimate θ_n is given by

$$\theta_n = \theta_c + \mathbf{s}_c \tag{E50}$$

where $\mathbf{s}_c \in \Re^p$ satisfies the following equation

$$\left[\mathrm{J}(\boldsymbol{\theta}_c)^T\, \mathrm{J}(\boldsymbol{\theta}_c) + \mu_c \mathrm{I}\right] \mathrm{s}_c = \mathrm{J}(\boldsymbol{\theta}_c)^T\, \mathrm{e}(\boldsymbol{\theta}_c) \tag{E51}$$

In equation (E51), $\mathbf{J}(\theta_c)$ is an $n \times p$ Jacobian matrix evaluated at θ_c, $\mathbf{I}$ is a $p \times p$ identity matrix, μ_c is a scalar control variable, and T is the matrix transpose operation. The algorithm uses a “trust region” approach with a step bound of δ_c. A solution of the equations is first obtained for $\mu_c = 0$. If $\left\|\mathbf{s}_c\right\| < \delta_c$, this update is accepted. Otherwise, μ_c is set to a positive value and another solution is obtained. Further details of this algorithm are given by Levenberg (1944), Marquardt (1963), and Dennis and Schnabel (1983).

References

Abernethy, R.B., et al. (1983): Weibull Analysis Handbook; Final Technical Report. PWA/GPD–FR–17579 (AFWAL–TR–83–2079).

Abernethy, Robert B. (1993): The New Weibull Handbook. Gulf Publishing Co., Houston, TX.

Andrews, M.J., et al. (2000): Strength and Fatigue of NT551 Silicon Nitride and NT551 Diesel Exhaust Valves. ORNL/TM–1999/332.

ANSYS (2004). ANSYS Documentation Overview. http://www.ansys.com/services/documentation/manuals.htm Updated July 20, 2004. Accessed September 17, 2004.

Baratta, Francis I.; Matthews, William T.; and Quinn, George D. (1987): Errors Associated With Flexure Testing of Brittle Materials. MTL–TR–87–35.

Barnett, R.L., et al. (1967): Fracture of Brittle Materials Under Transient Mechanical and Thermal Loading. AFFDL–TR–66–220.

Batdorf, S.B.; and Crose, J.G. (1974): Statistical-Theory for Fracture of Brittle Structures Subjected to Nonuniform Polyaxial Stresses. J. Appl. Mech. Trans. ASME, vol. 41, no. 2, pp. 459–464.

Batdorf, S.B. (1977a): Some Approximate Treatments of Fracture Statistics for Polyaxial Tension. Internat. J. Fracture, vol. 13, no. 1, pp. 5–11.

Batdorf, S.B. (1977b): Fundamentals of the Statistical Theory of Fracture. Fracture Mechanics of Ceramics, R.C. Bradt, D.P.H. Hasselman, and F.F. Lange, eds., Plenum Press, New York, NY, pp. 1–30.

Batdorf, S.B. (1978): Fracture Statistics of Polyaxial Stress States. Fracture Mechanics, Nicholas Perrone et al., eds., University Press of Virginia, Charlottesville, VA, pp. 579–592.

Batdorf, S.B.; and Heinisch, H.L. (1978a): Weakest Link Theory Reformulated for Arbitrary Fracture Criterion. J. Am. Ceram. Soc., vol. 61, nos. 7–8, pp. 355–358.

Batdorf, S.B.; and Heinisch, H.L., Jr. (1978b): Fracture Statistics of Brittle Materials With Surface Cracks. Eng. Fract. Mech., vol. 10, no. 4, pp. 831–841.

Batdorf, S.B. (1980): Comparison of the Best Known Fracture Criteria. Proceedings of an International Symposium, Martinus Nijhoff Publishers, The Hague, pp. 243–251.

Bathe, Klaus-Jürgen (1982): Finite Element Procedures in Engineering Analysis. Prentice-Hall, Englewood Cliffs, NJ.

Boehm, Franz (1989): A Stress-Strength Interference Approach to Fast and Delayed Fracture Reliability Analysis for Ceramic Components. Ph.D. Thesis, Northwestern University.

Bowman, K.J.; Reyes-Morel, P.E.; and Chen, I-W. (1987): Reversible Transformation Plasticity in Uniaxial Tension-Compression Cycling of Mg-PSZ. Advanced Structural Ceramics, P.F. Becher, M.V. Swain, and S. Sōmiya, eds., Mater. Res. Soc. Symp. Proc., vol. 78, pp. 51–60.

Broek, David (1982): Elementary Engineering Fracture Mechanics. Third Rev. Ed., Martinus Nijhoff, Netherlands.

Brückner-Foit, Angelika; Heger, Armin; and Munz, Dietrich (1994): Effect of Proof Testing on the Failure Probability of Multiaxially Loaded Ceramic Components. ASTM Special Technical Publication 1201, pp. 346–359.

Brückner-Foit, Angelika; and Ziegler, Christian (1999a): Design Reliability and Lifetime Prediction of Ceramics. Advances in Science and Technology, P. Vincenzini, ed., vol. 12, Part A (Ceramics: Getting Into the 2000's), Techna Srl, Faenza, Italy, pp. 585–595.

Brückner-Foit, A.; and Ziegler, C. (1999b): Time-Dependent Reliability of Ceramic Components Subjected to High Temperature Loading in a Corrosive Environment. ASME Paper 99–GT–233.

Chen, C.P.; and Knapp, W.J. (1974): Fatigue Fracture of an Alumina Ceramic at Several Temperatures. Plenum Press, New York, NY, pp. 691–707.

Cook, R.F.; and Clarke, D.R. (1988): Fracture Stability, R-Curves and Strength Variability. Acta Metall., vol. 36, no. 3, pp. 555–562.

Corum, J.M., et al. (1996): Design Analysis and Testing of Ceramic Exhaust Valve for Heavy Duty Diesel Engine. ORNL/TM–13253.

D'Agostino, Ralph B.; and Stephens, Michael A., eds. (1986): Goodness-of-Fit Techniques. Marcel Decker, New York, NY, pp. 97–193.

Daniels, H.E. (1945): The Statistical Theory of the Strength of Bundles of Threads. I. Proc. Roy. Soc., series A, vol. 183, no. 995, pp. 405–435.

Dauskardt, R.H.; Yu, W.; and Ritchie, R.O. (1987): Fatigue Crack Propagation in Transformation-Toughened Zirconia Ceramic. J. Am. Ceram. Soc., vol. 70, no. 10, pp. C248–C252.

Dauskardt, R.H.; Marshall, D.B.; and Ritchie, R.O. (1990a): Cyclic Fatigue-Crack Propagation in Magnesia-Partially-Stabilized Zirconia Ceramics. J. Am. Ceram. Soc., vol. 73, no. 4, pp. 893–903.

Dauskardt, R.H., et al. (1990b): Transient Subcritical Crack-Growth Behavior in Transformation-Toughened Ceramics. Acta Metall. Mater., vol. 38, no. 11, pp. 2327–2336.

Dauskardt, R.H., et al. (1992): Cyclic Fatigue-Crack Growth in a SiC-Whisker-Reinforced Alumina Ceramic Composite: Long- and Small-Crack Behavior. J. Am. Ceram. Soc., vol. 75, no. 4, pp. 759–771.

Dauskardt, R.H., et al. (1993): Cyclic Fatigue-Crack Propagation in a Silicon Carbide Whisker-Reinforced Alumina Composite: Role of Load Ratio. J. Mater. Sci., vol. 28, pp. 3258–3266.

Davies, D.G.S. (1973): The Statistical Approach to Engineering Design in Ceramics. Proc. Brit. Ceram. Soc., D.J. Godfrey, ed., no. 22, pp. 429–452.

Dennis, J.E., Jr.; and Schnabel, Robert B. (1983): Numerical Methods for Unconstrained Optimization and Nonlinear Equations. Prentice-Hall, Englewood Cliffs, NJ.

DeSalvo, G.J. (1970): Theory and Structural Design Applications of Weibull Statistics. WANL–TME–2688.

Dukes, W.H. (1971): Handbook of Brittle Material Design Technology. AGARD–AG–152–71.

Erdogan, F.; and Sih, G.C. (1963): On the Crack Extension in Plates Under Plane Loading and Transverse Shear (Crack Extension in a Large Plate Under Plane Loading and Transverse Shear, Studied in Terms of Local Stress and Strain Concentrations). J. Basic Eng., vol. 85, pp. 519–525.

Evans, A.G.; and Fuller, E.R. (1974): Crack Propagation in Ceramic Materials Under Cyclic Loading Conditions. Metall. Trans., vol. 5, no. 1, pp. 27–33.

Evans, A.G.; and Wiederhorn, S.M. (1974a): Crack Propagation and Failure Prediction in Silicon Nitride at Elevated Temperatures, J. Mater. Sci., vol. 9, pp. 270–278.

Evans, A.G.; and Wiederhorn, S.M. (1974b): Proof Testing of Ceramic Materials—Analytical Basis for Failure Prediction. Internat. J. Fracture, vol. 10, no. 3, pp. 379–392.

Evans, A.G.; and Linzer, M. (1976): High-Frequency Cyclic Crack-Propagation in Ceramic Materials. Internat. J. Fracture, vol. 12, no. 2, pp. 217–222.

Evans, A.G.; and Jones, R.L. (1978): Evaluation of a Fundamental Approach for Statistical-Analysis of Fracture. J. Am. Ceram. Soc., vol. 61, nos. 3–4, pp. 156–160.

Evans, A.G. (1980): Fatigue in Ceramics. Internat. J. Fracture, vol. 16, no. 6, pp. 485–498.

Ferber, Matt; and Breder, Kristin (2001): Subtask 9—Thermal Shock Testing of Advanced Ceramics. Final Report, International Energy Agency Implementing Agreement for a Programme of Research and Development on Advanced Materials for Transportation Applications.

Fett, T., et al. (1991): Determination of da/dN-Delta-K1 Curves for Small Cracks in Alumina in Alternating Bending Tests. J. Mater. Sci., vol. 26, no. 12, pp. 3320–3328.

Fett, T.; Munz, D.; and Thun, G. (1993): Influence of Frequency on Cyclic Fatigue of Coarse Grained Al_2O_3. J. Mater. Sci. Lett., vol. 12, no. 4, pp. 220–222.

Freudenthal, Alfred M. (1968): Statistical Approach to Brittle Fracture. Fracture, an Advanced Treatise, Vol. II. H. Liebowitz, ed., Academic Press, New York, NY, pp. 591–619.

Fuller, E.R., Jr., et al. (1980): Proof Testing of Ceramics. Part 2—Theory. J. Mater. Sci., vol. 15, pp. 2282–2295.

Giovan, M.N.; and Sines, G. (1979): Biaxial and Uniaxial Data for Statistical Comparisons of a Ceramic's Strength. J. Am. Ceram. Soc., vol. 62, nos. 9–10, pp. 510–515.

Grathwohl, G. (1984): Regimes of Creep and Slow Crack Growth in High-Temperature Rupture of Hot-Pressed Silicon Nitride. Deformation of Ceramic Materials II, Richard E. Tressler and Richard C. Bradt, eds., Plenum Press, New York, NY, pp. 573–586.

Griffith, A.A. (1921): The Phenomena of Rupture and Flow in Solids. Philos. Trans. Roy. Soc. London, Ser. A, vol. 221, pp. 163–198.

Griffith, A.A. (1925): The Theory of Rupture. Proceedings of the First International Congress for Applied Mechanics, C.B. Biezeno and J.M. Burgers, eds., Delft, Netherlands, pp. 55–63.

Gross, Bernard, and Gyekenyesi, John P. (1989): Weibull Crack Density Coefficient for Polydimensional Stress States. J. Am. Ceram. Soc., vol. 72, no. 3, pp. 506–507.

Gross, Bernard, et al. (1996): Fatigue Parameter Estimation Methodology for Power and Paris Crack Growth Laws in Monolithic Ceramic Materials. NASA TM–4699.

Gyekenyesi, J.P. (1986): SCARE: A Postprocessor Program to MSC/NASTRAN for Reliability Analysis of Structural Ceramic Components. J. Eng. Gas Turbines Power Trans., vol. 108, no. 3, pp. 540–546.

Gyekenyesi, J.P.; and Nemeth, N.N. (1987): Surface Flaw Reliability Analysis of Ceramic Components With the SCARE Finite Element Postprocessor Program. J. Eng. Gas Turbines Power Trans., vol. 109, no. 3, pp. 274–281.

Hamada, Seiichi; and Teramae, Tetsuo (1990): Reliability Evaluation System for Ceramic Gas Turbine Components. J. Soc. Mater. Sci. (Jpn.), vol. 39, no. 436, pp. 76–81.

Hamanaka, Jyunichi; Suzuki, Akihiko; and Sakai, Keiichi (1990): Structural Reliability Evaluation of Ceramic Components. J. Eur. Ceram. Soc., vol. 6, no. 6, pp. 375–381

Heger, A. (1991): Stau Programm Berech, Ph.D. Thesis, Universität Karlsruhe, Germany.

Hellen, T.K.; and Blackburn, W.S. (1975): Calculation of Stress Intensity Factors for Combined Tensile and Shear Loading. Int. J. Fract., vol. 11, no. 4, pp. 605–617.

Hoel, Paul Gerhard; Port, Sidney C.; and Stone, Charles J. (1971): Introduction to Probability Theory. Houghton Mifflin, Boston, MA, pp. 65 and 131.

Holland, Frederic A. Jr.; Choi, Sung R.; and Nemeth, Noel N. (1999): Machining Damage and Reliability Analysis of Glass Specimens Using the CARES/Life Design Code. Ceram. Eng. Sci. Proc., vol. 20, issue 3, pp. 573–580.

Horibe, Susumu (1988): Cyclic Fatigue Crack Growth From Indentation Flaw in Si_3N_4. J. Mater. Sci. Lett., vol. 7, no. 7, pp. 725–727.

Hoshide, T.; Ohara, T.; and Yamada, T. (1988): Fatigue Crack Growth From Indentation Flaw in Ceramics. Int. J. Fract., vol. 37, no. 1, pp. 47–59.

Ichikawa, Masahiro (1991): Proposal of an Approximate Analytical Expression of Maximum Energy Release Rate of a Mixed Mode Crack in Relation to Reliability Evaluation of Ceramic Components. J. Society of Materials Science, vol. 40, no. 449, pp. 224–227.

Jadaan, Osama M. (1990): Fast Fracture and Lifetime Prediction of Ceramic Tubular Components. Ph.D. Thesis, Pennsylvania State University.

Jadaan, O.M., et al. (1991): Prediction of the Strength of Ceramic Tubular Components: Part 1. Analysis, J. Test. Eval., vol. 19, no. 3, pp. 181–191.

Jadaan, O.M.; and Tressler, R.E. (1993): Methodology to Predict Delayed Failure Due to Slow Crack-Growth in Ceramic Tubular Components Using Data From Simple Specimens. J. Eng. Mater. Technol. Trans. ASME, vol. 115, no. 2, pp. 204–210.

Jadaan, O.M., et al. (1994): Design of High Temperature Ceramic Components Against Fast Fracture and Time-Dependent Failure Using CARES/Life. Ceram. Trans., vol. 50, pp. 121–134.

Jakus, K.; Coyne, D.C.; and Ritter, J.E. (1978): Analysis of Fatigue Data for Lifetime Predictions for Ceramic Materials. J. Materials Science, vol. 13, no. 10, pp. 2071–2080.

Jakus, Karl; and Ritter, John E., Jr. (1981): Lifetime Prediction for Ceramics Under Random Loads. Res. Mech., vol. 2, no. 1, pp. 39–52.

Jensen, D.G.; Zelizko, V.; and Swain, M.V. (1989): Small Flaw Static Fatigue Crack-Growth in Mg-PSZ. J. Materials Science Letters, vol. 8, no. 10, pp. 1154–1157.

Johnson, Leonard G. (1964): The Statistical Treatment of Fatigue Experiments. Elsevier Publishing Co., New York, NY.

Kanofsky, Paul; and Srinivasan, R. (1972): An Approach to the Construction of Parametric Confidence Bands on Cumulative Distribution Functions. Biometrika, vol. 59, no. 3, pp. 623–631.

Kawakubo, T.; and Komeya, K. (1987): Static and Cyclic Fatigue Behavior of a Sintered Silicon Nitride at Room Temperature. J. Amer. Ceramic Soc., vol. 70, no. 6, pp. 400–405.

Kendall, K., et al. (1986): Influence of Toughness on Weibull Modulus of Ceramic Bending Strength. J. Mater. Res., vol. 1, no. 1, pp. 120–123.

Kirchhoff, G., et al. (1994): Thermal Shock and Thermal Cycling Behavior of Silicon Nitride Ceramics. Key Eng. Mater., issue 89/91, pp. 605–610.

Kishimoto, H. (1991): Cyclic Fatigue in Ceramics. JSME International Journal Series I—Solid Mechanics Strength of Materials, vol. 34, no. 4, pp. 393–403.

Krohn, D.A.; and Hasselman, D.P.H. (1972): Static and Cyclic Fatigue Behavior of a Polycrystalline Alumina. J. Am. Ceram. Soc., vol. 55, no. 4, pp. 208–211.

Levenberg, Kenneth (1944): A Method for the Solution of Certain Non-Linear Problems in Least Squares. Q. Appl. Math., vol. II, no. 2, pp. 164–168.

Liu, Kenneth C.; and Brinkman, Charles R. (1986): Tensile Cyclic Fatigue of Structural Ceramics. Proceedings of the Twenty-third Automotive Technology Development Contractors' Coordination Meeting, SAE P–165, pp. 279–284.

Liu, S.Y.; and Chen, I.W. (1991a): Fatigue of Yttria-Stabilized Zirconia. I. Fatigue Damage, Fracture Origins, and Lifetime Prediction. J. Am. Ceram. Soc., vol. 74, no. 6, pp. 1197–1205.

Liu, S.Y.; and Chen, I.W. (1991b): Fatigue of Yttria-Stabilized Zirconia. II. Crack Propagation, Fatigue Striations, and Short-Crack Behavior. J. Am. Ceram. Soc., vol. 74, no. 6, pp. 1206–1216.

Liu, S.Y.; and Chen, I.W. (1992): Fatigue Deformation Mechanisms of Zirconia Ceramics. J. Am. Ceram. Soc., vol. 75, no. 5, pp. 1191–1204.

Margetson, J. (1976): A Statistical Theory of Brittle Failure for an Anisotropic Structure Subjected to a Multiaxial Stress State. AIAA–1976–632.

Marquardt, D.W. (1963): An Algorithm for Least-Squares Estimation of Nonlinear Parameters. J. Soc. Ind. Appl. Math., vol. 11, no. 2, pp. 431–441.

Masuda, Masaaki, et al. (1988): Fatigue of Ceramics (Part 1)—Fatigue Behavior of Sintered Si_3N_4 Under Tension-Compression Cyclic Stress. J. Ceram. Soc. Jpn., vol. 96, no. 3, pp. 275–280.

Mencik, J. (1984): Rationalized Load and Lifetime of Brittle Materials. J. Am. Ceram. Soc., vol. 67, no. 3, pp. C37–C40.

Munz, Dietrich; and Fett, Theo (1999): Ceramics: Mechanical Properties, Failure Materials Behaviour Selection. Springer, Berlin.

Mutoh, Y., et al. (1991): Fatigue Crack Growth of Long and Short Cracks in Silicon Nitride. Fatigue of Advanced Materials, Materials and Components Engineering Publications Ltd., Edgbaston, Birmingham, pp. 211–225.

Neal, D.; Vangel, M.; and Todt, F. (1987): Statistical Analysis of Mechanical Properties. Engineered Materials Handbook, vol. 1, ASM International, Metals Park, OH, pp. 302–307.

Nelson, Wayne (1982): Weibull and Extreme Value Distributions. Applied Life Data Analysis, John Wiley & Sons, New York, NY, pp. 333–346.

Nemeth, Noel N.; Manderscheid, Jane M.; and Gyekenyesi, John P. (1990): Ceramics Analysis and Reliability Evaluation of Structures (CARES). Users and Programmers Manual. NASA TP–2916.

Nemeth, Noel N., et al. (1993): Lifetime Reliability Evaluation of Structural Ceramic Parts With the CARES/LIFE Computer Program. AIAA Paper 93–1497.

Nemeth, Noel N., et al. (2003): CARES/LIFE Ceramics Analysis and Reliability Evaluation of Structures Life Prediction Program. NASA/TM—2003-106316, 2003. http://gltrs.grc.nasa.gov/cgi-bin/GLTRS/browse.pl?2003/TM-2003-106316.html

Pabst, R.F.; Bognar, I.; and Zwissler, J.B. (1980): Static, Dynamic and Cyclic Fatigue of Ceramic Materials. Ber. Deut. Keram. Gesell., vol. 57, no. 2, pp. 13–16.

Pai, Shantaram S.; and Gyekenyesi, John P. (1988): Calculation of Weibull Strength Parameters and Batdorf Flow-Density Constants for Volume- and Surface-Flaw-Induced Fracture in Ceramics. NASA TM–100890.

Palaniswamy, K.; and Knauss, W.G. (1978): On the Problem of Crack Extension in Brittle Solids Under General Loading. Mech. Today, vol. 4, pp. 87–148.

Paluszny, A.; and Nicholls, P.F. (1978): Predicting Time-Dependent Reliability of Ceramic Rotors. Ceramics for High Performance Applications—II: Proceedings of the Fifth Army Materials Technology Conference, Brook Hill Pub. Co., Chestnut Hill, MA.

Paluszny, A.; and Wu, W. (1977): Probabilistic Aspects of Designing With Ceramics. J. Eng. Gas Power Trans. ASME, vol. 99, no. 4, pp. 617–630.

Paris, P.; and Erdogan, F. (1963): A Critical Analysis of Crack Propagation Laws. J. Basic Eng. Trans. ASME, vol. 85, pp. 528–534.

Paris, Paul C.; and Sih, George C. (1965): Stress Analysis of Cracks. ASTM Special Technical Publication 381, pp. 30–83.

Paul, B.; and Mirandy, L. (1976): Improved Fracture Criterion for 3-Dimensional Stress States. J. Eng. Mater. Technol. Trans. ASME, vol. 98, no. 2, pp. 159–163.

Peirce, F.T. (1926): Tensile Tests for Cotton Yarns—The Weakest Link—Theorems on the Strength of Long and of Composite Specimens. J. Text Inst., vol. 17, pp. T355–T368.

Peralta, A.D., et al. (1996): Strength Prediction of Ceramic Components Under Complex Stress States. J. Eng. Gas Turbines Power, vol. 118, no. 4, pp. 856–862.

Petrovic, J.J.; and Stout, M.G. (1984): Mutiaxial Loading Fracture of Al_2O_3 Tubes. 2. Weibull Theory and Analysis. J. Am. Ceram. Soc., vol. 67, no. 1, pp. 18–23.

Powers, Lynn M.; Starlinger, Alois; and Gyekenyesi, John P. (1992): Ceramic Component Reliability With the Restructured NASA/CARES Computer Program. NASA TM–105856.

Quinn, G.D. (1987): Delayed Failure of a Commercial Vitreous Bonded Alumina. J. Mater. Sci., vol. 22, no. 7, pp. 2309–2318.

Rahman, Sharif; Nemeth, Noel N.; and Gyekenyesi, John P. (1998): Life Prediction and Reliability Analysis of Ceramic Structures Under Combined Static and Cyclic Fatigue. ASME Paper 98–GT–569.

Rettig, Uwe (1998): Laserschock-Messmethode—Ein Quantitatives Verfahren Zur Charakterisierung der Temperatur Wechselbestandigkeit Hochfester Keramischer Werkstoffe, Verlag, Dusseldorf.

Ritchie, R.O.; and Dauskardt, R.H. (1991): Cyclic Fatigue of Ceramics—A Fracture-Mechanics Approach to Subcritical Crack-Growth and Life Prediction. J. Ceram. Soc. Jpn., vol. 99, no. 10, pp. 1047–1062.

Ritter, J.E.; and Humenik, J.N. (1979): Static and Dynamic Fatigue of Polycrystalline Alumina. J. Mater. Sci., vol. 14, no. 3, pp. 626–632.

Ritter, J.E., Jr., et al. (1980): Proof Testing of Ceramics. Part 1—Experiment. J. Mater.Sci., vol. 15, pp. 2275–2281.

Rufin, Antonio C.; Samost, Dean R.; and Bollardt, R.J.H. (1984): Statistical Failure Prediction Models for Brittle Materials. AIAA J., vol. 22, no. 1, pp. 135–140.

Salem, J.A., et al. (1992): Mechanical-Behavior and Failure Phenomenon of an In Situ Toughened Silicon-Nitride. J. Mater. Sci., vol. 27, no. 16, pp. 4421–4428.

Salem, J.A., et al. (1996): Reliability Analysis of Uniaxially Ground Brittle Materials. J. Eng. Gas Turbines Power, vol. 118, no. 4, pp. 863–871.

Segall, Albert Eliot (1992): Thermal Shock and Fatigue Behavior of Ceramic Tubes. Ph.D. Thesis, Pennsylvania State University.

Service, Thomas H.; and Ritter, John E. (1986): Proof Testing to Assure Reliability of Structural Ceramics. Fracture Mechanics of Ceramics, R.C. Bradt, D.P.H. Hasselman, and F.F. Lange, eds., Plenum Press, New York, NY, pp. 255–264.

Shelleman, D.L., et al. (1991): Prediction of the Strength of Ceramic Tubular Components: Part 2. Experimental-Verification. J. Test. Eval., vol. 19, no. 3, pp. 192–200.

Shetty, D.K. (1987): Mixed-Mode Fracture Criteria for Reliability-Analysis and Design With Structural Ceramics. J. Eng. Gas Turbines Power, vol. 109, no. 3, pp. 282–289.

Shetty, D.K.; and Wang, J.S. (1989): Crack Stability and Strength Distribution of Ceramics That Exhibit Rising Crack-Growth-Resistance (R-Curve) Behavior. J. Am. Ceram. Soc., vol. 72, no. 7, pp. 1158–1162.

Shetty, D.K.; and Rosenfield, A.R. (1991): Slow Crack Growth in Glass in Combined Mode 1 and Mode II Loading. Scr. Metall. Mater., vol. 25, no. 5, pp. 997–1002.

Shih, T.T. (1980): Evaluation of the Probabilistic Approach to Brittle Design. Eng. Fract. Mech., vol. 13, no. 2, pp. 257–271.

Sih, G.C. (1973): Handbook of Stress-Intensity Factors; Stress-Intensity Factor Solutions and Formulas for Reference. Lehigh University, Bethlehem, PA.

Sih, G.C. (1974): Strain Energy Density Factor Applied to Mixed Mode Crack Problems. Internat. J. Fracture, vol. 10, no. 3, pp. 305–321.

Smith, F.W.; Emery, A.F.; and Kobayashi, A.S. (1967): Stress Intensity Factors for Semicircular Cracks. 2. Semi-Infinite Solid. J. App. Mech., vol. 34, no. 4, pp. 953–959.

Smith, F.W.; and Sorensen, D.R. (1974): Mixed Mode Stress Intensity Factors for Semielliptical Surface Cracks. NASA CR–134684.

Srinivasan, M.; and Seshadri, S.G. (1982): Probabilistic Design and Reliability of Silicon Carbide Ceramics. J. Mech. Des., vol. 104, pp. 635–642.

Stanley, P.; and Chau, F.S. (1983): A Probabilistic Treatment of Brittle-Fracture Under Non-Monotonically Increasing Stresses. Int. J. Fract., vol. 22, no. 3, pp. 187–202.

Stefansky, W. (1972): Rejecting Outliers in Factorial Designs. Technomet., vol. 14, no. 2, pp. 469–479.

Steffen, A.A.; Dauskardt, R.H.; and Ritchie, R.O. (1990): Cyclic Fatigue-Crack Propagation in Ceramics: Long and Small Crack Behavior. Proceedings of the 4th International Conference on Fatigue and Fatigue Thresholds, vol. 2, Materials and Component Engineering Publications, Edgbaston, Birmingham, pp. 745–752.

Stout, M.G.; and Petrovic, J.J. (1984): Multiaxial Loading Fracture of Al_2O_3 Tubes. 1. Experiments. J. Am. Ceram. Soc., vol. 67, no. 1, pp. 14–18.

Sturmer, G. (1991): Methodische Ansatze zur Konstruktiven Gestaltung Keramischer Flammrohrelemente von Bremmkammern. Ph.D. dissertation, Universität Karlsruhe, Germany.

Suresh, S.; and Brockenbrough, J.R. (1988): Theory and Experiments of Fracture in Cyclic Compression—Single-Phase Ceramics, Transforming Ceramics and Ceramic Composites. Acta Metall., vol. 36, no. 6, pp. 1455–1470.

Suresh, S. (1990): Fatigue Crack Growth in Ceramic Materials at Ambient and Elevated Temperatures. Fatigue 90—Proceedings of the 4th International Fatigue Conference, H. Kitagawa and T. Tanaka, eds, vol. II—Ceramics.

Swain, M.V.; and Zelizko, V. (1986): Comparison of Static and Cyclic Fatigue on Mg-PSZ Alloys. Advances in Ceramics, vol. 24B, pp. 595–606.

Sylva, L.A.; and Suresh, S. (1989): Crack Growth in Transforming Ceramics Under Cyclic Tensile Loads. J. Mater. Sci., vol. 24, no. 5, pp. 1729–1738.

Thiemeier, Thomas (1989): Lebensdauervorhersage für Keramische Bauteile Unter Mehrachsiger Beanspruchung. Ph.D. Thesis, Universität Karlsruhe, Germany.

Thoman, D.R.; Bain, L.J.; and Antle, C.E. (1969): Inferences on the Parameters of the Weibull Distribution. Technomet., vol. 11, no. 3, pp. 445–460.

Tracy, P.G., et al. (1982): On the Statistical Nature of Fracture. Internat. J. Fracture, vol. 18, no. 4, pp. 253–277.

Ueno, A., et al. (1990): Crack Propagation Behaviour of Sintered Silicon Nitride under Cyclic Load of High Stress Ratio and High Frequency. Proceedings of the Fourth International Conference on Fatigue and Fatigue Thresholds, vol. II, Materials and Components Engineering Publications Ltd., Edgbaston, Birmingham, pp. 733–738.

Visual Numerics (2004): IMSL™ Numerical Libraries Family of Products. http://www.vni.com/products/imsl/ Copyright 2004 and http://www.vni.com/company/dod/pdf/FortranFC.pdf

Walker, K. (1970): The Effect of Stress Ratio During Crack-Propagation and Fatigue for 2024–T3 and 7075–T6 Aluminum. Effects of Environment and Complex Load History on Fatigue Life. ASTM STP–462.

Weibull, Waloddi (1939a): A Statistical Theory of the Strength of Materials. Ingeniors Vetenskaps Akademien Handlingar, no. 151.

Weibull, W. (1939b): The Phenomenon of Rupture in Solids. Ingeniors Vetenskaps Akademien Handlingar, vol. 153, pp. 1–55.

Weibull, W. (1951): A Statistical Distribution Function of Wide Applicability. J. Appl. Mech. Trans. ASME, vol. 18, no. 3, pp. 293–297.

Wereszczak, Andrew W., et al. (1998): Strength Distribution Changes in a Silicon Nitride as a Function of Stressing Rate and Temperature. ASME 98–GT–527.

Wertz, John L.; and Heitman, Peter W. (1980): Predicting the Reliability of Ceramic Turbine Components. Advanced Gas Turbine Systems for Automobiles, SAE SP–465, pp. 69–77.

Wiederhorn, S.M. (1974a): Subcritical Crack Growth in Ceramics. Fracture Mechanics of Ceramics, Vol. 2, R.C. Bradt, ed., Plenum Press, New York, NY.

Wiederhorn, S.M. (1974b): Reliability, Life Prediction, and Proof Testing of Ceramics. Proceedings of the Second Army Materials Technology Conference, John J. Burke, Alvin E. Gorum, and R. Nathan Katz, eds., Brook Hill Publishing Co., Chestnut Hill, MA, pp. 633–663.

Wiederhorn, S.M.; Fuller, E.R., Jr.; and Thomson, R. (1980): Micromechanisms of Crack Growth in Ceramics and Glasses in Corrosive Environments. Metal Sci., vol. 14, pp. 450–458.

Wiederhorn, S.M.; and Fuller, E.R.J. (1985): Structural Reliability of Ceramic Materials. Mater. Sci. Eng., vol. 71, nos. 1–2, pp. 169–186.

Wiederhorn, S.M., et al. (1986): Creep and Fracture of a Vitreous-Bonded Aluminum-Oxide. J. Mater. Sci., vol. 21, no. 3, pp. 810–824.

Wittig, S.; Sturmer, G.; and Schulz, A. (1991): Life Time Prediction for Ceramic Gas Turbine Components. ASME Paper 91–GT–96.

Zelizko, V.; Grossmuller, A.; and Swain, M.V. (1988): Environment Assisted Fatigue Crack Behaviour of Mg-PSZ, Materials Science Forum, vol. 34–36, no. 1, pp. 201–205.

Zelizko, V.; and Swain, M.V. (1988): Influence of Surface Preparation on the Rotating Flexural Fatigue of Magnesium-PSZ, J. Mater. Sci., vol. 23, no. 3, pp. 1077–1082.

Ziegler, Christian (1998): Bewertung der Zuverlässigkeit keramischer Komponenten bei zeitlich veranderlichen Spannungen und bei Hochtemperaturbelastung. Ph.D. Thesis, Universität Karlsruhe, Germany.

REPORT DOCUMENTATION PAGE	*Form Approved* *OMB No. 0704-0188*

1. REPORT DATE *(DD-MM-YYYY)* xx-09-2005	**2. REPORT TYPE** Technical Paper	**3. DATES COVERED** *(From - To)*

4. TITLE AND SUBTITLE
Lifetime Reliability Prediction of Ceramic Structures Under Transient Thermomechanical Loads

5a. CONTRACT NUMBER

5b. GRANT NUMBER

5c. PROGRAM ELEMENT NUMBER

6. AUTHOR(S)
Nemeth, Noel, N.; Jadaan, Osama, M.; Gyekenyesi, John, P.

5d. PROJECT NUMBER

5e. TASK NUMBER

5f. WORK UNIT NUMBER
WBS-22-714-30-09

7. PERFORMING ORGANIZATION NAME(S) AND ADDRESS(ES)
National Aeronautics and Space Administration
John H. Glenn Research Center at Lewis Field
Cleveland, Ohio 44135-3191

8. PERFORMING ORGANIZATION REPORT NUMBER
E-14061

9. SPONSORING/MONITORING AGENCY NAME(S) AND ADDRESS(ES)
National Aeronautics and Space Administration
Washington, DC 20546-0001

10. SPONSORING/MONITOR'S ACRONYM(S)
NASA

11. SPONSORING/MONITORING REPORT NUMBER
NASA/TP-2005-212505

12. DISTRIBUTION/AVAILABILITY STATEMENT
Unclassified-Unlimited
Subject Category: 39
Available electronically at http://www.sti.nasa.gov
This publication is available from the NASA Center for AeroSpace Information, 443-757-5802

13. SUPPLEMENTARY NOTES
Noel N. Nemeth and John P. Gyekenyesi, NASA Glenn Research Center; and Osama M. Jadaan, University of Wisconsin, Platteville, Platteville, Wisconsin 53818. Responsible person, Noel N. Nemeth, organization code RSL, 216-433-3215. An errata was added to this document, August 2011.

14. ABSTRACT
An analytical methodology is developed to predict the probability of survival (reliability) of ceramic components subjected to harsh thermomechanical loads that can vary with time (transient reliability analysis). This capability enables more accurate prediction of ceramic component integrity against fracture in situations such as turbine startup and shutdown, operational vibrations, atmospheric reentry, or other rapid heating or cooling situations (thermal shock). The transient reliability analysis methodology developed herein incorporates the following features: fast-fracture transient analysis (reliability analysis without slow crack growth, SCG); transient analysis with SCG (reliability analysis with time-dependent damage due to SCG); a computationally efficient algorithm to compute the reliability for components subjected to repeated transient loading (block loading); cyclic fatigue modeling using a combined SCG and Walker fatigue law; proof testing for transient loads; and Weibull and fatigue parameters that are allowed to vary with temperature or time. Component-to-component variation in strength (stochastic strength response) is accounted for with the Weibull distribution, and either the principle of independent action or the Batdorf theory is used to predict the effect of multiaxial stresses on reliability. The reliability analysis can be performed either as a function of the component surface (for surface-distributed flaws) or component volume (for volume-distributed flaws). The transient reliability analysis capability has been added to the NASA CARES/*Life* (Ceramic Analysis and Reliability Evaluation of Structures/*Life*) code. CARES/*Life* was also updated to interface with commercially available finite element analysis software, such as ANSYS, when used to model the effects of transient load histories. Examples are provided to demonstrate the features of the methodology as implemented in the CARES/*Life* program.

15. SUBJECT TERMS
Reliability; Transient; Weibull; Fatigue; Failure; Batdorf; PIA; Proof test; Probability; Walker law; Power law; Slow crack growth; Stress; Strength; Ceramics; Brittle; CARES; Thermal shock; Cyclic loading; Silicon carbide; Silicon nitride; Alumina; Structural reliability; Component reliability

16. SECURITY CLASSIFICATION OF:			**17. LIMITATION OF ABSTRACT**	**18. NUMBER OF PAGES**	**19a. NAME OF RESPONSIBLE PERSON**
a. REPORT U	**b. ABSTRACT** U	**c. THIS PAGE** U	UU	187	STI Help Desk (email:help@sti.nasa.gov) **19b. TELEPHONE NUMBER** *(include area code)* 443-757-5802